



# International Agreement Report

## An Assessment of the CORCON-MOD3 Code

### Part I: Thermal-Hydraulic Calculations

Prepared by  
V. Strizhov, V. Kanukova, T. Vinogradova, E. Askenov  
Institute of Nuclear Safety  
Russian Academy of Sciences

V. Nikulshin  
Kurchatov Institute  
Russian Research Center

Office of Nuclear Regulatory Research  
U.S. Nuclear Regulatory Commission  
Washington, DC 20555-0001

September 1996

Prepared as part of the Agreement on Research and Technical Exchange under the International  
Thermal-Hydraulic Code Assessment and Application Program

Published by  
U.S. Nuclear Regulatory Commission

9612040179 960930  
PDR NUREG  
IA-0129 R PDR

0102  
0/1

## AVAILABILITY NOTICE

### Availability of Reference Materials Cited in NRC Publications

Most documents cited in NRC publications will be available from one of the following sources:

1. The NRC Public Document Room, 2120 L Street, NW., Lower Level, Washington, DC 20555-0001
2. The Superintendent of Documents, U.S. Government Printing Office, P. O. Box 37082, Washington, DC 20402-9328
3. The National Technical Information Service, Springfield, VA 22161-0002

Although the listing that follows represents the majority of documents cited in NRC publications, it is not intended to be exhaustive.

Referenced documents available for inspection and copying for a fee from the NRC Public Document Room include NRC correspondence and internal NRC memoranda; NRC bulletins, circulars, information notices, inspection and investigation notices; licensee event reports; vendor reports and correspondence; Commission papers; and applicant and licensee documents and correspondence.

The following documents in the NUREG series are available for purchase from the Government Printing Office: formal NRC staff and contractor reports, NRC-sponsored conference proceedings, international agreement reports, grantee reports, and NRC booklets and brochures. Also available are regulatory guides, NRC regulations in the *Code of Federal Regulations*, and *Nuclear Regulatory Commission Issuances*.

Documents available from the National Technical Information Service include NUREG-series reports and technical reports prepared by other Federal agencies and reports prepared by the Atomic Energy Commission, forerunner agency to the Nuclear Regulatory Commission.

Documents available from public and special technical libraries include all open literature items, such as books, journal articles, and transactions. *Federal Register* notices, Federal and State legislation, and congressional reports can usually be obtained from these libraries.

Documents such as theses, dissertations, foreign reports and translations, and non-NRC conference proceedings are available for purchase from the organization sponsoring the publication cited.

Single copies of NRC draft reports are available free, to the extent of supply, upon written request to the Office of Administration, Distribution and Mail Services Section, U.S. Nuclear Regulatory Commission, Washington, DC 20555-0001.

Copies of industry codes and standards used in a substantive manner in the NRC regulatory process are maintained at the NRC Library, Two White Flint North, 11545 Rockville Pike, Rockville, MD 20852-2738, for use by the public. Codes and standards are usually copyrighted and may be purchased from the originating organization or, if they are American National Standards, from the American National Standards Institute, 1430 Broadway, New York, NY 10018-3308.

## DISCLAIMER NOTICE

This report was prepared under an international cooperative agreement for the exchange of technical information. Neither the United States Government nor any agency thereof, nor any of their employees, makes any warranty, expressed or implied, or assumes any legal liability or responsibility for any third party's use, or the results of such use, of any information, apparatus, product, or process disclosed in this report, or represents that its use by such third party would not infringe privately owned rights.





NUREG/IA-0129  
Part I

# International Agreement Report

---

## An Assessment of the CORCON-MOD3 Code

### Part I: Thermal-Hydraulic Calculations

Prepared by  
V. Strizhov, V. Kanukova, T. Vinogradova, E. Askenov  
Institute of Nuclear Safety  
Russian Academy of Sciences

V. Nikulshin  
Kurchatov Institute  
Russian Research Center

Office of Nuclear Regulatory Research  
U.S. Nuclear Regulatory Commission  
Washington, DC 20555-0001

September 1996

Prepared as part of the Agreement on Research and Technical Exchange under the International  
Thermal-Hydraulic Code Assessment and Application Program

Published by  
U.S. Nuclear Regulatory Commission

## ABSTRACT

This report deals with the subject of CORCON-Mod3 code validation (thermal-hydraulic modeling capability only) based on MCCI experiments conducted under different programs in the past decade. Thermal-hydraulic calculations (i.e., concrete ablation, melt temperature, melt energy, concrete temperature, and condensible and non-condensable gas generation) were performed with the code, and compared with the data from 15 experiments, conducted at different scales using both simulant (metallic and oxidic) and prototypic melt materials, using different concrete types, and with and without an overlying water pool. Sensitivity studies were performed in a few cases involving, for example, heat transfer from melt to concrete, condensed phase chemistry, etc. Further, special analysis was performed using the ACE L8 experimental data to illustrate the differences between the experimental and the reactor conditions, and to demonstrate that with proper corrections made to the code, the calculated results were in better agreement with the experimental data.

Generally, in the case of dry cavity and metallic melts, CORCON-Mod3 thermal-hydraulic calculations were in good agreement with the test data. For oxidic melts in a dry cavity, uncertainties in heat transfer models played an important role for two melt configurations – a stratified geometry with segregated metal and oxide layers, and a heterogeneous mixture. Some discrepancies in the gas release data were noted in a few cases. These discrepancies were attributed, in part, to condensed phase chemical reactions modeling and, in part, to experimental uncertainties. In the case of wet cavity, good agreement was found between the experimental data and code calculations except, again, for the gas release data. With proper corrections made to the code to account for correct condensed phase chemistry and with corrections made to the input data to account for experimental uncertainties, better agreement between code calculations and experimental data was noted.

## CONTENTS

<b>1</b>	<b>INTRODUCTION</b>	<b>1</b>
1.1	Background . . . . .	1
1.2	Main Improvements of CORCON-Mod3 . . . . .	2
1.3	CORCON Assessment and Validation . . . . .	2
1.4	CORCON-Mod2 Previous Calculations . . . . .	3
<b>2</b>	<b>GENERIC CAPABILITIES OF CORCON-Mod3 MODELS</b>	<b>5</b>
2.1	CORCON-Mod3 General Approach . . . . .	5
2.2	Overall Energy Balance . . . . .	6
2.3	Concrete Behavior at High Temperatures . . . . .	7
2.3.1	Concrete Properties . . . . .	7
2.3.2	Concrete Decomposition Model . . . . .	9
2.4	Thermal Behavior of Layers . . . . .	10
2.4.1	Metal Layer Solidus and Liquidus Temperatures . . . . .	10
2.4.2	Oxide Layer Solidus and Liquidus Temperatures . . . . .	10
2.4.3	Crust Formation and Freezing . . . . .	12
2.4.4	Chemical Reactions . . . . .	12
2.5	CORCON Modifications for Modeling MCCI Tests . . . . .	14
2.5.1	Idiosyncrasies of MCCI Tests . . . . .	14
2.5.2	Modifications Made for Validation . . . . .	15

<b>3</b>	<b>MODELING OF ACE TESTS</b>	<b>17</b>
3.1	ACE Phase C MCCI Program . . . . .	17
3.1.1	ACE Test Apparatus and Instrumentation . . . . .	17
3.1.2	ACE Test Scenarios . . . . .	19
3.1.3	General CORCON Input Conditions for ACE Tests . . . . .	21
3.2	Modeling of the ACE L5 Test . . . . .	22
3.2.1	Test Conditions and Results . . . . .	22
3.2.2	Comparison to ACE L5 Test Data . . . . .	25
3.3	Modeling of the ACE L2 Test . . . . .	25
3.3.1	Test Conditions and Results . . . . .	25
3.3.2	Comparison to ACE L2 Test Data . . . . .	29
3.4	Modeling of the ACE L6 Test . . . . .	30
3.4.1	Test Conditions and Results . . . . .	30
3.4.2	Comparison to ACE L6 Test Data . . . . .	34
3.5	Modeling of the ACE L7 Test . . . . .	40
3.5.1	Test Conditions and Results . . . . .	40
3.5.2	Comparison to ACE L7 Test Data . . . . .	41
3.6	Modeling of the ACE L4 Test . . . . .	43
3.6.1	Test Conditions and Results . . . . .	43
3.6.2	Comparison to ACE L4 Test Data . . . . .	49
3.7	Modeling of the ACE L8 Test . . . . .	50
3.7.1	Test Conditions and Results . . . . .	50
3.7.2	Comparison to ACE L8 Test Data . . . . .	55
3.8	Detailed Analysis of ACE L8 Test Data . . . . .	62
3.8.1	Method of Data Analysis . . . . .	63
3.8.2	Results of ACE L8 Data Analysis . . . . .	65

<b>4</b>	<b>MODELING OF SURC TESTS</b>	<b>73</b>
4.1	Modeling of the SURC-1 Test . . . . .	75
4.1.1	Test Apparatus . . . . .	75
4.1.2	SURC-1 Test Results . . . . .	75
4.1.3	CORCON Input Parameters . . . . .	76
4.1.4	Comparison to SURC-1 Test Data . . . . .	77
4.2	Modeling of the SURC-2 Test . . . . .	78
4.2.1	SURC-2 Test Results . . . . .	78
4.2.2	Comparison to SURC-2 Test Data . . . . .	82
4.3	Modeling of the SURC-3 Test . . . . .	83
4.3.1	Test Apparatus and Results . . . . .	83
4.3.2	Comparison to SURC-3 Data . . . . .	87
4.4	Modeling of the SURC-3A Test . . . . .	88
4.4.1	Test Apparatus and Results . . . . .	88
4.4.2	Comparison to SURC-3A Data . . . . .	91
4.5	Modeling of the SURC-4 Test . . . . .	93
4.5.1	Test Apparatus and Results . . . . .	96
4.5.2	Comparison to SURC-4 Test Data . . . . .	101
<b>5</b>	<b>MODELING OF THE BETA V7.1 TEST</b>	<b>106</b>
5.1	Description of the BETA Facility . . . . .	106
5.2	Test Conditions and Results . . . . .	107
5.3	Comparison to BETA V7.1 Test Data . . . . .	107
<b>6</b>	<b>MODELING OF TESTS WITH AN OVERLYING WATER POOL</b>	<b>112</b>
6.1	Modeling of SWISS Tests . . . . .	112
6.1.1	SWISS Test Apparatus and Results . . . . .	112



6.1.2	Comparison to Test Data . . . . .	116
6.2	Modeling of the MACE-M1b Test . . . . .	124
6.2.1	Test Description and Results . . . . .	124
6.2.2	Comparison to MACE M1b Data . . . . .	125
<b>A INPUT DECKS</b>		<b>136</b>

## TABLES

1.1	Large scale tests . . . . .	3
2.1	Chemical compositions of concretes (values in w/o) . . . . .	8
2.2	Solidus and liquidus temperatures of concretes . . . . .	8
2.3	Range of uncertainties for $T_{dc}$ and enthalpies of decomposition . . . . .	9
2.4	Comparison of experimental and CORCON solidus and liquidus data . . .	11
2.5	Equilibrium chemical components for Si oxidation . . . . .	13
3.1	ACE MCCI test matrix . . . . .	18
3.2	Oxide components of the melt of the ACE tests . . . . .	19
3.3	Metal components of the melt of the ACE tests . . . . .	19
3.4	Scenarios of interaction for ACE tests . . . . .	20
3.5	Summary of ACE experiments thermal hydraulic results . . . . .	20
3.6	Summary of CORCON-Mod3 input parameters for ACE tests . . . . .	23
3.7	Gas release during test L5 . . . . .	24
3.8	Estimate of energy balance in test L5 . . . . .	24
3.9	Estimate of energy balance in test L2 . . . . .	28
3.10	Gas release during test L6 . . . . .	33
3.11	Energy balance summary in MJ for ACE L6 . . . . .	34
3.12	The composition of rebar insert for L6 test . . . . .	35
3.13	Energy balance summary for ACE L7 . . . . .	41

3.14	Gas release during test L7 . . . . .	41
3.15	Main parameters of concrete/metal insert in test L7 . . . . .	42
3.16	Energy balance summary for ACE L4 . . . . .	48
3.17	Gas release during test L4 . . . . .	48
3.18	Energy balance summary for ACE L8 . . . . .	54
3.19	Gas release during test L8 . . . . .	54
3.20	CORCON options to model insert rebar . . . . .	55
3.21	Calculated scenario of ACE L8 test . . . . .	57
3.22	Cumulative heat flows in melt for different times . . . . .	71
4.1	Melt components of the SURC tests . . . . .	73
4.2	Summary of SURC experiments thermal hydraulic results . . . . .	74
4.3	Summary of input data for CORCON-Mod3 . . . . .	74
4.4	SURC-1 test summary data . . . . .	76
4.5	SURC-2 test summary data . . . . .	81
4.6	Chemical composition of 304 stainless steel . . . . .	86
4.7	SURC-3 test summary data . . . . .	87
4.8	SURC-3A test summary data . . . . .	92
4.9	Events of SURC-4 test . . . . .	97
4.10	SURC-4 test summary data . . . . .	97
4.11	SURC-4 rough energy balance . . . . .	100
5.1	Melt composition (in kg) at the start of interaction with the concrete . .	107
5.2	Depths of concrete ablation in axial and radial directions for different heat transfer models . . . . .	108
6.1	Initial melt composition for SWISS tests . . . . .	113
6.2	Timing of events for SWISS-1 experiment . . . . .	113

6.3	Timing of events for SWISS-2 experiment . . . . .	114
6.4	CORCON input options . . . . .	117
6.5	Composition of the melt for MACE-M1b test . . . . .	124

## FIGURES

2.1	Binary equilibrium phase diagram of the $Fe - Zr$ system. . . . .	11
3.1	ACE L5 concrete erosion depth . . . . .	26
3.2	ACE L5 temperature of oxide layer . . . . .	26
3.3	Energy rate terms for ACE L5 test . . . . .	27
3.4	ACE L5 $CO_2$ and $H_2O$ flow rates . . . . .	27
3.5	ACE L5 mass of metals . . . . .	28
3.6	ACE L2 concrete erosion depth . . . . .	30
3.7	ACE L2 mass of metals ( $Fe, Si, Zr$ ) . . . . .	31
3.8	ACE L2 temperature of oxide layer . . . . .	31
3.9	Energy rate terms for ACE L2 test . . . . .	32
3.10	ACE L2 $CO$ flow rate . . . . .	32
3.11	ACE L2 $H_2$ flow rate . . . . .	33
3.12	ACE L6 concrete erosion depth . . . . .	36
3.13	Temperature of oxide layer for ACE L6 test . . . . .	37
3.14	Energy rate terms for ACE L6 test . . . . .	37
3.15	Mass of metals in the melt for ACE L6 test . . . . .	38
3.16	$CO$ flow rate for ACE L6 test . . . . .	38
3.17	$H_2$ flow rate for ACE L6 test . . . . .	39
3.18	Concrete erosion depth for ACE L6 (sensitivity case) . . . . .	39
3.19	Energy rate terms for ACE L6 test (sensitivity case) . . . . .	40



3.20	ACE L7 concrete erosion depth . . . . .	43
3.21	Temperature of oxide layer for ACE L7 test . . . . .	44
3.22	Energy rate terms for ACE L7 test . . . . .	44
3.23	ACE L7 mass of metals ( <i>Fe, Si, Zr</i> ) . . . . .	45
3.24	ACE L7 <i>CO</i> flow rate . . . . .	45
3.25	ACE L7 <i>CO</i> <sub>2</sub> flow rate . . . . .	46
3.26	ACE L7 <i>H</i> <sub>2</sub> flow rate . . . . .	46
3.27	ACE L7 <i>H</i> <sub>2</sub> <i>O</i> flow rate . . . . .	47
3.28	ACE L4 concrete erosion depth . . . . .	50
3.29	Energy rate terms for ACE L4 test . . . . .	51
3.30	Temperature of oxide layer for ACE L4 test . . . . .	51
3.31	Mass of metals in the melt for ACE L4 test . . . . .	52
3.32	<i>H</i> <sub>2</sub> flow rate for ACE L4 test . . . . .	52
3.33	<i>CO</i> flow rate for ACE L4 test . . . . .	53
3.34	Total <i>H</i> <sub>2</sub> release for ACE L4 test . . . . .	53
3.35	ACE L8 concrete erosion depth . . . . .	57
3.36	ACE L8 mass of metals ( <i>Fe, Si, Zr</i> ) . . . . .	58
3.37	Temperature of oxide layer for ACE L8 test . . . . .	58
3.38	Temperature of metal layer for ACE L8 test . . . . .	59
3.39	Energy rate terms for ACE L8 test . . . . .	59
3.40	Thickness of crust at the melt-concrete interface . . . . .	60
3.41	Comparison of <i>H</i> <sub>2</sub> flow rate for ACE L8 test . . . . .	60
3.42	Comparison of <i>H</i> <sub>2</sub> <i>O</i> flow rate for ACE L8 test . . . . .	61
3.43	Comparison of <i>CO</i> flow rate for ACE L8 test . . . . .	61
3.44	Comparison of <i>CO</i> <sub>2</sub> flow rate for ACE L8 test . . . . .	62
3.45	Thermocouples location in the ACE L8 basemat . . . . .	64

3.46	Temperature fronts at 0 min (vertical WE section) in ACE L8 . . . . .	66
3.47	Temperature fronts at 0 min (vertical NS section) in ACE L8 . . . . .	67
3.48	Time dependence of 400 K front (vertical WE section) . . . . .	67
3.49	Time dependence of 400 K front (vertical NS section) . . . . .	68
3.50	Comparison of the calculated and measured gas release in ACE L8 . . . . .	69
3.51	Total $CO_2$ release (symmetrical approach) . . . . .	69
3.52	Comparison of thermocouple data of 1673 K front with with 400 K, 700 K, and 1000 K fronts . . . . .	71
4.1	SURC-1 concrete erosion depth . . . . .	78
4.2	Energy rate terms for SURC-1 test . . . . .	79
4.3	SURC-1 Temperature of oxide layer . . . . .	79
4.4	Mass of metals in the melt for SURC-1 test . . . . .	80
4.5	SURC-1 $CO$ and $CO_2$ flow rates . . . . .	80
4.6	SURC-1 $H_2$ and $H_2O$ flow rates . . . . .	81
4.7	SURC-2 concrete erosion depth . . . . .	83
4.8	Energy rate terms for SURC-2 test . . . . .	84
4.9	SURC-2 temperature of oxide layer . . . . .	84
4.10	Mass of metals in the melt for SURC-1 test . . . . .	85
4.11	SURC-2 $CO$ and $H_2$ flow rates . . . . .	85
4.12	SURC-3 concrete erosion depth . . . . .	89
4.13	SURC-3 temperature of metal layer . . . . .	89
4.14	Energy term rates for SURC-3 test . . . . .	90
4.15	Mass of metals in the melt for SURC-3 test . . . . .	90
4.16	SURC-3 $CO$ and $H_2$ flow rates . . . . .	91
4.17	SURC-3A concrete erosion depth . . . . .	93
4.18	SURC-3A temperature of metal layer . . . . .	94

4.19	Energy term rates for SURC-3A test . . . . .	94
4.20	Mass of metals in the melt for SURC-3A test . . . . .	95
4.21	SURC-3A $H_2$ and $CO$ flow rates . . . . .	95
4.22	SURC-4 concrete erosion depth . . . . .	102
4.23	Energy rate terms predicted by CORCON for SURC-4 test . . . . .	103
4.24	SURC-4 predicted mass of metals in the meltpool . . . . .	103
4.25	SURC-4 comparison of predicted and experimental temperatures of metal layer . . . . .	104
4.26	SURC-4 comparison of CORCON $H_2$ flow rate results to test data . . . .	104
4.27	SURC-4 comparison of CORCON $CO$ flow rate results to test data . . . .	105
5.1	Energy rate terms for BETA . . . . .	109
5.2	BETA concrete erosion depth . . . . .	109
5.3	BETA temperature of metal layer . . . . .	110
5.4	Comparison to $H_2$ release for BETA 7.1 test . . . . .	110
5.5	Comparison to $H_2O$ release for BETA 7.1 test . . . . .	111
6.1	Comparison to SWISS-1 ablation results . . . . .	118
6.2	Energy rate terms predicted by CORCON for SWISS-1 test . . . . .	118
6.3	Predicted temperature for SWISS-1 test . . . . .	119
6.4	Predicted crust thickness for SWISS-1 test . . . . .	119
6.5	Gas flow rates predictions for SWISS-1 test . . . . .	120
6.6	Comparison to SWISS-2 ablation results . . . . .	121
6.7	Energy rate terms predicted by CORCON for SWISS-2 test . . . . .	121
6.8	Predicted temperature for SWISS-2 test . . . . .	122
6.9	Gas flow rates predictions for SWISS-2 test . . . . .	122
6.10	Predicted crusts thickness for SWISS-2 test . . . . .	123

6.11 Comparison to SWISS-2 upward heat flux . . . . .	123
6.12 MACE Concrete erosion depth . . . . .	126
6.13 Mass of metals for MACE-M1b test . . . . .	127
6.14 Predicted crust thickness for MACE-M1b test . . . . .	127
6.15 Predicted energy term rates for MACE-M1b test . . . . .	128
6.16 Comparison to MACE-M1b temperature of oxide layer . . . . .	128
6.17 Comparison to water mass in the test section . . . . .	129
6.18 Comparison to $CO$ flow rate for MACE-M1b test . . . . .	129
6.19 Comparison to $CO_2$ flow rate for MACE-M1b test . . . . .	130
6.20 Comparison to $H_2$ flow rate for MACE-M1b test . . . . .	130
6.21 Comparison to total $CO$ release for MACE-M1b test . . . . .	131
6.22 Comparison to total $CO_2$ release for MACE-M1b test . . . . .	131

## EXECUTIVE SUMMARY

Reactor risk studies such as NUREG-1150 have indicated the importance of several severe accident issues related to postulated core melt accidents in light water reactor nuclear power plants. Molten core concrete interaction (MCCI) is one such issue that is relevant in understanding the potential risk from ablation of concrete structures in the reactor cavity, fission products release into containment and environment, and flammable gas generation in the course of concrete decomposition. Debris coolability is a related issue that is relevant when considering countermeasures to prevent concrete ablation and mitigate other negative consequences of MCCI.

The CORCON-Mod3 computer code was developed for analyzing important core-concrete interaction phenomena, including those that are relevant to the assessment of containment thermal hydraulics and fission product release. Models in CORCON-Mod3 include heat transfer between core debris and concrete, and between core debris and coolant (an overlying water pool). Both homogeneous and stratified melts can be treated by the code. During core-concrete interaction, melt stratification from an initially homogeneous layer is modeled in the code as is layer inversion in a stratified geometry. Both gas-phase and condensed-phase chemical reactions are modeled in the code, largely in terms of equilibrium chemistry. The non-equilibrium chemistry model is implemented in the code in principle, but can only be utilized effectively for a very limited number of chemical species. Generation of aerosols and release of fission products are modeled in the code through its VANESA module.

During the past decade, a large number of experiments were performed to provide a data base for the validation of CORCON-Mod3. These experiments were conducted at different scales, using both simulant (metallic and oxidic) and prototypic melt materials, and with and without an overlying water pool. An axisymmetric reactor cavity geometry was used in these experiments, and the internal heat generation was simulated to represent reactor prototypic conditions. Most experiments were one dimensional in nature, i.e., the boundary conditions were such as not to permit any radial concrete erosion. The experimental measurements generally included concrete ablation depth, melt temperature, concrete basemat temperature, sidewall temperature, system pressure, condensable and non-condensable gas generation, and aerosol and fission product generation.

This report deals with the subject of CORCON-Mod3 validation (thermal-hydraulics modeling capability only) based on MCCI experiments conducted under different programs (SURC, ACE, MACE, SWISS and BETA). Specifically, 15 input decks were developed based on ACE (L2, L4, L5, L6, L7, L8), SURC (SURC-1, SURC-2, SURC-3, SURC-3A, SURC-4), SWISS (SWISS-1, SWISS-2), MACE M1b, and BETA7.1 tests, and the code calculations were performed with these decks. Thermal hydraulic calculations performed (i.e., concrete ablation, melt temperature, melt energy, and condensable and non-condensable gas generation) were compared with the experimental data to determine the predictive capability of the code. Sensitivity studies were performed in some cases involving, for example, heat transfer from melt to concrete, condensed phase chemistry, etc. A second report, to be published in the future, will describe the results of aerosol and fission product calculations, and comparison of the same with the experimental data. Attention was given to the energy balance in the experiments and its verification in the code exercise.



Generally, in the case of dry cavity and metallic melts, CORCON-Mod3 thermal-hydraulic calculations were found to be in good agreement with the test data. For oxidic melts in a dry cavity, uncertainties in heat transfer models played an important role for two melt configurations - a stratified geometry with segregated metal and oxide layers, and a heterogeneous mixture. Some discrepancies in the gas release estimates were noted in a few cases. These discrepancies were attributed, in part, to condensed phase chemical reactions modeling and, in part, to experimental uncertainties. In the case of wet cavity, good agreement was found between the experimental data and code calculations except, again, for the gas release data. The CORCON-Mod3 assessment against SWISS and MACE experiments indicate that the crust model in the code may often lead to sudden appearance and disappearance of crusts in a single calculational time step (very small time). This crust instability is an artifact of the model employed in the code.

Results of the code validation exercise made it evident that differences exist between the experimental data and the code predictions. Special analysis was performed using the ACE L8 data to illustrate the differences and to make code modifications so that the calculated values are in better agreement with the experimental data. The analysis involves construction of isotherms (400K, 700K, 1000K, and 1673K) from the thermocouple data and use of these isotherms to make proper corrections to temperature profiles. These isotherms revealed the three-dimensional nature of temperature profiles in the concrete basemat, thus explaining the significant differences between the experimental gas release data and the code calculations. The analysis also demonstrated that when proper corrections were made to the temperature profiles, the code prediction of gas release was in better agreement with the experimental data, for example, for carbon dioxide release (code overpredicted the experimental value by 5% after corrections whereas underpredicted by 20% before corrections). For water release, however, the difference between the experimental value and the predicted value was 30% when the same isotherm (1000K corresponding to the carbonate decomposition temperature used in carbon dioxide release calculations) was considered. Only when a lower isotherm (700K corresponding to the bound water release temperature) was considered, the code prediction of water release was in better agreement (within 15%) of the experimental data. While gas release predictions for individual species show improvements when three-dimensional temperature profiles are accounted for, the combined gas release prediction is not affected as such. This suggests that for integral plant calculations, further modifications of CORCON-Mod3 in this area is not warranted.

The validation exercise revealed that the CORCON-Mod3 model dealing with chemical reactions in the metallic melt is important with regard to the code's thermal-hydraulic capability. Specifically, two types of oxidation reactions with two metallic components - zirconium and silicon - are important. Silicon appears in the melt as a result of condensed phase reactions between zirconium and silica. The chemical heat release resulting from these reactions is exothermic at low temperatures, and endothermic at high temperatures when  $SiO(g)$  is formed. Using thermodynamic data bases, the temperature at which the reaction changes from exothermic to endothermic is estimated to be about 2350 K. The analysis, presented in this report, provides information concerning a possible range of uncertainties in calculations for tests where temperature exceeds the above value. The uncertainties are related to the formation of  $SiO(g)$  which is not modeled in the CORCON-Mod3 chemistry package. While in plant calculations involving siliceous concrete interacting with the core debris, consideration of the  $SiO$  chemistry model will improve the gas release prediction, overall improvement in thermal-hydraulic and fission product prediction over the entire duration of core-concrete interactions is not likely to be significant.

## ACKNOWLEDGMENTS

This work was sponsored by the U.S. Nuclear Regulatory Commission. The authors would like to express their gratitude to Dr. T. Speis of the Office of Nuclear Regulatory Research for his support of this work. Dr. S. Basu provided the technical guidance for this work. His many suggestions during the course of this work and preparation of the report are very much appreciated.

# 1 INTRODUCTION

It was recognized in the Reactor Safety Study (WASH-1400) that molten core concrete interaction (MCCI) during severe accidents plays an important role in risk estimates [1]. Potential hazards from MCCI include:

- Long-term thermal interaction of the melt with concrete basemat as a result of decay heat from fission products (FP) retained in the melt, and possible contamination of underlying soils and underground water after concrete basemat melt-through
- Containment failure due to overpressure by noncondensable gas release in course of interactions and concrete decomposition
- Flammable gas production, their burning and/or detonation and as a consequence, the dynamic containment loading and its failure
- High FP generation rate due to vaporization and contamination of atmosphere in case of containment failure.

These potential hazards may be mitigated by flooding the concrete reactor cavity. An overlying water pool may reduce significantly both the thermal loads to concrete structures and the FP release.

## 1.1 Background

The CORCON-Mod3 is a computer code for modeling molten core concrete interactions and fission products release into the containment in the course of severe core melt accident. The code was developed at the Sandia National Laboratories (SNL). The latest version of the code [2] was released in February 1993 and contains both thermal-hydraulic models and integrated VANESA model for radionuclide release in the course of MCCI. The first version of the code (CORCON-Mod1) was released in 1981 [3]. It considered thermal-hydraulic behavior of a molten pool and concrete structures, but had some limitations which were subsequently removed in the second version, CORCON-Mod2 [4]. Parallel development of aerosol release models due to MCCI was realized in the computer code VANESA [5] which was released in 1985. CORCON and VANESA codes were implemented in the Source Term Code Package [6] and later, incorporated in the system level severe accident codes MELCOR [7] and CONTAIN [8].

In addition to CORCON, WECHSL [9], DECOMP [10] and recently developed RASPLAV [11] codes are also used for the analysis of MCCI.

## 1.2 Main Improvements of CORCON-Mod3

The main modifications in CORCON-Mod3 are the follows:

- Implementation of the VANESA code which includes models for radionuclide release from the melt and aerosol scrubbing models
- Implementation of non-ideal chemistry treatment for metal and oxide phase constituents (full treatment for metals but limited for oxides)
- Implementation of the condensed phase reactions between oxide species and metals
- Improvement of molten core-concrete heat transfer models, and addition of slag model to simulate direct contact between the core debris and the concrete
- Improvement of coolant heat transfer model and models for bubble phenomena
- Implementation of a simple parametric model to simulate core spreading phenomena
- Implementation of interlayer mixing models due to entrainment and settling of droplets.

## 1.3 CORCON Assessment and Validation

Starting with transient TURC tests [12, 13] conducted at SNL to sustained core concrete interaction tests, the experimental work provided an extensive data base for code validation. Table 1.1 presents some of the large scale tests performed at SNL [31], Argonne National Laboratory (ANL) [30], and Kernforschungszentrum Karlsruhe (KfK) [32, 33]. These tests cover a broad range of input power conditions, different types of concrete (basaltic, limestone, limestone-common sand and siliceous), and both metallic and oxidic melts. The chemical reactions of zirconium (and other metals) at high temperatures were also investigated in some of these tests. Moreover, several MCCI experiments were conducted with an overlying water pool [34, 35]. These tests provide important information on the thermal hydraulic behavior of concrete basemat and fission product releases in the presence of an overlying water pool.

Assessments of the MCCI codes to experimental data fall into three main categories which are:

- Heat transfer behavior of the melt and basemat ablation
- Chemical reactions and gas release due to interactions of primary concrete materials with the melt (mainly flammable gas production due to chemical reactions in corium)
- Fission product release in the course of interaction.

Table 1.1: Large scale tests

Test	Melt Composition	Geometry(Size)	Concrete	Heating Method
SURC-4	SS+Zr	1D(40 cm)	Basaltic	Inductive
SURC-3	SS+Zr	1D(20 cm)	Limestone	Inductive
SURC-3A	SS+Zr	2D(20 cm)	Limestone	Inductive
SURC-1	Oxidic(Zr)	1D(40 cm)	Limestone	Inductive (5
SURC-2	Oxidic(Zr)		Basaltic	W rings inside the charge)
BETA-1,2,5	SS+Zr	2D(40 cm)	Siliceous	Inductive
BETA V7.1	SS+Zr	2D(38 cm)	Serpentine	Inductive
ACE L1-L8	Oxidic	1D(50x50 cm)	All types	Direct Current
SWISS-1,2	SS(Water)	1D(20 cm)	LCS	Inductive
MACE-0,1	Oxidic(Water)	2D(30 cm)	LCS	Inductive

## 1.4 CORCON-Mod2 Previous Calculations

For the validation of CORCON-Mod3, especially from the point of view of assessing the effects of modifications on the predictive capability of the code, it is important to discuss briefly calculations of MCCI experiments using previous versions of the code, specifically CORCON-Mod2.

In the first blind code comparison of the SURC-4 experiment [14], four participants used the CORCON-Mod2 code. Concrete erosion depth calculated by these participants varied widely, but most participants predicted within 20% of the experimentally measured value. More significant discrepancies were found in the predictions of *CO* release rate because in course of *Zr* oxidation, coking reaction with pure carbon formation was the only possibility in the CORCON-Mod2. Melt temperature increase was not predicted after zirconium addition, and the actual temperature increase observed in the experiment was interpreted as a manifestation of condensed phase reactions not modeled in the code. Recent calculations of SURC-4 test performed by Bradley [36] using CORCON-Mod3 (with condensed phase chemistry implemented) showed reasonable agreement with the experimental data in terms of temperature and erosion depth. These calculations assumed that foaming of the melt prevented radiative heat exchange after *Zr* addition so that upper boundary conditions were close to adiabatic.

Post-test analysis of SURC-4 experiment was also made at the the Institute of Nuclear Safety (IBRAE) [15] with both the CORCON-Mod2 and the RASPLAV codes. Calculations were performed with simple implementation of *Zr* - *SiO*<sub>2</sub> reaction, and coking reaction was disabled. Qualitative agreement was obtained in these calculations.

Bradley's calculations of SURC-1 test with CORCON-Mod3 [36] were made using adiabatic boundary conditions on the upper surface of the melt. Calculated results of erosion depth and



melt temperature behavior show good agreement with the experimental data. In both SURC-4 and SURC-1 tests, slag film model was used for the melt concrete interface boundary.

Calculations and comparison of several BETA tests with silicate concrete were performed using the CORCON-Mod2 and the WECHSL codes [16]. Initial calculations showed a wide transition region between the heat transfer governed by discrete bubbles and by a continuous gas film. Reasonable agreement between code predictions and test data was obtained after corresponding modifications of the pool/concrete interfacial heat transfer was made.

The blind comparison of the ACE L6 experiment [17] also showed a factor of two difference between various codes for the erosion depth, and the discrepancies in fission product releases [18] were much greater (up to an order of magnitude or more).

## 2 GENERIC CAPABILITIES OF CORCON-Mod3 MODELS

### 2.1 CORCON-Mod3 General Approach

CORCON represents the debris pool as a structure which consists of seven layers separated due to the density difference. The heavy oxide phase (HOX) constitutes core materials  $UO_2$  and  $ZrO_2$  which appear after the temperature escalation, intensive oxidation of cladding, and melting and relocation of molten materials. The metal phase layer (MET) is formed by metallic components ( $Fe, Cr, Ni, Zr$ ) of the core and supporting structures. Oxidic products of concrete decomposition ( $SiO_2, CaO$ , etc.) form a light oxide layer (LOX). Two intermediate layers, HMX and LMX, represent heterogeneous mixtures of heavy oxides and metals, and of light oxides and metals, respectively. Two remaining layers are used to define the presence of coolant (CLN) and atmosphere (ATM). The orientation of layers is governed by a special subroutine ORIENT which analyzes the densities of layers and rearranges the melt structure in the course of interaction. The change of layers (layer turnover) is allowed when the density difference criterion is satisfied.

The list of allowable chemical species included in the CORCON master list consists of about 70 elementary substances which represent the main oxide, metal and gas species. Some new species are included in the master list since CORCON-Mod2 (e.g.,  $Si, Al, U$ , etc. for metal layer,  $UO_3, U_3O_8$  for oxides, and gaseous components of aluminum, hydrogen and oxygen compositions). Several species are reserved for concrete components (e.g., chemically and physically bound water,  $CaCO_3$  and  $Ca(OH)_2$ , etc.) so concrete may be specified both in terms of compounds and in terms of pure species. A built-in data base allows calculation of main thermodynamic properties of species (heat capacity, enthalpy, entropy, free energy, thermal conductivity, viscosity, etc.). Special models are used to determine properties of multicomponent mixtures.

The concrete cavity is assumed to be two-dimensional axisymmetric. Three types of default concretes are defined in the code. These are basaltic aggregate concrete, limestone-common sand concrete and limestone concrete (later referred to as B, L/S and L, respectively). Other concrete types may be introduced through the input data defined by the user.

The VANESA species list differs from the CORCON master list and includes different compounds to account for vaporization of radionuclides through different chemical forms. Twentyfive main representative fission products are included in the VANESA species list, each of them forming about ten different chemical compositions.

## 2.2 Overall Energy Balance

The energy balance for each layer is governed by the heat transfer processes and by the mechanistic correlations for heat transfer. Energy generated in the molten pool in each layer due to decay heat and/or due to chemical reactions is distributed upward, downward, and sideward. While determining heat balance of the layers, it is assumed that each layer is a right circular cylinder. After solving the heat conduction equation analytically utilizing the steady state conditions, one obtains expressions relating the bulk temperature of a layer to the interface temperatures on each surface adjacent to the layer. These expressions employ heat transfer coefficients to determine the heat flux to the upper, lower, and the radial interface surfaces. Energy losses from the molten pool are defined with respect to the final surfaces formed by the interface surfaces between the melt and the coolant or atmosphere, and between the melt and the concrete cavity.

In the case of overlying water pool, full boiling heat transfer curve is used to specify heat transfer to the coolant layer. Special correlations are introduced to account for gas injection at the melt coolant interface.

For a dry cavity, energy losses from the upper boundary to the atmosphere is calculated using the formula:

$$q_{sur} = \sigma \epsilon_{eff} (T_i^4 - T_{sur}^4), \quad (2.1)$$

where  $\epsilon_{eff}$  is the effective emissivity calculated from emissivities of the melt and surroundings, and  $T_i$  and  $T_{sur}$  are upper interface temperature and surrounding temperature. Surrounding temperature and emissivities are the user input parameters. In the case of an overlying water pool, full boiling heat transfer curve is used to specify heat transfer to the coolant layer. Also, special correlations are used to account for gas injection at the melt-coolant interface.

Determination of upward heat losses using equation (2.1) may introduce one source of uncertainties since this equation is strictly valid for the case of two infinite and parallel planes under equilibrium conditions. The geometry of the concrete cavity in power plants and in test facilities is not necessarily axisymmetric and, therefore, estimation of radiative heat losses using the expression in equation (2.1) is, at best, approximate.

Two models are implemented in CORCON-Mod3 to calculate heat transfer at the melt concrete interfaces. The first is a stable gas film model which treats the interface boundary as a stable film in the gap between the melt and the concrete surface formed. In this case, both radiative and convective heat transfer through a gas film is calculated. The second is a slag film model in which the heat transfer coefficient is calculated as  $h_s = 0.41 h_p$ , where  $h_p$  is the pool heat transfer coefficient. The overall heat transfer coefficient between molten debris and concrete surface  $h_o$  equals to  $0.29 h_p$ .

## 2.3 Concrete Behavior at High Temperatures

### 2.3.1 Concrete Properties

As mentioned previously, three built-in concrete types (L, L/S, and B) were implemented in CORCON-Mod3 as default concretes. A special user-defined option in the CORCON input file allows modeling of almost all other concrete compositions. Two additional types of concretes examined in the large scale tests are siliceous (BETA, ACE L2, L6, L4) and serpentine (ACE L4) (marked later as S and M concretes, respectively).

Compositions of built-in and additional types of concrete (siliceous and serpentine) used in calculations and analysis are presented in Table 2.1. These data were taken from reference [19]. There are some differences in concrete compositions (even within the same type) reported in the literature. Variations in compositions, mainly water,  $CO_2$  and  $SiO_2$  content may influence the range of uncertainties in the analysis.

For each concrete type, three temperatures are defined in the input deck – solidus and liquidus temperatures of concrete and a decomposition temperature. Available information concerning concrete solidus and liquidus temperatures is summarized in Table 2.2. Data presented by Thompson [19] are based on experimental results performed at ANL by Roche et.al [20]. Data presented by Chevalier [21, 22] were calculated using the computer code GEMENI2 developed by THERMODATA. This code calculates complex multi-phase multi-component chemical equilibrium using Gibbs free energy minimization procedure. Comparison of values used in the CORCON-Mod3 to test data indicates that for L/S concrete, solidus temperatures are quite close while liquidus temperature in the code differs from the experimental values. For limestone concrete, both temperatures differ strongly from default values, in particular, liquidus temperature is underestimated in the CORCON data base. There are no default values for solidus and liquidus temperatures of siliceous and serpentine concretes. Experimental data for siliceous type of concrete are also presented in reference [19]. The estimated values of solidus and liquidus temperatures for serpentine, limestone and siliceous concretes, presented in Table 2.2, were determined by using the ternary phase [23, 24] diagrams of the main concrete species  $MgO - CaO - SiO_2$  for the first two concrete types and  $SiO_2 - CaO - Al_2O_3$  for the third concrete type, respectively. These values show satisfactory agreement between the experimental data and the calculated data.

Concrete decomposition temperature  $T_{dc}$  is the user defined parameter and may be chosen arbitrarily in the range between the solidus and the liquidus temperatures of concrete. No user guidance is provided for determining this value. Note that higher decomposition temperature leads to higher decomposition enthalpies and, as a consequence, higher melt temperatures. Also, the choice of  $T_{dc}$  affects the redistribution of heat flux between the concrete and the surrounding, and hence, influences the concrete erosion depth.

Table 2.1: Chemical compositions of concretes (values in w/o)

Species	B	L/S	L	S	M
$SiO_2$	54.84	35.80	3.60	69	34.3
$TiO_2$	1.05	0.18	0.12	0.8	0.0
$MnO$	0.0	0.03	0.01	-	-
$MgO$	6.16	0.48	5.67	0.7	30.7
$CaO$	8.82	31.30	45.40	13.5	9.8
$Na_2O$	1.80	0.082	0.0078	0.7	0.06
$K_2O$	5.39	1.22	0.68	1.4	0.1
$Fe_2O_3$	6.26	1.44	1.20	1.0	6.4
$Al_2O_3$	8.32	3.60	1.60	4.0	1.8
$Cr_2O_3$	0.0	0.014	0.004	-	-
$CO_2$	1.50	21.15	35.70	4.23	0.9
$H_2O_{evap}$	3.86	2.70	3.94	3.1	0.8
$H_2O_{chem}$	2.00	2.00	2.00	3.68	11.3

Table 2.2: Solidus and liquidus temperatures of concretes

Concrete	Temperature (K)		
	Solidus	Liquidus	Reference
B	1350	1650	CORCON [2]
L/S	1420	1670	CORCON [2]
	1393	1568	Exp. [19]
	1540	1700	Calc. [21]
L	1690	1875	CORCON [2]
	1495	2577	Exp. [19]
	1740	2550	Estimated
S	1403	1523	Exp. [19]
	1430	1980	Calc. [21]
	1520	1770	Estimated
M	1630	1920	Estimated



Table 2.3: Range of uncertainties for  $T_{dc}$  and enthalpies of decomposition

Concrete	$T_{dc}, K$	$\Delta H, MJ/kg$	Experimental, $MJ/kg$
B	1350-1650	1.5-2.3	2.3
L/S	1400-1700	2.3-3.2	1.5
L	1500-2550	2.9-5.1	-
S	1400-2000	1.6-2.7	-
M	1600-1900	3.0-3.8	-

### 2.3.2 Concrete Decomposition Model

The rate of concrete decomposition is calculated from one dimensional steady-state balance of energy at the interface boundary between the melt and the concrete surface:

$$\dot{x} = \frac{q}{\rho \Delta H_{dc}}, \quad (2.2)$$

where  $\dot{x}$  is the linear rate of concrete decomposition front due to energy ingresses,  $q$ , to concrete,  $\rho$  is the density of concrete, and  $\Delta H_{dc}$  is the specific enthalpy of concrete decomposition at temperature  $T_{dc}$ . Concrete decomposition enthalpy in CORCON- Mod3 is calculated on basis of the built-in thermodynamic properties data base of metallic and oxidic species using the model of mechanical mixture of concrete components. Table 2.3 presents the uncertainties in calculations of decomposition enthalpies calculated by CORCON when the user defined decomposition temperature equals to the solidus temperature (lower limit) and to the liquidus temperature (upper limit). These values, when compared with measured values from reference [25], indicate that they are within the range of uncertainties calculated by the CORCON model.

Equation (2.2) assumes that the temperature profile in concrete is quasi-steady. This assumption is valid when the heat to concrete,  $q$ , is much greater than the thermal conductivity flux through concrete. For long term interaction, the inaccuracy of this approach is relatively large. The second limitation of this approach becomes evident in modeling the SURC and ACE experiments. During the long preheating phase in these tests, heat conduction through concrete may be important mainly due to changes in concrete properties during heating up and melting of corium. In general, concrete decomposition at high temperatures accompanies the following processes:

- Vaporization of free water at about 400 K
- Decomposition of calcium and magnesium hydroxides at a temperature close to 700 K
- Decomposition of calcium and magnesium carbonates (temperature range 1000-1100 K)
- Melting of remaining species in a range between the solidus and the liquidus.

During the preheating phase, some compounds may also be formed due to chemical reactions between different species. The reactions are generally endothermic and need energy input to the

concrete. The chemical reactions during the preheating phase changes concrete properties and gas content in concrete.

## 2.4 Thermal Behavior of Layers

The thermal behavior of the melt layers depends on their thermodynamic properties. Heat transfer models are discussed in detail in Section 2 of reference [2]. A brief discussion of several models which are important for simulation of experiments and heat losses from molten pool is presented below. Specifically, models for determination of solidus and liquidus temperatures of the layers, crust formation and freezing, and condensed phase chemistry of a metal layer which influence the thermal behavior of layers, are discussed.

### 2.4.1 Metal Layer Solidus and Liquidus Temperatures

To simulate the process of crust formation, freezing, and remelting, certain assumptions are made for the calculation of solidus ( $T_{sol}$ ) and liquidus ( $T_{liq}$ ) temperatures of layers consisting of complex mixtures. For example, for metal layers, the approximation of ternary phase diagram for iron-chromium-nickel mixtures is used. The influence of other metals on  $T_{sol}$  and  $T_{liq}$  is neglected. The ACE and SURC experiments, on the other hand, contained molten zirconium with small amounts of iron and/or other metal species. The CORCON calculations of solidus and liquidus temperatures for these experiments were significantly different from the observed data. This is because the melting point of pure zirconium is considerably higher (about 2125 K instead of 1750 K for iron) whereas the solidus temperature of iron-zirconium mixture is about 1250 K as can be seen from the equilibrium phase diagram of  $Fe - Zr$  (reference [26]), presented in Figure 2.1. In some ACE tests, the silicon content in the melt as a result of condensed phase chemical reactions is quite significant. For these experiments, the solidus and the liquidus temperatures for the metal layer should be appropriately defined by either pure silicon or the iron-silicon mixture.

As noted above, the solidus/liquidus temperatures in some cases may differ from those calculated by the subroutine SOLLIQ incorporated into the CORCON code. The possibility of changing the metal layer solidus and liquidus temperatures is introduced through the user flexibility option but, in this case, these temperatures are constant during the calculations and do not depend on the composition of the melt. Low melting points of iron-zirconium mixtures may be introduced by incorporating equilibrium phase diagram into the CORCON data base.

### 2.4.2 Oxide Layer Solidus and Liquidus Temperatures

For the oxide layer solidus and liquidus temperatures, the pseudo-binary phase diagram is used in CORCON-Mod3. It is assumed that those two components they form an ideal solution both in liquid and solid states. Typical curves of solidus and liquidus temperatures are presented in Figure 3.15 of reference [2].



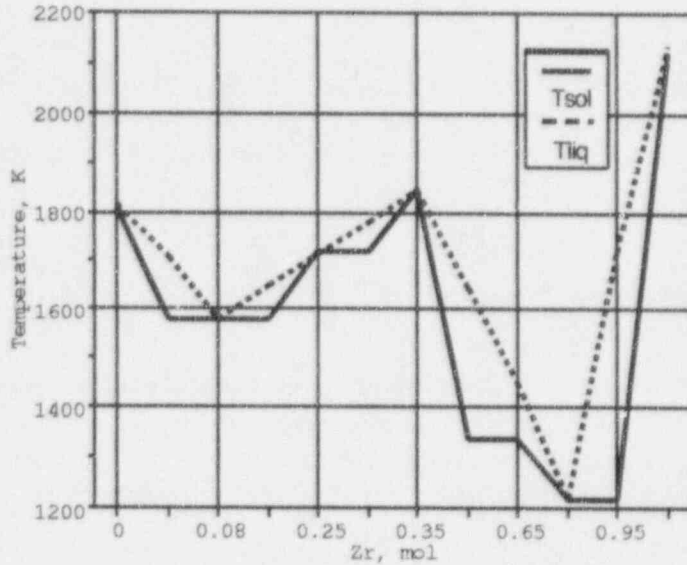


Figure 2.1: Binary equilibrium phase diagram of the  $Fe - Zr$  system.

Table 2.4: Comparison of experimental and CORCON solidus and liquidus data

Core concrete system	Solidus Temperature(K)			Liquidus Temperature (K)		
	Experim.	CORCON	Calc.	Experim.	CORCON	Calc.
Core+Siliceous	1400	1723	1434	2549	2437	2395
Core+Limestone	1520	1873	1550	2723	2373	2320
Core+Limestone/Sand	1360	1673	1450	2638	2400	2490

Measurements of solidus and liquidus temperatures for core concrete mixtures were carried out at the ANL using differential thermal analysis [20]. Three types of concrete were used in these tests: limestone, limestone-common sand and siliceous. Urania-zirconia mole ratio in these experiments was 1.6 : 1. The results show that the solidus temperatures of core-concrete mixtures drop to concrete solidus temperature if a mixture contains more than 20 wt% concrete.

Comparison of experimental results and CORCON calculations was performed by Ball and Mignanelli [27]. Calculations based on a thermodynamic model were also made and compared. Results of these calculations are presented in Table 2.4. The calculations were done using a code that was developed to describe the phase equilibria of  $UO_2 - ZrO_2 - SiO_2 - CaO - MgO - Al_2O_3$  oxide systems.

Comparison of the experimental data with code calculated values shows that CORCON underestimates liquidus temperatures for limestone and limestone common sand concrete. At the same

time, solidus temperatures are overestimated by CORCON. In contrast, the calculated values by Ball and Mignanelli are closer to the test data.

Note the calculation of solidus temperature of the core-concrete mixtures can be modified by a user flexibility option in CORCON-Mod3. In this case, the parameter XEUT is set to define the mole fraction when the solidus temperature of the mixture decreases to concrete solidus temperature.

### 2.4.3 Crust Formation and Freezing

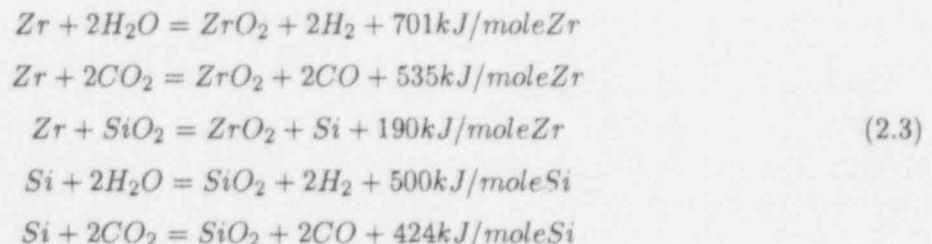
It is assumed in the CORCON code that during the melt cooling process, melt solidification and crust formation are possible at the interface boundaries with concrete and/or atmosphere. When a layer is partially or fully solidified, the heat transfer through this layer is governed only by heat conduction that is much less than the heat transfer due to forced convection induced by sparging bubbles.

The criterion of crust formation is that the temperature falls below the liquidus temperature of the mixture. The crust model does not contain the crust formation history; rather, it is treated only in terms of heat balance of the layers. The set of heat transfer equations in the bulk pool (together with crust) is solved iteratively (see Section 2.3.4 of reference [2]) to find the solution, preserving total energy and average temperature of a layer. This model often produces a sudden growth and disappearance of crust during one step of calculation.

### 2.4.4 Chemical Reactions

It is recognized that reactions in the condensed phase may play a very important role [28]. SURC-4 demonstrated that this condensed phase chemistry could influence strongly the temperature behavior and energy distribution of a bulk pool. Condensed phase reactions are particularly important when dealing with high silica, low gas concretes. This is evident from some ACE and SURC experiments which show the significant contributions of these reactions to the overall energy balance.

The list of reactions which significantly contribute to energy balance of metal layer due to chemical heat release is as follows:

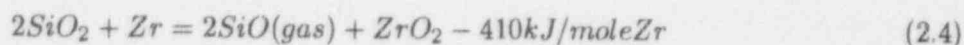


The above reactions are incorporated in the CORCON-Mod3 chemistry package. Additional reactions may play some role both for thermal analysis and aerosol release. For example, it was

Table 2.5: Equilibrium chemical components for Si oxidation

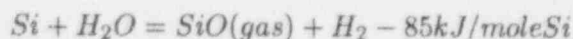
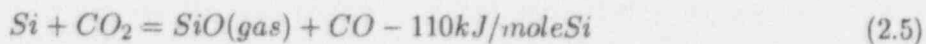
T,K	Si	SiO <sub>2</sub>	SiO	C	CO	H <sub>2</sub>	H <sub>2</sub> O
1800	48	1.99	0.0143	1.0	0.0014	2.0	$2.1 \cdot 10^{-5}$
1900	48	1.99	0.0433	1.0	0.005	2.0	$4.6 \cdot 10^{-5}$
2000	48	1.99	0.11	0.98	0.018	2.0	$9.1 \cdot 10^{-5}$
2100	47.9	1.82	0.305	0.95	0.0446	2.0	$1.64 \cdot 10^{-4}$
2200	47.6	1.55	0.77	0.88	0.11	2.0	$2.66 \cdot 10^{-4}$
2300	47.2	0.98	1.77	0.74	0.255	2.0	$3.52 \cdot 10^{-4}$
2400	46.7	0.39	2.83	0.62	0.38	2.0	$3.51 \cdot 10^{-4}$
2500	46.5	0.13	3.3	0.56	0.44	2.0	$3.1 \cdot 10^{-4}$
2600	46.5	0.04	3.44	0.53	0.47	2.0	$2.62 \cdot 10^{-4}$

found in some ACE tests with both limestone-common sand and siliceous concretes and with metals in the inventory, that silicate species dominated in the aerosols (see reference [29]). High silicon content in the aerosol deposits was assumed to be the result of  $SiO_2$  reactions with zirconium to form  $SiO$  gas as follows:



Thermodynamic calculations of this reaction indicate its importance at high temperatures (higher than 2000–2100 K). Such a temperature range is quite possible with prototypic melts and has been observed in the ACE test series (see reference [19]).

The analysis of silicon chemistry using the IVTANTERMO data base indicates that besides the possibility of endothermic oxidation of zirconium, two reactions of silicon are possible with the formation of  $SiO$  gas. These reactions are:



To determine the temperature effects of silicon oxidation, the equilibrium chemistry was calculated for the model mixture  $50Si + 2H_2O + CO_2$  containing 50 moles of silicon, 2 moles of water and 1 mole of  $CO_2$ . Results of these calculations are presented in Table 2.5. According to this table, at low temperatures (1800–2000 K),  $Si$  oxidation reaction leads to formation of  $SiO_2$ . At temperatures 2100–2300 K, both  $SiO$  and  $SiO_2$  form, while at high temperatures (above 2300 K) formation of  $SiO$  dominates in comparison to formation of  $SiO_2$ . The temperature at which the oxidation reaction changes its character from exothermic to endothermic is about 2350 K.

The main consequence of reaction with  $SiO$  formation is the faster oxidation of silicon in the course of interaction of zirconium with silica. The duration of  $Si$  oxidation and the ratio of output gases ( $H_2/H_2O$  and  $CO/CO_2$ ) may indicate the character of chemical reactions. Of course, other

evidences (including thermal aspects) are necessary to verify that these endothermic reactions are possible and important in the course of interactions.

## 2.5 CORCON Modifications for Modeling MCCI Tests

### 2.5.1 Peculiarities of MCCI Tests

The CORCON code validation exercise based on large scale tests presents some real challenges for several reasons which are discussed below.

1. The facility geometry for SURC and ACE tests are one-dimensional and, therefore, is different from that of real plants. The BETA test facility is two-dimensional and is the only facility that provides relative geometry correspondence to the reactor plant and simulates two-dimensional core concrete interaction. The CORCON code, on the other hand, is two-dimensional. The usual approach to model one dimensional tests with a two-dimensional code is to enlarge the radius of the concrete cavity thereby reducing the ratio of sideward to downward energy losses. To account for side losses in the tests, the internal heat generation is reduced proportionately to side losses which can not be modeled by the CORCON model. This approach is used, for example, in Bradley's calculations of SURC and ACE L6 [36] with CORCON-Mod3).

For ACE tests, a special design was employed in the facility for direct electric heating of the melt. Water-cooled panels were used to provide cooling of the test apparatus. Such peculiarities of the test facility resulted in the existence of solid crusts near the side interface boundaries [19] so the cavity area was reduced by 15 to 20 percent. This reduction of an interaction area may be a source of uncertainties in the calculations. Also in the ACE tests, special concrete/metal inserts were used to incorporate zirconium into the melt. Additionally, in several tests, iron rebars were inserted in the concrete basemat. More details with respect to the test apparatus are provided in Section 3.1.1.

2. Most MCCI (except transient TURC tests) used one of the two modes of heating — inductive heating for metallic melts (SURC and BETA tests) and direct electric heating (ACE L1-L8 tests). Inductive heating provides non-uniform spatial distribution of generating power in the metal charge due to the skin effect. This non-uniformity of heat generation in the tests may influence thermal-hydraulic results. For instance, SURC-4 test data demonstrates that the penetration of erosion front at the outer radius is deeper than at the center of concrete charge. Special inductive heating method was designed for oxidic melts used in the SURC-1 and SURC-2 tests. Inductively heated tungsten rings located in the prototypic melt were used. It is impossible to determine exactly the real distribution of input power while modeling these experiments.

The direct electric heating uses the usual Joule heating technique which is proportional to the electrical conductivity of the charge. Thus, volumetric distribution of power is defined by distribution of temperatures in the melt pool which is really unknown.

3. Test results depend on heat losses from upper surface of the molten pool. In the ACE tests, heat losses from the upper surface were measured so the data could be used to compare

upward heat losses calculated by the code. The SURC tests, on the other hand, provided temperature data in the upper enclosure and in the ceramic walls, so heat losses could only be estimated from these data. In particular, in the SURC-1 and SURC-2 tests, there was significant uncertainties associated with the upper boundary conditions due to the use of tungsten rings as heating elements. In the BETA tests, there was no available data on heat losses from the upper melt surface.

4. All experiments except BETA had a relatively long preheating phase. The long heat up period may change concrete properties and concrete decomposition enthalpy as well as influence gas releases and, as a consequence, chemical reactions with melt species. For instance, in the ACE tests, only 50-75% of concrete decomposition gases (taking into account composition and gas content in concrete) were detected in the offgas system [29]. The temporal behavior of gases released in the ACE tests differs strongly from the model predictions and does not follow exactly the erosion front. Due to the difference in temperatures of free and bound water evaporation, total gas release is governed by a combination of processes. CORCON-Mod3 calculations accounting for such processes will be presented later.

Another difference between the test results and the code calculations relates to the shape of the erosion front. A special analysis is presented later to illustrate this difference for the ACE L8 test, and results are discussed.

5. Many condensed phase reactions do not involve oxidation and hence, do not result in hydrogen production although these reactions may influence the thermal-hydraulic behavior of the melt. While validating the chemistry package, this fact should be taken into account.

The above peculiarities of test facilities seem to be quite important in the interpretations of experimental data and comparison of the same with code predictions. It is possible to eliminate or reduce some of the uncertainties through special analysis and through code modifications as well as data modifications which should be performed to account for specific features of each experimental facility.

## 2.5.2 Modifications Made for Validation

In the previous section, some peculiarities of the test facilities were discussed. Currently, CORCON-Mod3 does not allow to account for many of these peculiarities. At the same time, some modifications can be made and, indeed, have been made in a relatively simple manner to address these peculiarities. These are:

1. Implementation of a layered structure of concrete for the ACE tests;
2. Implementation of  $Fe - Zr$  phase diagram to account for the addition of pure zirconium (for SURC-4 and ACE tests);
3. Accounting for vanishing of the metal layer in the oxidic tests (especially in the ACE tests) where relatively small masses of metal layers lead to fast oxidation and floating point errors in the calculations; and

4. Implementation of  $\text{SiO}$  properties into CORCON-Mod3 to account for the oxidation reactions and chemical heat release at temperatures higher than 2300 K.



### 3 MODELING OF ACE TESTS

This section deals with the modeling of ACE tests and comparison of CORCON-Mod3 predictions to test data. General input conditions are discussed and code calculations are presented. Input decks for ACE L5, L2, L6, L4, L7 and L8 are presented in Appendix A.

#### 3.1 ACE Phase C MCCI Program

A series of molten core-concrete interactions (MCCI) experiments were carried out in the framework of cooperative research Advanced Containment Experiments Program (ACE) Phase C, with the following objectives [30]:

1. To evaluate the release of low volatility fission products
2. To measure physical and chemical characteristics of generated aerosols
3. To define thermal-hydraulic behavior of corium and concrete during the interaction, i.e., concrete ablation rate, gas generation rate, etc.
4. To validate MCCI models including both thermal analysis and chemical interaction models
5. To support code comparison activities.

The Phase C program was completed in 1991. The test matrix is shown in Table 3.1. Principal parameters varied in the tests were: concrete type, the zirconium content in corium mixture (both PWR and BWR corium compositions with the corresponding control materials used in the tests) and net heat generation. Each of the tests employed about 300 kg of corium mixture. The fission products simulants were added to corium to detect releases during the interaction. Both thermal-hydraulics and aerosol data were generated in the tests, and these data were used for the assessment and validation of the MCCI codes.

##### 3.1.1 ACE Test Apparatus and Instrumentation

The ACE test facility consists of a test apparatus, a power supply, water cooling systems, an exhaust system, a gas/aerosol diagnostic system, and a data acquisition system (DAS). The test apparatus has a square cross-section and usually consists of two vertical sections: a lower section of concrete



Table 3.1: ACE MCCI test matrix

Test No.	Concrete Type	Net Power W/kg $UO_2$	Corium Mixture	Initial Zr Oxidation, %	Absorber Material
L5	L/S	325	PWR	100	-
L2	S	450	PWR	70	-
L1	L/S	350	PWR	70	-
L6	S	350	PWR	30	$Ag, In$
L4	M and S	250	BWR	50	$B_4C$
L7	L/S	250	BWR	70	$B_4C$
L8	L/L	350	PWR	70	$Ag, In$

basemat and an upper section that contains the melt. The test apparatus has a provision for zirconium (metal) insert above the concrete basemat. Two assemblies made from tungsten rods form the north and the south inner walls of the apparatus and serve as electrodes. The electrode assemblies are connected together near the top of the corium inventory by four spirally wound tungsten coils for heating the corium locally until it becomes conducting. The internal heat generation in corium is simulated by the direct electric current. Nominal input of power is sustained at the level of 250–450 W/kg of  $UO_2$  that correspond to the decay heat at 2 hours after the reactor shutdown.

Thermocouples were installed in the concrete basemat, in the sidewall, and in the melt pool. In addition, thermocouples were installed on the upper lid to estimate the upward heat loss and to provide an upper temperature boundary condition for MCCI code calculations. Basemat ablation was considered to begin when thermocouples registered ablation temperature at the initial concrete surface. The same criterion was used to determine the beginning of insert ablation.

Two main concrete types were investigated in the ACE experiments – limestone-common sand (tests L5, L1 and L7) and siliceous (tests L2, L6 and L4) concrete with different melt compositions and fission products simulants. One test (L4) used two types of Soviet concrete: serpentine and ordinary concrete (the latter is very close in composition to the siliceous concrete) and one test (L8) was conducted with limestone concrete basemat. Typical size of concrete basemat in the test was 50 × 50 cm with a thickness of 25 cm.

Metal and fission products were incorporated into the melt in several ways. In two tests (L2 and L1), zirconium metal rods were located on top of the concrete basemat. Three tests contained special concrete/metal insert made of basemat concrete and zirconium rods cast into concrete. Special stainless steel rods were used to model reinforced concrete. Metals (zirconium, etc.) were introduced in the melt after the melt front reached the special concrete/metal insert which usually consisted of the basemat concrete (except ACE L4 that had two concrete layers — serpentine and siliceous concretes) and metal rods. Tables 3.2 and 3.3 summarize the content of oxide and metal species at the beginning of corium concrete/metal inserts ablation.

Decomposition gases generated by downward concrete ablation passed through the melt pool,

Table 3.2: Oxide components of the melt of the ACE tests

Species	Content of corium, kg						
	L5	L2	L1	L6	L4	L7	L8
$UO_2$	184.2	216	216	219	192	188.5	211.5
$ZrO_2$	34.0	42.5	42.5	18.5	43.2	59.4	41.6
$Fe_2O_3$	54.1	-	-	-	-	-	-
$NiO$	5.2	-	-	-	-	-	-
$Cr_2O_3$	13.4	-	-	-	-	-	-
$CaO$	-	3.0	11.4	7.3	-	11.5	20.6
$MgO$	-	-	-	-	7.2	-	-
$SiO_2$	-	20.9	12.4	16.9	16.8	12.5	3.4

Table 3.3: Metal components of the melt of the ACE tests

Species	Content of corium, kg						
	L5	L2	L1	L6	L4	L7	L8
Zr	-	13.4	13.4	21.1	30.3	17.7	12
Zry-4	-	-	-	1.8	1.1	1.1	1.1
Type 304 SS	-	-	-	9.1	0.6	0.6	-

and carried by an argon dilution gas into the aerosol collection system. There was some leakage the decomposition gases through the concrete basemat (and installed thermocouples. This explains why measured gases in the tests were always lower than what might be expected. The total time needed to heat up the corium powder to melting was approximately 2 to 3 hours. Typical duration of the concrete ablation phase was about 1 to 2 hours.

### 3.1.2 ACE Test Scenarios

According to the experimental approach, test scenarios may be divided into three phases:

- Preliminary heating up and melting of corium powder. Some metal (if present) oxidation takes place during this phase.
- Interaction of melt with concrete/metal insert (if it is present). This phase is characterized by simultaneous interaction of the melt with concrete and with metal rods which define gradual entrance of metal components into the melt. Intensive oxidation reactions provide high

Table 3.4: Scenarios of interaction for ACE tests

Events	Times of events, s					
	L5	L2	L6	L4	L7	L8
Heating and melting of corium mixture, min	-154	-220				-244
Concrete/metal insert ablation beginning			-2500	-3000	-800	-600
Concrete basemat ablation beginning	0	0	0	0 700	0	0
End of interaction	7260	7260	2460	7500	3200	6000

Table 3.5: Summary of ACE experiments thermal hydraulic results

Experiment	L5	L2	L1	L6	L4	L7	L8
Concrete type	L/S	S	L/S	S	Soviet	M and S	L
Mass of reinforcing rods, kg	2.8	2.8	2.9	2.9	2.6	0	0
Insert depth, cm	-	-	-	7	7.9	5.7	4.3
Net power, kW	60	60	75	75	50	50	75/35
Temperature K	1870	2420	2625	2425	2300	2515	2480
Ablation Depth	11	12.7	4	16	14.2	3	13

level of chemical heat release and high-temperature interaction with concrete. Parameters which define uncertainties of interaction during this phase are: enthalpies and temperature of concrete/metal insert decomposition, chemical reactions scenario (due to high temperature difference, for instance, between concrete decomposition and melting of zirconium).

- Interaction of the melt with basemat concrete. This stage is relatively long and describes steady-state phase of interaction with concrete.

Table 3.4 presents the summary of interaction scenarios and timing of different stages of interactions. It should be mentioned that the starting points of these stages were detected on the basis of thermocouple measurements. For test L4, two numbers in the second row show the beginning of serpentine concrete ablation and the beginning of siliceous concrete ablation.

The summary of thermal hydraulic tests results was presented in reference [19] and is given in Table 3.5.

### 3.1.3 General CORCON Input Conditions for ACE Tests

In developing the CORCON input data for ACE tests, attention was paid to the energy balance predicted by CORCON-Mod3 and its correspondence to test data. The following procedure was used:

1. Surrounding temperature was adjusted to fit experimental upward energy losses. Surrounding temperature and surrounding emissivity were used to vary upward heat losses in the simulation of the test.
2. To understand heat transfer in the calculations, melt temperature and erosion depths were used for the comparison. If the predicted results disagreed qualitatively with the test data, sensitivity calculations were performed. Concrete decomposition temperature in the range between solidus and liquidus temperatures was a variable parameter to achieve better agreement with test data.
3. Ratios of  $H_2O$  to  $H_2$  and  $CO_2$  to  $CO$  release rates were used to check the chemistry in the melt and to understand possible scenarios of metal species oxidation.

To check general energy balance in the tests, heat loss to concrete was calculated using the formula:

$$Q_{dn} = m_c \Delta H_{dc}, \quad (3.1)$$

where  $m_c$  is the mass of eroded concrete, and  $\Delta H_{dc}$  is the enthalpy of concrete decomposition. This value was used to calculate

$$P_{dn} = \frac{Q_{dn}}{\Delta t_{int}} \quad (3.2)$$

which gives an estimate of average power during the interaction period  $\Delta t_{int}$ . The same procedure was used to calculate the total energy needed to decompose the concrete-metal insert:

$$Q = m'_c \Delta H_{dc} + m_{Zr} \Delta H_{Zr} + m_{Fe} \Delta H_{Fe}, \quad (3.3)$$

where  $m'_c$  is the mass of concrete in the concrete/metal insert,  $m_{Zr}$  and  $m_{Fe}$  are masses of zirconium and iron in the insert, and  $\Delta H_{Zr}$  and  $\Delta H_{Fe}$  are corresponding changes in enthalpies including melting of metal species. Usually, a temperature near 2000 K was used as the decomposition temperature of concrete/metal insert.

The initial square geometry of the ACE tests was modeled by a circular cylinder of 56 cm diameter to scale the interaction area. Initial conditions of ACE tests are characterized by the use of oxidic powder, its heating and melting. To implement metals into the melt, zirconium was placed atop the concrete surface in the form of rods or as a concrete/metal insert. To account for this approach, initial melt configuration for CORCON simulation was assumed to be layered (ILYR=0). Interlayer mixing option was turned off. In the calculations, the metal layer was assumed to be

always below the oxidic melt, and rearrangement of the layer structure was disabled by changes in the code.

When zirconium metal was used in the tests in the form of metal/concrete insert or as rods, two (and even more) types of concrete were used. One type is with high zirconium content in concrete (negative RBR option, which allows to implement rebar composition). In this case, concrete decomposition temperature was defined to be higher than  $T_{dc}$  of pure concrete to account for the presence of Zr. This approach was used before [36] for modeling interactions with metal/concrete insert. The decomposition temperature was usually chosen to be slightly lower than the melting point of metal.

Non-standard concrete type option was used in the calculations to account for the differences in concrete compositions compared with the default concrete types implemented into CORCON-Mod3 (see Table 3.6). Concrete solidus and liquidus temperatures were chosen to be equal to the experimental values [20], and the decomposition temperature was chosen to be relatively close to the solidus temperature of concrete.

Typical time step during calculations was about 2-5 s because thin metal layers existing in the calculation did not allow larger time steps. Everywhere in the calculations, 40 rays were used to represent the interaction interface.

All but one (ACE L5) tests employed zirconium metal. Thus, in all calculations, a condensed phase chemistry option was used without taking into account coking reaction (ICHEM = 01). In almost all calculations, the option IFILM=10 was used meaning that at the bottom interaction surface, stable gas film model was employed. Sensitivity calculations were performed to assess differences due to the changes in the heat transfer model.

## 3.2 Modeling of the ACE L5 Test

### 3.2.1 Test Conditions and Results

Test L5 was the first test performed under the ACE program [37]. This experiment utilized a fully oxidized corium (see Table 3.2) with the total mass of 293 kg. Limestone common sand concrete basemat with typical dimensions of  $50.2 \times 49.2$  cm and a height of 30 cm was used in the test. Concrete density was  $2400 \text{ kg/m}^3$ .

Eight reinforcing rods, 1.3 cm in diameter and 36.8 cm in length, were placed into the concrete block. Four of them were located 5.1 cm below the top of the concrete, and four additional rods were located 10.2 cm below the top concrete surface. Total mass of the rods was 2.8 kg, with iron being the main constituent of the reinforcing rods (about 99%). The test facility and the concrete block were instrumented to measure: melt temperature, net power, heat losses, erosion front, and gas composition. Average net power to the melt was sustained at the level of 60 kW.

Ablation of the concrete basemat began at 154 min when the temperature measured by the thermocouple located on the basemat surface reached 1673 K. During 121 min of interaction, about



Table 3.6: Summary of CORCON-Mod3 input parameters for ACE tests

Experiment	ACE L7	ACE L2	ACE L4		ACE L5	ACE L6	ACE L8
Initial Layer Configuration	0	0	0	0	0	0	0
Interlayer Mixing	No	No	No	No	No	No	No
Concrete Type	N/S	N/S <sup>1</sup>	N/S	S	L/S	N/S	L/L
SiO <sub>2</sub> ,%	28	69	34	69	38	69	7
CaO,%	27	13	9	-	24	13	46
CO <sub>2</sub> ,%	21.4	2	2	4	20	4	33
H <sub>2</sub> O,%	6.1	4	13	6	6	4	6
Concrete Ablation Temperature, K	1745	1653	1550	1980	1500	1653	1500
Initial Concrete Temperature, K	300	300	300	300	300	300	300
Concrete Solidus Temperature, K	1420	1413	1500	1430	1420	1413	1495
Concrete Liquidus Temperature, K	1710	1653	1900	1980	1670	1653	2400
Concrete Emissivity	0.6	0.6	0.6	0.6	0.6	0.6	0.6
Time Step, s	10	5	2	2	5	2	5
Number of Rays	40	40	40	40	40	40	40
Melt Temperature, K	2500	2160	2400	2250	2200	1870	2500
Metal Layer Emissivity	0.8	0.8	0.8	0.8	0.8	0.8	0.8
Oxide Layer Emissivity	0.8	0.8	0.8	0.8	0.8	0.8	0.8
Surroundings Emissivity	0.6	0.6	0.6	0.6	0.6	0.8	0.6
Chemistry Flag (ICHEM)	01	01	01	01	01	01	01
Heat Flow Index (IFILM)	10	10	10	10	00	01	10
Surroundings Temperature, K	1600	1600			1700	1300	1750
Power, kW	50	60	50	50	60	50-70	75
Radius, m		0.28	0.28	0.28	0.28	0.28	0.28

<sup>1</sup> Nonstandard user defined concrete

Table 3.7: Gas release during test L5

Species	Inventory, mol	Released gases, mol	
		Prior to ablation	During Ablation
$H_2O$	200	N/A*	50
$CO_2$	290	N/A	200
Total	490	N/A	250

\* Not available

Table 3.8: Estimate of energy balance in test L5

	Power, kW	Total, MJ
Input energy	60	430
Upward heat losses	24	170
Heat concrete erosion	25	180

10 cm of concrete was ablated. Average erosion rate at the start of ablation was estimated to be about 1.33 mm/min. During the test, the ablation rate slowed down and at the end of interaction, it was about 0.57 mm/min. At the beginning of the test, the melt temperature was about 1870 K. During the test, temperature increased to a peak estimated temperature of 2050 K.

Both  $CO_2$  and  $H_2O$  concentrations remained relatively constant during ablation. Concentration of  $H_2O$  varied in off-gas between 15 and 18 mol %. Estimates based on water and carbon dioxide contents in the L/S concrete indicate that the mole fraction of water is expected to be about 35 %, which is twice the amount observed in the test. The estimate for the chemically bound water, released only at higher temperatures, yields 18 mol % which is very close to the test value.

Table 3.7 presents comparison of gas inventories calculated using the erosion rate and the carbon dioxide content in the L/S concrete. This comparison shows that water detected during the ablation phase comprises only about 25% of the total water inventory in the concrete (10 cm thickness). No data is available for gas release prior to the onset of concrete ablation. Average  $H_2O$  and  $CO_2$  release rates were about 0.007 mol/s and 0.03 mol/s, respectively.

Table 3.8 presents energy terms calculated from the test data. Downward heat transfer was calculated using the concrete erosion depth and estimated enthalpy of concrete decomposition. The total of 60 kW power input was distributed between upward and downward heat losses.



### 3.2.2 Comparison to ACE L5 Test Data

According to the data presented in reference [37], the lid temperature during the interaction phase was about 1700 K. This temperature was chosen as the surrounding temperature  $T_{sur}$  in the calculations. The slag film model (IFLM = 0) was used in the base case for CORCON-Mod3 analysis. Concrete ablation temperature for limestone common sand concrete was equal to 1600 K. To model rebar in the concrete, metal addition was initiated (ISRABL=1) around 3000 s (corresponding to about 5.1 cm of ablation). Other input parameters are presented in Table 3.6.

Comparison of CORCON-Mod3 predictions with the test data is presented in Figures 3.1 through 3.5. Initial temperature of the oxidic melt was 2200 K. Erosion depth at the end of calculations is approximately 10 cm or very close to the test data. Temperature predictions are also quite close to test data as shown in Figure 3.2.

Figure 3.3 presents different energy terms calculated by CORCON. Starting with the radiated power of 30 kW and the temperature of 1870 K, radiation increases with temperature and exceeds 40 kW. Power to concrete is about 30 kW during the initial phase of ablation, later it reaches the value of 20 kW or very close to the estimated value presented in Table 3.8. Comparison of the test data with the calculated data for the energy balance indicates good agreement.

Due to the absence of metal components initially, there were no changes in gas composition. Only  $H_2O$  and  $CO_2$  gases were released during the interaction period except (see Figure 3.4). According to the analysis of test gas composition, CORCON-Mod3 overpredicts the  $H_2O$  release rate by a factor of 3 to 4, while the  $CO_2$  release rate is overpredicted only during the initial ablation phase. Figure 3.5 shows the addition of iron in the melt at about 3000 s. The oxidation rate of iron is very high, so the metal phase existed for a very short time and did not influence significantly the melt behavior.

Simulation of the ACE-L5 test indicates good agreement between predictions and the test data. The difference in the predictions of gas flow rate is attributed to heatup and dehydration of concrete slug prior to the onset of ablation.

## 3.3 Modeling of the ACE L2 Test

### 3.3.1 Test Conditions and Results

Test L2 was the second test in the ACE series and was performed to investigate PWR corium interaction with concrete basemat [38, 39]. Concrete basemat in the test, made of siliceous concrete, had a typical height of 30 cm and a surface of 50.2 cm × 49.2 cm. Initial configuration included 13.47 kg of zirconium metal which was located immediately below the surface of the basemat. The basemat also contained eight reinforcing rods located at two levels, 6.35 cm and 11.43 cm below the concrete basemat surface. Total mass of the rods was 2.79 kg. After 220.2 minutes of heating up and melting, ablation of the basemat began. Initial melt composition is presented in Table 3.2. It contains about 216 kg of uranium dioxide and 42.5 kg of zirconium dioxide. Small amounts of

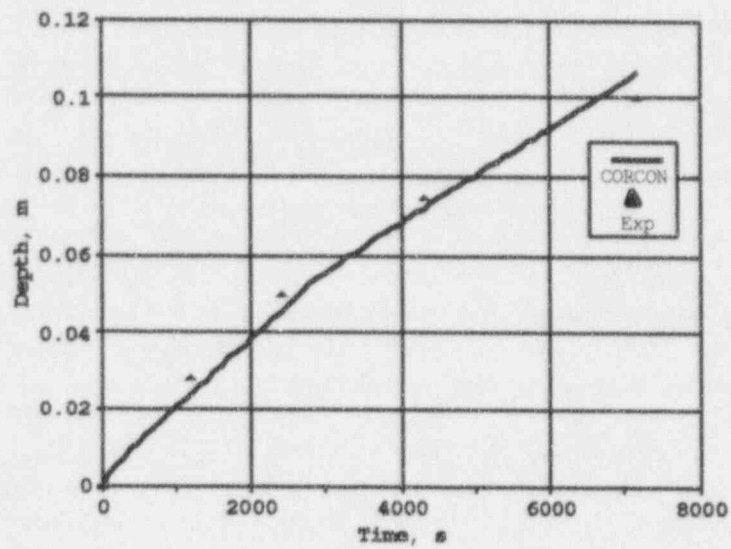


Figure 3.1: ACE L5 concrete erosion depth

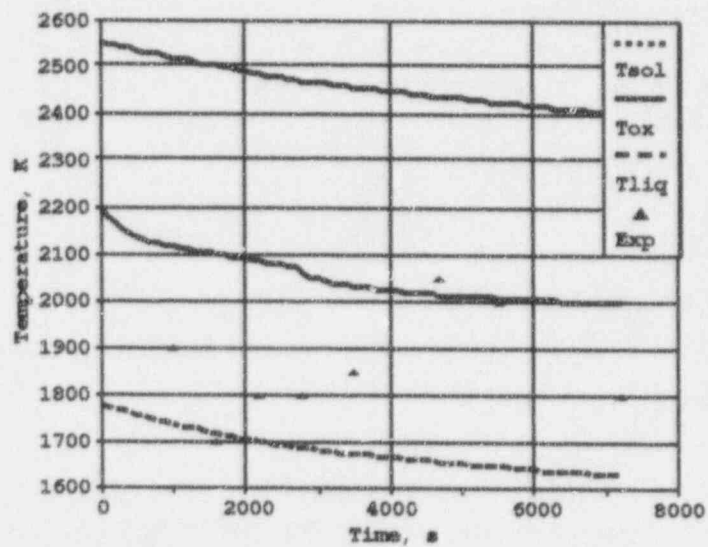


Figure 3.2: ACE L5 temperature of oxide layer

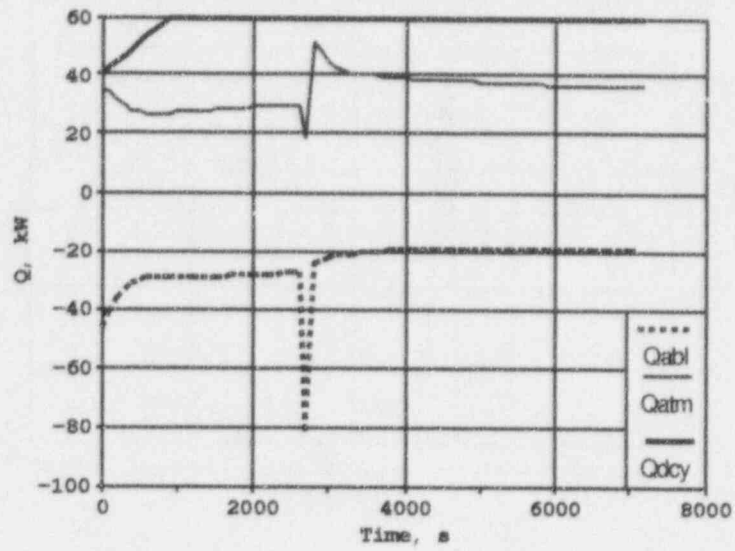


Figure 3.3: Energy rate terms for ACE L5 test

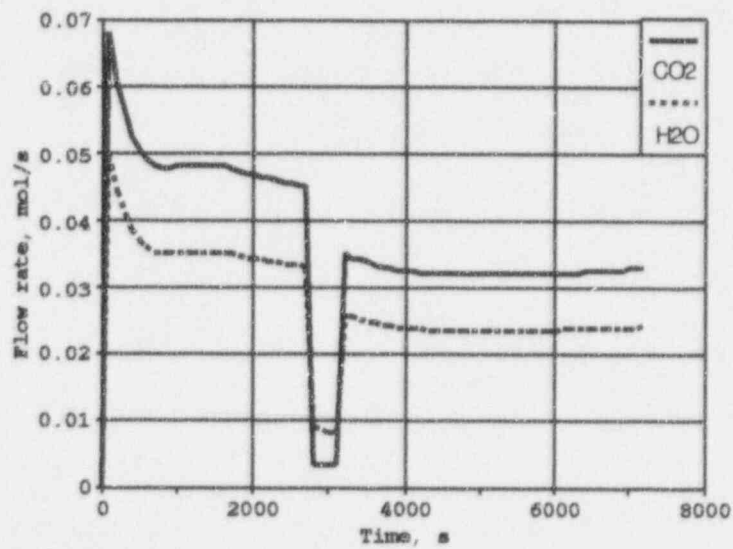


Figure 3.4: ACE L5  $CO_2$  and  $H_2O$  flow rates

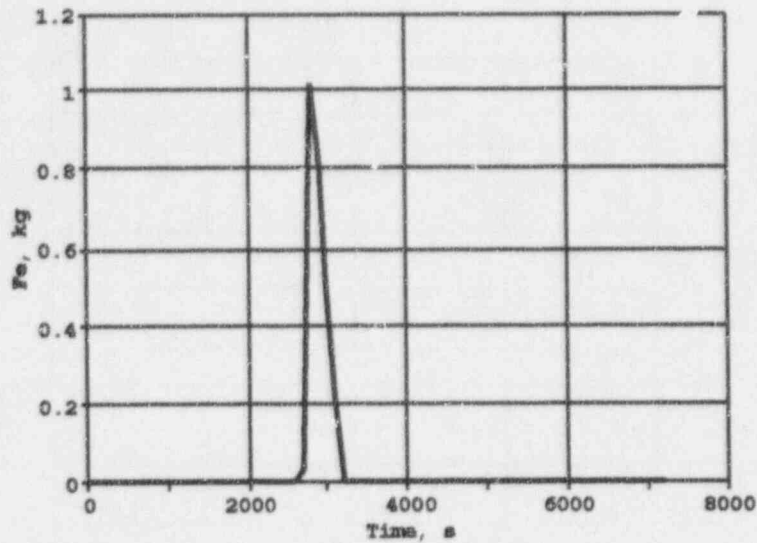


Figure 3.5: ACE L5 mass of metals

Table 3.9. Estimate of energy balance in test L2

	Power, kW	Total, MJ
Net Input	110	300
Upward heat losses	60-65	170
Heat to concrete	30	80-85

$SiO_2$  and  $CaO$  were added to the melt to reduce solidus and liquidus temperatures of mixtures.

Test duration from the onset of ablation was 46 minutes. Total ablation depth during the interaction was about 13 cm. Melt temperature at the start of concrete ablation was 2400 K. Average temperature during the test was about 2200 K. The average power in the melt was sustained at the level of 110-120 kW during ablation to account for sidewall heat losses. The upward heat losses were about 60-65 kW (see Table 3.9), and the downward heat losses to concrete was estimated at 30 kW. This means the heat balance is satisfied to within 15 %.

Gas releases were observed only at the initial phase of interaction so there is no possibility to compare release rates. High hydrogen concentration, coupled with a low  $H_2O$  content at the initial phase of interaction, indicated intensive oxidation of zirconium metal.

### 3.3.2 Comparison to ACE L2 Test Data

The average lid temperature measured during the interaction phase was about 1800 K [38] with peak values higher than 2000 K. This average temperature was chosen as the surrounding temperature  $T_{sur}$  in the calculations. Stable gas film model (IFILM=10) was used as a base case for CORCON-Mod3 analysis. Concrete ablation temperature for siliceous concrete was 1650 K and was close to the liquidus temperature. Other input parameters are presented in Table 3.6. Siliceous concrete contains about 70% of silica, thus, the condensed phase chemistry option ICHEM was chosen to be equal to 1 (CPC on, coking reaction off).

Calculations were performed by taking into account silicon chemistry with formation of  $SiO$  gas. Two concrete layers according to the initial configuration in the L2 test were specified in calculations. Properties of the first layer were chosen to account for the presence of 13.47 kg of zirconium metal. This allows for introduction of zirconium gradually. Results of CORCON-Mod3 predictions are presented in Figures 3.6 through 3.11.

In Figure 3.6, erosion depth is presented as a function of time. Calculations began at the time of -500 s to account for interaction with zirconium metal. Gradual entrance of zirconium and simultaneous oxidation leads to the maximum zirconium mass of 11.5 kg (see Figure 3.7). Total amount of  $Si$  accumulated in the melt is equal to 4 kg (about 140 moles). This value corresponds to the total oxidation of zirconium (13.47 kg or 148 moles). During fast zirconium oxidation phase, calculated temperature of the melt is sustained at approximately constant level of 2450 K (see Figure 3.8). Silicon oxidation starts at about 200 s of concrete ablation phase and lasts for up to 1600 s.

In Figure 3.9, energy rate terms are presented. Consideration of energy balance for the ACE L2 test indicates that oxidation chemistry provides about 100 kW during zirconium oxidation phase and 25 kW during oxidation of silicon. Together with chemical heat release, total input power was estimated as 150 kW during oxidation of  $Zr$ . Radiation power to surrounding was calculated at about 50 kW, slightly lower than the measured value. Temperature drop provided additional heat to concrete, and the average energy flux to concrete in calculations was about 80 kW during the test or two times the estimated value. Overestimation of heat to concrete leads to overprediction of erosion depth by a factor of 60%. Metal layer that appeared in the initial phase of interaction existed at the end of calculations indicating high power input to concrete.

Negative value of chemical heat near 100 s is due to the  $SiO$  formation in course of silicon oxidation. After temperature dropped below 2350 K (at about 400 s), chemical heat release became positive and oxidation reactions had an exothermic character. Endothermic phase of oxidation lasted very short time in comparison with the total test duration due to fast temperature drop.

Comparison of the calculated  $H_2$  and  $CO$  flow rates with the test data (see Figures 3.11 and 3.10) indicates that during zirconium oxidation phase,  $H_2$  flow rate is twice as low as the test data while  $CO$  flow rate is slightly lower than the measured values. There are no test data for gas release some 8 minutes after the onset of interaction due to blockage of main gas line.

Modeling of the ACE-L2 test indicates that CORCON predicts existence of a metal layer in calculations which determines heat transfer to concrete. Heat transfer to concrete is overpredicted

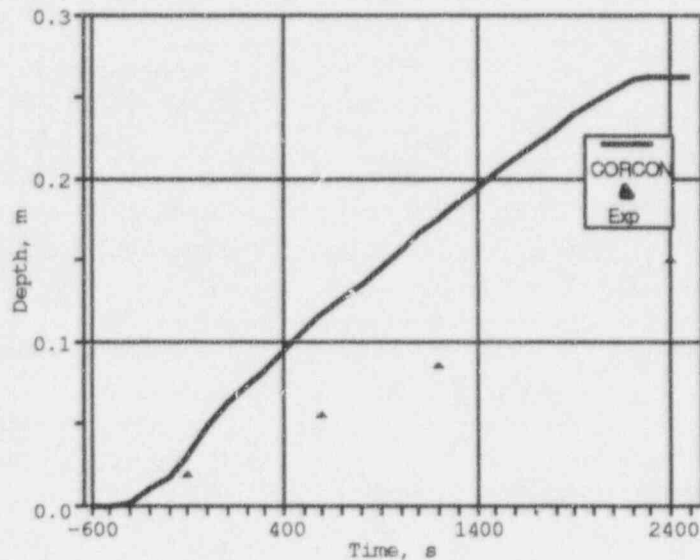


Figure 3.6: ACE L2 concrete erosion depth

in this case even after accounting for the endothermic *Si* oxidation.

### 3.4 Modeling of the ACE L6 Test

#### 3.4.1 Test Conditions and Results

The L6 [40, 41] test was performed with the siliceous concrete. The net electrical power was determined to be the total electric power input increased by the side losses to the cooling panels. Power was maintained at approximately 70 kW throughout the test during the ablation phase. Tables 3.2 and 3.3 present the composition of the charge and concrete/metal insert. The ACE L6 experiment used a predominantly oxidic mixture containing urania and zirconia. Small amounts of *CaO* and *SiO<sub>2</sub>* were added to the mixture. The charge contained also about 5 kg of fission product simulants. Total mass of the oxidic melt at the start of interaction was about 260 kg. Composition of siliceous concrete is presented in Table 2.1. Thickness of concrete/metal insert was 7.1 cm. The insert contained 22.4 kg of siliceous concrete, 24 kg of the zirconium, and 9.1 kg of 304 stainless steel. The basemat contained also 2.85 kg of reinforcing rods made of steel located at 5.1 cm and 10.2 cm below the basemat surface. The density of concrete/metal insert was equal to 3300 kg/m<sup>3</sup>.

Basemat ablation began approximately 2500 s after the initiation of core-concrete interactions. Total ablation depth in the test was about 20 cm, including 7 cm of insert and about 13 cm of concrete basemat. Initial temperature was 2550 K, and after ablation of concrete/metal insert, temperature declined to 2500 K. The temperature dropped another 300 K at the end of the test.



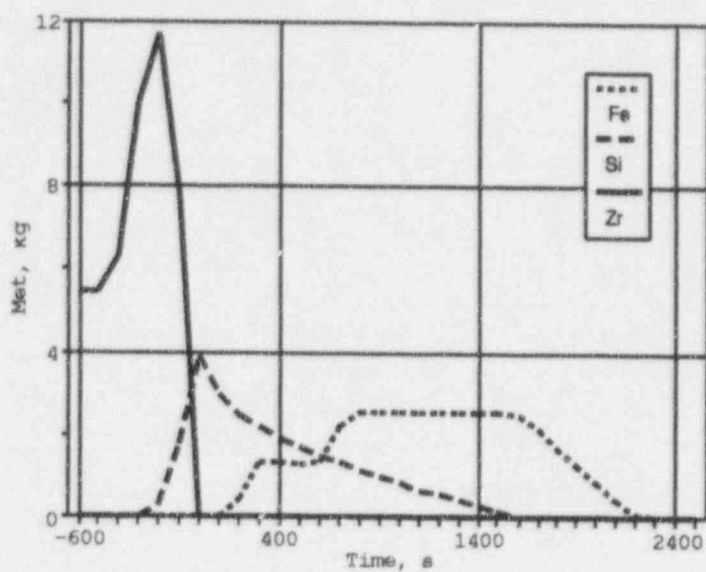


Figure 3.7: ACE L2 mass of metals (*Fe*, *Si*, *Zr*)

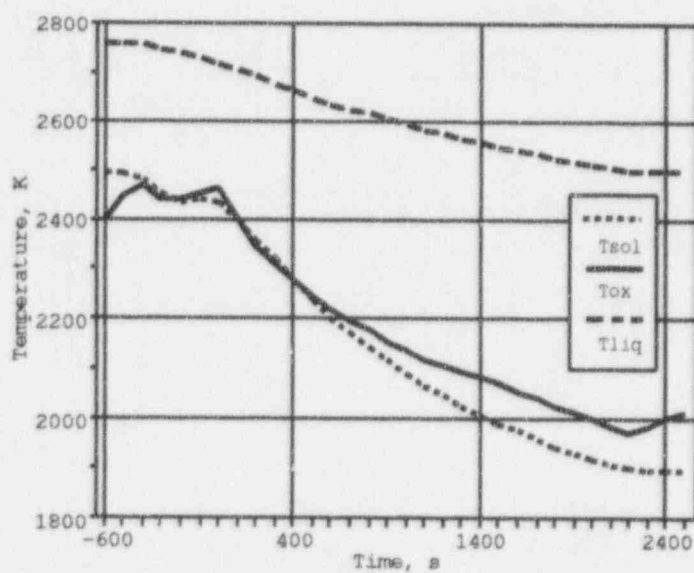


Figure 3.8: ACE L2 temperature of oxide layer



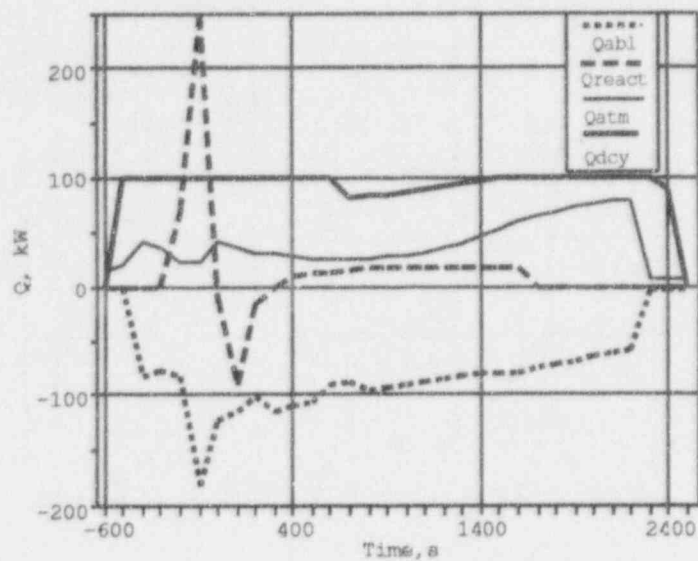


Figure 3.9: Energy rate terms for ACE L2 test

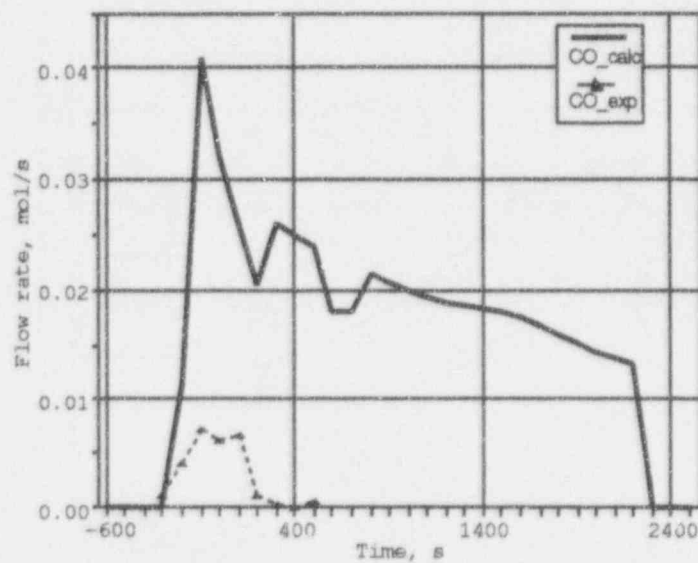


Figure 3.10: ACE L2 CO flow rate

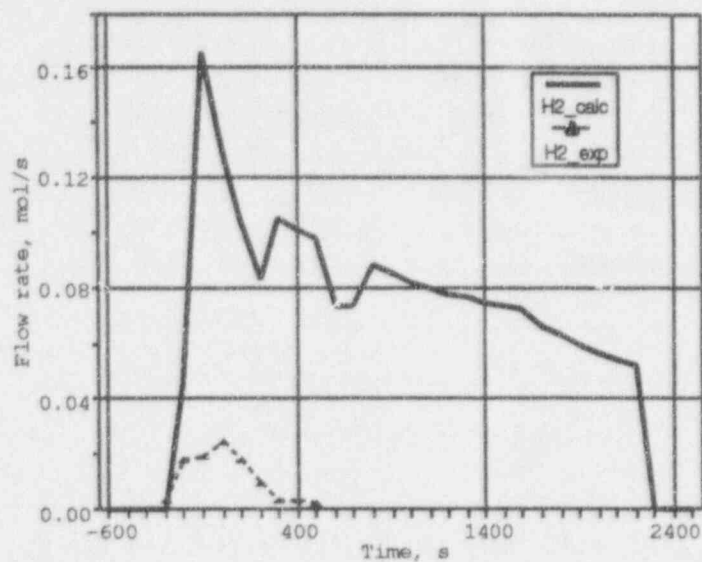


Figure 3.11: ACE L2  $H_2$  flow rate

Table 3.10: Gas release during test L6

Species	Inventory, mol		Released gases, mol			
	Insert	Basemat*	Prior to ablation	Insert Ablation	Basemat* Ablation	Total
$H_2O + H_2$	46	176	28.4	27.6	25	81
$CO_2 + C$	21	35	4.0	8.0	12	24
$SiO_2$	258	700				
Zr	250					

\* Referred to the time of 31 min after basemat ablation when erosion depth was about 6.5 cm

Table 3.11: Energy balance summary in MJ for ACE L6

	Phase 1	Phase 2
Input Power	180(96%)	172 (71%)
Cooling of melt	7 (4%)	56 (23%)
Chemical Heat	-19(11%)	15 (6%)
Total input	168	243
Downward losses	61(36%)	102 (47%)
Upward losses	58 (41%)	69 (32%)
Heating up	37 (23%)	44 (21%)
Total losses	165	215

The initial inventory of gases based on the concrete composition indicates that a total gas release of about 125–150 moles for  $H_2$  and  $H_2O$  and 50–70 moles for  $CO$  and  $CO_2$  is expected. Measured gas release was much less than these expected values (see Table 3.10). The reason for this was mentioned previously and is discussed in the L6 data report [41]; i.e., gas leakage through the bottom of the basemat crucible and the hood. The observed  $H_2$  and  $H_2O$  release for the first phase (interaction with concrete/metal insert) was 55 moles which is slightly more than expected, while the  $CO/CO_2$  release was about 12 moles or half of the expected value. The second phase shows a much lower release than expected; i.e., 3 to 5 times less than actually observed.

Experimental values of the ratio  $H_2/H_2O$  in the test were between 10 and 15 for both phases, and the ratio  $CO/CO_2$  was near 7, indicating almost complete gas reduction due to metal oxidation reactions. Detailed analysis of gas releases and energy rate terms was performed in [42].

Estimates of main energy terms for L6 test is presented in Table 3.11. About 25–30 kW in the test were reported as upward heat losses during both phases. Assessment of heat to concrete gives the value of 25 kW during concrete/metal insert ablation phase and about 43 KW during basemat ablation. Temperature drop provides additional power input. The experimental heat balance is quite good taking into account the chemical reaction in the condensed phase for both the first and the second stage of experiment. Table 3.11 presents main results of analysis. Reaction with formation of  $SiO$  gas is taken into account assuming that during the interaction with concrete/metal insert, temperature is higher (2400 K) so it exceeds the lower limit of  $SiO$  formation. During the second phase, it is assumed that 50% of  $Zr$  reacts with formation of  $SiO$  gas. Remaining 50% of  $Zr$  forms silicon as a result of oxidation.

### 3.4.2 Comparison to ACE L6 Test Data

While modeling the test by the CORCON code, it was assumed that concrete basemat consisted of several layers two of which represented concrete/metal insert. Two special layers were introduced to represent the reinforcing rods in the basemat due to possible influence of the metal layer content on the chemistry. The first part of concrete/metal insert includes  $Zr$  only while the second part

Table 3.12: The composition of rebar insert for L6 test

	1 part	2 part
<i>RBR</i>	-1.42	-1.42
<i>Fe</i>		0.2
<i>Cr</i>		0.1
<i>Ni</i>		0.05
<i>Zr</i>	1.0	0.65
<i>T<sub>dc</sub></i> , K	2100	2100

of concrete/metal insert includes *Zr* and stainless steel. Depths of these parts were 2 cm and 5 cm, correspondingly. Such nodalization of concrete/metal insert was made to account for gradual entrance of zirconium and iron into the melt in accordance with the structure of concrete/metal insert in the test. CORCON-Mod3 input parameters for these two layers is presented in Table 3.12.

It is assumed that during concrete insert ablation, the decomposition temperature is close to the melting point of zirconium metal and, therefore, chosen to be 2100 K. Calculations began at time -2500 s which corresponded to the start of concrete metal insert ablation and were continued up to the end of the test at approximately 2400 s after onset of basemat ablation. Initial time in the test corresponds to the time of 900 s in the calculations. In Figure 3.12, calculated and experimental concrete ablation distance for the ACE L6 test are presented. Initial 7 cm of concrete metal insert was ablated during 1700 s, faster than it was observed in the test. CORCON underpredicts time of the start of concrete basemat ablation. Due to underprediction of insert ablation time, total erosion depth is overpredicted. At the same time comparison of erosion during basemat ablation phase shows qualitative agreement of the predicted and measured ablation depth. Namely, during basemat ablation phase (duration of 2400 s) predicted erosion depth (time period between 2500 and 5000 s) is 15 cm. This value is very close to the test data. The same may be said with respect to the predicted temperature. Comparison of calculated temperature to test data is presented in Figure 3.13. Due to underprediction of insert ablation time, temperature drop in calculations occurred earlier than in the test.

High erosion rate during concrete/metal ablation is due to the high value of chemical heat caused by zirconium metal oxidation. Chemical heat during insert ablation phase allows for temperature in the calculations to remain at approximately constant value (see Figure 3.13). Chemical heat input to the melt is about 60 kW, and upward losses predicted by the CORCON are about 25-30 kW during the test. Thus, energy input during the initial phase is about 120 kW so downward heat is sustained at the average level of 60-70 kW. High level of downward heat provides high erosion rate in the calculations. Energy terms calculated by CORCON are presented in Figure 3.14. For concrete basemat ablation phase, heat to concrete is about 50 kW and close to the estimated value above. However, heat release due to oxidation reactions is much lower (15-20 kW).

Oxidation scenario in calculations is presented in Figure 3.15. Zirconium oxidation is completed approximately by the start of basemat ablation. This oxidation rate corresponds to the initial

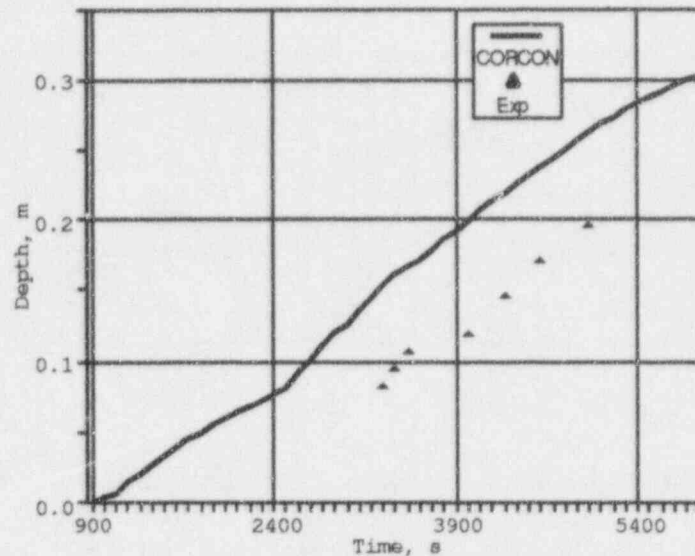


Figure 3.12: ACE L6 concrete erosion depth

inventories of species in the concrete metal insert presented in Figure 3.10. For instance,  $\text{SiO}_2$  inventory in the insert is about 258 moles or approximately equal to the zirconium inventory. This is why CORCON predicts full zirconium oxidation by the end of insert ablation. Later, oxidation of silicon defines chemical heat in the melt. Silicon (and metal layer) exists by the end of calculations defining relatively high heat transfer to concrete and high erosion rate.

Predicted  $\text{CO}$  and  $\text{H}_2\text{O}$  flow rates are presented in Figures 3.16 and 3.17. Qualitatively, gas releases correspond to the test data but calculated rates are much higher than measured data. Small gas release rates have already been discussed above.

There are several reasons which may influence the behavior of melt during concrete/metal insert ablation phase, such as decomposition temperature and oxidation reactions of  $\text{Zr}$  and  $\text{Si}$  with formation of  $\text{SiO}$  gas. These reactions are endothermic and may lead to reduction of chemical heat. Temperature limit for these reactions (2300 K) existed during relatively long time in the test. Special sensitivity calculations were made to estimate the influence of  $\text{SiO}$  gas formation. Results of calculations are presented in Figures 3.18 and 3.19. Accounting for these reactions leads to longer time for concrete/metal insert ablation, but again interaction time is underpredicted. Behavior of oxide layer temperature is similar to the base case behavior. Lower heat release (about 40 kW) causes reduction of downward heat and as a consequence, erosion rate (see Figure 3.19).

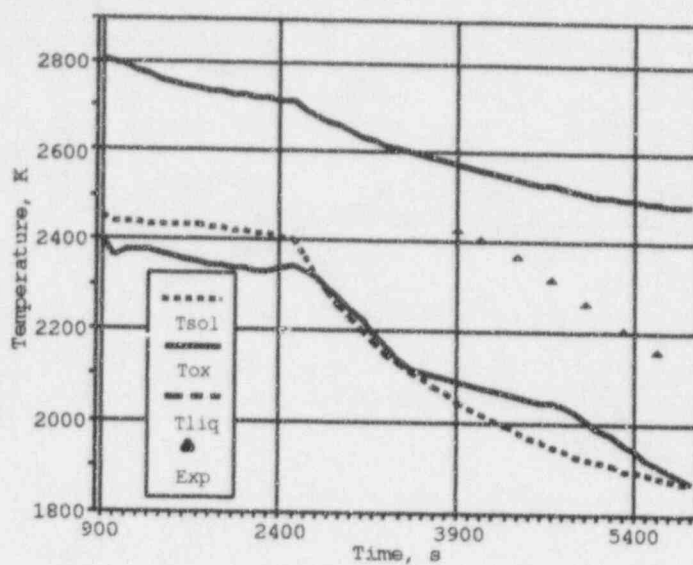


Figure 3.13: Temperature of oxide layer for ACE L6 test

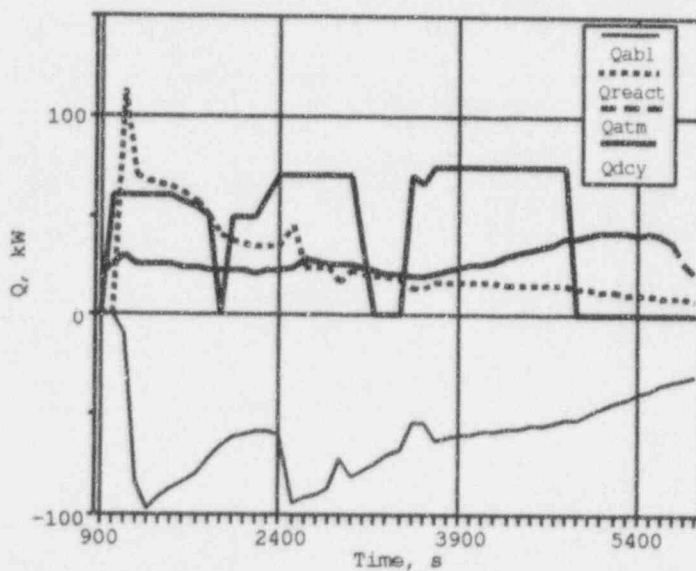


Figure 3.14: Energy rate terms for ACE L6 test



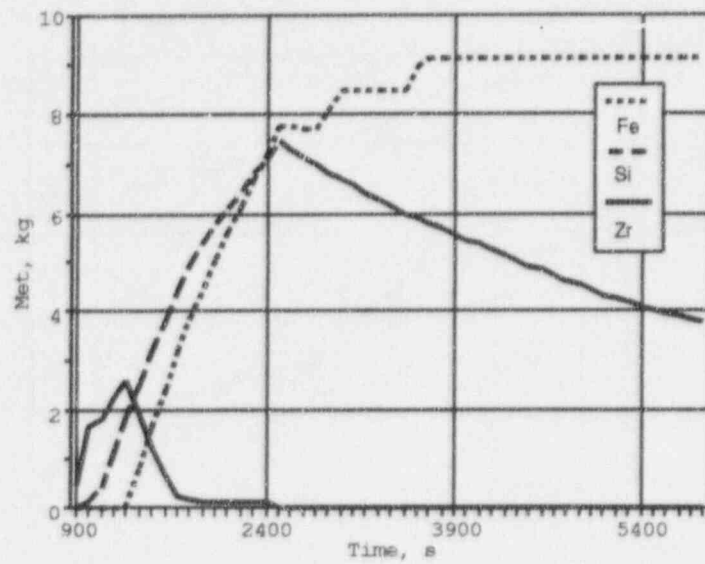


Figure 3.15: Mass of metals in the melt for ACE L6 test

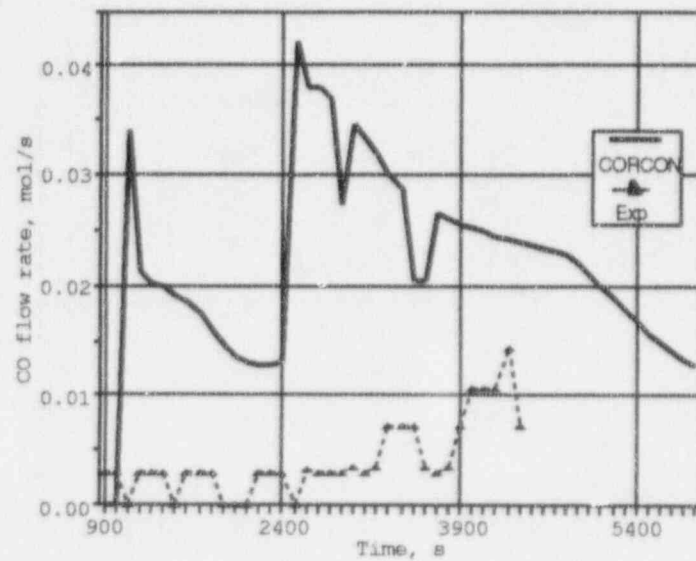


Figure 3.16: CO flow rate for ACE L6 test

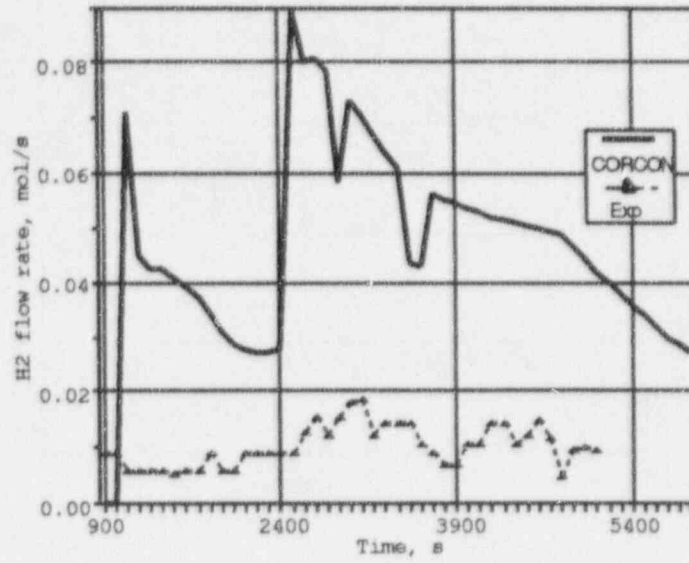


Figure 3.17: H<sub>2</sub> flow rate for ACE L6 test

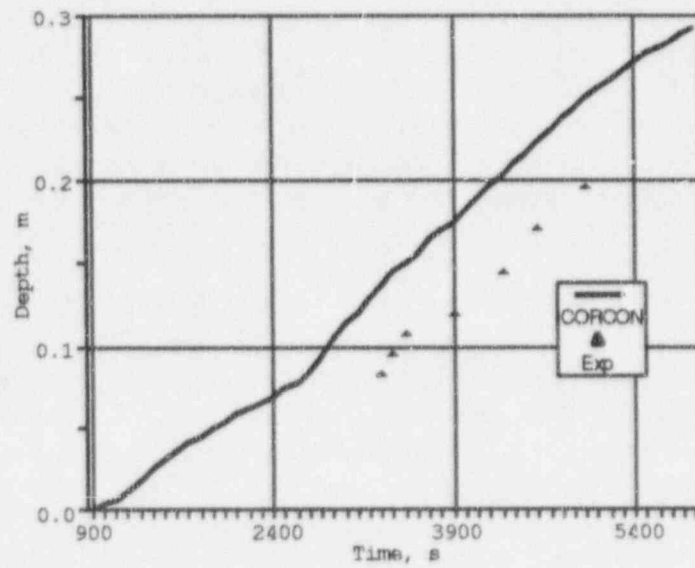


Figure 3.18: Concrete erosion depth for ACE L6 (sensitivity case)

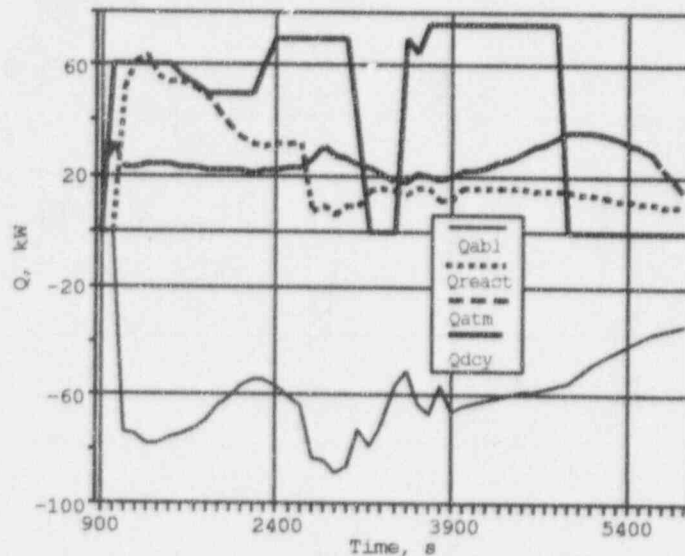


Figure 3.19: Energy rate terms for ACE L6 test (sensitivity case)

### 3.5 Modeling of the ACE L7 Test

#### 3.5.1 Test Conditions and Results

The ACE L7 experiment used a predominantly oxidic mixture containing  $UO_2$ ,  $ZrO_2$  and limestone common sand concrete [43, 44]. Tables 3.2 and 3.3 present the composition of the charge and the concrete/metal insert. The charge contained approximately 8 kg of fission product simulants. Metallic zirconium and boron carbide in thin stainless steel tubes were incorporated into concrete metal insert. Insert for L7 test included 18.8 kg of  $Zr$ , 0.6 kg of  $Fe$ , and 18.1 kg of limestone-common sand concrete.

When erosion front reached concrete metal insert, all species entered the melt gradually during the concrete/metal insert ablation. The thickness of concrete/metal insert was 5.7 cm. Its average density was equal to 3300 kg/m. There was no reinforcing rod below surface of the concrete basemat, which had dimensions of 50.2 cm  $\times$  49.3 cm, and a density of 2.45g/cm<sup>3</sup>. Composition of limestone common sand concrete is presented in Table 2.1. The basemat contained 65 thermocouples to determine erosion front and temperature of the melt.

During the experiment, the voltage was adjusted to maintain electric power to the charge at approximately 120 kW during the interaction phase of the test. Taking into account side losses, the net power to the melt was estimated to be 50 kW. Table 3.13 presents energy terms which determine thermal behavior of melt.

Beginning of concrete metal insert ablation was detected at 22.5 minutes prior to the onset of

Table 3.13: Energy balance summary for ACE L7

	Power, kW			Energy, MJ		
	Net	Upward	Downward	Net	Upward	Downward
Insert ablation	50	25	80	66	33	110
L/S concrete ablation	50	30	26	90	54	47
Total				154	87	157

Table 3.14: Gas release during test L7

Species	Inventory, mol		Released gases, mol			
	Insert	Basemat	Prior to ablation	Insert Ablation	Basemat Ablation	Total
$H_2O + H_2$	61	55	52	29	5	86
$CO_2 + CO$	88	80	41	41	33	125
$SiO_2$	85	77				
Zr	206					

basemat ablation. During concrete metal insert ablation, some foamed melt was drawn into the gas line. After about 30 minutes of basemat ablation, test was terminated when additional melt foam plugged the line connecting the test apparatus to the aerosol system. Erosion of 5.7 cm of concrete metal insert occurred during 22.5 min with average ablation rate of 2.5 mm/min. About 3 cm of basemat was ablated during 30 minutes of interaction. Temperature during the test was estimated to be about 2500 K.

According to data presented in reference [44], prior to basemat ablation, main gases were detected in the form of  $H_2$  and  $CO$ . After start of basemat ablation,  $H_2$  disappeared in the offgas, and the ratio of  $CO/CO_2$  became much lower than that during the first phase. This fact indicates changes in the character of oxidation. Total gas release during different phases of interaction is presented in Table 3.14. About 50% of total water and  $CO_2$  content in the insert was detected during the insert ablation phase. During basemat ablation, only 10% of  $H_2O$  and 50% of  $CO_2$  were detected.

### 3.5.2 Comparison to ACE L7 Test Data

In accordance with the test arrangement, two different concrete layers were modeled: concrete/metal insert with the thickness of 5.7 cm and concrete basemat. Decomposition temperature of concrete metal insert was defined in the input deck as 1745 K, and limestone-common sand concrete basemat was assumed to ablate at temperature of 1500 K (100 K greater than solidus

Table 3.15: Main parameters of concrete/metal insert in test L7

Depth	5.7 cm
RBR	-1.1
Fe	0.03
Zr	0.97
TW, K	1745

temperature for L/S concrete). Table 3.6 presents most initial parameters of the ACE L7 test. Concrete metal insert composition was modeled using RBR parameter to define the composition of rebar in the concrete (see Table 3.15).

As shown in Figure 3.20, ablation rate during the first phase of interaction (concrete/metal insert erosion) is in good agreement with the experimental data while ablation during the second basemat ablation phase is overpredicted approximately two times in comparison to the test data. The insert ablation takes about 1000 s which is slightly lower than the measured value (1300 s).

Predicted temperature of the oxide layer is presented in Figure 3.21. Temperature of melt drops quickly while experimental temperature remains at the level of 2500 K. Figure 3.22 presents heat losses to the surrounding, heat to concrete ablation and energy release due to chemical reactions. During the first stage of interaction which is characterized by the gradual zirconium entrance into the melt and by intensive chemical interaction with gases, high energy release due to the oxidation of metallic components is predicted. Heat to the surrounding is overpredicted about two times while heat to concrete corresponds to the estimated value. Overestimation of upward heat loss leads to the temperature drop.

Temporal behavior of different metallic species in the metal layer is presented in Figure 3.23. High  $CO_2$  and  $SiO_2$  contents in the L/S concrete define very rapid oxidation of Zr (reactions in the condensed phase were included in the calculations). At 300 s after start of basemat ablation, zirconium metal is predicted to be fully oxidized. At about 1400 s from the start of basemat ablation, metallic phase fully disappears. The comparison of gas release rates is presented in Figures 3.24-3.27. All release rates demonstrate very good qualitative agreement with the test data. For example, the disappearance of metallic phase at about 1400 s changes significantly the chemistry of the melt (there are no oxidation reactions after this time) when primary concrete gases are released. This time is predicted by the code very well. The total gas release measured during the test is about 75% of the expected value. For concrete/metal insert ablation phase, gas release predicted by the code is three times higher than the actually observed values. This difference is due to the gas release prior to ablation (see Table 3.14). Relatively long preheating phase leads to the early gas release. During basemat ablation phase, both  $CO_2$  and  $CO$  rates correspond to the test data, but one should take into account that the erosion rate is overpredicted by the CORCON code.

CORCON predictions for ACE L7 test are in good agreement for temporal scenario of interac-

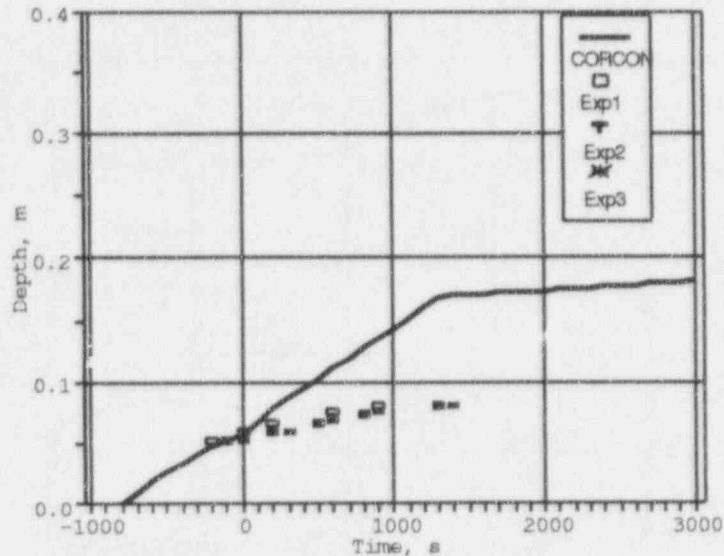


Figure 3.20: ACE L7 concrete erosion depth

tion. In particular, CORCON predicts disappearance of metal layer at about 1400 s. This leads to the change of released gas composition as it was really detected in the experiment.

### 3.6 Modeling of the ACE L4 Test

#### 3.6.1 Test Conditions and Results

Test L4 [45, 46] was performed utilizing two types of concretes used in the basemat of nuclear power plants with VVER type reactors. The upper layer, made of thermoresistant serpentine concrete of 5.1 cm thickness, was located atop structural concrete which was close in composition to the siliceous concrete. The thickness of the structural concrete block was 25.4 cm. Densities of serpentine and ordinary structural concrete were 2.37 and 2.28  $g/cm^3$ , respectively. Six reinforcing rods were located in the basemat, two of them having a total mass of 0.74 kg located in the middle of serpentine layer. Four other rods (1.85 kg) were located 10.2 cm below the concrete surface. Concrete/metal insert, made of serpentine concrete and metal rods, was located above the basemat. The thickness of the concrete/metal insert in this test was 7.9 cm. About 31.4 kg of zirconium rods and 1.0 kg of boron carbide were cast into serpentine concrete. Total mass of the insert was 57.2 kg. Initial composition of melt at the start of concrete/metal insert ablation, and the composition of metals in the melt are presented in Table 3.3 and 3.2, respectively.

Temporal scenario of interaction presented in Table 3.4 shows that concrete/metal insert ablation began -2400 s prior to the basemat ablation. Interaction with serpentine concrete was very



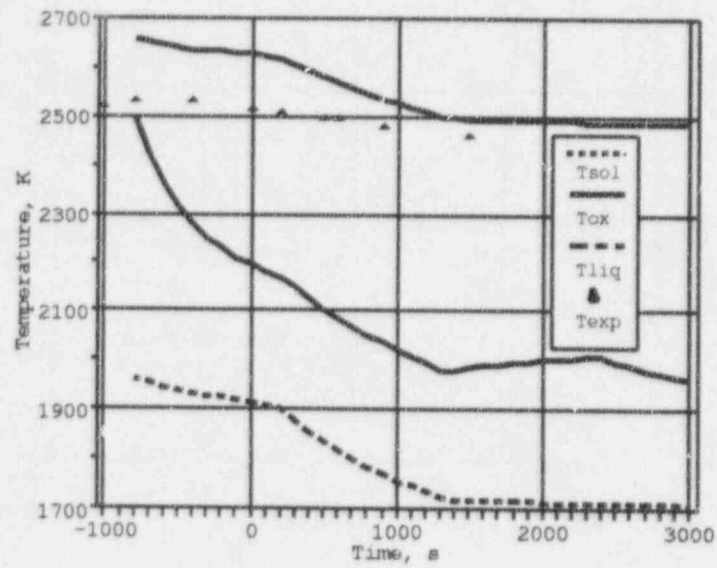


Figure 3.21: Temperature of oxide layer for ACE L7 test

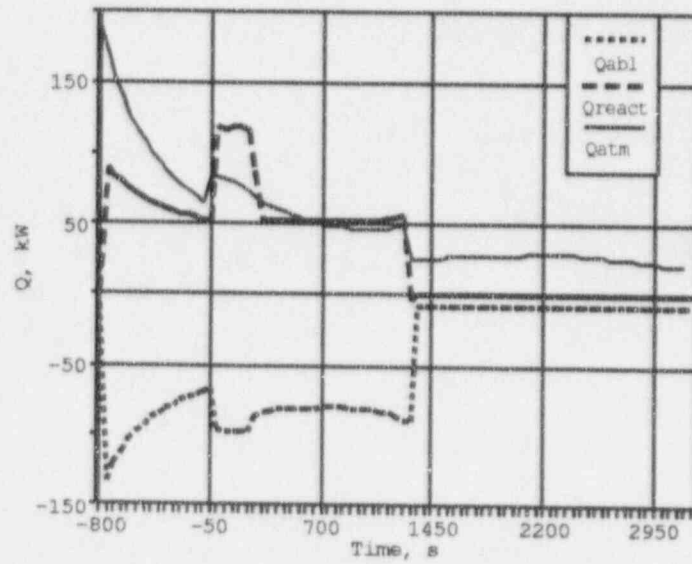


Figure 3.22: Energy rate terms for ACE L7 test

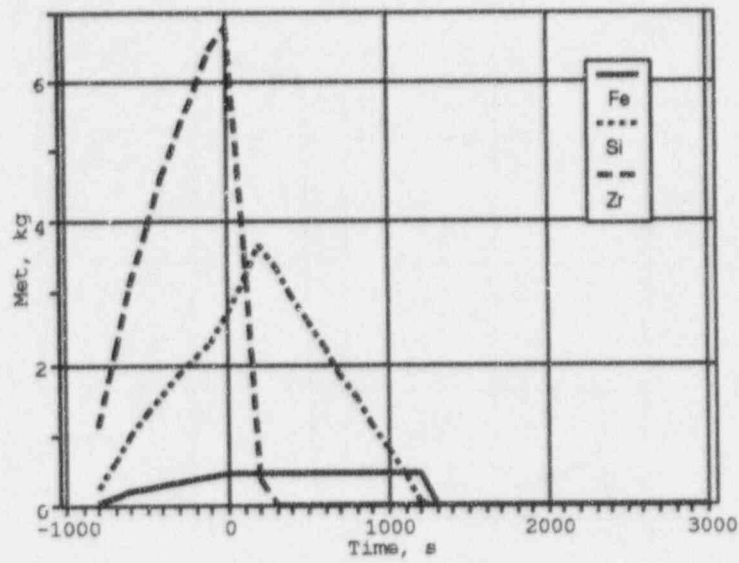


Figure 3.23: ACE L7 mass of metals (*Fe*, *Si*, *Zr*)

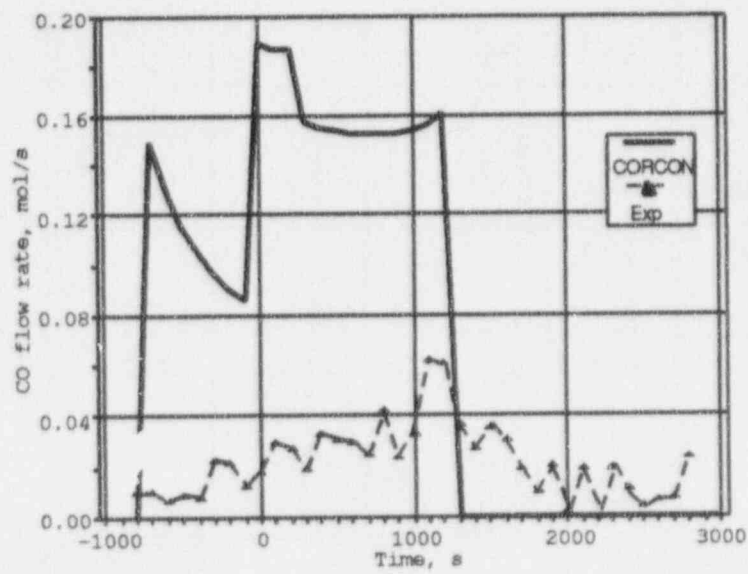


Figure 3.24: ACE L7 CO flow rate

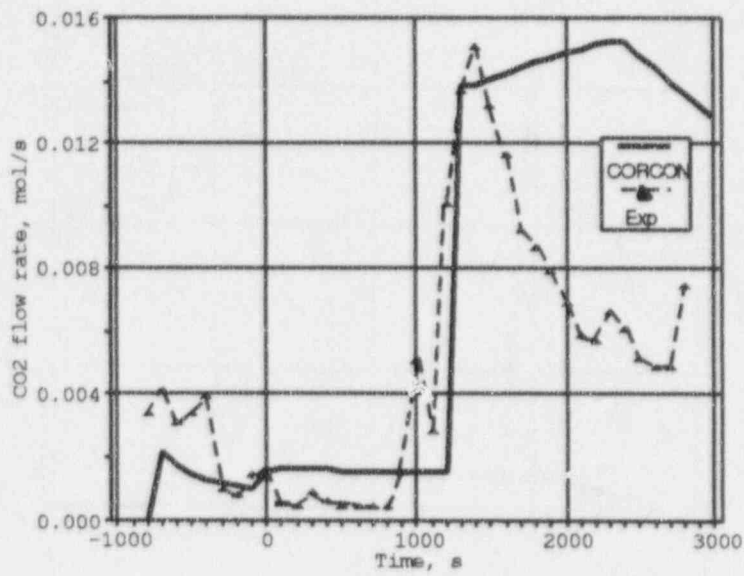


Figure 3.25: ACE L7 CO<sub>2</sub> flow rate

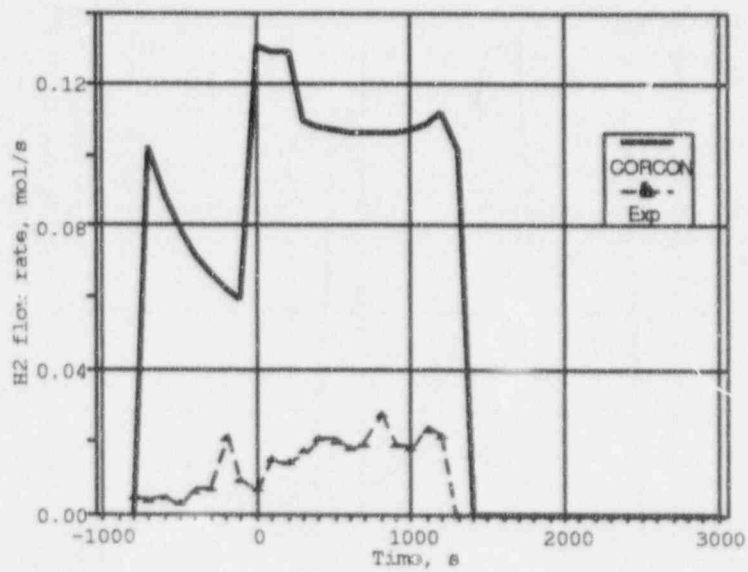


Figure 3.26: ACE L7 H<sub>2</sub> flow rate

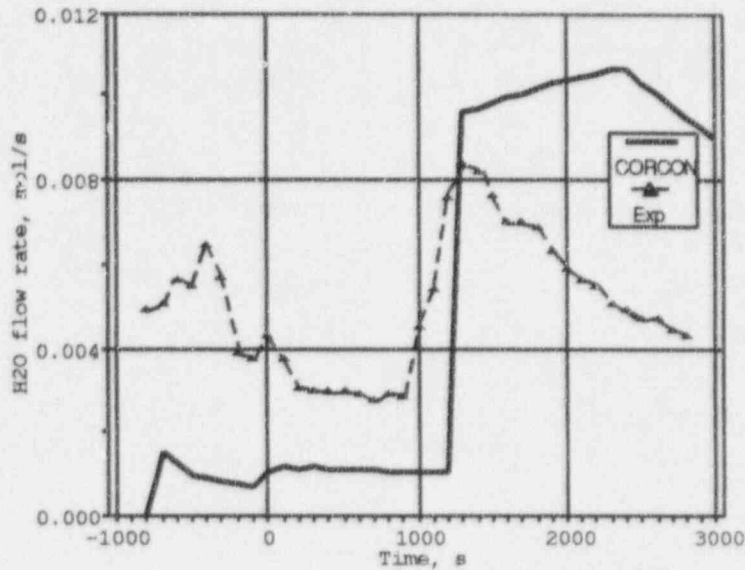


Figure 3.27: ACE L7 H<sub>2</sub>O flow rate

fast, total duration of interaction being about 700 s. The erosion rate slowed down significantly when structural concrete began to ablate. Total erosion depth observed in the test was about 14.2 cm including 5.2 cm of serpentine concrete. Accounting for insert ablation, the total ablation depth in the test was about 22 cm.

Net power to the melt (without side losses) was maintained at the level of 50 kW during the test. The upward heat losses were measured to be 12–20 kW. Estimated melt temperature was 2100–2200 K throughout the ablation phase. Assessment of different energy terms is presented in Table 3.16. Marked increase of downward heat during the serpentine ablation phase is a result of very short erosion time. At the same time, total net power input is lower than total heat losses by about 10 %. Chemical heat release is expected to be significant during the serpentine ablation phase due to very high water content. The temperature during the test was lower than the temperature of SiO formation (about 2300 K), so SiO gas formation did not play an important role in this test.

Offgas behavior in the test was a function of erosion depth. First spike of offgas flow rate was measured at the start of insert ablation. When erosion front reached serpentine concrete surface, considerable increase in flow rates was detected. The flow rate decreased later due to the change of concrete type with much lower water content. In Table 3.17, comparison of inventory of gaseous species and detected gases is presented. Total inventory of H<sub>2</sub>O in the eroded concrete is about 490 moles, about 390 moles of which (or 80 %) was detected. Detected CO<sub>2</sub> and CO was 32 moles or 130 % of the total inventory. This difference was due to the addition of B<sub>4</sub>C to the melt. High contents of SiO<sub>2</sub> and gaseous species in both concretes used in the test provided intensive oxidation of zirconium metal in the condensed phase.

Table 3.16: Energy balance summary for ACE L4

	Power, kW			Energy, MJ		
	Net	Upward	Downward	Net	Upward	Downward
Insert Ablation	50	15.5	90	135	42	220
Serp. Concrete Ablation	50	17	100	43.5	15	90
Silicon Concrete Ablation	50	18	15	363	124	110
Total				542	181	420

Table 3.17: Gas release during test L4

Species	Inventory, mol			Released gases, mol				
	Insert	Serp. Basemat	Silic.* Basemat	Prior to ablation	Insert Ablation	Serp. Basemat	Silic. Basemat	Total
$H_2O + H_2$	194	240	53	35	62	118	170	385
$CO_2 + CO$	5	6	14	2	8.5	6.2	15.5	32.2
$SiO_2$	139	170	576					
Zr	345.5							

\* Near 8 cm of siliceous concrete was ablated.

### 3.6.2 Comparison to ACE L4 Test Data

Modeling of ACE L4 test was performed with CORCON-Mod3 input parameters presented in Table 3.6. Values of decomposition temperatures (TW) for concrete/metal insert was assumed to be 1780 K, for serpentine concrete 1550 K, and for siliceous concrete 1700 K. The value of the decomposition enthalpy calculated by CORCON-Mod3 for serpentine concrete is equal to 2.9 MJ/kg which is 1.3 times greater than the value for basalt concrete (2.3 MJ/kg) and two times greater than that for the limestone concrete (1.5 MJ/kg). For concrete insert reinforced by Zr rods with filling factor of 0.6 as in the L4 experiment, it is assumed that the decomposition temperature is equal to 1780 K. Calculated ablation enthalpy for concrete/metal insert is 3.9 MJ/kg, which is about 30 % greater than that for pure concrete.

The analysis of offgases, presented in Table 3.17, indicates that only 80 % of total water content was detected in the offgases. During the serpentine concrete ablation phase, detected gases were about 50 % of what was expected to be released. Thus, in the calculations of ACE L4, gas contents in the concrete were changed. To define the gas content in concrete, experimental data on the gas release was used in the following way. When preparing input data for the ACE L4 test, it was assumed that during the serpentine concrete ablation only 120 moles of  $H_2O$  was released while total water inventory in the test was 240 moles. It means that average water content based on this assessment in the serpentine concrete is about of 6.5 %. These data were the basis to change the composition, e.g. the total amount of water in serpentine concrete was assumed to be 6.5%, and the amount of  $CO_2$  to be 4.2%. Reduction of gaseous species in serpentine concrete changes the chemistry of the metal layer, but taking into account actual gases passing through the metal layer, this reduction is appropriate to account for early gas release in the tests. Moreover, it may provide better agreement with test data due to more appropriate calculations of heat generation.

Results of modeling by CORCON-Mod3 are presented in Figures 3.28–3.34. Comparison to the erosion depth data is presented in Figure 3.28. This figure contains all erosion information including erosion of the concrete/metal insert. In the code calculations, concrete/metal insert was ablated slightly earlier than it was observed in the test. As in the test, erosion of serpentine layer lasts about 900 s. This prediction is in good agreement with the test data. Erosion rate of siliceous concrete is slightly overpredicted by CORCON. The start of serpentine concrete ablation led to significant increase in the chemical heat release (see Figure 3.29). Heat to concrete calculated by CORCON is about 30 kW during the insert ablation, and 20 kW during the siliceous concrete ablation.

Temperature of oxide layer is presented in Figure 3.30. Temperature of oxide layer is about 2100 K during the test and very close to the measured melt temperature in the test. Masses of metals constituting metal layer are presented in Figure 3.31. Oxidation of zirconium metal was over by 1600 s.

Comparison of gas release rates (presented in Figure 3.32 for  $H_2$  and Figure 3.33 for  $CO$ ) indicates adequate qualitative agreement with the test data. Peaks in the  $H_2$  and  $CO$  releases at about 360 s correspond to the start of serpentine concrete ablation. Relatively large water content in this concrete leads to the increase in the gas flow rates. The width of  $H_2$  peak is caused by the zirconium oxidation time that depends both on gas reactions and on  $SiO_2$  content in the concrete. This content is also relatively large for serpentine concrete, and hence, the peak is quite narrow.



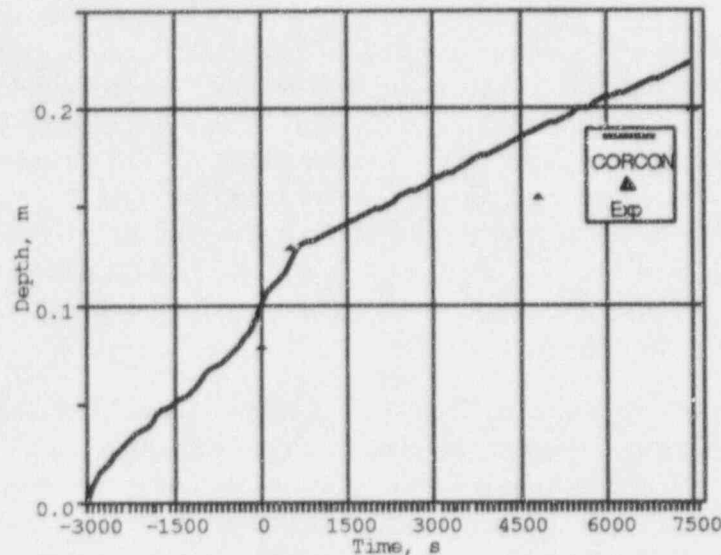


Figure 3.28: ACE L4 concrete erosion depth

Qualitatively, the  $CO$  release is similar to the  $H_2$  release. Figure 3.34 shows the total  $H_2$  release predicted by the CORCON code. The calculated curve is very close to the measured data due to justification of  $H_2O$  content in the serpentine concrete.

Modeling of ACE L4 test shows good agreement of calculated and measured data. Thermal hydraulic behavior of materials during the test is governed by heat transfer to concrete through metal layer. Chemical heat release provides high erosion rates during ablation of concrete/metal insert and serpentine concrete.

### 3.7 Modeling of the ACE L8 Test

#### 3.7.1 Test Conditions and Results

ACE L8 experiment [47, 48] used an oxidic mixture containing primarily  $UO_2$  and  $ZrO_2$  species to simulate the interaction with the limestone/limestone concrete. To introduce metals into the melt, concrete/metal insert containing zirconium metal was located above the basemat to preclude early oxidation. The concrete/metal insert includes 13 kg of  $Zr$ , 1 kg of  $Ag$ , 0.22 kg of  $In$ , and 16.3 kg of limestone concrete. Net power in the test was 75 kW during the initial stage of interaction and later, was reduced to 35 kW after metal oxidation completed. There were no reinforcing rods in the L8 basemat. The average density of concrete/metal insert equals  $3300 \text{ kg/m}^3$ . Tables 3.2 and 3.3 present the composition of the initial melt and concrete metal insert.

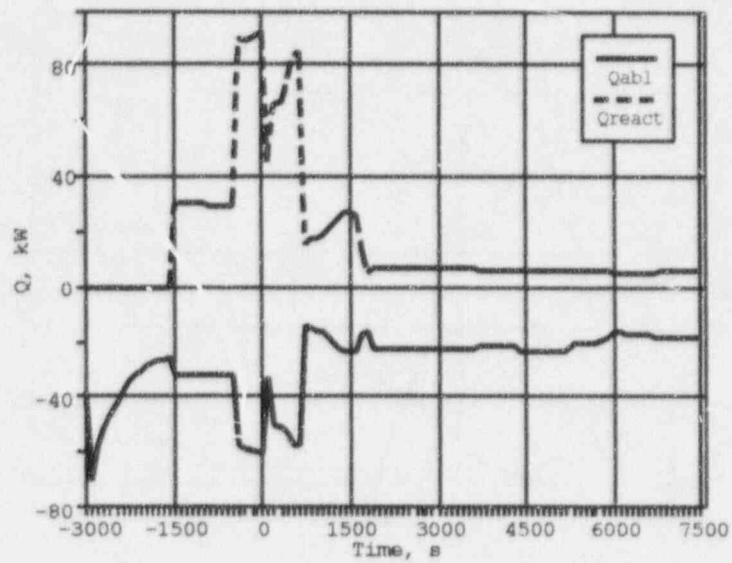


Figure 3.29: Energy rate terms for ACE L4 test

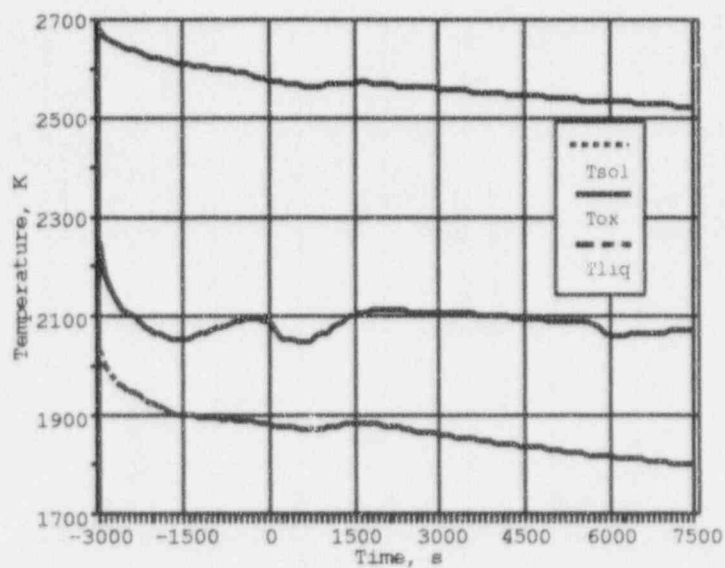


Figure 3.30: Temperature of oxide layer for ACE L4 test

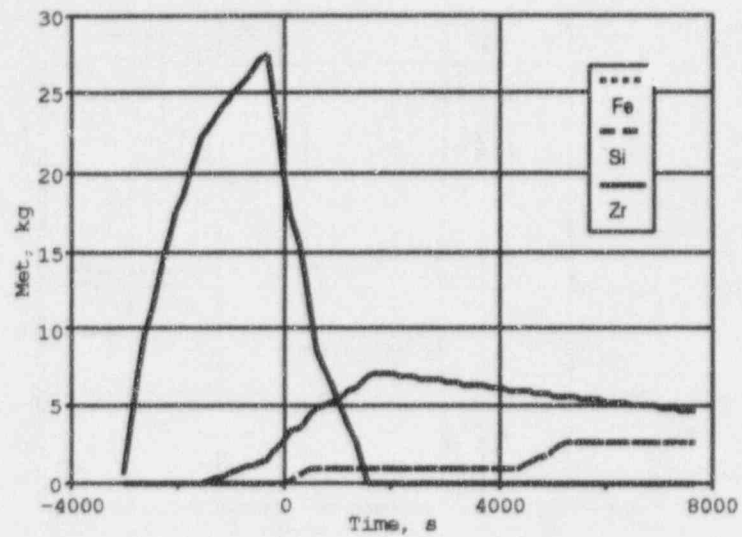


Figure 3.31: Mass of metals in the melt for ACE L4 test

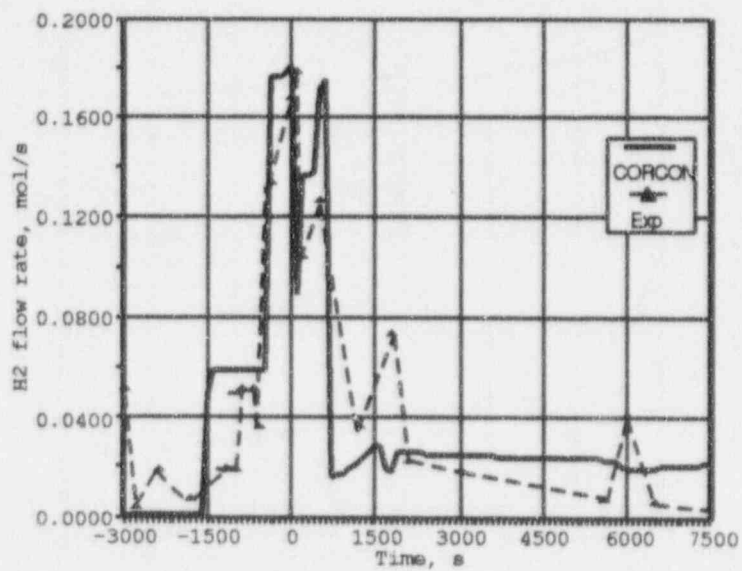


Figure 3.32:  $H_2$  flow rate for ACE L4 test

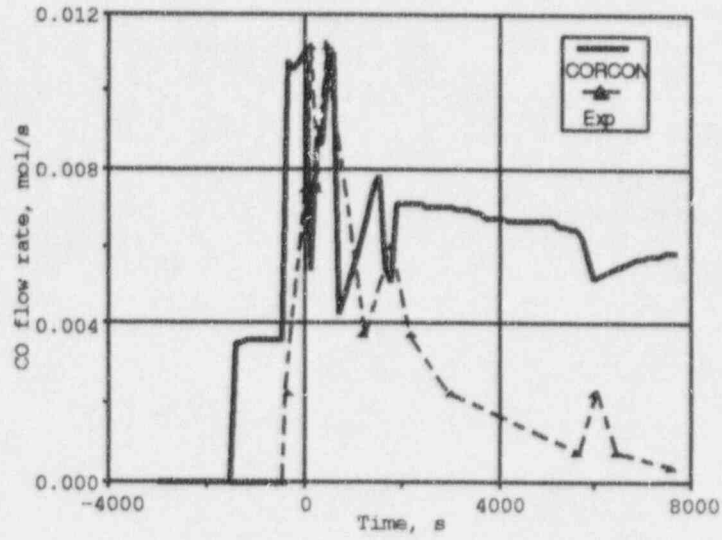


Figure 3.33:  $CO$  flow rate for ACE L4 test

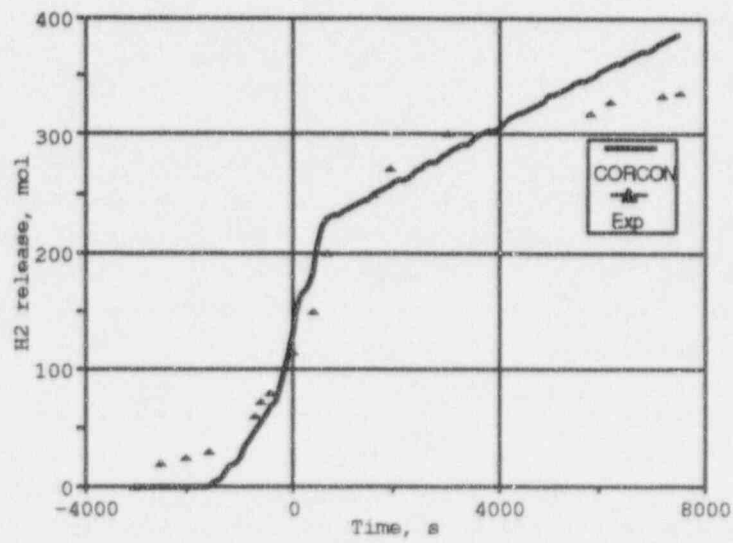


Figure 3.34: Total  $H_2$  release for ACE L4 test

Table 3.18: Energy balance summary for ACE L8

	Power, kW			Energy, MJ		
	Net	Upward	Downward	Net	Upward	Downward
Insert ablation (-10-0 min.)	60	17	140	36	10	84
L/L concrete ablation (0-30 min)	75	23	40	135	42	72
L/L concrete ablation (30-101 min)	35	18	17	147	76	42
Total				319	128	198

Table 3.19: Gas release during test L8

Species	Inventory, mol		Released gases, mol			
	Insert	Basemat	Prior onset of ablation	Insert Ablation	Basemat Ablation	Total
$H_2O + H_2$	55	220	95	55	55	205
$CO_2 + CO$	123	495	5	133	472	610
$SiO_2$	17	61				
Zr	144					

Ablation of concrete metal insert began 10.8 minutes prior to the onset of basemat ablation. Net power was sustained at the level of 75 kW, but it fluctuated sharply prior to and during insert ablation. After the basemat ablation began, the power was stabilized at the indicated level. After 30 minutes of interaction, net power was reduced from 75 to 35 kW and was sustained at this level through the end of the test. Upward power loss was at the level of 17 kW during insert ablation, 23 kW during initial 30 minutes of basemat ablation, and then decreased to 13 kW. Estimated chemical reaction power had a very sharp spike at 150-160 kW with an average value of 36 kW from the start of basemat ablation to 30 min, when the power was reduced. Summary of energy rate terms is presented in Table 3.18. Melt temperature decreased gradually in the test from 2500 K at the start of insert ablation to 2200 K at 100 minutes.

After initial 10.8 minutes, erosion of 4.2 cm of concrete metal insert was completed with average erosion rate of 0.07 mm/s. During initial 10 minutes of interaction with limestone basemat, 4 cm of concrete was ablated at approximately the same rate of 0.07 mm/s. Later, erosion rate decreased slowly and, after power reduction, was about 0.012 mm/s. Total depth of ablation was nearly 12.7 cm. Measurements of the 1673 K isotherm location in the basemat showed significant differences in the timing when thermocouples, located at the same level but at different coordinates, indicated 1673 K temperature.

Tables 3.2 and 3.3 present the inventory of main species in the concrete/metal insert and basemat concrete. Only those species which influence significantly chemical heat generation and

Table 3.20: CORCON options to model insert rebar

Depth, cm	4.2
RBR	0.9
Zirconium content	1.0
TW, K	1745

offgas composition are included in these tables. In the experiment, about 95 moles of  $H_2O$  and 5 moles of  $CO$  were released prior to the onset of ablation. Thus, during the ablation phase, only part of gas inventory was measured. Gas release during the insert ablation phase corresponds to the test data. Dehydration front at the start of insert ablation was located in the basemat. More detailed analysis is presented in the next section. About 98% of available  $CO_2$  was detected [48]. There was no hydrogen release after 30 minutes of basemat ablation in the test, indicating changes in the chemistry of oxidation. Total  $H_2O + H_2$  release was 205 moles or about 75% of initial water inventory in the insert and concrete.

### 3.7.2 Comparison to ACE L8 Test Data

Table 3.6 presents most initial parameters of the ACE L8 test. To provide gradual zirconium entrance to the melt, the composition of concrete/metal insert was specified using CORCON input options. Parameter RBR was defined as 0.9 to represent the zirconium content in concrete. The corresponding zirconium content in the rebar was selected as 1. Thickness of the insert was 4.2 cm. After the melt front reached this level, concrete properties were changed to correspond to the pure limestone concrete. Due to the presence of zirconium in the insert, and because concrete contains nearly 7.1% of silica, the condensed phase chemistry (CPC) option was enabled in the computations.

The limestone concrete was assumed to ablate at 1500 K. This is the solidus temperature of limestone concrete. Concrete/metal insert was assumed to ablate at a higher temperature (equal to 1745 K) to take into account the presence of zirconium rebar (with higher melting point) in the concrete. Surrounding temperature was defined in the range of  $T_{sur} = 1650 - 1850 K$ . Calculations started at  $-600$  s to account for the insert ablation. Start of basemat ablation in the test corresponds to time zero. Table 3.20 presents the composition of the concrete/metal insert used in this experiment as well as the parameters for CORCON input.

Initial 3600 seconds of interaction was modeled by the CORCON-Mod3 code. Results of calculation and comparison to test data are presented in Figures 3.35 through 3.44. Figure 3.35 presents CORCON predictions for ablation depth and summary of experimental results [47]. Data shown in this figure represent experimental front measurements at different positions of thermocouples. Duration of the concrete metal insert ablation phase, characterizing the initial phase of interaction, is in good agreement with the test data. Start of basemat ablation predicted by CORCON is approximately equal to the time observed in the test, and calculations indicate that 4.2 cm of concrete/metal insert was eroded. After beginning of the basemat ablation, erosion rate remains almost identical to that for insert ablation.



Slowing down of the predicted erosion rate after 500 s from the start of concrete basemat ablation was due to a change in the melt composition. This is characterized by the disappearance of the metal layer in the calculations. Figure 3.36 shows that at 500 s, metal layer disappears in the calculations (including iron) due to rapid oxidation of metal components by outcoming gases and silica. The zirconium mass in the metal layer was found to be about 6 kg instead of initially loaded 13 kg. The reason is oxidation of zirconium in course of gradual entrance. At the end of metal insert interaction, total inventory of Zr was about 144 moles. The inventory of gaseous species (both  $H_2O$  and  $CO_2$ ) in the concrete/metal insert was 178 moles. Taking into account that two moles of gas react with one mole of Zr, total calculated Zr oxidation by gases was 90 moles whereas the maximum zirconium content in the melt is 45 moles. Maximum inventory of the silicon in the melt after full oxidation of zirconium was about 30 moles due to low silica content in the limestone concrete.

Temperature of oxide and metal layers are presented in Figures 3.37 and 3.38 together with calculated solidus and liquidus temperatures of metal and oxide layers. The solidus curve for metal layer represents the solidus and liquidus temperatures calculated by  $Fe - Zr$  phase diagram. Temperature of the metal layer is significantly higher than the liquidus temperature so there is no metal crust in the calculations. Calculated oxide layer temperature is lower than the experimental value.

Chemical heat generation during insert ablation predicted by CORCON was about 70 kW. Start of the basemat ablation leads to an increase of chemical power to 130 kW due to a change of the oxidation rate by incoming gases to the melt. At 500 seconds after the start of basemat ablation, chemical power becomes zero. Elimination of the metal species is followed by a decrease of power to concrete and results in reduction of erosion rate. Figure 3.39 illustrates main energy terms predicted by CORCON. During the insert ablation phase, CORCON overpredicts upward heat losses. This may be a probable reason why temperature in the calculations is lower than the actual measured temperature. Average power to concrete at the moment of total oxidation of metal layer is about 120 kW. Start of oxidic melt interaction with basemat concrete immediately leads to the formation of the bottom crust due to lower solidus temperature. The thickness of the crust is shown in Figure 3.40.

Comparison of the gas release data presented in Figures 3.41 - 3.44 indicates that the flow rates for all gases are in good qualitative agreement with the experimental data. Elimination of metal layer is accompanied by the changes in gas composition. Release of  $H_2$  and  $CO$  becomes very small immediately after full oxidation of metals (500 s), and only  $H_2O$  and  $CO_2$  are predicted to be released. Changes in gas composition coincide with changes in offgas composition in the test. Absolute values of the released gases are lower than the calculated data for all gases. At the same time, difference in predictions of  $H_2$  and  $H_2O$  release rates is higher than that for  $CO$  and  $CO_2$ .

Calculated timing of events in the test is summarized in Table 3.21 and compared with test data. Estimate of zirconium oxidation time is based on the changes in offgas composition. Temporal characteristics of interactions predicted by CORCON are very close to test data.

Considering the assessment of the calculated data and their correspondence to the test data, one can conclude that CORCON-Mod3 predictions for ACE L8 test are in good qualitative and quantitative agreement with the test data. Some differences with respect to the gas release data

Table 3.21: Calculated scenario of ACE L8 test

Events	Time, s Calculated	Time, s Estimated
Start of concrete/metal insert ablation, s	-600	-648
Start of basemat ablation, s	0	0
End of Zirconium oxidation, s	140	100
End of Silicon oxidation, s	500	600

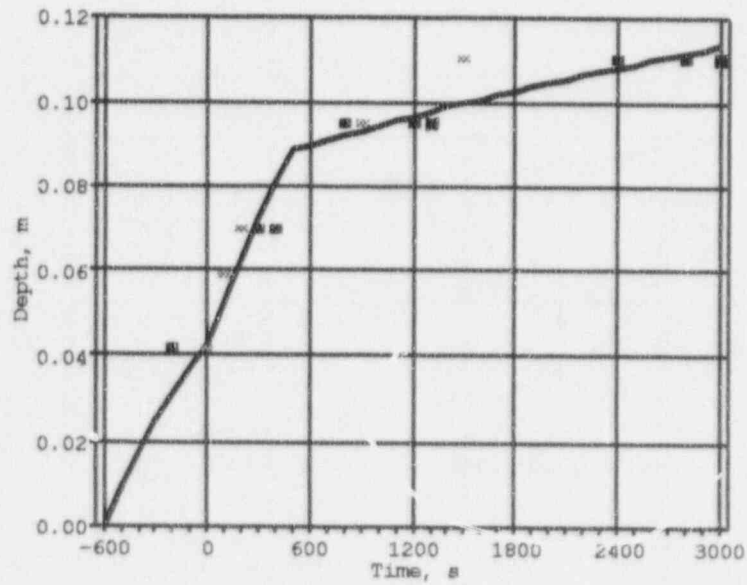


Figure 3.35: ACE L8 concrete erosion depth

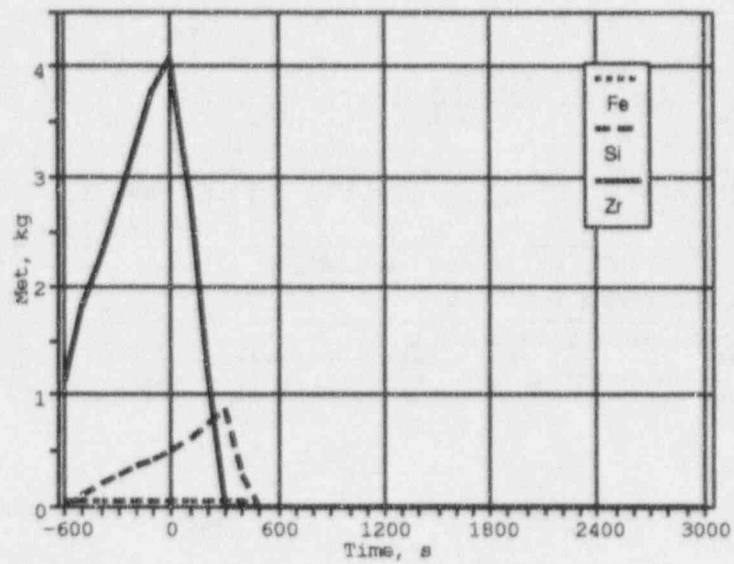


Figure 3.36: ACE L8 mass of metals (*Fe, Si, Zr*)

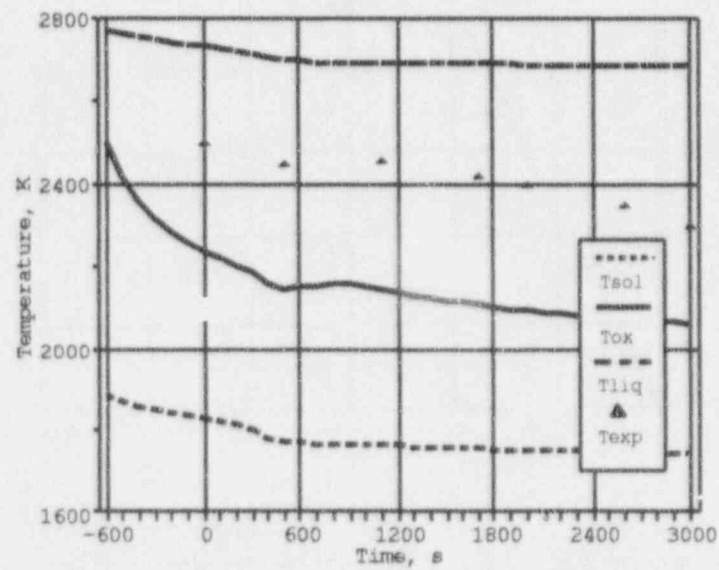


Figure 3.37: Temperature of oxide layer for ACE L8 test

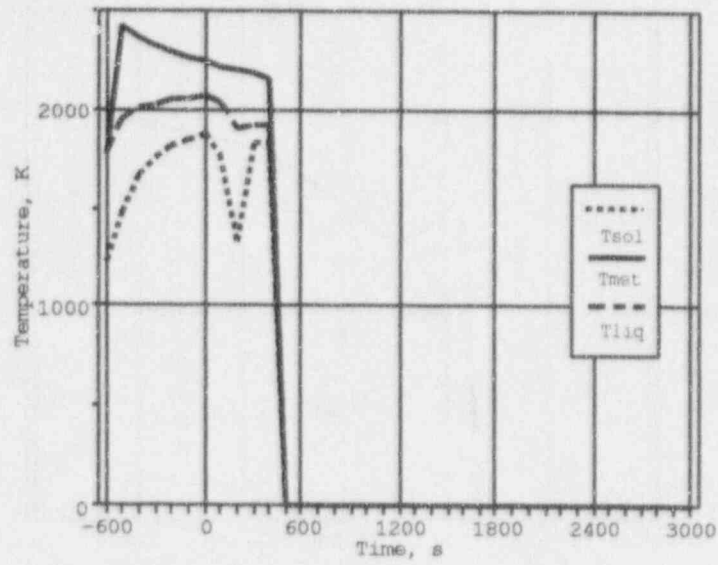


Figure 3.38: Temperature of metal layer for ACE L8 test

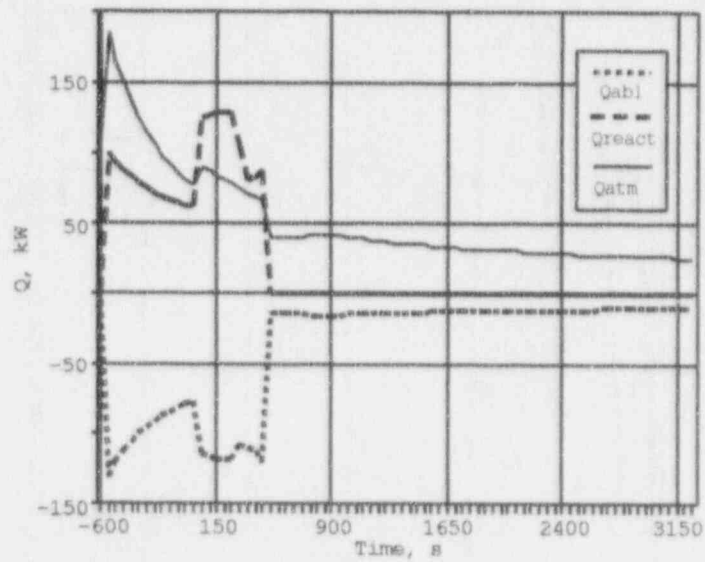


Figure 3.39: Energy rate terms for ACE L8 test

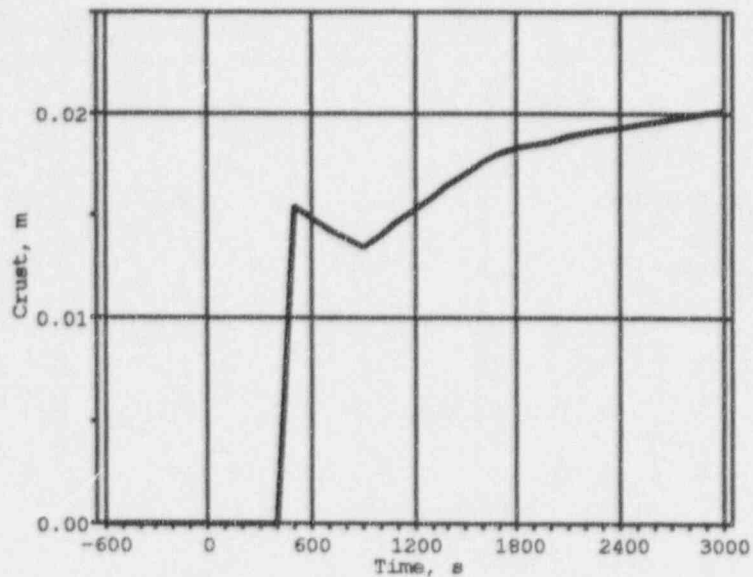


Figure 3.40: Thickness of crust at the melt-concrete interface

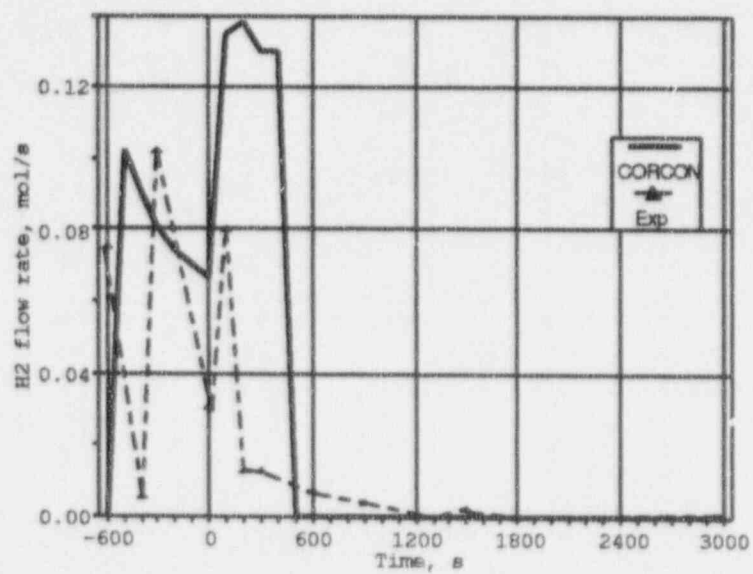


Figure 3.41: Comparison of  $H_2$  flow rate for ACE L8 test

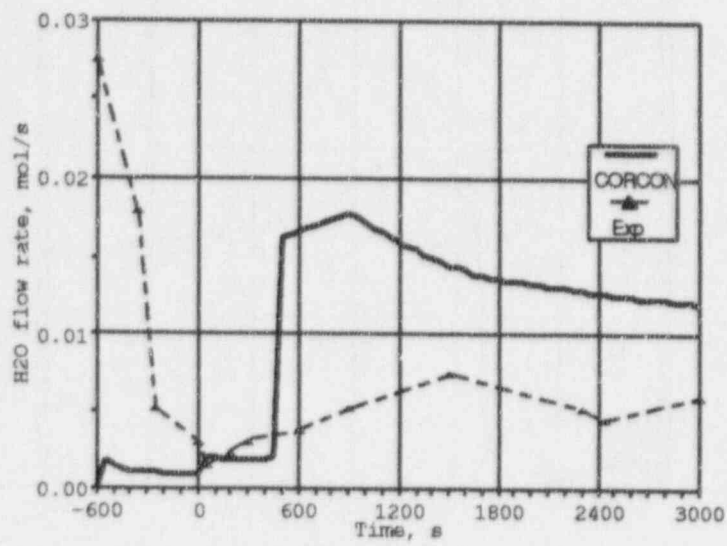


Figure 3.42: Comparison of  $H_2O$  flow rate for ACE L8 test

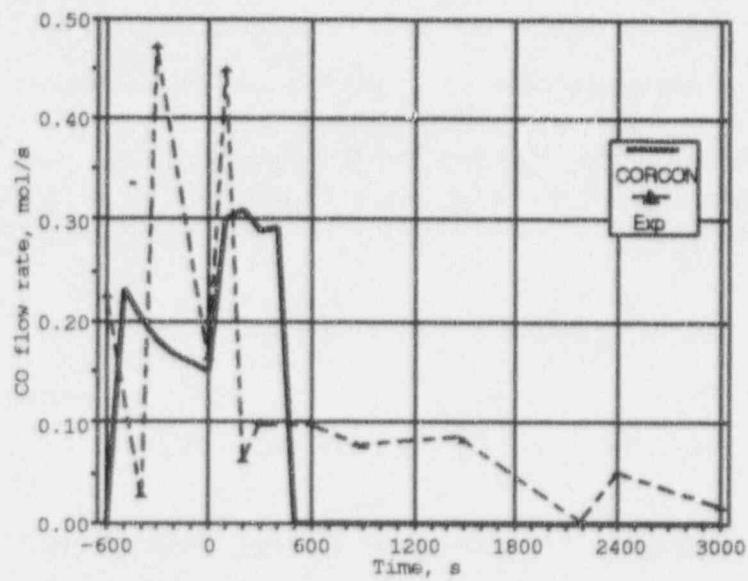


Figure 3.43: Comparison of  $CO$  flow rate for ACE L8 test



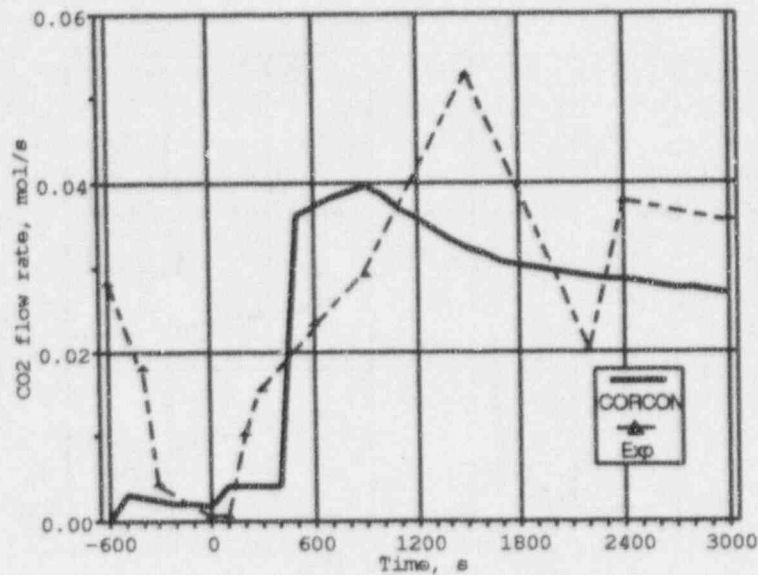


Figure 3.44: Comparison of  $CO_2$  flow rate for ACE L8 test

are due to changes in concrete properties during the preheating phase.

### 3.8 Detailed Analysis of ACE L8 Test Data

The purpose of this analysis is to perform additional thermal-hydraulic assesment of the test data in order to determine adequacy of the CORCON models, and to quantify uncertainties due to differences in the CORCON-Mod3 approach and the experimental approach. These differences were discussed qualitatively in section 2.5.1. ACE L8 test [47] for the present analysis for the following reasons:

- This test was one of the most successful in the series;
- It was very well instrumented;
- Blind numerical calculations using different codes were performed.

Test description and main results were already discussed above. According to the approach, test scenario may be divided into three main parts:

- Heating up and melting of the initial charge;
- Decomposition of concrete metal insert and gradual entrance of zirconium metal;

- Basemat ablation.

In the ACE L8 test, corium heating had begun 3.9 hours before the start of MCCI. After concrete/metal insert melted for 244.6 minutes (counting from the beginning of the experiment), a temperature of 1673 K was measured on the top surface of concrete. That moment was considered to be the initial point of molten core concrete interaction. Temperature chosen for determination of the ablation front was higher than the solidus temperature of concrete (1495 K), but time difference between these two temperatures is negligible [47]. Note that the liquidus temperature of limestone concrete is equal to 2500 K.

Duration of the MCCI was about 100 minutes. The temperature of the melt was maintained in the 2200–2500 K range and the erosion front reached 12.7 cm in 90–100 min. While the experiment was in progress, more than 90 different data channels were registered. More than 50 of these data channels were for the thermocouples. Most of them were located in the concrete basemat and were logically divided into four quadrants: north-east (NE), north-west (NW), south-east (SE) and south-west (SW). Five thermocouple arrays were located at different depths at the center of the basemat and at the centers of each quadrant. These data are the main source of information concerning the temperature front movement. Besides, there were thermocouples near the boundaries of the basemat. They provided additional information about the heating process in the boundary regions of concrete. Later in the analysis, coordinates of the thermocouples will be marked as  $(x, y)$  where numbers in parentheses identify the  $x$  and  $y$  coordinates of the thermocouple location. In Figure 3.45, horizontal section of concrete basemat with thermocouple array locations is shown. In the south and in the north sides of the cross-section, the locations of electrode assemblies are shown. To restore peripheral temperature profiles, some hypotheses were used during the analysis of the thermocouple data.

### 3.8.1 Method of Data Analysis

The main purpose of the analysis presented in this section is to reproduce temperature fronts movement, determine heat balance, and analyze the correspondence of gas release to erosion data. As discussed before, gas release from concrete is a complicated process which depends on a number of factors. The CORCON approach to calculate gas release is based on the steady state temperature profile assumption. It means to estimate gas release, erosion rate is calculated (at the decomposition temperature) and the total mass of concrete ablated is multiplied by the gas content in the concrete. During steady state phase of interaction, this approach is correct but transient concrete response may influence the interpretation of the test data for two reasons. The first is that CORCON deals with axisymmetric and hence, a two dimensional, cavity while experimental approach is inherently three dimensional. The second is that long preheating phase results in some changes of thermodynamic properties of concrete particularly, those very sensitive parameters like released water (especially free water) from concrete. For example, in ACE L8 test, about 50 % of detected  $H_2$  and  $H_2O$  was released prior to concrete/metal insert ablation.

While investigating concrete behavior under high temperature conditions, it was found that free water evaporates easily at temperature about 400 K (see, for instance, reference [51]). Bound water is retained in concrete up to 700 K.  $CO_2$  release is initiated within the range of 1000–1100 K when

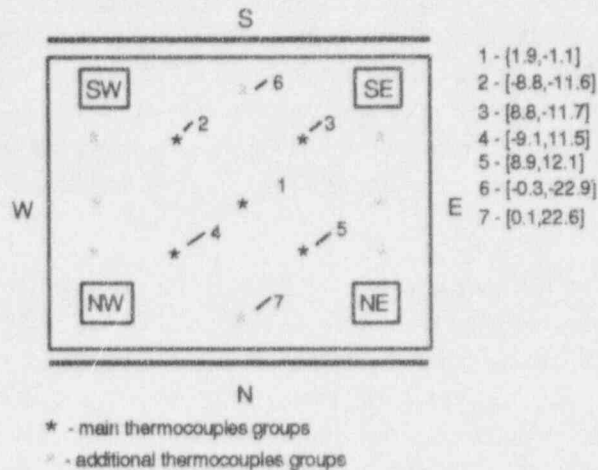


Figure 3.45: Thermocouples location in the ACE L8 basemat

carbonates start to decompose. These temperatures define three important temperature fronts. The fourth front is a concrete decomposition temperature (chosen as 1673 K in the experiment).

Using the real thermocouple data presented in the test data report [47], volume of concrete inside each corresponding isotherm was calculated. Simple hypothesis that the total gas release is proportional to the corresponding volume was used in calculations. Concrete volume inside the ablation front was treated as fully melted and decomposed. Interpretation of the thermocouple data in this way allows to check for the correspondence of concrete degassing to temperature measurements in the concrete basemat.

While reproducing temperature fronts, two remarks should be taken into account. Thermocouple data provides information about spatial distribution of temperature fields and their behavior in the test. The characteristic distance between any pair of thermocouples is about 10 cm (in horizontal cross-section). To restore spatial temperature fields in the whole volume (see Figure 3.45), it is necessary to use some hypothesis concerning these distributions. Another reason is that there were no thermocouples near the boundaries in the east and in the west sides of the assembly. In this case, facility symmetry argument was used relative to mid planes in the EW and in the NS directions.

Figure 3.45 indicates that electrodes had thermal contact with concrete in the south and in the north boundary regions. It resulted in some preliminary heating up of the adjacent regions and, as a result, earlier gas release. Taking into consideration the lack of information about temperatures in this region, one may expect significant uncertainty in the definition of the temperature front shape. For example, measurements made by two thermocouples in the south and in the north sides at (-0.3, -22.9) and (0.1, 22.6) locations exceeded 400 K temperature limit at 20 and 110 minutes before

the start of MCCI, while other thermocouples detected this temperature 3-4 minutes before MCCI. Besides, the thermocouple at (-0.3, -22.9) indicated a peak of 700 K in 7 minutes before MCCI. Preliminary heating up through the north and the south electrodes may serve as an explanation of these facts. Unfortunately, there were no systematic measurements in the peripheral regions; thus, to get dynamic information, it was necessary to use the nearest thermocouples data. For example, to get dynamic information from the thermocouples located at (-15.7, 2.3) in the NW quadrant and (-16.3, -1.7) in the NE quadrant, they were combined in one group. In other cases, axial or relative NS and EW plane symmetry hypothesis was used to get additional information. Finally, two hypotheses were analyzed:

- Symmetry hypothesis relatively to NS and EW midplanes. Data of thermocouples located in (-0.3, -22.9) and (0.1, 22.6) were taken into account.
- Hypothesis concerning axial symmetry of temperature fronts. This assumption was analyzed to find uncertainties between 3D data and 2D approach in modeling. Note that thermocouple data located at (-0.3, -22.9) and (0.1, 22.6) were not taken into account.

Data obtained from analysis were used to compare calculated gas release and to estimate other parameters (e.g., energy balance, temperature behavior) with the help of simplified MCCI dynamic model.

To summarize the approach described above, the following was taken to analyze the consistency of thermocouple data and gas release data:

- Use of thermocouple data to allow restoration of different temperature fronts in concrete (in our analysis they were 400 K, 700 K, 1000 K and 1673 K);
- Calculations of concrete volumes characterized by temperatures lower than indicated above to allow determination of expected gas release, and comparison of outcoming gases with test data to estimate degassing temperatures;
- Tracking of the melt volume to allow estimation of heat to concrete.

Because of considerable differences in the positions of 400 K and 700 K fronts, total amount of evaporated water was calculated by the formula:

$$R_{H_2O} = \rho(\alpha_{free}V_{400} + \alpha_{bound}V_{700}), \quad (3.4)$$

where  $\alpha_{free}$  and  $\alpha_{bound}$  are free and bound water contents in concrete. The same formula was used for  $CO_2$  release.  $CO_2$  part in concrete basemat (33.33%) was assumed to release at 1000 K.

### 3.8.2 Results of ACE L8 Data Analysis

#### 3.8.2.1 Concrete decomposition and gas release analysis

The starting point for the analysis of gas release and concrete decomposition was the beginning of basemat ablation. Data from thermocouples in the basemat were analyzed to restore initial

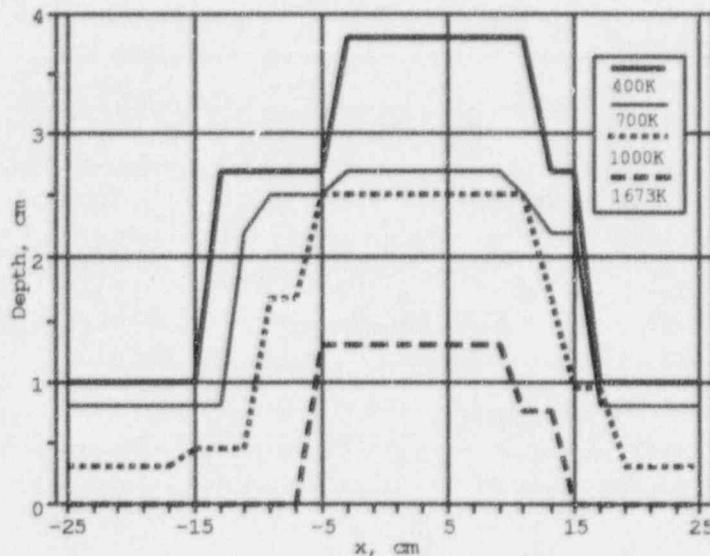


Figure 3.46: Temperature fronts at 0 min (vertical WE section) in ACE L8

temperature fronts in the concrete. Figures 3.46 and 3.47 present the isotherms 400, 700, 1000 and 1673 K in SN and WE midplane sections at the moment when MCCI began (0 minute). From both figures, one can conclude that at the start of basemat ablation, some erosion had already existed. The second conclusion is that along the NS direction, different temperature fronts have different shapes. The 400 K temperature front with different shapes in the SN and the WE vertical sections were obtained from additional thermocouples located at (0.1, 22.6, -5.8) and (-0.3, -22.9, -8.9). Both thermocouples indicated temperatures above 700 K. In the SN section, 400 K isotherm had a concave form and in the WE section, it was convex.

Figures 3.48 and 3.49 illustrate the behavior of 400 K front in time and in different cross sections of the concrete basemat. At the beginning of basemat ablation, NS concrete cross section indicates a deep penetration of the evaporation front into concrete due to the thermal contact with tungsten electrodes. In the WE cross section, evaporation was observed only in the central part. Probable reason is that near the WE boundaries concrete was cooled by water passing through cooling plates. All fronts change their shape with time and only in the range between 50 and 70 min of interaction, one finds relatively the flat evaporation front. The sensitivity of the results to the assumed thermocouple data interpretation is illustrated in Figure 3.49. Region near tungsten electrodes (about 5-7 cm) cannot be restored due to the lack of detailed temperature data in this region. Only two thermocouples located at elevations -5.8 cm and -8.9 cm provide temperature data near electrodes.

A more probable explanation of the behavior of evaporation front is heating of concrete close to the electrodes during three phases of experimental approach as evidenced from the results of gas release shown in Figure 3.50. It was assumed that free water in concrete basemat (2.36%) was released at 400 K, but bound water (3.74%) was released at 700 K. Total release of water was



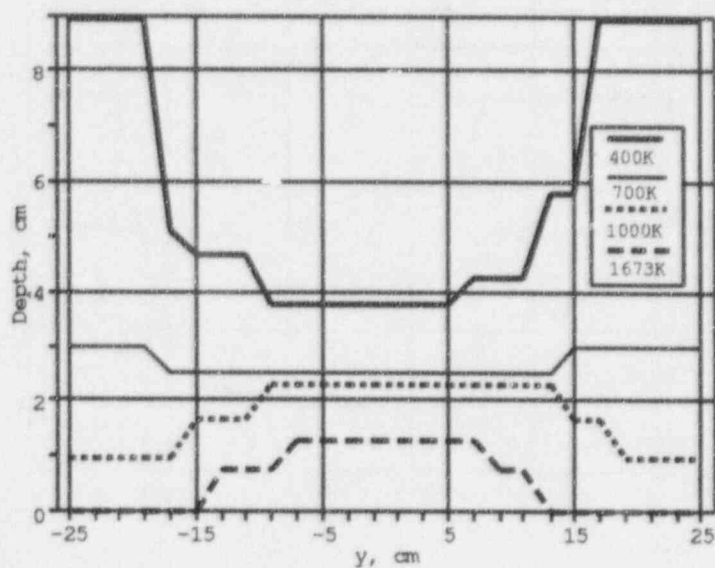


Figure 3.47: Temperature fronts at 0 min (vertical NS section) in ACE L8

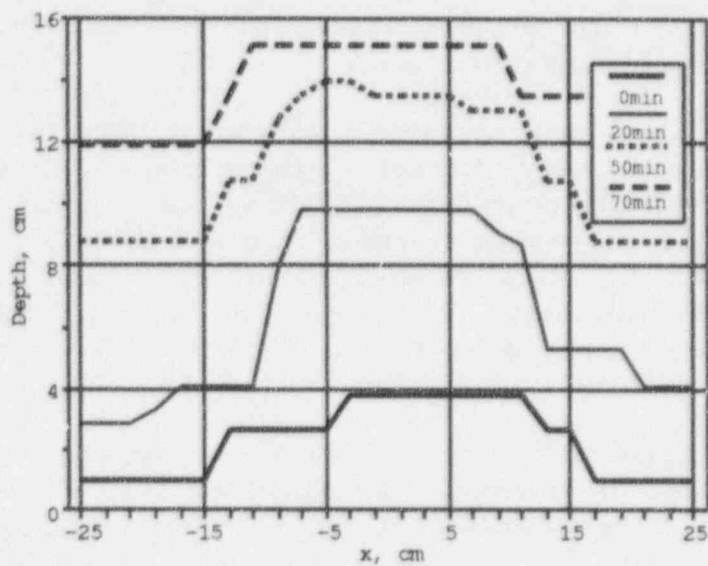


Figure 3.48: Time dependence of 400 K front (vertical WE section)



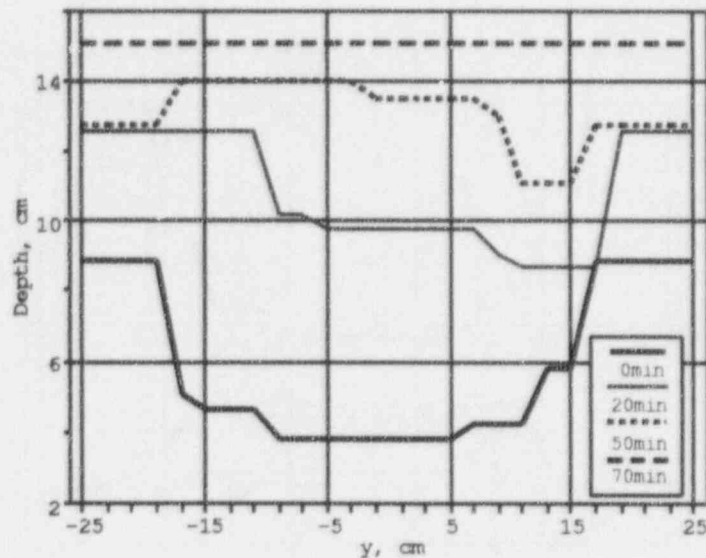


Figure 3.49: Time dependence of 400 K front (vertical NS section)

estimated by equation (3.4). Comparison with test data presented in the figure indicates very good correlation for experimental  $CO_2$  release. Water release is underestimated at the start of concrete ablation and overestimated after 60 minutes of ablation. It should be mentioned that only about 75 % of water inventory was detected in the test. At the same time, simple estimate indicates that total inventory of water from unresolved peripheral regions (in both directions) may cover the difference between calculated and measured values.

To check the suitability of the 2D approach in analyzing the 3D experimental data, the axial symmetry hypothesis was assumed. In this case, the erosion results were made symmetrical with respect to the axis located at the center of the facility. Thus, data from peripheral thermocouples 6 and 7 indicated in Figure 3.45 were not considered. Figure 3.51 shows  $CO_2$  release which may be expected using a symmetry hypothesis. Three temperatures of  $CO_2$  release: 700, 1000 and 1673 K were assumed. It was also assumed that all inventories of  $H_2O$  and  $CO_2$  in corresponding volumes are released at the indicated temperatures. Total water and carbon dioxide content was 6.1% and 33.33%, respectively.

Total amount of  $CO_2$ , estimated from the calculation is in good agreement with the test data. In Figure 3.51,  $CO_2$  release curve corresponding to the isotherm of 1000 K is very close to the experimental curve that corresponds to the fact that carbonates decomposition temperature is in the 1000–1100 K range. At the same time, relative error in the  $CO_2$  release is very close to the test data even for decomposition temperature.

This analysis shows that code predictions for total  $CO_2$  should be in good agreement with the test data even when the carbonate decomposition temperature coincides with the concrete ablation temperature. With respect to water release from concrete, 2D models cannot provide

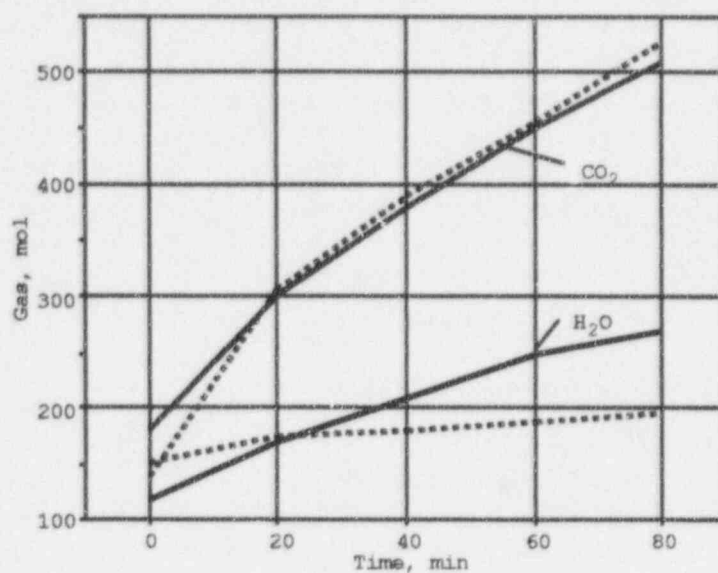


Figure 3.50: Comparison of the calculated and measured gas release in ACE L8

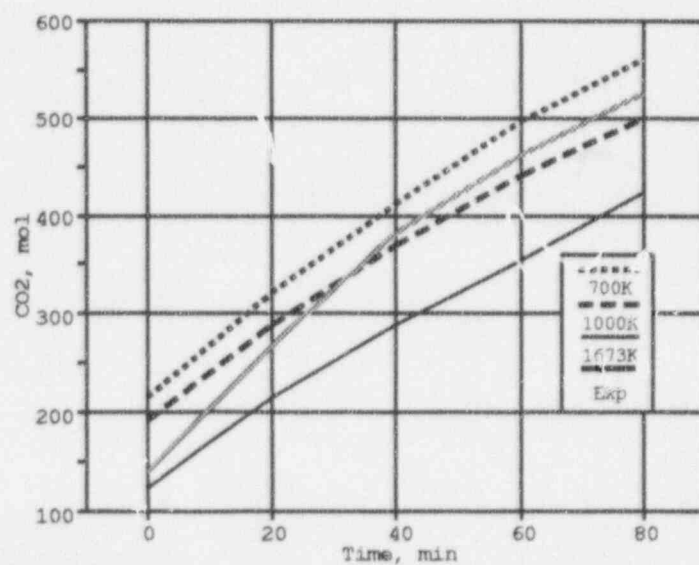


Figure 3.51: Total CO<sub>2</sub> release (symmetrical approach)

correct estimates of time dependence of hydrogen and water release rates and only integral values may be compared. To provide agreement between code predictions and real  $H_2O$  release rate data, it is necessary to adjust the water content in concrete taking into account 3D penetration of evaporation fronts because real thermodynamic properties of concrete during ablation phase differs from those of initial concrete. Corrections in concrete properties will cause also corrections in the energy balance due to the influence of gas inventory in concrete on the melt chemistry. Another result is reduction of the concrete decomposition enthalpy. Evaluation of the uncertainty due to early water evaporation gives the value of 10–15 % (ratio between enthalpy of water evaporation and concrete decomposition enthalpy).

### 3.8.2.2 ACE L8 Heat Balance Calculation

In modeling the ACE L8 test by CORCON, one should define the cylindrical cavity with flat bottom at the beginning of MCCI. Because the flat bottom in calculations remains flat in time, to interpret erosion and gas release data one needs to change concrete properties with respect to gas content in concrete. From the previous ACE L8 analysis, it was found that in this experiment the bottom melt surface was not flat at the initiation of MCCI. As can be seen from Figures 3.47 and 3.46, the interaction surface is slightly curved in both sections. At the same time, the distortion of 400 K isotherm is very large. For higher temperature fronts, distortion is not so important.

Figure 3.52 shows results of reduction in volume inside corresponding isotherms relative to a flat bottom border. Comparison with test data indicates that at the beginning of MCCI, more than 4 cm of concrete basemat does not contain free water. At the same time, this leads to the reduction of ablation volume in accordance with the average decomposition temperature front. In Figure 3.52, thermocouple data located at the center of horizontal basemat section and at the centers of NE, ES, SW and WN quadrants were taken into account. Due to the curved shape of isotherm surfaces, erosion depth is lower than that measured in the test. Estimates of different front locations are within experimental data obtained from thermocouple data.

Upon identifying all important fronts of concrete decomposition, simplified MCCI dynamic model was used to analyze heat balance in the system. The approach is as follows:

- Calculated fronts are used to determine heat losses to concrete due to gas release and concrete ablation;
- Test data for side and upward heat losses are used to specify melt boundary conditions;
- Chemical reactions of metal components  $Zr, Cr, Fe$  with gases and  $Si$  coming from concrete are employed in the model;
- Above items allow determination of melt temperature as a function of time. Experimental melt temperature behavior is used in the analysis as a criterion for the correctness of calculations.

As input data, experimental data for net electric power and upward (lid and off-gas) heat losses [47] were used. The results of these calculations are summarized in Table 3.22.

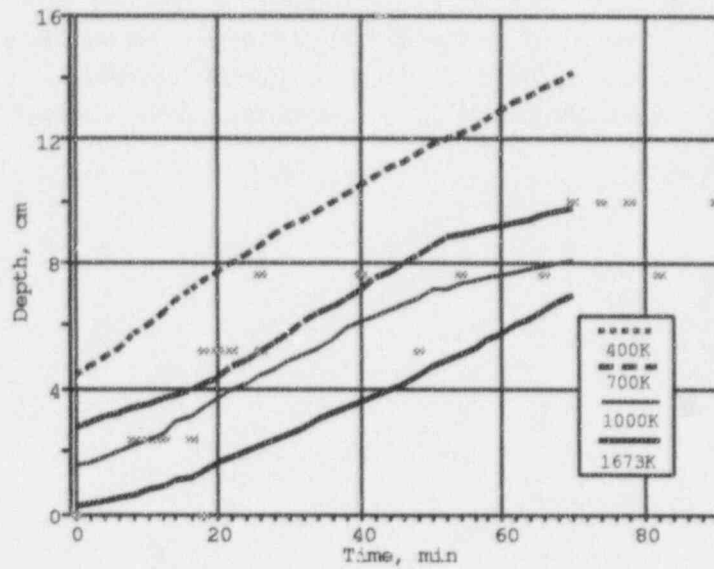


Figure 3.52: Comparison of thermocouple data of 1673 K front with with 400 K, 700 K, and 1000 K fronts

Table 3.22: Cumulative heat flows in melt for different times

Total Energy, MJ	0 min	20 min.	50 min.	70 min.
Net + Chemical Energy	49.1	168.6	248.2	288.1
Net Energy Input	11.5	109.3	201.3	247.3
Chemical Heat	58.4	85.0	80.5	78.3
Decomposition Products Heating	19.8	25.1	34.0	39.3
Upward Energy Losses	50.8	72.5	109.6	134.4
Heat to Concrete	44.6	103.0	182.7	225.1

Considering the assessment of calculated data and their correspondence to the test data, one may conclude that CORCON-Mod3 predictions for ACE L8 test are in good qualitative and quantitative agreement with test data. Differences with the test data concerning  $H_2$  and  $H_2O$  releases are connected with the heating of concrete and changes in the water inventory. Estimates of possible uncertainties in the energy terms predictions are about 15 %. Special estimates should be made with respect to oxidation of metals during preheating phase because test data indicates that large amount of water is released in the form of hydrogen. Recalculations of evaporation front in the basemat permits quantitative estimates of water content in the concrete in modeling.

## 4 MODELING OF SURC TESTS

The SURC test series, conducted at the Sandia National Laboratories, was intended to provide a data base for MCCI with different concretes and melt compositions. Three tests (SURC-4, SURC-3, and SURC-3A) employed the stainless steel melt with zirconium addition to investigate the influence of zirconium oxidation on the interaction process. In the SURC-3A test, two dimensional effects were investigated. Two tests (SURC-1 and SURC-2) were conducted with oxidic melts and zirconium metal. Two types of concrete were examined in these tests namely, limestone and basalt concretes. Initial melt compositions for these tests are presented in Table 4.1.

Summary of thermal hydraulic results for all SURC tests is presented in Table 4.2. SURC-1 and SURC-2 tests were conducted at very high temperature of oxidic melts (about 2600 K). Net power in the tests varied in the range of 300-400 W/kg (without accounting for side losses through magnesium sidewall). In tests SURC-3 and SURC-3A, input power was sustained at the level of 700 W/kg. Ablation depth in the tests was 30 cm or above. Typical duration of the experiments was 1-2.5 hours.

Input data for modeling of SURC tests with the CORCON-Mod3 code are presented in Table 4.3. In modeling of SURC tests, sidewall losses were estimated, and input power to melt was reduced to account for side losses.

Table 4.1: Melt components of the SURC tests

Species	Content of corium, kg				
	SURC-1	SURC-2	SURC-3	SURC-3A	SURC-4
UO <sub>2</sub>	138.4	138.6	-	-	-
ZrO <sub>2</sub>	46.0	45.2	-	-	-
Zr	18.7	18.7	5+5	5	20
SS - 304	-	-	45	50	200
Total mass	200.8	200.5	50	55	220



Table 4.2: Summary of SURC experiments thermal hydraulic results

Experiment	SURC-1	SURC-2	SURC-3	SURC-3A	SURC-4
Concrete type	L/L	B	L/L	L/L	B
Net power, kW	65-85	60-85	35	32	62
Peak melt temperature, K	2600	2600	2050	2120	1920
Ablation Depth, cm	27	35	35	27	25
Interaction Time, min	130	150	150	80	60

Table 4.3: Summary of input data for CORCON-Mod3

Experiment	SURC-1	SURC-2	SURC-3	SURC-4	SURC-3A
Initial Layer Configuration	0	0	0	0	0
Interlayer Mixing	No	No	No	No	No
Concrete Type <sup>1</sup>	L	B	L/S	B	L/S
SiO <sub>2</sub> ,%	3	55		55	
CaO,%	45	8		8	
CO <sub>2</sub> ,%	35	2		2	
H <sub>2</sub> O,%	6	4		4	
Concrete Ablation Temperature, K	1650	1553	1500	1353	1650
Initial Concrete Temperature, K	300	300	300	300	300
Concrete Solidus Temperature, K	1690	1350	1690	1353	1690
Concrete Liquidus Temperature, K	1875	1650	1875	1650	1875
Concrete Emissivity	0.6	0.6	0.6	0.6	0.6
Time Step, s	30.	30.	30.	30.	
Number of Rays	47	47	47	47	47
Melt Temperature, K	2600	2600	2100	1817	2150
Metal Layer Emissivity	0.8	0.8	0.8	0.8	0.8
Oxide Layer Emissivity	0.8	0.8	0.8	0.8	0.8
Surroundings Emissivity	0.6	0.6	0.6	0.6	0.6
Chemistry Flag (ICHEM)	01	01	01	01	01
Heat Flow Index (IFILM)	10	10	10	10	10
Surroundings Temperature, K	1400	1400	1400	1400	1600
Power, kW	74	60-80	11-8.6	45	110
Radius, m	0.2	0.2	0.1	0.2	0.1

<sup>1</sup> For all SURC tests build-in standard concrete types used for calculations

## 4.1 Modeling of the SURC-1 Test

SURC-1 and SURC-2 experiments were conducted to measure and assess core debris-concrete interactions. Both tests were made using an oxide debris of  $UO_2 - ZrO_2$  with identical power input of 200 to 300 W/kg corresponding to initial 2 to 10 hours of interaction. SURC-1 test utilized the limestone concrete basemat while SURC-2 test dealt with basaltic type of concrete.

### 4.1.1 Test Apparatus

The interaction crucible for SURC tests was designed from  $MgO$  ceramic to prevent radial erosion. The overall dimensions of the crucible were 60.0 cm diameter and 100.0 cm high. Limestone concrete cylinder with a diameter of 40.0 cm and 40.0 cm thickness was located at the bottom of the interaction crucible. The crucible together with the interaction coil were placed into the water-cooled aluminum containment vessel. Three thermocouple arrays located in the concrete cylinder allowed measurement of the temperature response and erosion front in the concrete. The first array was located on the axial centerline, the second one was located on a line parallel to the axis at a radius of 10.0 cm, and the third array was installed near the interface boundary with ceramic walls at a radial distance of 18.0 cm. Thirteen other thermocouple arrays were used to monitor sidewall and cover temperatures and allowed an estimation of heat losses through ceramic walls.

Five tungsten ring susceptors were utilized to provide sustained heating of oxide charge. All of the rings were 35.6 cm in diameter and had a central hole diameter of 7.6 cm. Net power to the tungsten susceptors was estimated to be 50% of the gross power input.

Total mass of the charge was 200 kg for both tests. The masses of individual species are presented in Table 4.1. Initial charge consisted of  $UO_2 - ZrO_2$  mixture in the form of powder. To account for the influence of zirconium, about 16 kg of  $Zr$  chips were added in order to provide heterogeneous mixture.

### 4.1.2 SURC-1 Test Results

According to the test scenario [49], interaction with concrete slug began at about 135.0 min when the surface thermocouple failed at the mid radius array. The test proceeded in four distinct stages as follows:

1. Preheating and melting phase;
2. Early phase characterized by vigorous oxidation of zirconium metal;
3. Intermediate phase after oxidation processes were completed;
4. Late phase of interaction with increased power input to the melt.

Summary of thermal hydraulic results of SURC-1 test is presented in Table 4.4. Taking into account erosion data presented in reference [49], the early phase of interaction resulted in the

Table 4.4: SURC-1 test summary data

Parameter	Preheating Phase	Early Phase (Zr oxidation)	Mid Phase	Late Phase (Increased Power)
Time, min	60-135	135-190	190-220	220-280
Temperature, K	1300-2600	2650-2400	2400-2150	2250-1750
Gas Flow Rate, slpm	29	150	40	80
mol/s	0.02	0.11	0.03	0.06
Gas Composition vol. %				
$H_2$	50	5	10	10
$H_2O$	20	5	-	-
$CO$	20	84	80	80
$CO_2$	10	6	10	10
Erosion Rate, cm/h	-	14.2	2.5	12.5

formation of steady-state radial temperature profile in the concrete slug. Initial 10 - 12 minutes of erosion resulted in intensive melt penetration near the mid radius (about 10 cm). Next 10-12 minutes resulted mainly in the erosion along centerline of facility and after 40 minutes of interaction, the steady-state temperature profile was established. Average erosion rate was very high (about 14 cm/hr) in the initial phase of interaction. During midphase of interaction, erosion rate dropped considerably. After increase of net input power to 90 kW, erosion rate became higher (12.5 cm/hr) again, and was comparable to that during the early phase.

According to the composition of limestone concrete, there are about 4 % of  $H_2O$  and 35.7% of  $CO_2$ . These weight percent correspond to about 22 mol % of  $H_2O$  and 78 mol % of  $CO_2$  in the gas mixture that are expected to be released from the concrete. Thus, the ordinary ratio of flow rates ( $CO + CO_2/H_2 + H_2O$ ) is about 3.5. During preheating phase, about 78 mol of gases were released from concrete basemat with about 70% or 50 mol of  $H_2 + H_2O$ . Thus, the ratio of ( $CO + CO_2/H_2 + H_2O$ ) is about 0.4. At the beginning of ablation phase, the wet-dry front located at about 5-6 cm depth. This concrete layer contains about 40 mol of  $H_2O$  (both bound and free). About half of reported water content is bound water. Total mass of concrete with the thickness of 6 cm was practically dehydrated. Thus, during the basemat ablation phase, the ratio is about 9. Early phase of ablation provided flow rate of 150 slpm or about 0.11 mol/s. Then flow rates dropped to 0.03 - 0.06 mol/s.

#### 4.1.3 CORCON Input Parameters

CORCON input parameters for SURC-1 and SURC-2 tests are presented in Table 4.3. Calculations were performed using heterogeneous mixture option ( $ILYR = 3$ ) (mixture of oxide and metallic species) without interlayer mixing option as the base case. Concrete ablation temperature was

assumed to be 1650 K for SURC-1 test (limestone concrete) and 1550 K for SURC-2 test (basaltic concrete). These values are close to the concrete solidus temperatures. Initial melt temperature was 2600 K. For limestone concrete, condensed phase reactions do not play a significant role due to small amount of  $\text{SiO}_2$  in the concrete. For basaltic concrete, this option was used due to the presence of zirconium and high silica content in the basaltic concrete.

More sensitive parameters for modeling of both tests are sidewall power loss and upward power loss. Input power to the melt was determined by subtraction of sidewall heat loss from net input power. Estimates of side losses were based on the data presented in [49]. According to these data, side heat losses were estimated up to  $200 \text{ kW/m}^2$ . Assuming that the melt thickness was 20 cm during the test, one gets an estimated value of side losses in the range 50–60 kW. Buss power during the initial phase of interaction was about 150 kW and net power was estimated to be about 65 kW. At 220 min, net power was increased to 90 kW. Taking into account sidewall power loss, the estimated actual power input to the melt was at the level of 5–10 kW. After power was increased, net power to the melt became 30–40 kW. Power increase is reflected in the test result which showed that during late phase of interaction, erosion rate became 5 times higher than that during midphase. Due to the presence of heated tungsten rings above the melt, upward power loss cannot be estimated. Thus, the adiabatic boundary conditions were used. Such kind of boundary conditions may be implemented by small emissivity coefficients for surrounding.

#### 4.1.4 Comparison to SURC-1 Test Data

Initial time for modeling of SURC-1 test was chosen as 150 min that corresponded to the time when axial surface thermocouple failed. In the experiment, ablation started at 135 min with the failure of midradius surface thermocouple. In Figure 4.1, comparison of measured and calculated erosion depth results is presented. Experimental data presents thermocouple measurements of erosion front in three radii. Duration of initial phase of interaction is about 1000 s. During this time period, nearly 10 cm of concrete is predicted to be decomposed with an average ablation rate of about 33–36 cm/hr. Experimental erosion rate is about 32 cm/hr. High erosion rate is sustained due to oxidation of zirconium metal. The erosion rate during mid phase is very close to test data also. Significant increase in the erosion rate was observed after net power had been increased to 35 kW or 7 times higher than that during the midphase. During late phase of interaction (after 13000 s), erosion rate is nearly 10–12 cm/hr or very close to the test data.

Energy rate terms are presented in Figure 4.2. In spite of relatively high chemical heat release (about 50 kW), calculated temperature (see Figure 4.3) decreases rapidly from initial 2600 K to about 2300 K by the end of Zr oxidation phase. Temperature behavior during the test allows to draw a conclusion that the duration of zirconium oxidation phase was not longer than 2000 s. This period is characterized by approximately constant temperature. CORCON-Mod3 underpredicts temperature slightly during this phase. Predicted and measured temperatures differ 100–150 K during midphase of interaction and are very close during late phase.

Predicted zirconium oxidation rate is about 0.14 mol/s (see Figure 4.4). Total oxidation time is about 1500 s. Calculated gas release rate during oxidation phase is about 0.2 mol/s for CO gas and 0.06 mol/s for  $\text{H}_2$  (see Figures 4.5 and 4.6). Both values are higher than those measured in the test. This fact may be explained by the degassing of concrete during the heat up phase. According

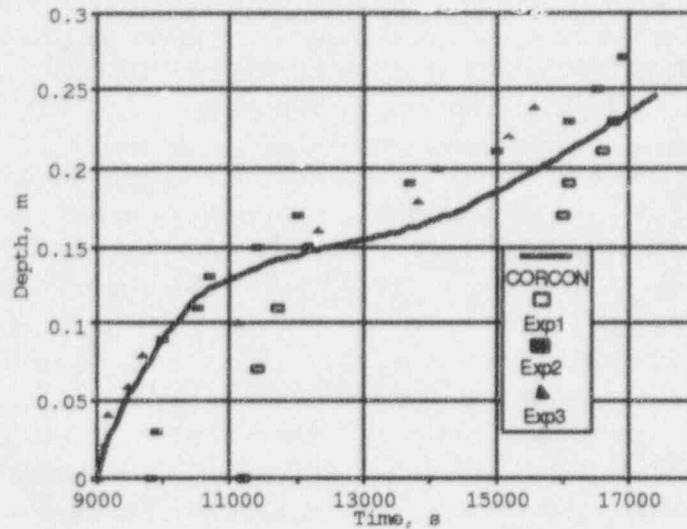


Figure 4.1: SURC-1 concrete erosion depth

to measured temperatures in the concrete slug, rate of advancement of wet-dry front was about 5.6 cm/hr. During early phase of interaction, erosion front moves rapidly and after about initial 30 minutes of interaction, both fronts become close to each other. During late phase of interaction, predicted gas releases are in good agreement except for the fact that gas species in the test are  $H_2$  and  $CO$  while after oxidation of zirconium, CORCON predicts  $H_2O$  and  $CO_2$  release. Possible explanation is the oxidation of tungsten susceptors.

General conclusion with respect to the modeling of SURC-1 test is that CORCON predictions are in good qualitative and quantitative agreement with test data.

## 4.2 Modeling of the SURC-2 Test

### 4.2.1 SURC-2 Test Results

Test apparatus for SURC-2 test was similar to that of SURC-1. SURC-2 test [50] was conducted to investigate the molten core concrete interactions of oxidic melt with the basaltic basemat. The charge became molten at temperature about 2600 K after 120 minutes of heating. Net power to the charge, which was estimated to be about 42% of the gross power, was about 65 kW at the onset of ablation. After 210 minutes, the power was increased to a level of 84 kW.

The 204 kg charge of  $UO_2-ZrO_2-Zr$  material was heated during 130 minutes prior to the onset



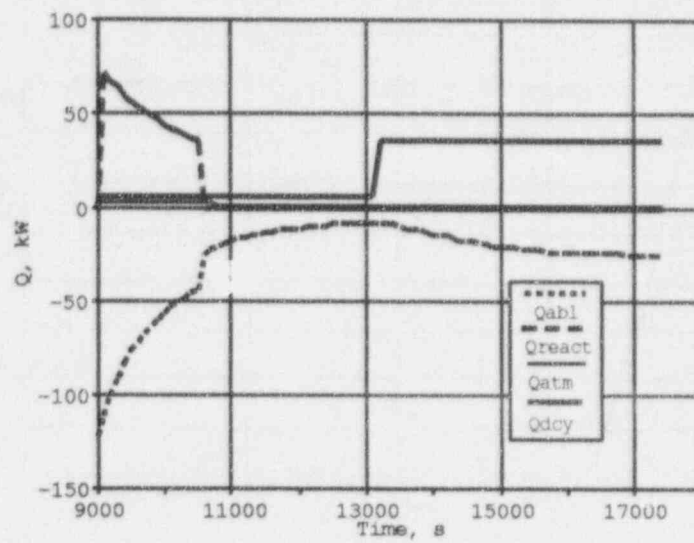


Figure 4.2: Energy rate terms for SURC-1 test

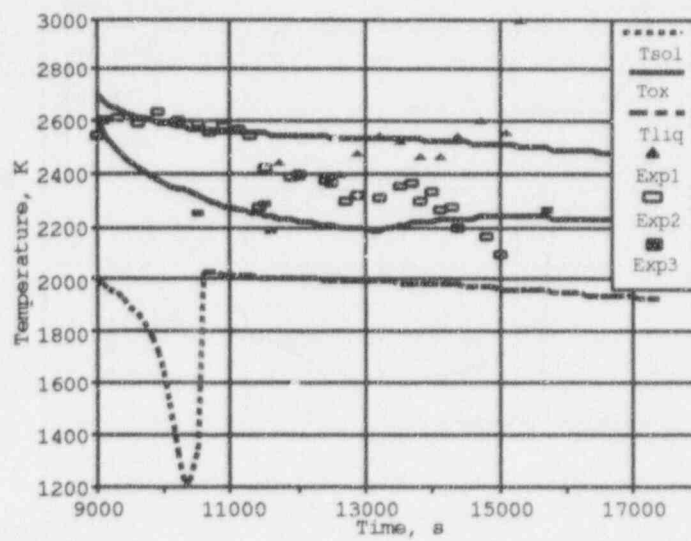


Figure 4.3: SURC-1 Temperature of oxide layer



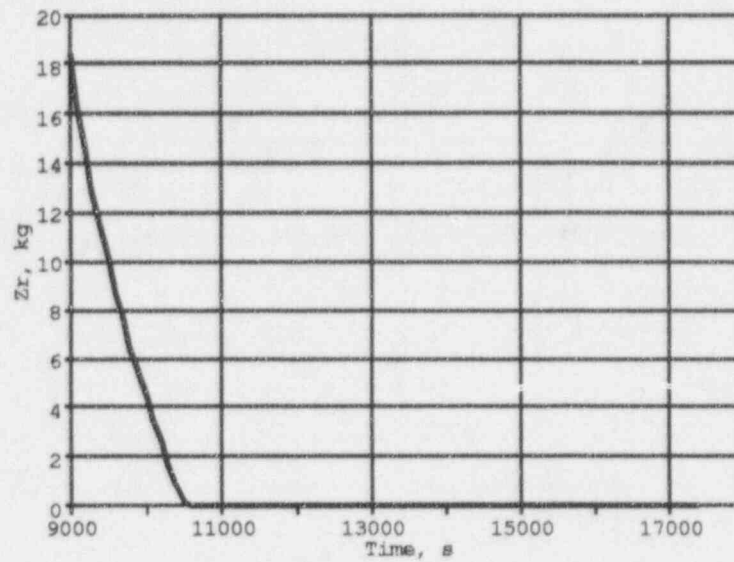


Figure 4.4: Mass of metals in the melt for SURC-1 test

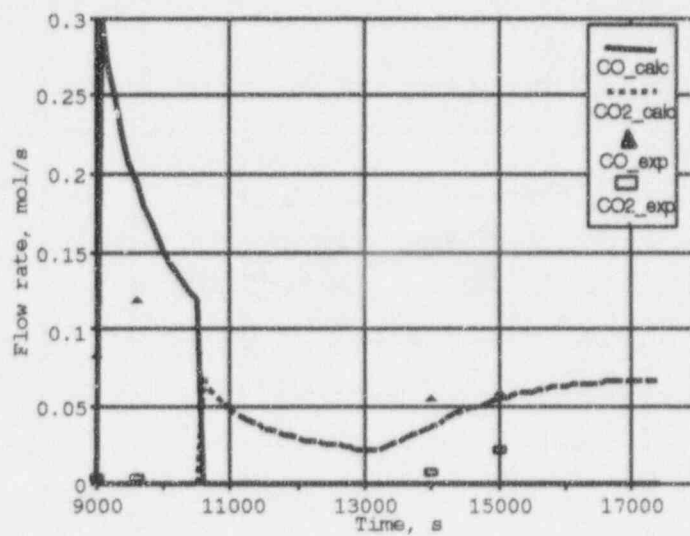


Figure 4.5: SURC-1 CO and CO<sub>2</sub> flow rates

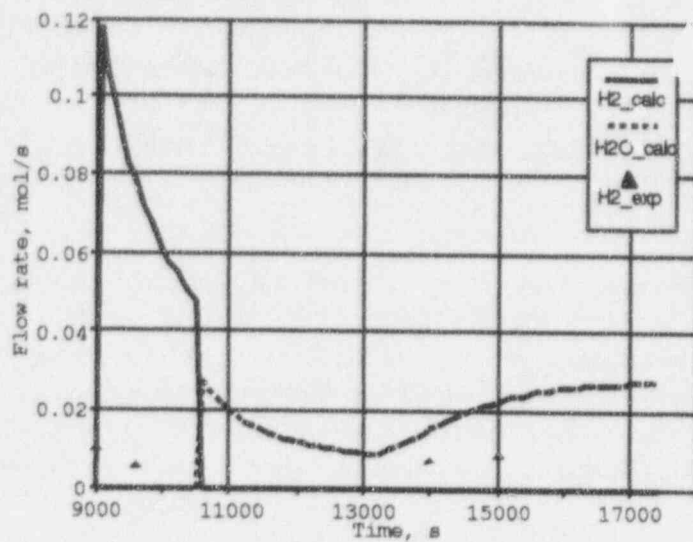


Figure 4.6: SURC-1  $H_2$  and  $H_2O$  flow rates

Table 4.5: SURC-2 test summary data

Parameter	Preheating Phase	Early Phase (Zr oxidation)	Mid Phase	Late Phase (Increased Power)
Time, min	50-130	130-160	160-220	220-280
Temperature, K	1400-2600	2600-2700	2100-2050	2050-2150
Gas Flow Rate, slpm	20-35	110	20	40
mol/s	0.015-0.03	0.08	0.015	0.03
Gas Composition vol %				
$H_2$	77	75	71	70
$H_2O$	9	6	5	5
CO	13	14	12	16
CO <sub>2</sub>	1	5	12	9
Erosion Rate, cm/h	-	30	5	15

of concrete erosion. During the preheating phase, melt pool temperature increased to 2600 K. Gas flow rate increased from 20 to 35 slpm. Offgases were enriched by hydrogen indicating reduction of water released from concrete. Basaltic concrete melts in the range of 1350–1650 K and typically liberates 1.5 wt%  $CO_2$  gas and 5 wt%  $H_2O$  vapor when heated to melting. About 2.5 wt% of total water is free water. Gas inventory in the concrete gives normal value of  $H_2 + H_2O$  to  $CO + CO_2$  ratio equals to 9. The ratio corresponding to free water is 5 or approximately, half of the previous value. Experimental values of ratio varied from 6 during the preheating phase to about 3 during mid and late phases. Location of 400 K isotherm at the start of concrete ablation was measured at the level of 6 cm.

After onset of ablation during the early phase, when zirconium oxidation played an important role, erosion rate was about 30 cm/hr. Gas flow rate increased to 110 slpm (0.08 mol/s) with high  $H_2$  and  $CO$  content in the offgases. Ratio of  $H_2$  to  $H_2O$  and  $CO/CO_2$  were 12 and 3, respectively, indicating high rate of oxidation. Only  $CO/CO_2$  ratio became lower during mid and late phases of interaction (1–1.5) indicating changes in the oxidation processes. Typical content of  $SiO_2$  in the basaltic concrete is 55 wt% that might cause accumulation of silicon in the melt and its oxidation. Melt pool temperature dropped quickly from 2540 K at the beginning of ablation to about 1950 K and was sustained at this level during mid and late phases.

#### 4.2.2 Comparison to SURC-2 Test Data

Input parameters for simulation of the SURC-2 test were chosen in the way similar to that of SURC-1. Input power to the melt was reduced to the value of 5 kW during initial phase of interaction and was increased to 50 kW during late phase of interaction. The only difference in the input deck was the choice of condensed phase reactions due to the very high silica content in the basaltic concrete.

Initial time for modeling of SURC-2 test was chosen as 135 min that corresponds to the time when axial surface thermocouple failed. In Figure 4.7, comparison of measured and calculated erosion depth is presented. Thermocouple measurements of erosion front were taken in three radii. During the initial phase of interaction (about 1000 s), nearly 7 cm of concrete is predicted to be decomposed with an average ablation rate of about 23 cm/hr. Experimental erosion rate during this phase was about 32 cm/hr. Significant increase in the erosion rate was observed after power had been increased to 50 kW or 10 times higher than that during the midphase. During late phase of interaction (after 13000 s), erosion rate is nearly 30 cm/hr or higher than the measured value.

Energy rate terms are presented in Figure 4.8. After short initial time period, which corresponds to the zirconium oxidation in the melt, CORCON predicts negative chemical power in spite of silicon presence in the melt. Predicted temperature of the melt (see Figure 4.9) is close to the test data. Predicted zirconium oxidation rate is about 0.4 mol/s (see Figure 4.10). Total oxidation time is about 500 s. Short duration of oxidation is due to the high silica content in the concrete. Calculated gas flow rate during oxidation phase is about 0.06 mol/s for  $H_2$  gas and 0.01 mol/s for  $CO$  (see Figure 4.11). Both values are close to those measured in the test, but the values are based on underprediction of the erosion rate.

In general, CORCON predictions of SURC-2 test results are in qualitative and quantitative

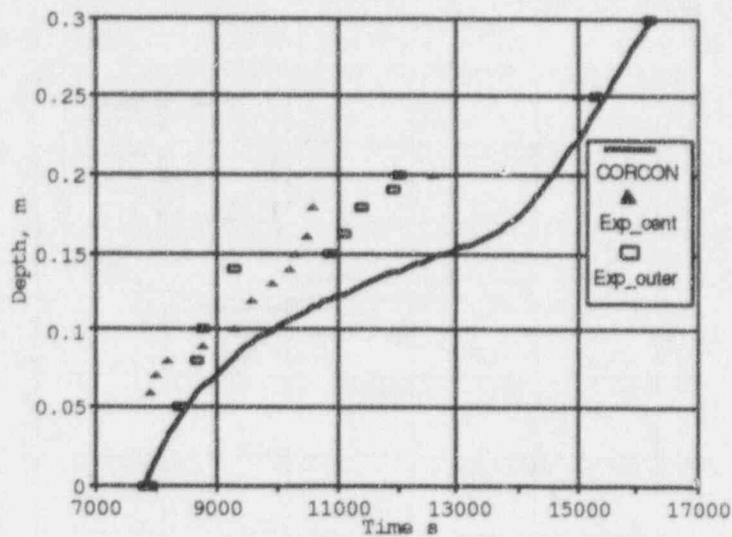


Figure 4.7: SURC-2 concrete erosion depth

agreement with test data except for the negative reaction heat. The reason for negative reaction heat is not clear. The hypotheses that some silica decomposes to silicon and oxygen (endothermic reaction) is not confirmed by the oxygen gas release.

### 4.3 Modeling of the SURC-3 Test

Two inductively heated experiments SURC-3 and SURC-3A [51] were performed to investigate the additional effects of zirconium metal chemistry on molten core concrete interactions with stainless steel as core debris simulant. Both tests utilized limestone concrete and about 45 kg of initial melt. Test SURC-3 was conducted to investigate 1D interaction while SURC-3A test was designed to investigate two dimensional effects of interaction. The metal charge used in these experiments was a solid stainless steel cylinder with 21.6 cm diameter and 17.3 cm high. The composition of 304 steel is presented in Table 4.6.

#### 4.3.1 Test Apparatus and Results

The crucible consists of an instrumented limestone concrete cylinder 21.6 cm in diameter and 40.0 cm high placed in the  $MgO$  ceramic wall of 10 cm thickness. The SURC-3 crucible was positioned in an induction coil operating at a frequency of 1000 Hz. Total power supply of 280 kW was applied to sustain the interaction of steel and zirconium with concrete. Net coil power during

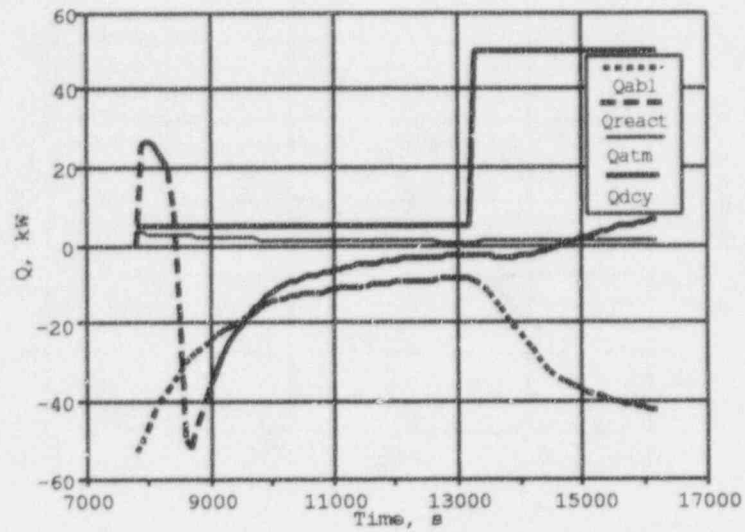


Figure 4.8: Energy rate terms for SURC-2 test

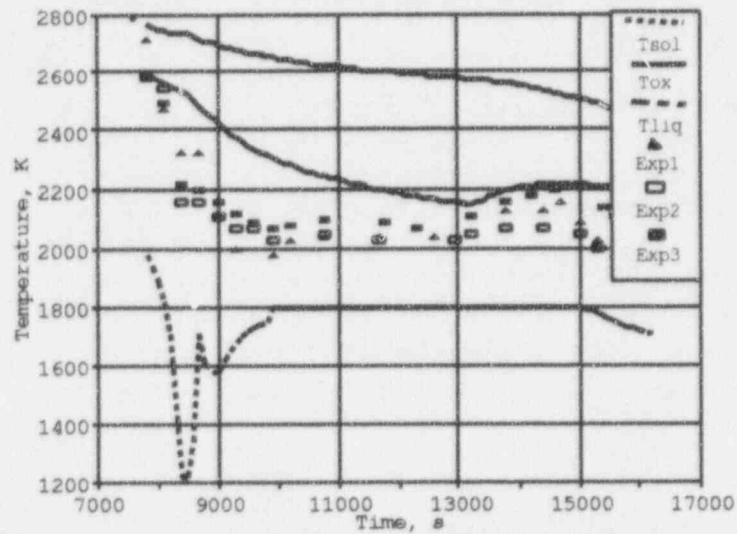


Figure 4.9: SURC-2 temperature of oxide layer

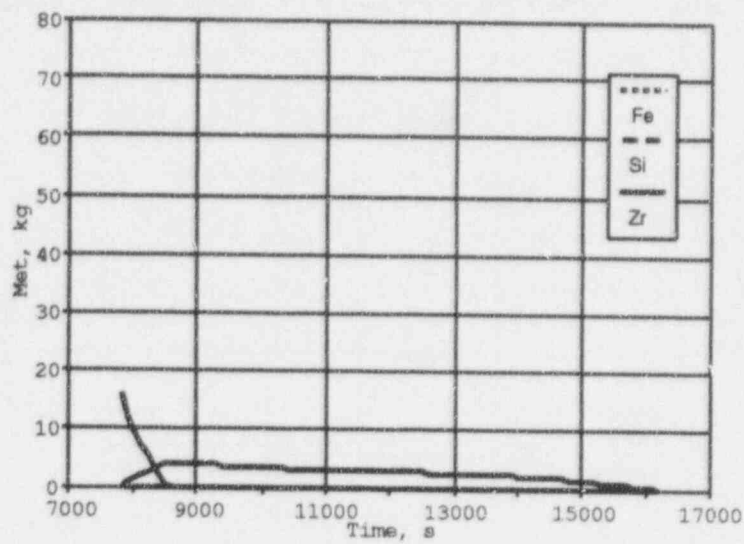


Figure 4.10: Mass of metals in the melt for SURC-1 test

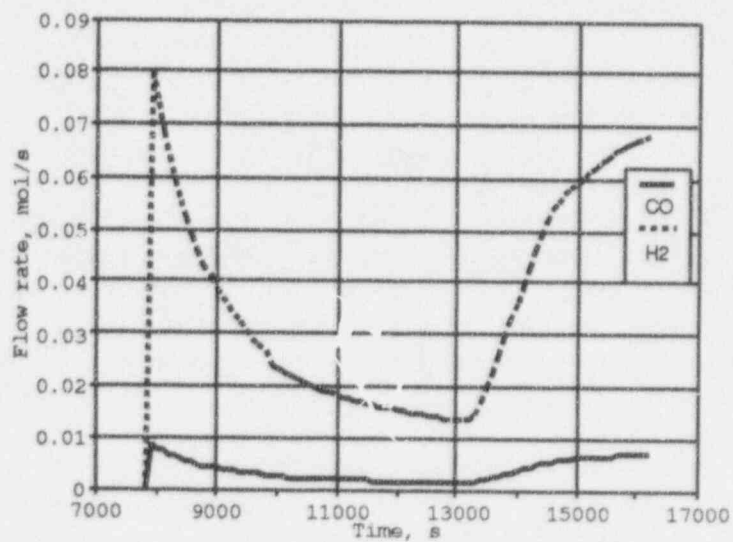


Figure 4.11: SURC-2 CO and H<sub>2</sub> flow rates



Table 4.6: Chemical composition of 304 stainless steel

Element	Weight%
<i>Fe</i>	71.18
<i>Cr</i>	18.50
<i>Ni</i>	8.25
<i>Si</i>	0.50
<i>Cu</i>	0.25
<i>Mo</i>	0.25
<i>Mn</i>	1.0
<i>C</i>	0.04
<i>P</i>	0.02
<i>S</i>	0.01
Total	100.00

the test was about 170 kW. Taking into account the efficiency of 68.7%, net power to the melt was estimated at the level of 35 kW during the test.

Erosion of concrete in the test began at around 90 min as indicated by thermocouple failure on the concrete surface. During the steady-state phase of interaction when 6 to 8 cm of concrete was eroded (133 min into the test), 5 kg of zirconium metal was incorporated into the stainless steel melt. A significant zirconium-steel-concrete interaction lasted about 15 minutes. The melt front propagation rate after the zirconium addition increased from about 14 cm/hr to 27 cm/hr. Summary of SURC-3 test data is presented in Table 4.7.

A second addition of zirconium was made at 177 min. No significant changes in erosion and aerosol production occurred after the second Zr addition. At 225 min (after 135 minutes of interaction), the power was shut down. A total erosion depth of 34 cm was indicated by the end of the test. The temperature of the melt estimated by thermocouples was measured to be between 1950 and 2050 K during the test.

Gas flow data showed four time periods of interest as indicated in Table 4.7. During preheating phase, about 10 slpm was released. After ablation of limestone concrete began, increase of flow rates between 90 and 110 minutes was detected. Peak gas release at the level of 200 slpm was observed after zirconium addition. The average value during the oxidation period was about 80 slpm. Typical ratio ( $CO + CO_2/H_2 + H_2O$ ) for limestone concrete is about 3.5 as was estimated for SURC-1 test. However, the value of this ratio measured in the SURC-3 test was nearly 15. Monitoring of  $CO/CO_2$  ratio in the test allows estimation of chemistry in the melt. During ablation (prior to and after zirconium addition), typical ratio was between 6.5 and 8.7 indicating significant reduction of carbon dioxide release from concrete. After zirconium was added, this ratio became higher than 20. During late phase of interaction, the ratio dropped to the steady state value.

Table 4.7: SURC-3 test summary data

Parameter	Preheating Phase	Phase 1	Phase 2	Zr oxidation	Late phase
Time, min	50-90	90-110	110-135	135-150	150-235
Temperature, K	800-1700	1700-1950	1950	1950-2200	1950
Gas Flow Rate, slpm	10	20	40	80	25-30
mol/s	0.007	0.015	0.03	0.06	0.02
Gas Composition vol %					
$H_2$	6	5	2.5	2	5
$CO$	79	82	87	94	84
$CO_2$	15	13	10	3	11
Erosion Rate, cm/hr	-	14	14	27	14

#### 4.3.2 Comparison to SURC-3 Data

General CORCON input parameters are presented in Table 4.3. Initial melt was defined in accordance with Table 4.6 without zirconium. Estimated net power to the melt was nearly 32 kW. Main uncertainties in the test modeling are connected with the estimates of sidewall losses through ceramic annulus. Measured heat flux in the middle of metallic charge was about 100–150 W/m<sup>2</sup>. Taking into account that metallic melt had a height of 20 cm, total heat through ceramic sidewall may be estimated as 15–20 kW. Thus, estimated net power to the melt is between 12–15 kW. 12 kW of net power was used in the input deck for SURC-3 test. Surrounding temperature was equal to 1600 K throughout the test. Both values determine thermal interactions and distribution of energy rates between heat to concrete and upward heat losses.

According to the test scenario, two zirconium additions were initiated when the test was in progress. At 43 minute into interaction (133 minutes after start of test), 5 kg (55 moles) of Zr metal was delivered to the melt. Other 55 moles were added at 88 min (177 min of test time). CORCON input option ISRABL was switched on. Mass addition rate was specified as 0.25 kg/s for 20 seconds.

Main results of calculations are presented in Figures 4.12–4.16. Comparison of erosion data (see Figure 4.12) shows that CORCON predictions are in good agreement with the test data. Ablation depth is very close to the test data. After zirconium addition, predicted ablation rate is slightly lower than experimental values. This difference may be due to an overestimated concrete decomposition enthalpy and/or due to overprediction of upward heat loss. For instance, Figure 4.13 illustrates that temperature drops below 1900 K during initial phase and increases after zirconium addition, but in the test only small temperature variations were detected (from 1950 to 2020). Heat to concrete becomes approximately two times higher than during initial the phase (see Figure 4.14). Chemical heat release after zirconium addition is four times as high as that prior to addition.

Temporal behavior of  $Zr$  and  $Si$  species in the metal layer is presented in Figure 4.15. Oxidation rate of zirconium is relatively low and lasts about 2200 s. Second zirconium addition does not cause changes in the melt chemistry and consequently, has no effect on main thermal characteristics of the interaction, for example, erosion rate. This fact may explain actual observation in the SURC-3 test when no gas production was detected after second addition. Even considering high flow rate of gases (80 slpm or 0.06 mol/s) measured in the test after zirconium addition, oxidation rate of  $Zr$  is two times lower than the gas release rate of 0.03 mol/s.

Figure 4.16 shows gas flow rates of  $CO$  and  $H_2$ . CORCON predicts very high reduction of incoming gases. Prior to zirconium addition, some water vapor and carbon dioxide existed in the predicted gases. Typical ratio of  $CO$  to  $H_2$  flow rates is about 2.6 in calculations. This difference is due to the use of CORCON default concrete composition. For limestone, default concrete content of water is 5.94 wt% instead of 4 wt% as indicated in the report [51]. Total gas flow rate predicted by CORCON is 0.023 mol/s prior to zirconium addition and 0.035 mol/s after addition. These values are in reasonable agreement with the test data (see Table 4.7). Best agreement was observed between 110 and 135 min. During Phase 1, CORCON overpredicts gas release due to smaller gas content in the concrete. At about 110 min, steady state temperature profile exists in the concrete, therefore, gas release is well predicted by the code. After zirconium addition, CORCON predicts nearly 0.05 mol/s which is very close to the average experimental flow rate (0.05 mol/s).

Thus, simulation of SURC-3 test by CORCON-Mod3 indicates good quantitative agreement with test data. Some discrepancies may be explained in terms of general uncertainties of experimental data and assumptions with respect to the values which were not exactly measured in the test.

## 4.4 Modeling of the SURC-3A Test

### 4.4.1 Test Apparatus and Results

The SURC-3A experiment was similar to the SURC-3 test in design and basic dimensions [51]. This test was intended to examine additional aspects of zirconium behavior in the stainless steel melt. The main purpose of the test was investigation of relative rates of axial and radial erosion when zirconium was added to the meltpool. The test utilized about 50 kg of stainless steel as the melt material. The crucible was made entirely from limestone concrete. The limestone concrete slug was 21.6 cm diameter and 40.0 cm high. Limestone concrete annulus was 50.8 cm outer diameter so the thickness of side walls was 14.6 cm.

Power to the induction coil was applied at a level of 170 kW. Net efficiency was estimated to be about 19 %, so the net power sustained during the test was about 31 kW. After 35 minutes of constant heating, the steel charge became molten and concrete ablation started at 40 minutes. Steady state erosion of concrete lasted for about 35 minutes. During this time, about 4 cm of axial and 2 cm of radial erosions were indicated. 5 kg of zirconium metal was added to the meltpool at this time (75 minutes). A substantial increase in gas flow and aerosol production was observed after zirconium addition. The test was terminated at 148 min (after about 110 minutes of ablation). The axial erosion depth during the test was about 25 cm, and 3-5 cm of concrete was ablated in the

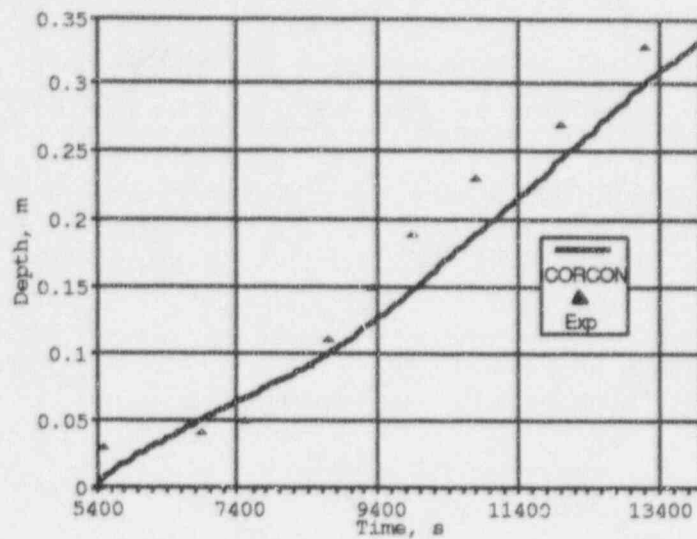


Figure 4.12: SURC-3 concrete erosion depth

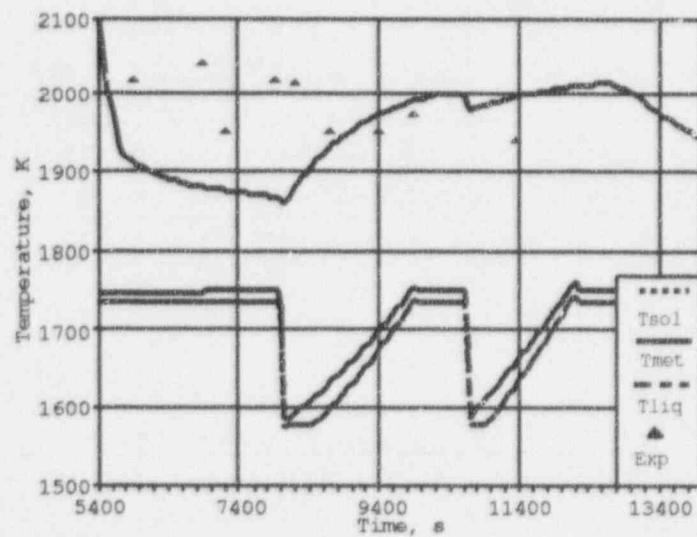


Figure 4.13: SURC-3 temperature of metal layer

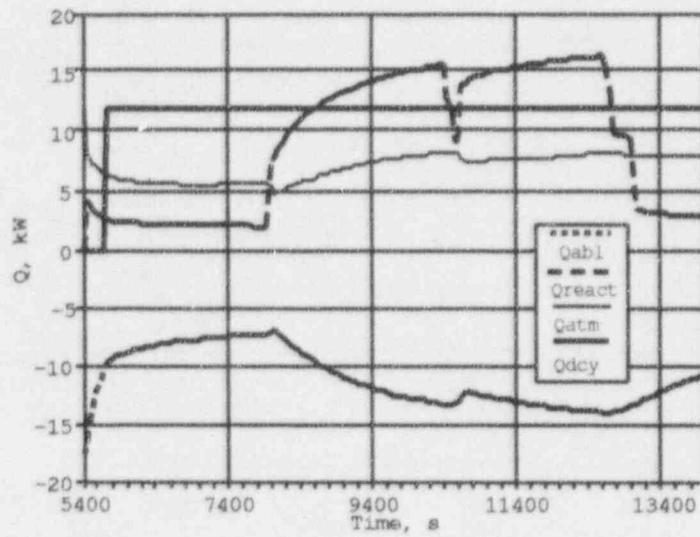


Figure 4.14: Energy term rates for SURC-3 test

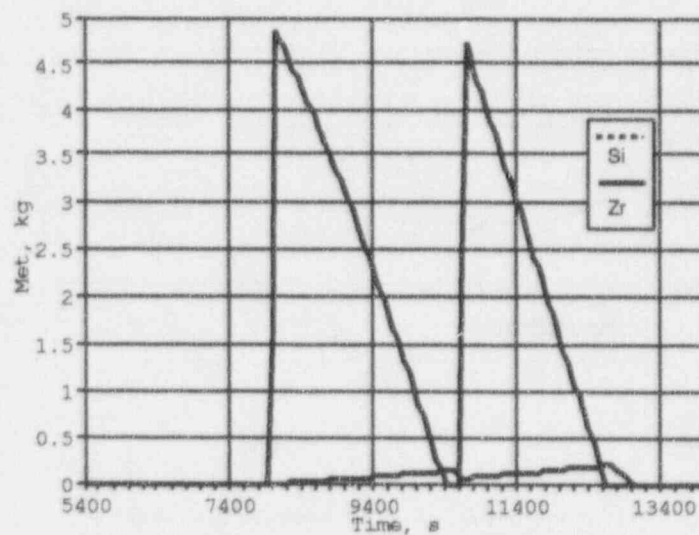


Figure 4.15: Mass of metals in the melt for SURC-3 test

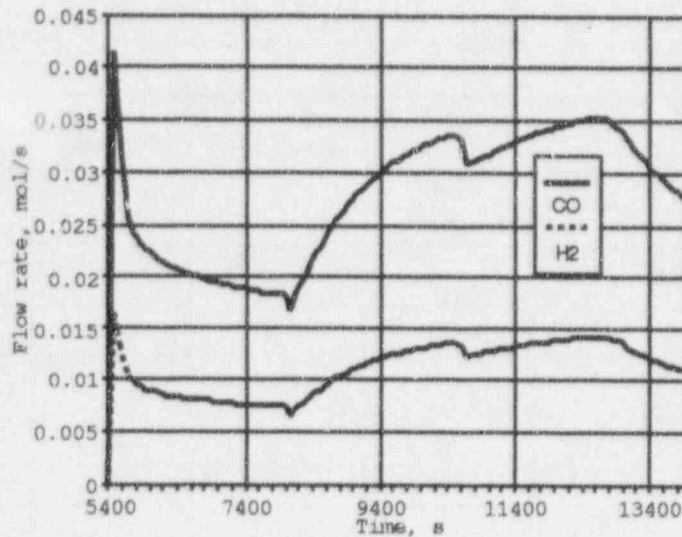


Figure 4.16: SURC-3 CO and H<sub>2</sub> flow rates

radial direction. Melt temperature at the start of concrete ablation was 1950 K. After zirconium addition, temperature increased to 2120 K and then dropped gradually to the level of 1900 K. Summary of thermal hydraulic results is presented in Table 4.8.

Gas flow data shows four time periods of interest as indicated in Table 4.8. During heating and melting phase, gas flow rate increased gradually and ranged up to 45 slpm (0.03 mol/s). After the onset of ablation, flow rate increased to the value of 170 slpm. Average flow rate during steady state ablation phase was 120 slpm (0.09 mol/s). Zirconium addition to the melt resulted in large increase in gas flow rate. Average flow rate between 75 and 100 minutes was 220 slpm or 0.16 mol/s. Monitoring of CO/CO<sub>2</sub> ratio in the test allows to estimate chemistry in the melt. During ablation (prior to and after zirconium addition), typical ratio was about 3.5 whereas during zirconium oxidation period, it was about 12. In comparison with SURC-3 test, these values are lower which may indicate that only part of outgoing gases reacted with metallic species in the melt.

#### 4.4.2 Comparison to SURC-3A Data

General CORCON input parameters are presented in Table 4.3. Initial melt was defined in accordance with Table 4.1 without zirconium. Composition of 304 stainless steel and total mass of the melt were used to determine mass of metallic species. The beginning of interaction was chosen to be at 50 min. In accordance with the SURC-3A test scenario, zirconium addition was initiated at 75 minutes after start of the test. CORCON input option ISRABL was switched on. Mass addition rate was defined as 0.25 kg/s during 20 seconds that allowed addition of 5 kg (55 moles) of Zr metal.



Table 4.8: SURC-3A test summary data

Parameter	Preheating Phase	Steady state phase	Zr oxidation	Late phase
Time, min	25-45	45-75	75-100	100-150
Temperature, K	800-1900	1950-1970	1950-2120	1900
Gas Flow Rate, slpm	16	120	220	130
mol/s	0.01	0.09	0.16	0.1
Gas Composition vol %				
$H_2$	6	3	4	2
$CO$	40	70	83	70
$CO_2$	60	20	7	20
Erosion Rate				
Axial, cm/hr	-	8	20	8
Radial, cm/hr	-	4	6	4

Surrounding temperature was set at 1600 K. Condensed phase chemistry option was specified in the simulation but this option did not influence the computational results due to low silica content in the melt. Because of two dimensional erosion, it was necessary to specify downward and side heat transfer. Slag film model was specified at the bottom and gas film heat transfer model to the side (option *IFILM* = 01).

Main results of calculations are presented in Figures 4.17-4.21. Comparison of erosion data (see Figure 4.17) shows that CORCON predictions are in good qualitative agreement with the test data. Ablation depth is higher than test data during the initial phase of interaction. There is a shift in test data with respect to the time of zirconium addition (about 1500 s).

Figure 4.18 illustrates that temperature after zirconium addition increases, but in the test only small temperature rise was detected (from 1950 to 2020). Calculated temperature is lower during all time period. In calculations, influence of the zirconium addition on the erosion depth is significant. Heat to concrete is about 30 kW during the initial phase (see Figure 4.19). Chemical heat release after zirconium addition is 8 times greater. Due to the two-dimensional character of interaction, the oxidation rate of zirconium metal is very fast in comparison with SURC-3. Temporal behavior of metal species in the melt presented in Figure 4.15 shows that zirconium metal exists in the melt only for 500 s. To estimate possible rate of Zr oxidation during the test, average flow rate data was used. Gas flow rate was 0.16 mol/s and about 80 % of total gas release was reduced. This means that oxidation rate of Zr was nearly 0.06-0.07 mol/s. Estimated zirconium oxidation time is about 800-900 s.

Figure 4.21 shows flow rates of  $CO$  and  $H_2$  gases. CORCON predictions for  $CO$  and  $CO_2$  flow rates are in good qualitative agreement with test data but total gas flow rate is about 1.5 times greater than it was measured. Zirconium oxidation period is in good agreement with analytical

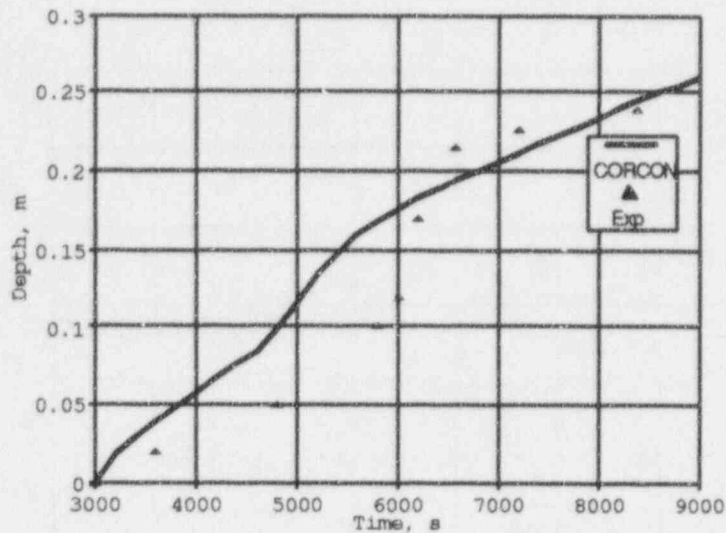


Figure 4.17: SURC-3A concrete erosion depth

assessment and CORCON prediction. In the test, just before zirconium addition, dehydration front was located 4 to 5 cm ahead of the erosion front. Because the axial erosion rate in the SURC-3A test was less than in the SURC-3 test, difference of zirconium oxidation was a result of radial concrete erosion which provided additional gas flow (in all 2.5 times larger). At 100 minutes, flow rate dropped to approximately the initial level. The main oxidation process is considered to be oxidation of iron.

Thus, simulation of SURC-3A test by CORCON-Mod3 shows good quantitative agreement with test data. Some discrepancies may be explained in terms of general uncertainties of experimental data and assumptions with respect to the values which were not exactly measured in the test.

## 4.5 Modeling of the SURC-4 Test

The SURC-4 test was conducted at the Sandia National Laboratories in 1987 [52]. The main objectives of the experiment were: measurements of gas generation, aerosol release, and the interaction characteristics of steel-zirconium melt with basaltic concrete.

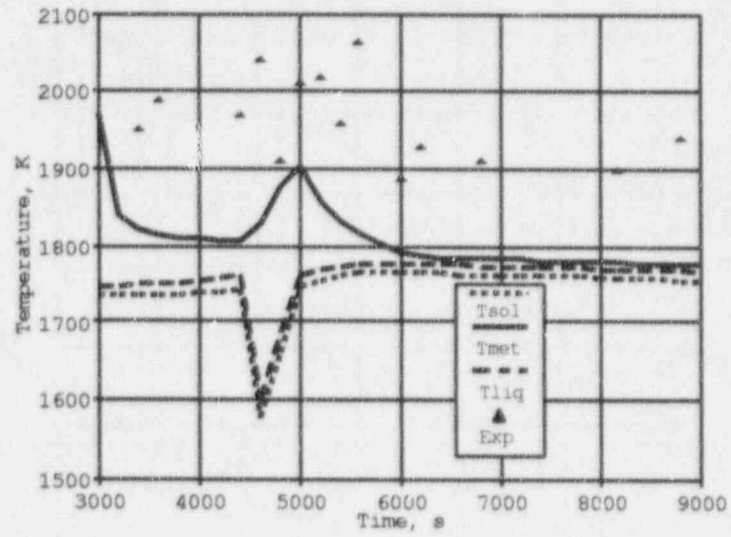


Figure 4.18: SURC-3A temperature of metal layer

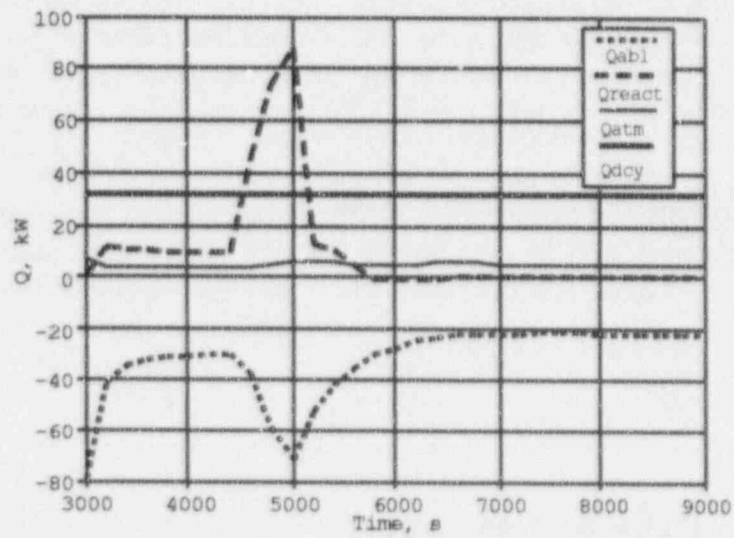


Figure 4.19: Energy term rates for SURC-3A test

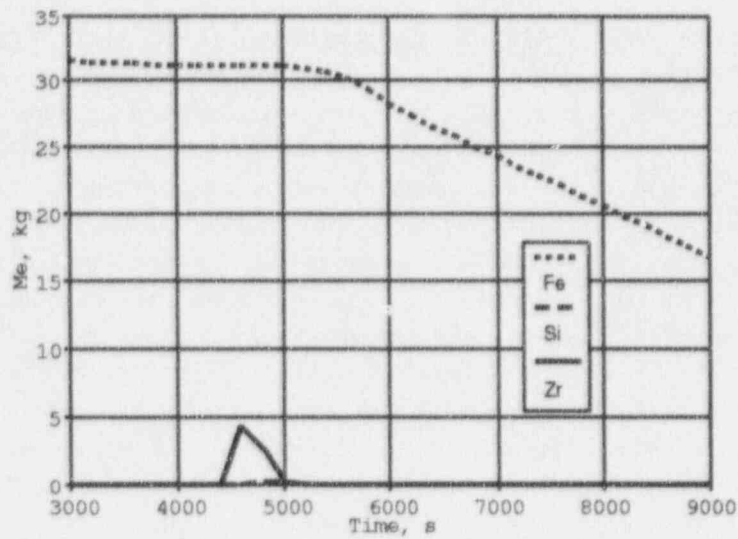


Figure 4.20: Mass of metals in the melt for SURC-3A test

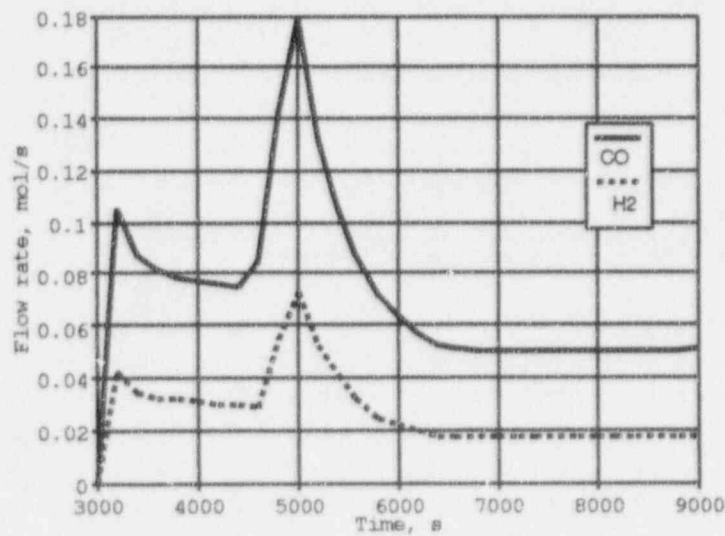


Figure 4.21: SURC-3A  $H_2$  and  $CO$  flow rates

#### 4.5.1 Test Apparatus and Results

The interaction crucible, made of  $MgO$  ceramics with wall thickness of 10 cm, outer diameter of 60 cm, and height of 110 cm was placed into the induction furnace. Concrete sample with diameter of 40 cm and 40 cm in height, together with the heated stainless steel cylinder of total weight 200 kg (diameter 40 cm, height 20 cm), were put into the ceramic crucible. The experimental facility was instrumented for the analysis of the composition of outcoming gases and for analysis of the aerosol composition. Thermocouples cast within the concrete cylinder and  $MgO$  sidewall allowed the measurement of temperatures in the concrete basemat at different locations. The thermocouple data provided important information concerning the behavior of the wet-dry front as well as decomposition front in the concrete. Thermocouples installed in the magnesium oxide annulus allowed an estimate of the sidewall heat losses. Alongside the main experiment, the calorimeter experiments for determining the efficiency of energy input into the melt were conducted. As a result of these experiments, it was found that  $25 \pm 2\%$  of power supplied to the induction coil was transferred into the metal charge.

In Table 4.6, composition of the initial metal charge is presented. In addition, 6 kg of the fission products simulants was added to the interaction crucible. During the quasi-steady phase of concrete decomposition, 20 kg (220 moles) of zirconium cylinders was also added to the melt. Inductive coils were connected to a power supply of 245 kW. Taking into account net efficiency of heating, total net power to the melt was sustained at the level of 62 kW during the test. The experiment started at 0.8 atm pressure, and the initial temperature was  $325^\circ C$ . The overall duration of the experiment was about 3 hours whereas steady state concrete decomposition phase lasted about 100 minutes. In Table 4.9, the main external and internal events for the SURC-4 experiment are given. During the experiment, there was an unplanned power switching off to the inductive furnace.

Beside measurement of inductive heating efficiency, calorimetric tests demonstrated that power input to the charge was strongly nonuniform due to the skin effect. Estimates of the nonuniformity of power input, made in reference [15], indicated that central power input was less than the outer radii input by a factor of 10 (lower estimate). This nonuniformity may be one reason for possible uncertainties in the calculations. Moreover, as indicated in Table 4.9, erosion at the outer radius array was detected prior to central thermocouple failure.

In the SURC-4 experiment, four time intervals are of interest. Summary of thermal hydraulic results in these intervals is presented in Table 4.10. At about 100 minutes, stainless steel was melted at temperature 1710 K. Prior to ablation at 45 min, gas release was detected. Gas flow rate increased gradually and at the start of concrete ablation, was nearly 40 slpm (0.03 mol/s). Location of 400 K isotherm was about 6.5 cm below the concrete surface. Hydrogen constituted about 50 vol% of offgases. After concrete erosion began, gas flow rate increased to 50 slpm (0.037 mol/s). Hydrogen concentration in the effluent increased and the  $CO_2$  concentration decreased. After the addition of zirconium, gas composition changed to a mixture rich in hydrogen (83 vol%). Concentration of both  $CO$  and  $CO_2$  dropped rapidly to zero for a period of 5-10 minutes after which  $CO$  concentration recovered to a level above the value indicated before zirconium addition while the  $CO_2$  concentration recovered to a level below those value.

Basaltic concrete typically liberates 1.5 wt%  $CO_2$  gas and 5 wt% water vapor when heated to melting. Thus, in the case of simultaneous gas release, about 90 volume percent of  $H_2$  and

Table 4.9: Events of SURC-4 test

Time(min)	Time(sec)	Event
0.0	0.0	Start of data acquisition system
10.7	642.0	Power supply on power meter reading 98 kW
44.0	2640.0	Power increased to 200 kW (power meter)
80.5	4030.0	Power increased to 245 kW (power meter)
102.8	6168.0	Thermocouple $C_{41}$ failed ( $r=18.0$ cm, $z=0.0$ cm)
105.4	6324.0	Thermocouple $C_1$ failed ( $r=0.0$ cm, $z=0.0$ cm) This moment is taken to be the onset of the interaction with the concrete.
111.9	6714.0	Thermocouple $C_{21}$ failed ( $r=10.0$ cm, $z=0.0$ cm)
119.0	7140.0	Zirconium metal delivered to the melt (20 kg)
124.1	7446.0	Power supply off
131.7	7902.0	Power supply on (245 kw)
144.8	8688.0	Power supply off
145.1	8706.0	Power supply on (245 kw)
162.5	9750.0	Power supply off
177.6	10656.0	Data acquisition system terminated

Table 4.10: SURC-4 test summary data

Parameter	Preheating Phase	Initial phase	Zr oxidation	Late phase
Time, min	45-105	105-119	119-135	135-160
Temperature, K	850-1750	1750-1780	1780-1940	1830
Gas Flow Rate, slpm	17	50	120	90
mol/s	0.01	0.04	0.09	0.07
Gas Composition vol %				
$H_2$	50	65	83	80
$CO$	30	20	14	14
$CO_2$	20	15	1.4	2
Axial Erosion Rate, cm/hr	-	16	29	29



$H_2O$  may be expected. Prior to ablation, only part of water is liberated (probably free water). During initial ablation, offgases were rich in  $CO$  and  $CO_2$  because dehydration front passed ahead of erosion front. Only after 130–135 minutes, erosion front was coincident with dehydration front and  $H_2$  to  $CO$  ratio became about 6.

The basaltic concrete used in the SURC-4 experiment melts over the temperature range of 1350 to 1650 K. Analysis of concrete response data [52] allowed reconstruction of the erosion front in the basaltic basemat. It was reported that during the initial period of ablation (prior to zirconium addition), erosion rate was calculated to be 16 cm/hr. The propagation rate after zirconium addition was calculated to be 29 cm/hr between 119 and 162 minutes. Thus, it was found that zirconium addition significantly increased the ablation rate of concrete. At the same time, the eight minute loss of power between 124 and 132 minutes did not affect the ablation rate.

Before analysis of energy balance for SURC-4, erosion rate data was reevaluated. Three thermocouple arrays were installed in the concrete basemat at three different radial positions (along centerline  $r = 0$  cm, mid radius array,  $r = 10$  cm, outer radius array,  $r = 18$  cm). Outer radius array data may be fit by a line with average erosion rate of 26.7 cm/hr. Mid radius array data may also be fit by a line with average erosion rate of 26.0 cm/hr. These data show no changes after zirconium addition to the melt. The center array data gives following values of erosion rate: prior to zirconium addition (104–119 minutes) 21.4 cm/hr, after zirconium addition 28.5 cm/hr, and in the interval of 126–160 minutes, 22.5 cm/hr. Taking into account geometric factor which is proportional to  $r^2$  (mass of concrete eroded is proportional to area of interaction), the average erosion rate was evaluated as 26 cm/hr during the experiment. This value was used in the calculations of energy balance.

The melt temperature ranged between 1785 and 1925 K. Concrete erosion began when the melt pool temperature increased from its melting point (1710 K) to 1785 K. This temperature was maintained for 20 minutes during the initial phase of ablation. Immediately after zirconium addition, the melt pool temperature began to rise and reached a peak value of 1925 K. At 124 minutes, the power to the melt was lost and temperature dropped to 1835 K. The melt pool temperature decreased to 1790 K at 160 minutes.

Assessment of the zirconium oxidation is based on the following assumptions:

1. All offgases interact with zirconium;
2. Silica formed during concrete ablation first interacts with zirconium;
3. After zirconium oxidation is completed, silicon begins to interact;
4. Heat release due to oxidation reactions is calculated using equation (2.3). Oxidation of other melt species is neglected.

To calculate zirconium oxidation rate, assessment of silica release rate should be made. After zirconium addition, average erosion rate from test data was 26 cm/hr or 0.008 cm/s. Assuming an interaction area based on 40 cm diameter, it gives an erosion rate about 23–25 g/s. 55 wt% of basaltic concrete mass is silica. That means that silica release rate is about 0.22 mol/s. Total zirconium oxidation rate is equal to

$$R_{Zr} = 0.5R_{H_2} + 0.5R_{CO} + R_{SiO_2}$$

Taking into account gas release rate presented in Table 4.10, zirconium oxidation rate is nearly 0.27 mol/s, and more then 80% of this value is due to silica. Zirconium oxidation time was calculated using formula  $M_{Zr}/R_{Zr}$  and equals 820 s or less then 14 minutes. Thus, oxidation of zirconium in the test was nearly complete by 133 minutes just after power was switched on. Because of this, second and third time intervals in Table 4.11 are connected with zirconium oxidation while fourth time interval is with silicon oxidation phase. This interpretation is qualitatively confirmed by the slight change in offgas composition.

At the end of zirconium oxidation, about 175 moles (4.9 kg) of silicon is accumulated in the melt. Gas flow rate of 0.07–0.08 mol/s provides silicon oxidation rate at the level of 0.035–0.04 mol/s. Total silicon oxidation time may be estimated at about 70 minutes. Thus, about half of silicon inventory in the melt is expected to be oxidized by the end of the test.

Estimates of sidewall heat losses made in [52] give the value of flux about 100 kW/m<sup>2</sup>. Taking into account area adjacent to the melt, the minimum value of sidewall energy loss rate is about 25 kW. A higher value of average heat losses through the sidewall of the crucible (29 kW) was estimated in reference [36]. Downward heat rate may be estimated taking into account erosion rate and decomposition enthalpy which was assumed to be 2 kJ/g (see Table 2.3).

Before zirconium addition, estimated heat to concrete was nearly 42 kW (without accounting for evaporation front location and preheating of concrete layer adjacent to the metal slug). Because the dehydration front at the start of concrete ablation was located 6–7 cm below the concrete surface, downward heat losses may be estimated by subtraction of decomposition energy. This procedure gives the reduction of decomposition enthalpy by 10 % due to small content of H<sub>2</sub>O and CO<sub>2</sub> in the basaltic concrete. Average temperature of this concrete layer may be estimated as 900 K (mean value between decomposition and initial temperature of concrete). Thus, decomposition enthalpy of partially decomposed and heated concrete may be estimated at the level of 1 kJ/g or half as much as for unheated concrete. It gives the value of 20–25 kW for average downward energy loss. Remaining power or nearly 20 kW may be estimated as upward heat loss and heating of concrete decomposition products to the meltpool temperature.

After zirconium was added to the melt, the temperature in the experiment grew very quickly. The characteristic rate of heating up was about 0.5 K/s. Assessment of the power source required in neglecting possible additional energy loss gives:

$$Q_h = Mc\dot{T} \approx 80kW$$

where  $M$  is mass of the melt (kg),  $c$  is specific heat of the melt (795 J/kg/K for stainless steel 304 above 1700 K [52]), and  $\dot{T}$  is the rate of heating (K/sec). Energy deficit during this phase is about 15 kW even if upward heat losses are neglected. The first possible source of uncertainty is preheating phase. Strictly speaking, behavior of 400 K and 1600 K isotherms becomes similar after 124 minute so previous reasoning may have a meaning in this time interval too. Also, some additional energy sources may exist. For example, one phenomenon which may influence thermal behavior of the melt is heat release during dissolution of molten zirconium in the iron meltpool.

Table 4.11: SURC-4 rough energy balance

Parameter	Initial phase	Zr oxidation	Power off	Late phase
Time, min	105-119	119-124	124-132	132-160
Axial Erosion Rate, cm/hr	26	26	26	26
Erosion rate, g/s	13	24	24	24
H <sub>2</sub> release, mol/s	0.026	0.075	0.075	0.056
CO release, mol/s	0.008	0.013	0.013	0.01
Silica release, mol/s	-	0.22	0.22	-
Net power to the melt, kW	62	62	0	62
Sidewall losses, kW	-25	-25	-25	-25
Chemical heat, kW	5	70	70	16
Melt pool heating up, kW	-	-80	30	4
Heat to concrete, kW	-20	-43	-43	-43
Balance, kW	22	-16	32	5

After loss of input power for eight minutes, temperature dropped 70 K with an average rate of -0.18 K/s. Energy release due to cooling of melt is about 30 kW. Together with chemical heat, total power input during this phase is about 100 kW. About 27 kW may be interpreted as energy rate to surrounding and concrete decomposition product heating. Late phase of interaction shows that heat generation and estimated heat losses are in correspondence with each other. In reality it means that some additional energy source should be found to maintain heat balance.

In the calculations performed by Bradley [36], initial phase of interaction prior to zirconium addition gives the erosion rate of 16 cm/hr, same as in reference [52]. After zirconium addition and prior to power loss, average erosion rate was 38.4 cm/hr, and temperature increase was close to experimental data. Higher erosion rate provided higher chemical heat in comparison with data presented in Table 4.11. Rough estimate gives the value about 100 kW. Power switch off did not influence erosion line so ablation rate remained approximately at the same level. Heat to concrete was about 63 kW. Summarizing all energy loss rates, one gets an energy balance of -3 kW. In the calculations, upper boundary condition was nearly adiabatic due to reduction of the melt emissivity. After loss of power, erosion rate remained the same but temperature did not increase, so energy balance gives a value of 10 kW. Late phase erosion in calculations was nearly 25 cm/hr and corresponded to data presented in the table. Thus, to simulate experiments, Bradley neglected upward heat loss. In such a situation, temperature rise is due to difference between chemical heat release and decomposition enthalpy. To decompose 1 kg of concrete, about 2.0 MJ of total energy should be provided. Chemical heat release due to oxidation of zirconium by concrete decomposition products is about 3.5 MJ. Heating up of concrete decomposition products to the melt pool temperature gives no more than 0.4 MJ/kg. Remaining heat is 1.5 times larger in comparison with decomposition enthalpy. Thus, a positive feedback between erosion rate and chemical energy rate exists, and only additional energy loss or temperature increase (the higher the temperature, the larger energy required to heat concrete products) may limit the process. In

the cited calculations, power switch off reduced significantly total energy input. Full oxidation of zirconium in this simulation interrupted further temperature increase. Silicon oxidation provided only about 0.75 MJ of chemical heat due to decomposition of 1 kg of concrete so positive feedback was impossible for late phase of erosion.

#### 4.5.2 Comparison to SURC-4 Test Data

Modeling of SURC-4 test was initiated from the start of concrete ablation (6300 s). The experimental value of the temperature at 6300 sec, which is equal to 1750 K, was chosen. Standard layer configuration (ILYR=0) was used in the calculations. Because of high influence of condensed phase chemistry for SURC-4 experiment, ICHEM was equal to 1. To account for sidewall energy loss, input power to the melt was defined as 37 kW. Standard basaltic concrete option was used.

Scenario of modeling was the same as presented in Table 4.9. At 7100 s, addition of zirconium was initiated with average mass addition rate of 0.2 kg/s. Power history in the calculation was defined in accordance with power history in the test. According to the efficiency of the heating, about 25% of the total power to the coil (64 kW) was supplied to the melt. At the same time, the estimate of the average sidewall heat losses gives the value of 25–30 kW. After subtracting this value from the total energy input, the result is about 35–40 kW. In the calculations 40 kW of input power was used.

Concrete decomposition temperature in calculation was equal to 1650 K (liquidus temperature of concrete) that corresponded to decomposition enthalpy of about 2.0 MJ/kg. This value of concrete decomposition enthalpy was used in the analysis above. Emissivity of the surrounding was defined as 0.01 during all the test. According to the energy balance analysis performed in the previous section, during initial phase of ablation decomposition enthalpy assessment gives the value two times lower due to preheating. To compensate for reduction of decomposition enthalpy, upward heat loss was reduced. After zirconium addition, foaming was detected in the test. To account for foam formation in the calculations, it was assumed (see reference [36]) that there is no upward heat loss. Same conclusion can be made from the analysis of energy balance in the test.

According to the above analysis, four phases of interaction are of interest after start of basemat ablation. CORCON predictions are analyzed and compared with estimates made in the previous section. Main results of calculations are presented in Figures 4.22–4.27. In Figure 4.22, erosion depth is well predicted by the code. Average erosion rate prior to zirconium addition is about 20 cm/hr. This data is in good agreement with test erosion rate of 21.6 cm/hr. After zirconium addition and before loss of power, average predicted erosion rate is about 40 cm/hr or higher than it was reported. At the same time, this value is very close to the ablation rate indicated by thermocouples installed along the centerline of the concrete basemat. After power loss and at the end of the test, predicted erosion rate follows outer radius array data.

In Figure 4.23, energy terms predicted by CORCON are presented. The whole power feed to the melt, in this case, goes to concrete decomposition, and heat up of the melt and concrete decomposition products. Average value of the heat to concrete is about 45 kW prior to zirconium addition. Then power to concrete increases to about 80–90 kW due to high value of chemical power. Peak value of oxidation power reaches 120 kW. Complete oxidation of zirconium metal during the

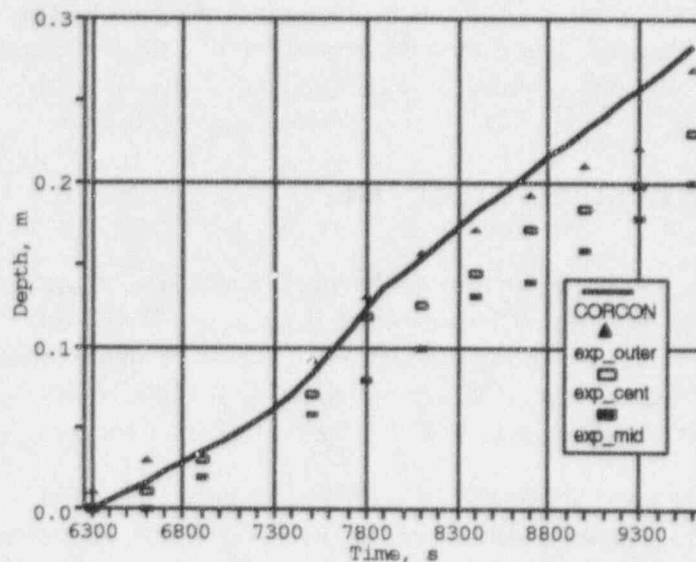


Figure 4.22: SURC-4 concrete erosion depth

900 s interval is predicted by CORCON (see Figure 4.24). This value is in good agreement with estimated oxidation time. After zirconium oxidation, about 5 kg of silicon accumulated in the melt. Predicted value of the silicon oxidation power is about 25 kW. This power provides higher values of erosion rate and temperature of the melt, which is presented in Figure 4.25. Initial phase as well as maximum temperature due to oxidation reactions are predicted very well. Higher value of moltpool temperature during the late phase of interaction is a consequence of silicon oxidation in the melt. Peak temperature during zirconium oxidation phase is lower than the measured value.

Predicted values of gas release, presented in Figures 4.26 and 4.27, indicate that the chemistry package correctly describes the gas behavior. Overprediction of hydrogen release rate during initial phase of interaction is due to dehydration of the concrete layer adjacent to the metallic melt. During and after zirconium oxidation, overprediction is much lower (about 30%) relative to the test flow rate.  $CO$  flow rate qualitatively and quantitatively corresponds to the test data due to better correspondance of  $CO_2$  release temperature to the concrete melting temperature.



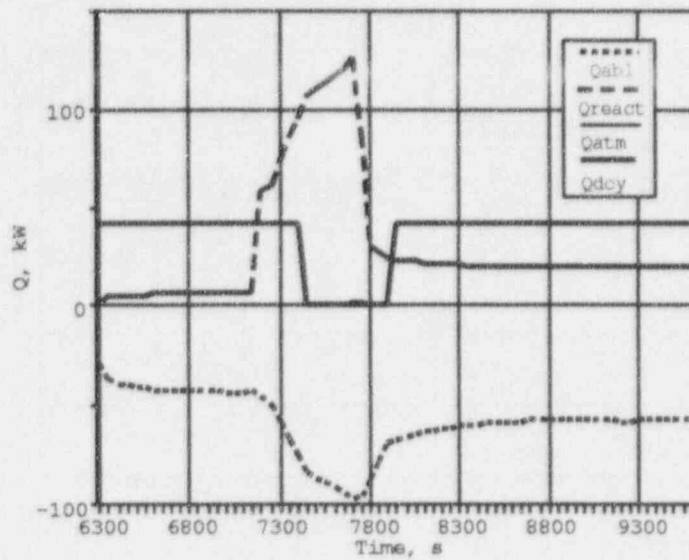


Figure 4.23: Energy rate terms predicted by CORCON for SURC-4 test

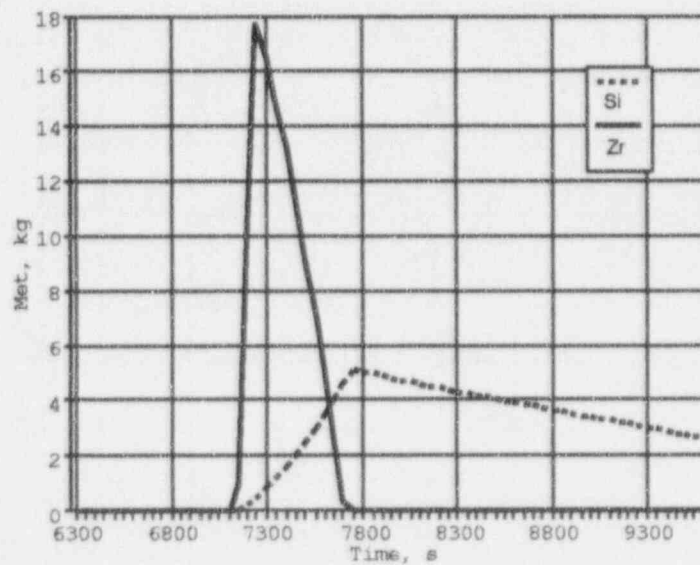


Figure 4.24: SURC-4 predicted mass of metals in the melt pool



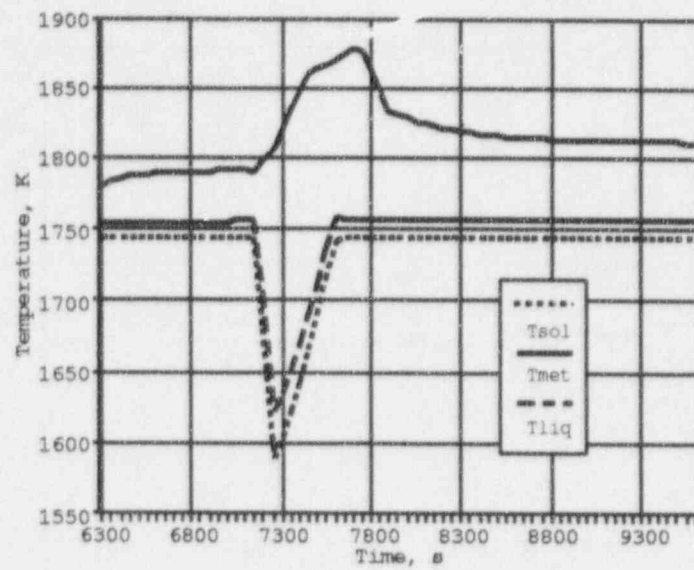


Figure 4.25: SURC-4 comparison of predicted and experimental temperatures of metal layer

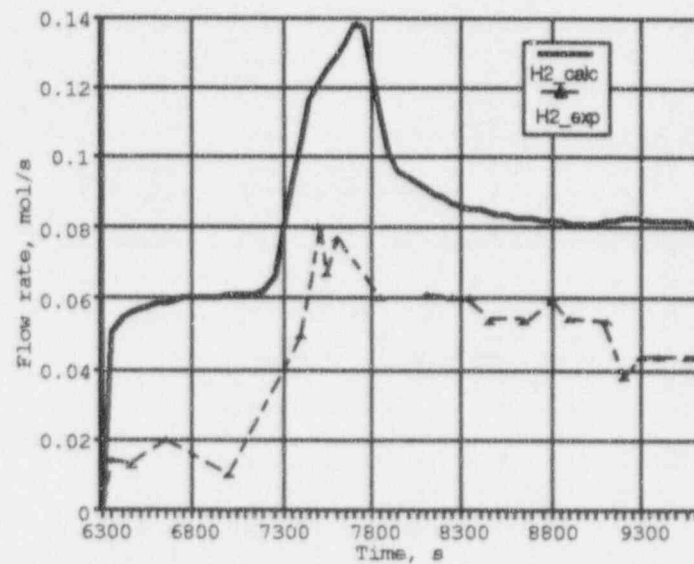


Figure 4.26: SURC-4 comparison of CORCON  $H_2$  flow rate results to test data

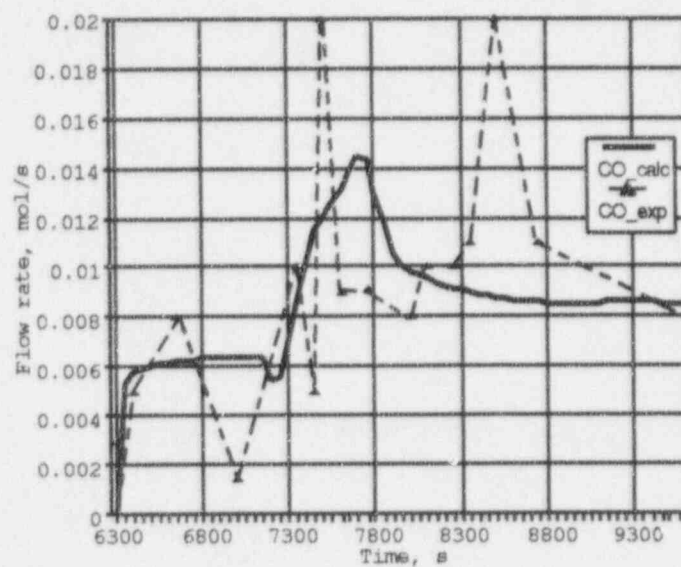


Figure 4.27: SURC-4 comparison of CORCON CO flow rate results to test data

## 5 MODELING OF THE BETA V7.1 TEST

### 5.1 Description of the BETA Facility

Experiments conducted in the BETA facility present an opportunity for two dimensional simulation of core concrete interaction. The facility consists of a furnace with inductive coil for heating the melt and cylindrical concrete crucible with conical upper part. This conical part is used for preparation of the initial melt by thermite reaction. The furnace can accommodate a melt mass up to 850 kg. The maximum power to the induction coil 3 MW, sufficient to achieve a melt temperature of 2200 - 2300 K. During the experiment the following parameters are measured:

- temperature inside the melt by downcoming thermocouples;
- temperature of upper surface of the melt by optical pyrometer;
- temperature inside the concrete crucible by thermocouples;
- electrical power of inductor;
- amount and chemical composition of outcoming gases and aerosols.

Melt front position during the interaction as well as temperature are measured by 110 thermocouples located in the concrete crucible. Temperature of the melt is measured by the *Pt10Rh/Pt* and *W5Re/W26Re* thermocouples while temperature of concrete and interaction front by *Cr/Al* and *Ni/Cr/Al* thermocouples. Optical pyrometer measures the temperature of the upper surface of the melt. Visual observations of the surface conditions are performed by the telecamera with the possibility of video recording. Chemical composition of released gases is measured by the mass spectrometer. To provide the safety of the facility due to hydrogen release, special argon diluter is installed in the interaction chamber.

All BETA experiments deal with thermite burning of the mixtures using  $Fe_2O_3$  and *Al*. In the V5 and V7 series of experiments, about 750 kg of mixture was loaded into the furnace including about 574 kg of thermite mixture. After exothermic reaction, about 350 kg of melt was relocated into the concrete crucible. This melt contained 300 kg of metals (excluding zirconium which was added later) and 50 kg of light oxides. The melt temperature was 2190-2270 K.

Table 5.1: Melt composition (in kg) at the start of interaction with the concrete

<i>Fe</i>	270.0
<i>Zr</i>	80.0
<i>Al<sub>2</sub>O<sub>3</sub></i>	32.5
<i>Cr</i>	15.0
<i>Ni</i>	15.0
<i>SiO<sub>2</sub></i>	10.0
<i>CaO</i>	7.5

## 5.2 Test Conditions and Results

BETA V7.1 experiment was conducted with serpentine concrete. The composition of concrete determined before experiment differs from the results presented in Table 2.1. Real concrete composition was defined in accordance with reference [53]). The composition of corium at the start of interaction is presented in Table 5.1.

For experiment V7.1, 80 kg of zirconium was added before the start of interaction. To prevent early oxidation of *Zr* it was placed into the interaction crucible 1 minute before melt relocation. About 8 kg of fission product simulants were also added into crucible (*CeO* — 1 kg, *BaO* — 1 kg, *La<sub>2</sub>O<sub>3</sub>* — 0.5 kg, *Mo* — 1 kg, *BC* — 6 kg).

For the metal layer containing relatively large amount of *Zr* temperatures *Fe-Zr* phase diagram was used in the calculations to determine the solidus and the liquidus. Concrete decomposition temperature (TW) was assumed to be 1653 K.

## 5.3 Comparison to BETA V7.1 Test Data

Modeling of two dimensional interaction in the BETA tests permits validation of different heat transfer models in CORCON-Mod3. In the following calculations, different combinations of slag and gas film models on the bottom and on the side were used with the same set of input data. Table 5.2 presents the results of erosion depth calculations using different heat transfer models at 600 s. This stage of interaction is characterized by intensive zirconium oxidation and, as a consequence, chemical heat production which maintains the melt temperature at relatively high values. Test data for axial erosion is about 12 cm, and radial erosion in this test was about 3–5 cm.

Comparison to test data indicates that thermal resistance of the gas film model is higher than that for the slag film. Moreover, the slag film model provides better correspondence to the test data. Figure 5.1 illustrates the heat balance in the calculations of V7.1 test. Net power to the melt as well as heat to atmosphere, chemical heat, and heat to concrete are presented in this figure. In Figure 5.2, the comparison of erosion depth to the test data is presented. The initial phase

Table 5.2: Depths of concrete ablation in axial and radial directions for different heat transfer models

Type of heat transfer		Erosion, cm	
downward	sideward	downward	sideward
G	S	4.5	13.7
G	G	5.9	5.8
S	G	19.0	4.5
S	S	12.0	5.0

G — gas film model

S — slag film model

of interaction is well predicted by the code while long term interaction is underpredicted. The reason for slowing down of the erosion rate is that stable crust was formed on the bottom interface surface after the oxidation of zirconium was completed. Figure 5.3 shows temperature of metal layer. Comparison to the gas release data is presented in Figures 5.4 and 5.5. Hydrogen release is well predicted by the code, but water vapor release is overpredicted.

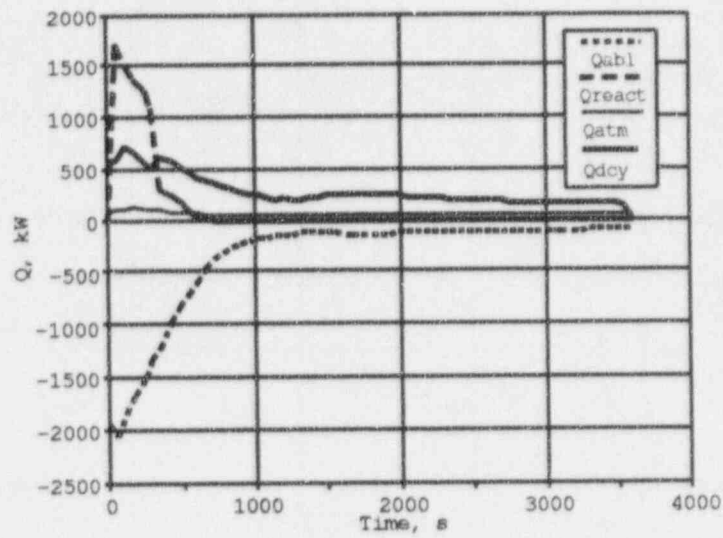


Figure 5.1: Energy rate terms for BETA

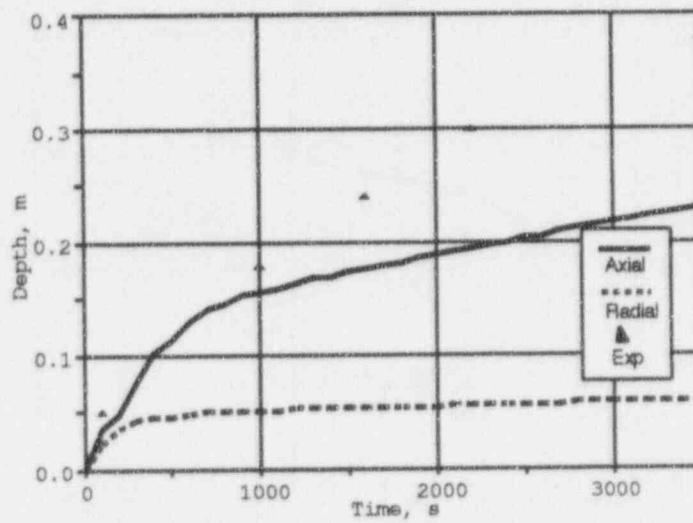


Figure 5.2: BETA concrete erosion depth



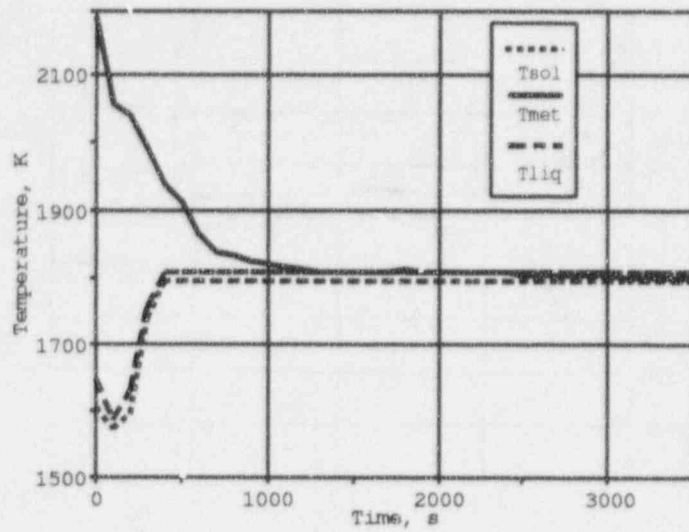


Figure 5.3: BETA temperature of metal layer

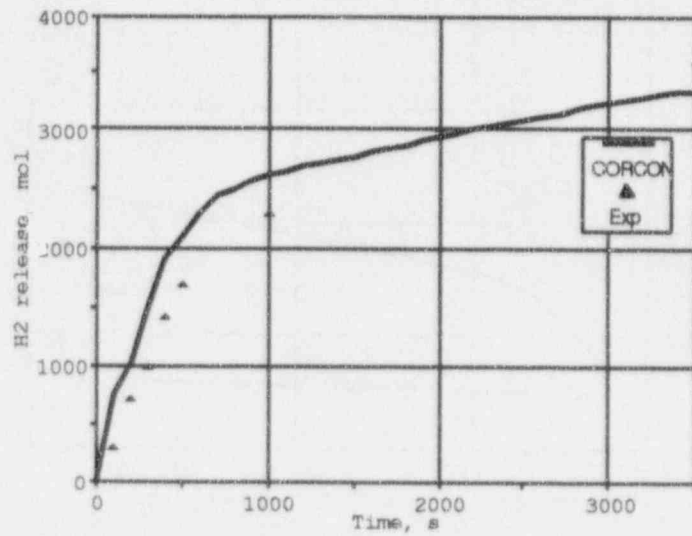


Figure 5.4: Comparison to  $H_2$  release for BETA 7.1 test

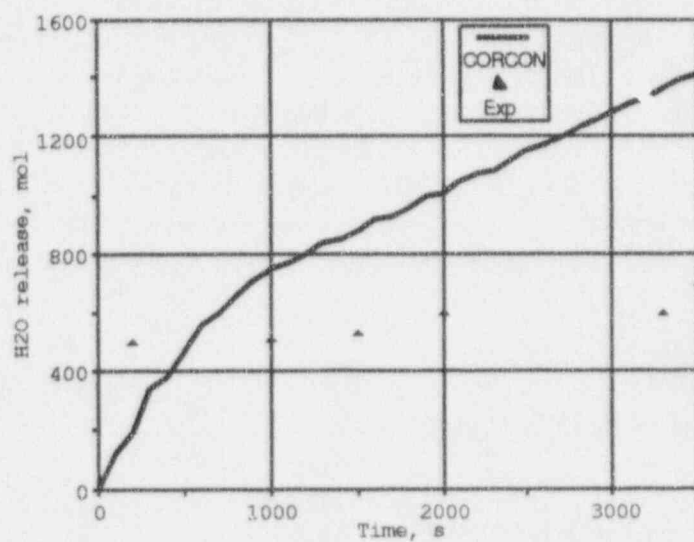


Figure 5.5: Comparison to  $H_2O$  release for BETA 7.1 test

## 6 MODELING OF TESTS WITH AN OVERLYING WATER POOL

Analysis of accident scenarios have shown that core debris interaction with concrete may be complicated by the presence of water. Water may appear in the reactor cavity as a result of loss of coolant accident. Moreover, addition of water may be considered as one of the countermeasures to prevent containment failure due to melt through of concrete basement. In addition to heat removal due to boiling of water at the top surface of the melt, overlying water pool can significantly reduce ex-vessel aerosol release rates during an accident [5]. For these reasons, core-concrete interactions in the presence of an overlying water pool in the cavity is of interest in the study of severe accident phenomena. To study effects of water, several tests were conducted to provide necessary data base for analysis of both thermal hydraulic behavior of molten pool and fission product release. SWISS tests were intended to examine the effect of water on metallic melt. Several oxidic tests were performed under the MACE program. This section deals with modeling of interactions in the presence of an overlying water pool. Three tests were chosen for analysis: two SWISS experiments and the MACE-M1b test.

### 6.1 Modeling of SWISS Tests

#### 6.1.1 SWISS Test Apparatus and Results

Two experiments in the SWISS series [54] simulated the interactions of molten core with limestone/common sand concrete in the presence of an overlying water pool. A total of 44 kg of 304 stainless steel with the initial temperature about 1810 K was delivered to the interaction crucible made of *MgO* ceramics. Initial melt composition for both tests was identical and is presented in Table 6.1. Stainless steel charge was chosen as the core debris material to simulate the formation of the topmost metal layer during the initial phase of melt relocation. When the density of oxide layer exceeds the density of metal layer, the latter will be directly exposed to the coolant.

Fission product simulants were added to the melt to simulate release and decontamination of aerosols by water pool. Similar tests utilizing metallic melts and fission product simulants in dry cavity conditions were performed under the SURC program.

Cylindrical ceramic crucible in the experiments had an inner diameter of 21.6 cm. LCS concrete base had a height of 22.9 cm. Sustained heating was provided by 125 kW induction power supply. About 65% of total input power was applied to the melt. Both SWISS tests were similar in every respect with the only difference being the timing of water addition. Tables 6.2 and 6.3 present

Table 6.1: Initial melt composition for SWISS tests

Constituent	Mass(kg)
<i>Fe</i>	30.0
<i>Cr</i>	8.55
<i>Ni</i>	4.525
<i>Mo</i>	0.475
<i>Mn</i>	1.150

Table 6.2: Timing of events for SWISS-1 experiment

Time (min:sec)	Time sec	Event
0:00	0	Melt delivered to crucible
0:11	11	Power Supply on (92 kW)
18:43	1123	Power Supply off
22:11	1331	Power Supply on (95 kW)
31:54	1914	Water quench initiated ( $8.9 \cdot 10^{-4} m^3/s$ )
34:57	2097	Water flow reduced to $1.1 \cdot 10^{-4} m^3/s$
36:44	2204	Water flow increased to $1.4 \cdot 10^{-4} m^3/s$
37:34	2254	Power Supply off

timing of main events in the course of tests including power history and history of water addition. Initial time corresponds to the delivery of the melt from melt generator to the crucible. These tables indicate that in the SWISS-1 test, water was added 32 minutes after melt delivery during steady state ablation phase while in the SWISS-2 test, water was supplied immediately after delivery of the melt to the crucible. Total duration of both tests was about 40 minutes.

The interaction crucible was instrumented with a total of 59 thermocouples located in various arrays. 23 thermocouples were cast into the concrete basemat at two radii — along the centerline of the crucible and 5.4 cm from the axial centerline. These thermocouples were used to measure thermal response of the concrete. Eight thermocouple arrays measured temperatures in the ceramic sidewall at different elevations. Remaining thermocouples were used to measure temperature of the water pool above the melt.

#### 6.1.1.1 SWISS-1 test results

According to Table 6.2, experiment on concrete erosion was activated by melt delivery from the melt generator. Initial temperature of the melt was between 1912 and 2048 K. Total mass of stainless

Table 6.3: Timing of events for SWISS-2 experiment

Time (min:sec)	Time sec	Event
0:00	0	Melt delivered to crucible
0:25	25	Power Supply on (100 kW)
1:39	99	Water quench initiated $9.2 \cdot 10^{-4} m^3/s$
1:58	118	Water flow reduced to $2.7 \cdot 10^{-4} m^3/s$
3:08	188	Water flow increased to $4.1 \cdot 10^{-4} m^3/s$
4:05	245	Water flow reduced to $3.1 \cdot 10^{-4} m^3/s$
5:35	395	Water flow reduced to $2.3 \cdot 10^{-4} m^3/s$
24:16	1454	Power Supply off
26:29	1589	Power Supply on (100 kW)
27:30	1650	Water flow reduced to $1.2 \cdot 10^{-4} m^3/s$
29:32	1772	Water flow increased to $2.2 \cdot 10^{-4} m^3/s$
35:41	2141	Power Supply off
36:43	2203	Water flow off
37:13	2233	Power Supply on (100 kW)
41:00	2460	Power Supply off

steel 304 melt was about 46 kg. Eleven seconds later, power was applied to the coils, and 92–95 kW was sustained during the test. Net power to the melt was about 60 kW. Assessment of side losses through *MgO* ceramics gave a value of heat flux nearly  $200 \text{ kW}/m^2$ . Taking into account area of sidewall adjacent to the melt, the energy loss was about 22–25 kW.

When the SWISS-1 test was in progress, there was a broad dip in power from about 60 kW at 250 seconds to about 40 kW at 670 seconds. At 1123 seconds, there was unexpected power loss due to a fuse failure. Power supply was back 3.5 minutes later. Water injection was activated at 1914 seconds with a flow rate of  $8.9 \times 10^{-4} m^3/s$ . At 2097 s, water flow rate was reduced to  $1.1 \times 10^{-4} m^3/s$ . Post-test observation showed a large void above residual concrete at the base. The crust serving as the upper boundary of the large void was between 5 and 6.4 cm thick. The top of the crust was located 11 cm above the original concrete surface.

There was a delay of about 8 minutes after melt delivery before a thermocouple embedded 1 cm below the concrete surface registered 1600 K. This temperature was assumed to be the ablation temperature of limestone common sand concrete. Erosion depth for SWISS-1 test was about 17 cm during 35 min of ablation with the average erosion rate of 0.5 cm/min or 28.6 cm/hr. There was no decrease of erosion rate after water addition.

Volumetric gas flow rate during the test in progress had a peak of  $0.007 m^3/s$  STP or 0.3 mol/s just after melt delivery. It was sustained at the level of  $0.0035\text{--}0.005 m^3/s$  STP (0.15–0.22 mol/s) prior to water addition into the interaction crucible. A peak gas flow rate of 0.6 mol/s was detected just after water supply.

Limestone common sand concrete liberates about 21 wt% carbon dioxide gas and 5 wt% water vapor when heated to melting. Corresponding mole ratio of liberated gases  $CO_2/H_2O$  is about 1.7. Expected flow rate based on the concrete erosion rate of 30 cm/hr gives a value of 0.02 mol/s for  $H_2O$  and 0.034 mol/s for  $CO_2$  so that the total rate is 0.054 mol/s. This value is 3 times lower than that measured during the test. Typical hydrogen content in the offgas prior to water addition is 60%. When compared with the expected ratio, released gas was found rich in hydrogen. This fact may be explained by comparison with data of 400 K isotherm location in concrete. The width between wet and dry fronts reached 7–10 cm. Dehydration front propagation rate is between 55 cm/hr and 30 m/hr. Considering that about 3 wt% of concrete is free water, an upper limit of expected free water vapor release is 0.02 mol/s. In this case, total gas release rate of 0.07 mol/s may be expected. Higher flow rates measured in the test may be a result of additional  $CO_2$  release if temperature gradient in the concrete is not steady state. The second reason discussed is the presence of  $N_2$  and  $O_2$  which might suggest a gas leak within the sample system. Their concentration ranged between 26 % at the beginning of the test and 90% before the test was terminated.

#### 6.1.1.2 SWISS-2 test results

According to Table 6.3, experiment on LCS concrete erosion was activated by melt delivery from the melt generator. Initial temperature of the melt was between 1912 and 2048 K. Total mass of 304 stainless steel melt was about 44 kg. Power was applied 25 seconds later to the coils at the level of 100 kW. Net power to the melt was sustained about 60 kW early in the test and increased to 70 kW later in the test. Assessment of side losses through  $MgO$  ceramics gave a value of heat flux about  $200 \text{ kW/m}^2$ . Taking into account area of sidewall adjacent to the melt, the energy loss is about 22–25 kW. Power was disrupted twice during the test due to fuse failures: between 1454 and 1589 seconds, and between 2141 and 2233 seconds. Water injection was activated at 99 seconds with a flow rate of  $9.2 \times 10^{-4} \text{ m}^3/\text{s}$ . History of water addition is presented in Table 6.3.

Post-test observation showed a large void above residual concrete at the base. The crust serving as the upper boundary of the large void was between 5 and 6.4 cm thick. The top of the crust was located 25 cm above the original concrete surface. The ablation of concrete was delayed nearly 6 minutes after melt delivery and progressed at nearly a constant rate of 27.3 cm/hr. Erosion depth for SWISS-2 test was nearly 17 cm during 35 min of ablation.

Volumetric gas flow rate measured during the test had a peak of  $0.01 \text{ m}^3/\text{s}$  STP or 0.45 mol/s just after water addition. Later in the test it was measured at the level of  $0.0035\text{--}0.005 \text{ m}^3/\text{s}$  STP (0.15–0.22 mol/s). As discussed in the previous section, mole ratio of liberated gases  $CO_2/H_2O$  is about 1.7. Estimates of expected flow rate based on concrete erosion rate gives approximately the same value as for the SWISS-1 test (0.054 mol/s). Again, this value is 3 times lower than that measured during the test. Possible reasons have already been discussed before. The ratio of offgases at the beginning of interaction had a value of nearly 1.5. After water addition, this ratio became 2. Compared to the expected ratio, the offgas was rich in hydrogen. At about 20 minutes into the test, considerable decrease in  $H_2$  content was detected. Ratio of  $CO/CO_2$  was between 8 and 4 at the beginning of the test indicating high degree of oxidation of metals. After 8 minutes of interaction, this ratio was between 2 and 3.

Heat flux to the water pool was calculated neglecting any steam lost from the water pool. The



initial flux was  $2.0 \text{ MW/m}^2$  because of heat transferred to the water from the hot sidewall of the crucible. A stable heat flux was estimated at approximately  $0.8 \text{ MW/m}^2$ . Two depressions were detected resulting from power reduction to the melt pool. A  $27.3 \text{ cm/hr}$  erosion rate gives a value of  $16\text{--}20 \text{ kW}$  for downward heat flux. About  $30 \text{ kW}$  is attributed to the upward heat loss. The total energy loss is between  $70$  and  $75 \text{ kW}$ . Net power to the melt pool was sustained at approximately the same level and chemical reactions did not provide a significant power addition.

### 6.1.2 Comparison to Test Data

Built-in concrete properties were used in the calculations ( $ICON = 2$  for limestone common sand concrete). Concrete ablation temperature (TW) was chosen to be  $1600 \text{ K}$  which is between LCS concrete solidus and liquidus temperatures. Initial melt temperature was equal to  $1980 \text{ K}$  for both tests. Chemistry flag was chosen to be  $0$  (ICHEM=0) because initial melt did not contain zirconium. Coking reaction was off. Heat transfer at the bottom was defined by the option  $IFILM = 01$ , that corresponded to the slag gas film model. General CORCON-Mod3 options were chosen in accordance with Table 6.4. Initial layer configuration was defined as a single metal layer ( $ILYR = 1$ ) without interlayer mixing.

To account for side losses, the input power was reduced by  $30 \text{ kW}$  for SWISS-1 test and by  $25 \text{ kW}$  for SWISS-2 test, correspondingly. Water addition history was specified in accordance with test scenarios presented in Tables 6.2 and 6.3. Water flow rate was very high for both experiments. For instance, for SWISS-2 test flow rate was  $2 \times 10^{-4} \text{ m}^3/\text{s}$ . Initial temperature was assumed to be  $1800 \text{ K}$  at the beginning of interaction.

#### 6.1.2.1 Comparison to SWISS-1 Test Data

There was a  $7\text{--}8$  minutes delay in the experiment between melt delivery to the interaction crucible and start of interaction. For this reason, calculations started at  $450 \text{ s}$  with the initial temperature of  $1800 \text{ K}$ . Figure 6.1 presents comparison of CORCON results with SWISS-1 results. CORCON predictions correspond very well to the test data. Erosion depth follows power behavior (see Figure 6.2). Heat to concrete is about  $20 \text{ kW}$  (assessment of power to concrete based on the concrete decomposition enthalpy and ablation rate of  $30 \text{ cm/hr}$  gives a value of  $20\text{--}22 \text{ kW}$  to concrete). Oxidation of metals does not play an important role, and provides additional power at the level of  $5\text{--}6 \text{ kW}$  only. Water addition at  $2040 \text{ s}$  leads to substantial increase of upward heat losses. Temperature of the melt is predicted at the level of  $1800 \text{ K}$  during test time as shown in Figure 6.3.

Figure 6.4 presents crust thickness predictions for SWISS-1 test. Crust thickness follows power input to the melt and is equal to  $1\text{--}2 \text{ cm}$ .  $H_2$  and  $CO$  releases are presented in Figure 6.5. Average value of  $H_2$  release is about  $0.02 \text{ mol/s}$ . Release of  $CO$  is about  $0.035 \text{ mol/s}$ . These gas release rates correspond to the values estimated above. Again, gas release rates follow power input to the melt. Results of CORCON predictions are in very good agreement with test data except for gas release data. Experimental gas release data is approximately three times higher. Probable reasons for this have already been discussed above.

Table 6.4: CORCON input options

Experiment	SWISS-1	SWISS-2	MACE-M1b	BETA-7.1
Initial Layer Configuration	0	0	0	0
Interlayer Mixing	No	No	No	No
Concrete Type	L/S	L/S	L/S	Serp.
SiO <sub>2</sub> ,%	12	12	28	34
CaO,%	45	45	26	9
CO <sub>2</sub> ,%	21	21	21	2
H <sub>2</sub> O,%	4.7	4.7	6	13
Concrete Ablation Temperature, K	1650	1650	1568	1550
Initial Concrete Temperature, K	300	300	300	300
Concrete Solidus Temperature, K	1423	1423	1400	1500
Concrete Liquidus Temperature, K	1673	1673	1568	1900
Concrete Emissivity	0.6	0.6	0.6	0.6
Time Step, s	8.	8.	20.	2.0
Number of Rays	40	40	40	63
Melt Temperature, K	1980	1980	2500	2150
Metal Layer Emissivity	0.8	0.8	0.8	0.8
Oxide Layer Emissivity	0.8	0.8	0.8	0.8
Surroundings Emissivity	0.6	0.6	0.6	0.6
Chemistry Flag (ICHEM)	0	0	01	01
Heat Flow Index (IFILM)	01	01	10	00
Surroundings Temperature, K	1750	1750	1750	
Power, kW	48	48	130-90	
Radius, m	0.108	0.108	0.28	

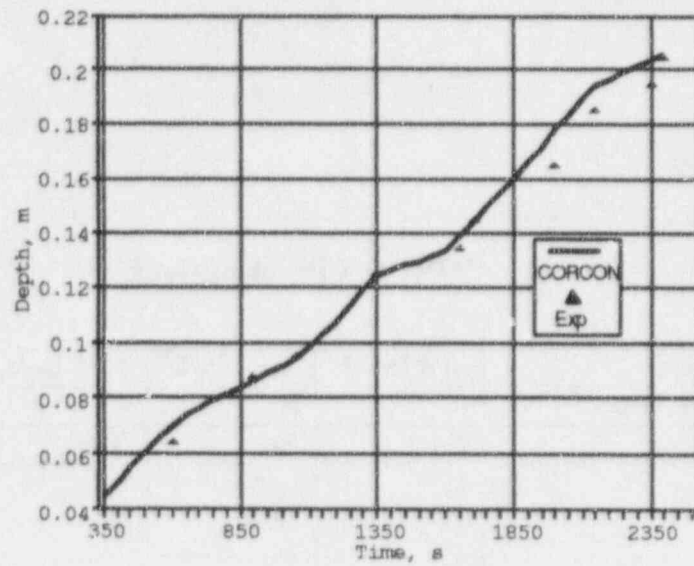


Figure 6.1: Comparison to SWISS-1 ablation results

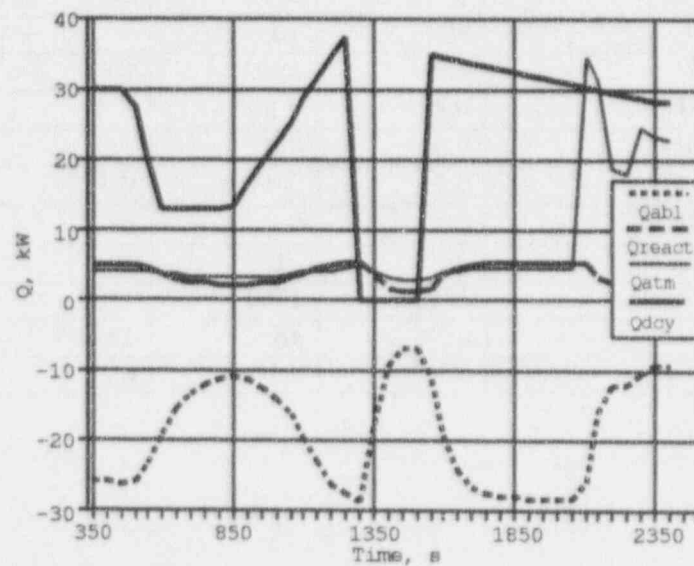


Figure 6.2: Energy rate terms predicted by CORCON for SWISS-1 test

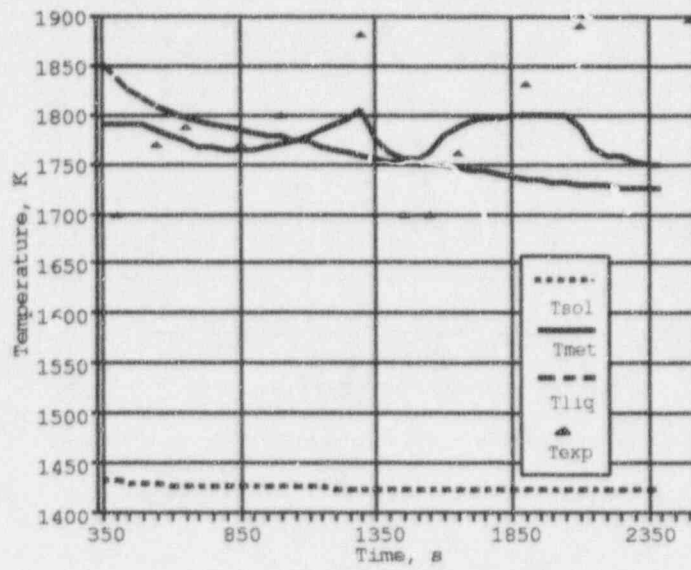


Figure 6.3: Predicted temperature for SWISS-1 test

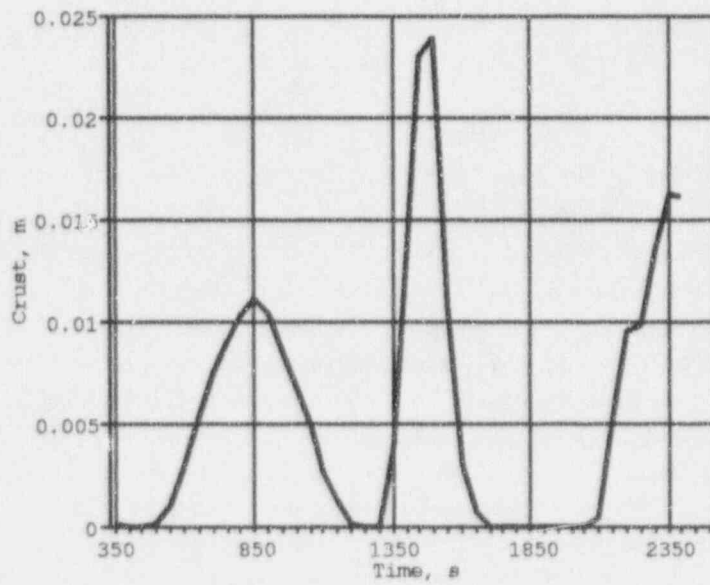


Figure 6.4: Predicted crust thickness for SWISS-1 test

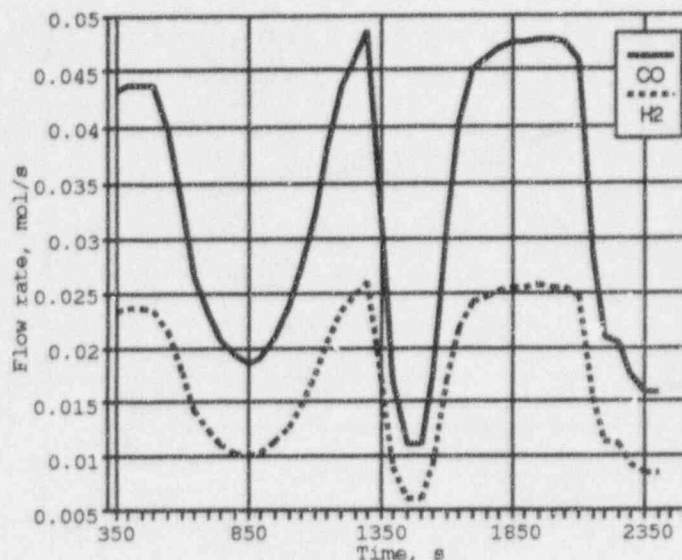


Figure 6.5: Gas flow rates predictions for SWISS-1 test

#### 6.1.2.2 Comparison to SWISS-2 test data

There was a 7 minutes delay in the experiment between melt delivery to the interaction crucible and start of interaction. For this reason, calculations started at 350 s with the initial temperature of 1780 K. Water addition was initiated in accordance with the test scenario. Figure 6.6 presents comparison of CORCON results with SWISS-2 results. CORCON predictions correspond very well to the test data. Erosion depth follows power behavior (see Figure 6.7). Heat to concrete is about 20 kW then drops to about 15 kW (assessment of power to concrete based on the concrete decomposition enthalpy and ablation rate of 30 cm/hr gives a value of 20-22 kW to concrete). Oxidation of metals does not play an important role at the level of 5-6 kW. Water addition just after the beginning of ablation gives about 30 kW of power to the water. Temperature of the melt is predicted at the level of 1750 K during test time as shown in Figure 6.8. This temperature is slightly lower than that for SWISS-1 test.

Figure 6.10 presents crust thickness predictions for SWISS-2 test. Crust thickness follows power input to the melt and is equal to 1-2 cm.  $H_2$  and  $CO$  releases are presented in Figure 6.9. Average value of  $H_2$  release is about 0.02 mol/s. Release of  $CO$  is near 0.03 mol/s. These gas release rates correspond to the values estimated above. Figure 6.11 presents comparison of calculated and estimated in reference [54] heat flux to the water pool. CORCON predictions are in very good agreement to the test data.

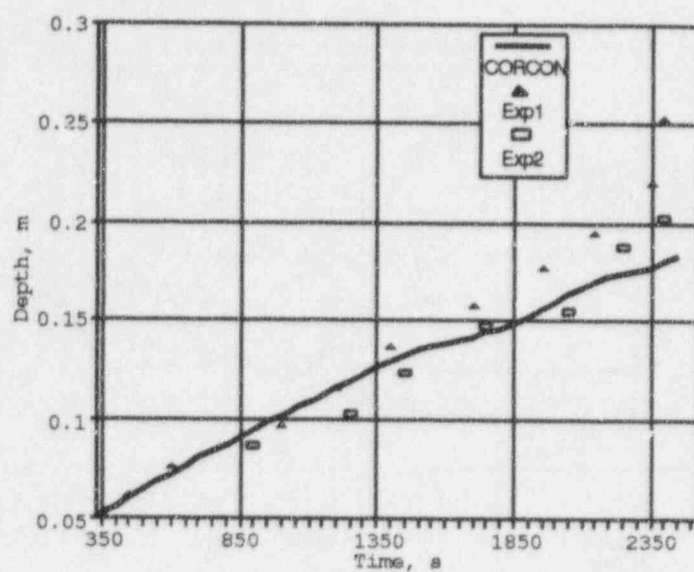


Figure 6.6: Comparison to SWISS-2 ablation results

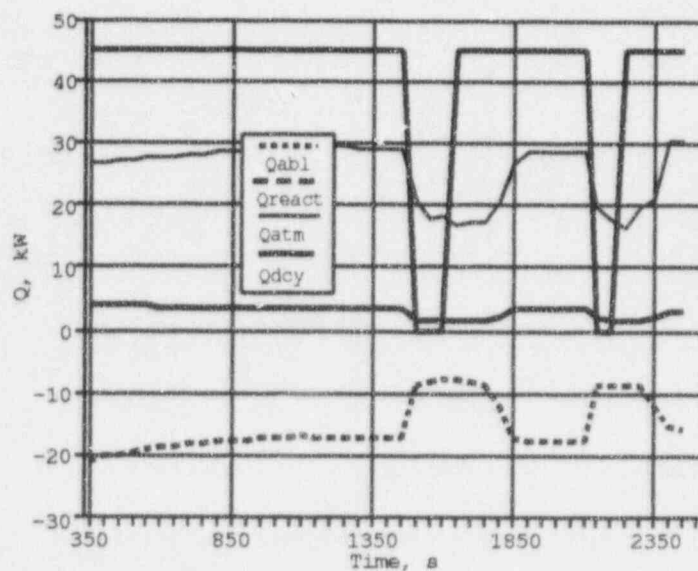


Figure 6.7: Energy rate terms predicted by CORCON for SWISS-2 test



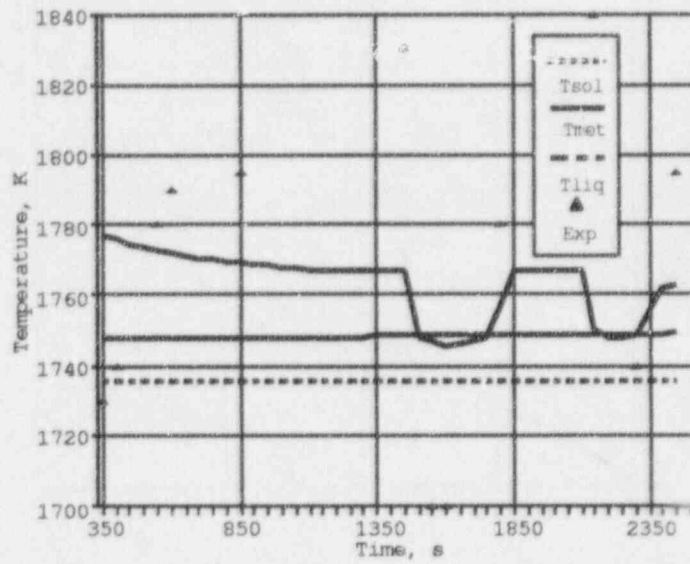


Figure 6.8: Predicted temperature for SWISS-2 test

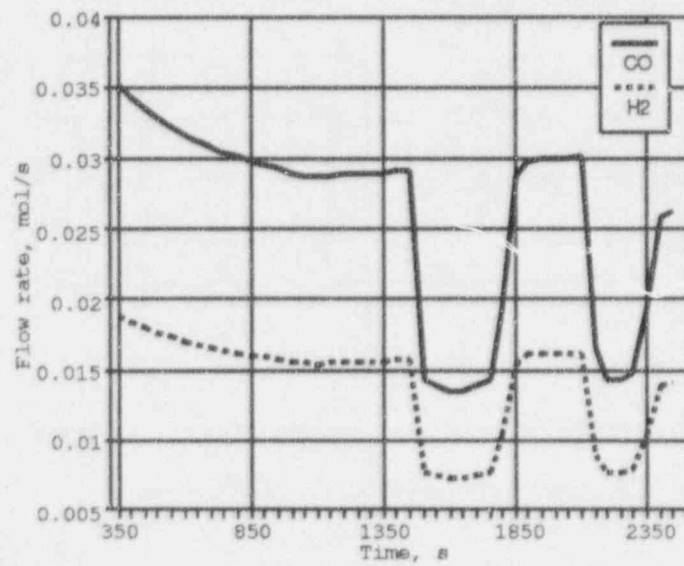


Figure 6.9: Gas flow rates predictions for SWISS-2 test

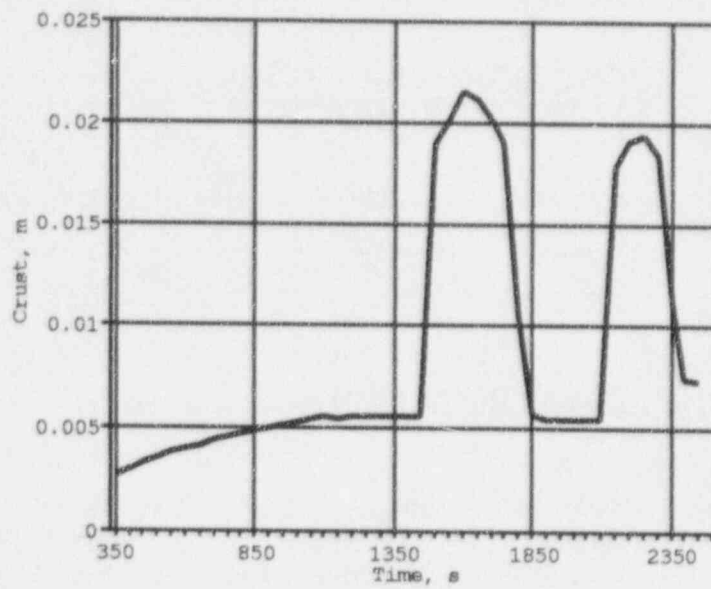


Figure 6.10: Predicted crusts thickness for SWISS-2 test

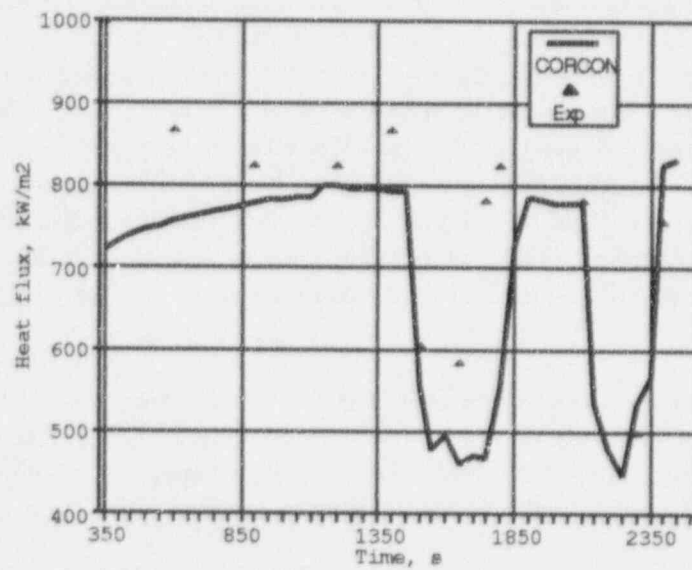


Figure 6.11: Comparison to SWISS-2 upward heat flux

Table 6.5: Composition of the melt for MACE-M1b test

Constituent	Mass, kg	Mass %
$UO_2$	309.1	77.4
$ZrO_2$	64.0	16.0
$SiO_2$	13.5	3.4
$CaO$	12.5	3.2
	399.1	

## 6.2 Modeling of the MACE-M1b Test

A series of large scale tests to study melt coolability under MCCI conditions have been conducted under the internationally sponsored MACE (Melt Attack and Coolability Experiment) Program. Test M1b was the third successful MACE test, performed in April 1992. This experiment with prototypic debris materials was intended to determine the ability of overlying water pool to remove decay heat during ex-vessel MCCI, and to investigate the ability of resulting debris for permanent coolability under severe accident conditions [55].

### 6.2.1 Test Description and Results

The limestone/common sand concrete basemat had an inner cross section of  $50.2\text{ cm} \times 50.2\text{ cm}$ , and a height of 45.0 cm. The lower sidewall was fabricated from  $MgO$  ceramics to provide insulation of the test section. The wall thickness was 25 cm. About 400 kg of initial corium powder was loaded atop the concrete basemat. The composition of the powder is presented in Table 6.5.  $Zr$  metal with total mass of 13.48 kg was incorporated into the melt through two layers of zirconium rods one of which was located immediately atop the concrete block (5.0 kg) and the other was cast into the upper part of the basemat (8.48 kg). The water supply system provided a nominal flow rate of 2 l/s to the top test section from a 2000 l water tank. The water volume inside the test section was maintained at constant value of about 125 l that corresponded to an overlying water pool depth of about 50 cm.

Test apparatus was instrumented to monitor principal parameters during the course of the test including input power to the melt, supply water temperature and flow rate, water volume and temperature within the test apparatus, melt and concrete temperatures, offgas composition and flow rate, and water temperature and level in the quench tank.

The initial decay heat power for M1b, simulated by direct electrical heating, was chosen to be 350 W/kg  $UO_2$  which corresponded to a net power input level of 108 kW. Additional 22 kW compensated for anticipated sidewall heat losses, thus, a gross power of 130 kW was adopted for the test. When the test was in progress, thermocouples cast into ceramic sidewall measured temperature gradient and estimated power loss through sidewall. Total power loss was between 20

and 22 kW during initial 80 minutes of interaction, then decreased gradually to a level of 8–10 kW. Chemical reaction power due to oxidation of zirconium by steam and carbon dioxide was estimated to have a peak value of 160 kW at time  $t=8$  minutes.

Power supply operation began at about -370 minutes relative to the onset of basemat ablation. Gas release was detected 250 minutes prior to basemat ablation. Corium preheating phase resulted in significant heatup of concrete basemat. About 180 moles of  $H_2$  and 55 moles of  $CO + CO_2$  were released by the time concrete ablation started. This amount is equivalent to dryout of free water in the concrete volume of  $32.5 \times 10^3 \text{ cm}^3$ . This is approximately 30% of total concrete slug volume. As discussed above in connection with ACE-L8 test data analysis, more probable areas of water release are the upper part of concrete basemat and concrete regions adjacent to the tungsten electrodes. At the end on the test, a total of 405 moles of hydrogen and 520 moles of  $CO + CO_2$  gas were detected. Total amount of zirconium (nearly 148 moles) was fully oxidized since only 300 moles of water vapor and carbon dioxide were required to oxidize zirconium.

A peak value of hydrogen flow rate of nearly 370 slpm (0.28 mol/s) was detected at 8 minutes after the beginning of ablation. The peak value of carbon monoxide was about 520 slpm (0.39 mol/s). For limestone common sand concrete, total water content was 6.1 w/o and  $CO_2$  content was 21.4 w/o. Ratio of flow rates  $CO + CO_2/H_2O + H_2$  is estimated to be 1.5. Prior to ablation, effluent gas was rich in hydrogen. It was found that during the ablation period,  $CO + CO_2$  flow rate corresponded to the ablation rate data. Ablation front reached the upper Zr concrete layer at -1.2 min. After initial 6.5 min of interaction, ablation front was detected at 6.3 cm so initial concrete erosion rate was very high (about 1 cm/min) due to significant heat release during zirconium oxidation phase. Water addition was started at 14.7 min. Later, depth of water level was about 50 cm.

Test was terminated at 362 min. Total erosion depth was about 19 cm and ablation rate was about 0.1 mm/min. Initial temperature of the melt was estimated to be about 2300 K. This value of temperature was sustained during the first 10–14 min of interaction due to zirconium oxidation. Later, temperature dropped to lower values and was quite close to the concrete solidus temperature at the end of the test. Measured gas release was influenced by the oxidation processes including oxidation of the tungsten during the test. This oxidation changed the offgas composition.

### 6.2.2 Comparison to MACE M1b Data

According to the geometry of MACE M1b test, standard initial configuration was defined with two concrete layers – one with the zirconium rebar and the second pure L/S concrete. Initial data for calculations are presented in Table 6.4. Solidus and liquidus temperatures of concrete were equal to 1400 and 1568 K, respectively. Initial melt temperature was 2350 K, and power history was determined according to reference [55]. Due to the presence of zirconium metal atop the concrete basemat and relatively high  $SiO_2$  content in the concrete basemat (21.4 w/o), condensed phase chemistry option was turned on.

Water addition was defined according to test data presented in [55]. Time dependence of water supply tank volume was averaged and after differentiation, the average flow rate to the test facility was determined. Finally, this data was used in the calculations as flow rate parameters. Initial

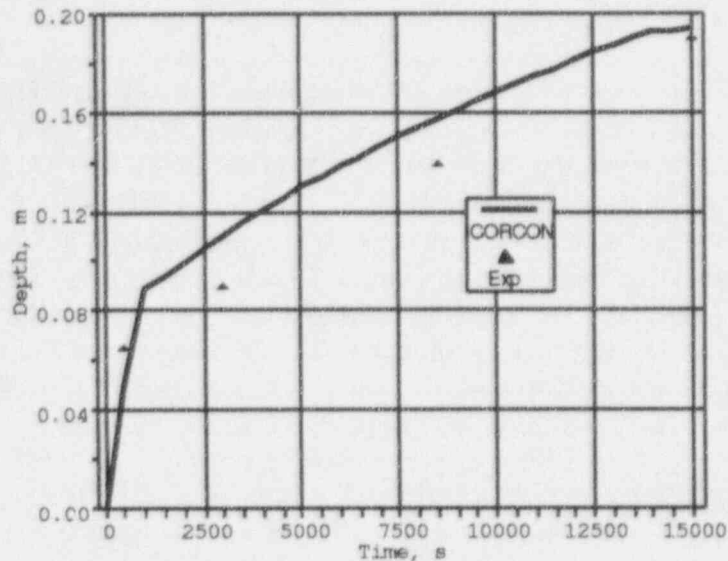


Figure 6.12: MACE Concrete erosion depth

temperature of water was defined as 300 K according to test data.

In Figure 6.12, comparison of predicted and measured erosion depth is presented. As in the test, initial erosion rate was about 1 cm/min. Then ablation rate became much lower due to two reasons - water addition at 14.5 min and complete oxidation of the metal layer. Figure 6.13 presents predicted mass of metal in the metal layer for MACE M1b test. Quick oxidation leads to the disappearance of metal layer at the time close to water addition. Immediately after water addition, both upper and lower crusts are predicted to appear (see Figure 6.14).

Energy rate terms are presented in Figure 6.15. After water addition, about 60 kW of power is estimated as an upward heat loss. Then heat to water drops gradually during the test and reaches the value about 30 kW. Temperature of the melt is well predicted by the code as seen from Figure 6.16. Temperature decreases gradually during the test and follows experimental results. Water inventory in the facility is presented in Figure 6.17. CORCON predictions are in very good agreement with the test data indicating that heat transfer to the overlying water pool is predicted well.

Comparison to gas release data is presented in Figures 6.18-6.22. Predicted peak value of  $CO$  release is slightly lower than that measured in the test but initial period of oxidation of metal layer is predicted very well.  $CO_2$  release rate is in good agreement with test data. The same remarks are true for  $H_2$  release presented in Figure 6.20. After oxidation period, released gases contain only  $CO_2$ . Total released gases are compared in Figures 6.21 and 6.22. Total  $CO$  is slightly underpredicted by the code while  $CO_2$  release is predicted well. Thus, CORCON predictions for MACE-M1b test are in good qualitative and quantitative agreement with the test data.

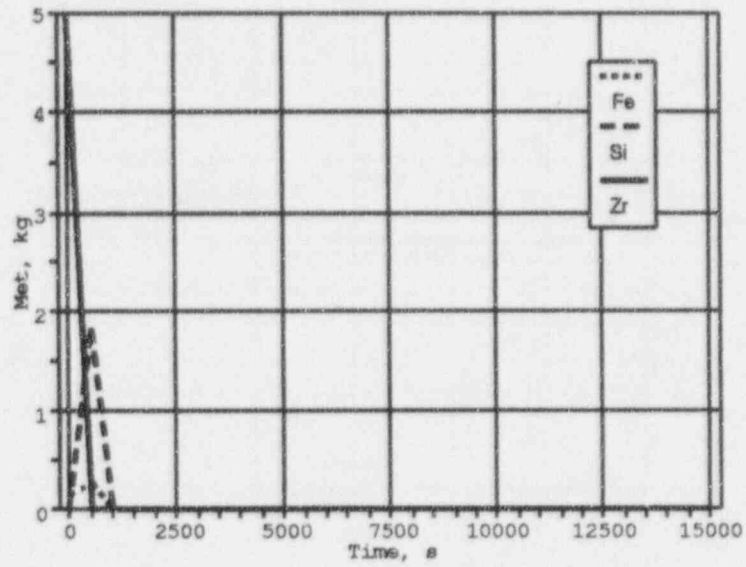


Figure 6.13: Mass of metals for MACE-M1b test

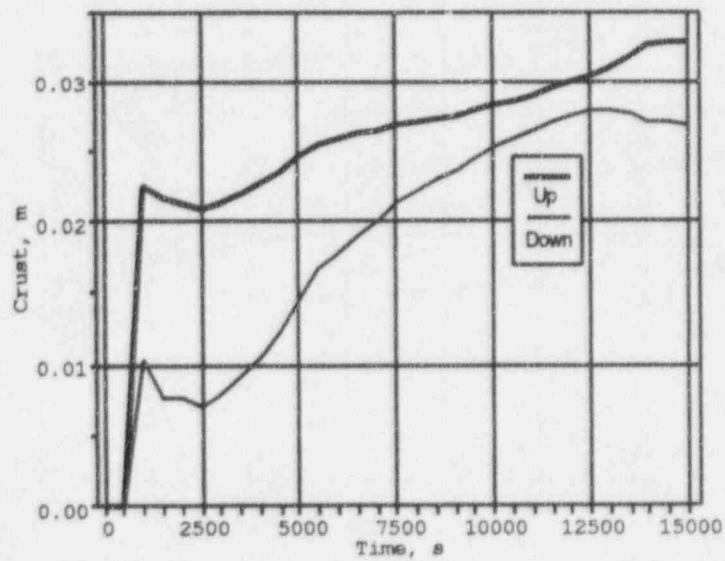


Figure 6.14: Predicted crust thickness for MACE-M1b test



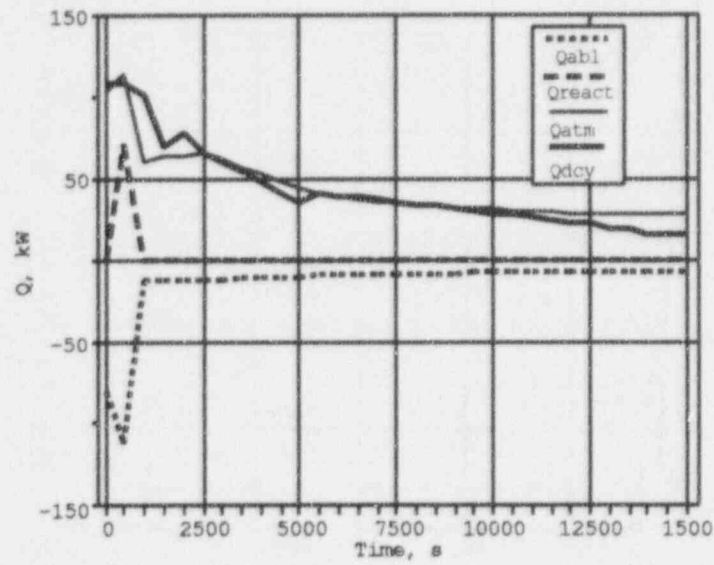


Figure 6.15: Predicted energy term rates for MACE-M1b test

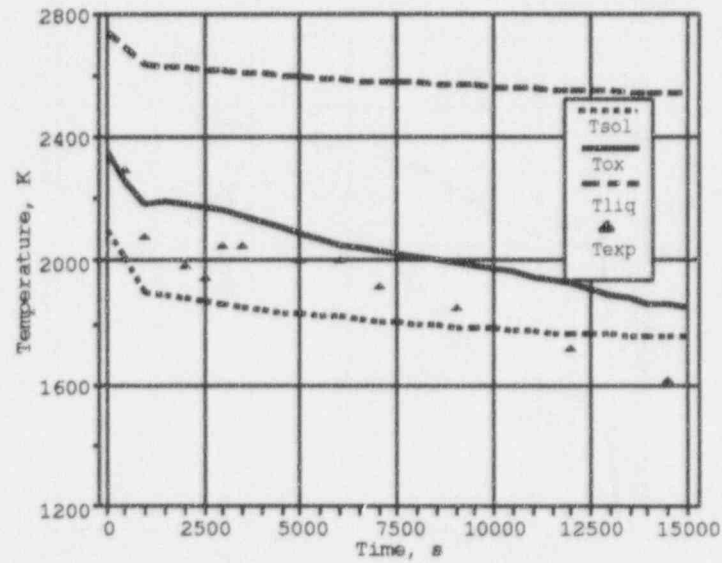


Figure 6.16: Comparison to MACE-M1b temperature of oxide layer

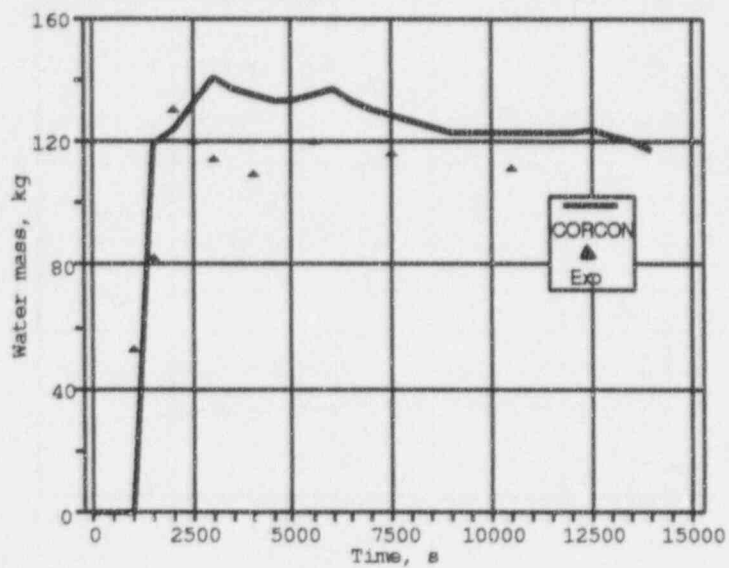


Figure 6.17: Comparison to water mass in the test section

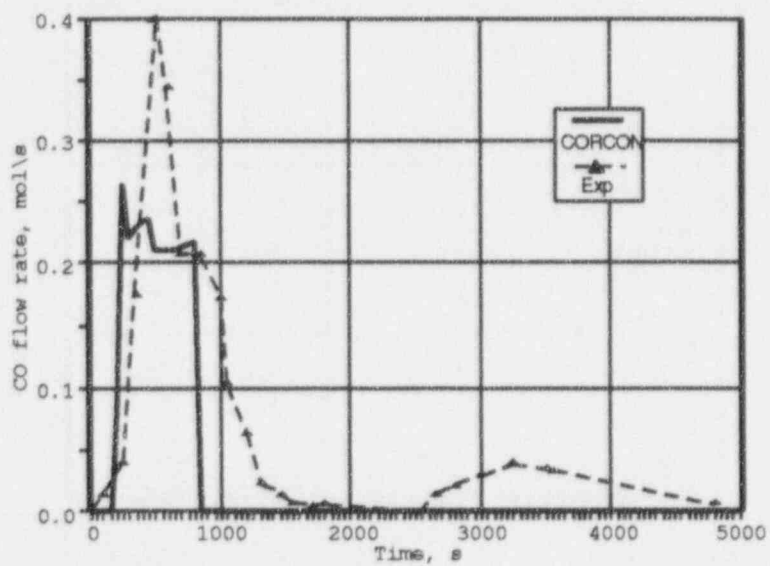


Figure 6.18: Comparison to *CO* flow rate for MACE-M1b test

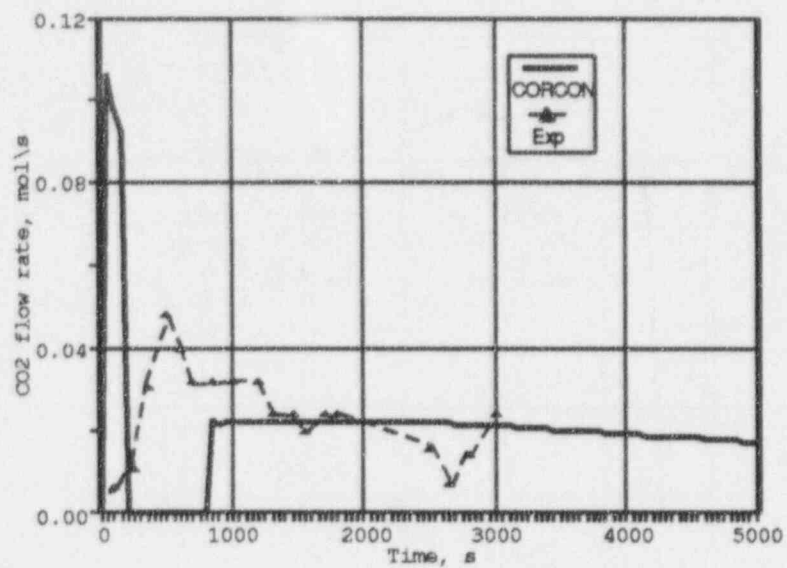


Figure 6.19: Comparison to  $CO_2$  flow rate for MACE-M1b test

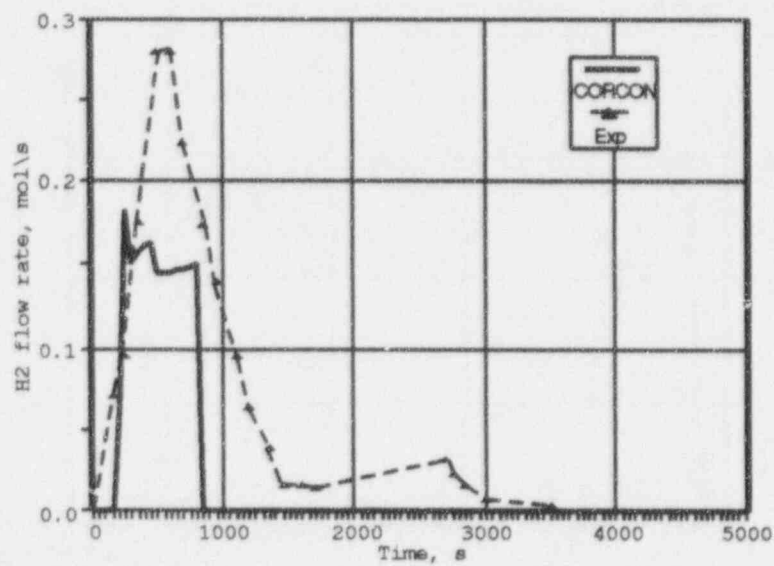


Figure 6.20: Comparison to  $H_2$  flow rate for MACE-M1b test

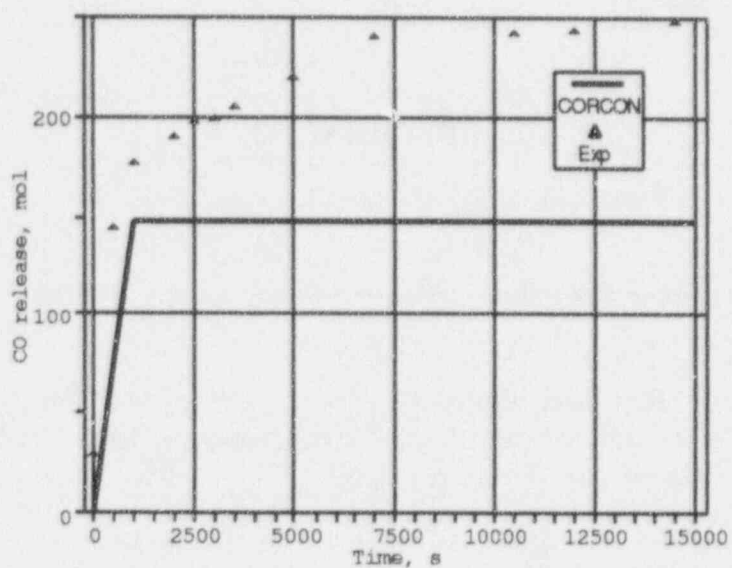


Figure 6.21: Comparison to total  $CO$  release for MACE-M1b test

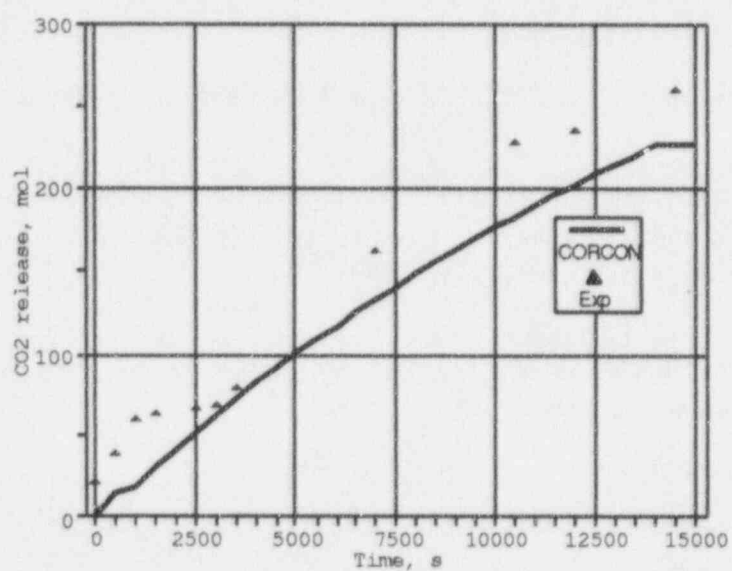


Figure 6.22: Comparison to total  $CO_2$  release for MACE-M1b test

## REFERENCES

- [1] U.S.Nuclear Regulatory Commission, Reactor Safety Study, NUREG-75-014, WASH-1400, 1975.
- [2] D.R.Gardner, and D.R.Bradley, CORCON-Mod3: An Integrated Computer Model for Analysis of Molten Core-Concrete Interactions, Users Manual, NUREG/CR-5843, SAND92-0167, Sandia National Laboratories, Albuquerque, NM, 87185, 1993.
- [3] J.F.Muir, et al., CORCON-Mod1: An Improved Model for Molten-Core/Concrete Interactions, NUREG/CR-2171, SAND80-2415, Sandia National Laboratories, Albuquerque, NM, 1981.
- [4] R.K.Cole, D.P.Kelly, and M.A.Ellis, CORCON-Mod2: A Computer Program for Analysis of Molten-Core Concrete Interactions, NUREG/CR-3920, SAND84-1246, Sandia National Laboratories, Albuquerque, NM, 1984.
- [5] D.A.Powers, J.E.Brockman, and A.W.Shiver, VANESA: A Mechanistic Model of Radionuclide Release and Aerosol Generation During Core Debris Interactions With Concrete, NUREG/CR-4308, SAND85-1370, Sandia National Laboratories, Albuquerque, NM, 1985.
- [6] J.A.Gieseke, et al., Source Term Code Package: A User's Guide, NUREG/CR-4587, BMI-2138, US NRC, 1986.
- [7] R.M.Summers, et al., MELCOR 1.8.0: A Computer Code for Nuclear Reactor Severe Accident Source Term and Risk Assessment Analyses, NUREG/CR-5531, SAND90-0364, Sandia National Laboratories, Albuquerque, NM, 1991.
- [8] K.K.Murata, et al., User's Manual for CONTAIN 1.1: A Computer Code for Severe Nuclear Reactor Accident Containment Analysis, NUREG/CR-5026, SAND87-2309, Sandia National Laboratories, Albuquerque, NM, 1989.
- [9] M.Reinmann, and S.Stiefel, The WECHSL-Mod2 Code: A Computer Program for the Interaction of a Core Melt with Concrete Including the Long Term Behaviour, KfK 4477, 1989.
- [10] M.G.Plys, and K.B.Gady, Modeling and Validation Progress with MAAP 4 DECOMP, Second OECD (NEA) CSNI Specialist Meeting on Molten Core Debris-Concrete Interactions, Karlsruhe, Germany, 1-3 April, 1992. pp.129-146.
- [11] R.V.Arutjunjan, et al., Computer Code RASPLAV for Molten Core Concrete Interaction, Institute of Nuclear Safety, Preprint N16, Moscow, 1991.

- [12] D.A.Powers, and F.E.Arellano, Large Scale Transient Tests on the Interaction of Molten Steel with Concrete, NUREG/CR-2282, SAND81-1753, Sandia National Laboratories, Albuquerque, NM, 1982.
- [13] J.E.Gronager, A.J.Suo-Anttila, and J.E.Brockmann, TURC2 and 3: Large Scale  $UO_2/ZrO_2/Zr$  Melt Concrete Interaction Experiments and Analysis, NUREG/CR-4521, Sandia National Laboratories, Albuquerque, NM, 1986.
- [14] G.A.Green, and R.A.Bari, International Standard Problem No.24, SURC-4 Experiment on Core Concrete Interaction, Brookhaven National Laboratory, 1988.
- [15] R.V.Arutjunjan, et al., Modeling of SURC-4 Experiment, Preprint N17, Institute of Nuclear Safety, Moscow, 1991.
- [16] M.Corradini, and H.H.Reineke, A Review of the BETA Experimental Results and Code Comparison Calculations, Nuclear Science and Engineering, 102 (1989) 260-282.
- [17] J.Ptacek, and M.Corradini, Post-Test Blind Benchmark Exercise L6 Experiment: Summary of Thermal-Hydraulics Results, ACE-TR-C28, 1991.
- [18] J.K.Fink, et al., Results of Aerosol Code Comparisons with Releases from ACE MCCI Tests, Second OECD (NEA) CSNI Specialist Meeting on Molten Core Debris-Concrete Interactions, Karlsruhe, Germany, 1-3 April, 1992, pp.533-546.
- [19] D.H.Thompson, et al., Thermal Hydraulic Aspects of the Large-scale Integral MCCI Test in the ACE Program, Second OECD (NEA) CSNI Specialist Meeting on Molten Core Debris-Concrete Interactions, Karlsruhe, Germany, 1-3 April, 1992.
- [20] M.F.Roche, L.Leibowitz, J.K.Fink, and L.Baker, Jr., Solidus and Liquidus Temperatures of Core-Concrete Mixtures, NUREG/CR-6032, ANL-93/9, June 1993.
- [21] P.Y.Chevalier, and G.Cenerino, Thermodynamic Data Bases and Calculation Code Adapted to the Modeling of Molten Core Concrete Interaction, Second OECD (NEA) CSNI Specialist Meeting on Molten Core Debris-Concrete Interactions, Karlsruhe, Germany, 1-3 April, 1992.
- [22] P.Y.Chevalier, Thermodynamical Calculation of Phase Equilibria in a Quinary Oxide System  $Al_2O_3 - CaO - SiO_2 - UO_2 - ZrO_2$ : Determination of Liquidus and Solidus Temperatures, Journal of Nuclear Materials, 186 (1992) 212-215.
- [23] Fisitscheckaya Chimia Silicatos (Physics and Chemistry of Silicates), (in Russian), Ed. by Paschenko A.A., Moscow, Vysshaya Shkola, 1986.
- [24] N.A.Toporov, et al., Diagrammy Sostoyaniya Silikatnyh Sistem (Phase Diagrams of Silicate Systems), Vol.1-4, Nauka, Leningrad, 1965-1972.
- [25] M.Peehs, A.Skokan, and M.Reimann, The Behaviour of Concrete in Contact with Molten Corium in the Case of a Hypothetical Core Melt Accident., Nuclear Technology, 46 (1979) 192-198.
- [26] P.Hofmann, S.Hagen, G.Schanz, and G.Skokan, Reactor Core Materials Interactions at Very High Temperatures, Nuclear Thechnology 87 (1989) 146-186.



- [27] R.G.J.Ball, and M.A.Mignanelli, The Calculations of Phase Equilibria of Oxide Core-Concrete Systems, Second OECD-CSNI Specialist Meeting on Molten Core Debris-Concrete Interactions, Karlsruhe, Germany, 1-3 April, 1992.
- [28] H.Alsmeier et al., BETA Experimental Results on Melt-Concrete Interactions:Silicate Concrete Behavior, OECD-CSNI Specialist Meeting on Core Debris-Concrete Interactions, Palo Alto, CA, September 1986.
- [29] J.K.Fink, D.H.Thompson, B.W.Spencer, and B.R.Sehgal. Aerosols Released During Large-Scale MCCI Tests in the ACE Program, Second OECD-CSNI Specialist Meeting on Molten Core Debris-Concrete Interactions, Karlsruhe, Germany, 1-3 April, 1992, 111-125.
- [30] B.R.Sehgal and B.W.Spencer, ACE Program Phase C: Fission Product Release From Molten Corium Concrete Interaction MCCI, Second OECD-CSNI Specialist Meeting on Molten Core Debris-Concrete Interactions, Karlsruhe, Germany, 1-3 April, 1992, 83-96.
- [31] E.R.Copus and D.A.Powers, The SURC Test Series, Second OECD-CSNI Specialist Meeting on Molten Core Debris-Concrete Interactions, Karlsruhe, Germany, 1-3 April, 1992, 51-66.
- [32] H.Alsmeier et al., BETA-Experiments on Zirconium Oxidation and Aerosol Release During Melt-Concrete Interaction. Second OECD-CSNI Specialist Meeting on Molten Core Debris-Concrete Interactions, Karlsruhe, Germany, 1-3 April, 1992, 67-82.
- [33] H.Alsmeier, Melt-Concrete Interaction during Severe Light Water Reactor Accidents, *Kern-technik*, 53 (1988) 30-37.
- [34] B.R.Spencer, et al., Results of MACE Tests M0 and M1, Second OECD-CSNI Specialist Meeting on Molten Core Debris-Concrete Interactions, Karlsruhe, Germany, 1-3 April, 1992, 357-374.
- [35] E.R.Copus, Core Concrete Interactions with Overlying Water Pool, Second OECD-CSNI Specialist Meeting on Molten Core Debris-Concrete Interactions, Karlsruhe, Germany, 1-3 April, 1992, 375-389.
- [36] D.R.Bradley, Development and Validation of CORCON-Mod3, Second OECD-CSNI Specialist Meeting on Molten Core Debris-Concrete Interactions, Karlsruhe, Germany, 1-3 April, 1992, 173-194.
- [37] D.H.Thompson, and J.K.Fink, ACE MCCI Test L5, Test Data Report. ACE-TR-C7, Argonne National Laboratory, 1988.
- [38] D.H.Thompson, and J.K.Fink, ACE MCCI Test L2, Test Data Report, Volume I: Thermal Hydraulics, ACE-TR-C10, Argonne National Laboratory, 1989.
- [39] J.K.Fink, and D.H.Thompson, ACE MCCI Test L2, Test Data Report, Volume II: Aerosol Analysis, ACE-TR-C10, Argonne National Laboratory, 1989.
- [40] D.H.Thompson, and J.K.Fink, ACE MCCI Test L6, Test Data Report, Volume I: Thermal Hydraulics, ACE-TR-C26, Argonne National Laboratory, 1991.
- [41] J.K.Fink, and D.H.Thompson, ACE MCCI Test L6, Test Data Report, Volume II: Aerosol Analysis, ACE-TR-C26, Argonne National Laboratory, 1991.

- [42] V.Strizhov, J.Ptacek, and M.Corradini. Energy Modelling of the ACE MCCI Experiment L6, Second OECD-CSNI Specialist Meeting on Molten Core Debris-Concrete Interactions, Karlsruhe, Germany, 1-3 April, 1992, 195-209.
- [43] D.H.Thompson, and J.K.Fink, ACE MCCI Test L7, Test Data Report, Volume I: Thermal Hydraulics, ACE-TR-C31, Argonne National Laboratory, 1991.
- [44] J.K.Fink, and D.H.Thompson, ACE MCCI Test L7, Test Data Report, Volume II: Aerosol Analysis, ACE-TR-C31, Argonne National Laboratory, 1991.
- [45] D.H.Thompson, and J.K.Fink, ACE MCCI Test L4, Test Data Report, Volume I: Thermal Hydraulics, ACE-TR-C32, Argonne National Laboratory, 1992.
- [46] J.K.Fink, and D.H.Thompson, ACE MCCI Test L4, Test Data Report, Volume II: Aerosol Analysis, ACE-TR-C32, Argonne National Laboratory, 1992.
- [47] D.H.Thompson, and J.K.Fink, ACE MCCI Test L8, Test Data Report, Volume I: Thermal Hydraulics, ACE-TR-C32, Argonne National Laboratory, 1992.
- [48] J.K.Fink, and D.H.Thompson, ACE MCCI Test L8, Test Data Report, Volume II: Aerosol Analysis, ACE-TR-C32, Argonne National Laboratory, 1991.
- [49] E.R.Copus, R.E.Blose, J.E.Brockmann, R.B.Simpson, and D.A.Lucero, Core-Concrete Interactions Using Molten Urania with Zirconium on a Limestone Concrete Basemat, The SURC-1 Experiment, NUREG/CR-5443, SAND90-0087, Sandia National Laboratories, Albuquerque, NM, 1992.
- [50] E.R.Copus, R.E.Blose, J.E.Brockmann, R.B.Simpson, and D.A.Lucero, Core-Concrete Interactions Using Molten  $UO_2$  with Zirconium on a Basaltic Basemat, The SURC-2 Experiment, NUREG/CR-5564, SAND90-1022, Sandia National Laboratories, Albuquerque, NM, 1992.
- [51] E.R.Copus, et.al., Experimental Results of Core-Concrete Interactions Using Molten Steel with Zirconium, NUREG/CR-4794, SAND86-2638, Sandia National Laboratories, Albuquerque, NM, 1990.
- [52] E.R.Copus, et.al., Core-Concrete Interactions Using Molten Steel with Zirconium on a Basaltic Basemat: The SURC-4 Experiment, NUREG/CR-4994, Sandia National Laboratories, Albuquerque, NM, 1989.
- [53] Yu.L.Zvonarev, G.N.Abyshev and E.V.Gibner, Large Scale Test V7.1 at BETA Facility to Study the Process of Melt Interaction with Serpentine Concrete, Part 1, Preliminary Results of the Test, Russian Research Center "Kurchatov Institute", Moscow, 1992 (In Russian).
- [54] R.E.Blose, J.E.Gronager, A.J.Suo-Antilla, and J.E.Brockman, SWISS: Sustained Heated Metallic Melt/Concrete Interaction with Overlying Water Pools, NUREG/CR-4727, SAND85-1546, 1987.
- [55] M.T.Farmer, B.W.Spencer, and D.R.Armstrong, MACE Test M1B, Data Report, ACE-TR-D6, Argonne National Laboratory, Argonne, IL, 1992.

## A INPUT DECKS

### ACE L2 Input Deck

L2 EXPERIMENT. CONCRETE SILICIOUS

```
\$ilyr icool igeom icon ichem ifp isur iabl isp ipin iflm first imov ipg
      0      0      2      0      01      2      1      0      0      10      11      0      0      -2      0      0
```

```
\$ ITR IFVAN IVANFP
```

```
& 0 1 2 0
```

```
\$ deltim      time0      timend      dprin      tprin
      5.0      0.      4000.      10000.
```

```
\$nray      r0      z0
      40      0.0      0.
```

```
\$      zt      rad      hit      radc      rw      hbb nbot ncorn
      0.0      28.      1.0      0.1      28.5      0.5 10 6
```

```
\$concrete
```

```
\$      tic      tdc      ew      rbr
      300.0      1553.      .6      0.0
```

```
\$ CONCRETE
```

```
\$ ninp
```

```
17
```

```
TIO2      0.008
NA2O      0.007
K2O      0.014
SI02      0.6962
CAO      0.135
FE2O3      0.01
AL2O3      0.04
MGO      0.007
CO2      0.022
MNO      0.0003
BAO      0.0002
SRO      0.0002
CR2O3      0.0002
H2OEVAP      0.017
H2OCHEM      0.020
ZRO2      0.0000
NIO      0.0000
```

```
\$      rho      Tsol      Tliq
```

	2420.	1413.	1653.						
--	-------	-------	-------	--	--	--	--	--	--

\ \$MELT  
 \ \$nosi nmesi Tox Tml  
     4      3      2420.      2420.  
 UO2          216.0e4  
 ZRO2         42.5e4  
 SIO2         20.9e4  
 \$MOO2         0.9e4  
 CAO          3.0e4  
 ZR           13.47e4  
 FE           1.41e4  
 NI           0.01e4  
 \ \$POWER  
 \ \$COOLANT  
 \ \$ATMOSPHERE  
 \ \$  
 \ \$      VA      PA      TA      ngas  
          5.0     1.E5     900.     1  
 N2          1.00  
 \ \$POWER FOR OXIDIC AND METALLIC PHASES (ONLY IF IFP=2)  
     2      0  
     0.0     4.0e8     3100.     4.e8  
 \ \$SURROUNDING TEMPERATURE HISTORY  
 \ \$ NTP  
     3  
    -2500.     1900.     600.     1900.     7500.     1900.  
 \ \$ABLATION  
 \ \$EMISSIVITIES  
 \ \$IREO IREM IRES  
 TIMETIMETIME  
 \ \$ NEO NEM N3  
     1      1      1  
       0.0      0.8  
       0.0      0.8  
       0.0      0.11  
 \ \$VANESA  
 \ \$IBUB KATIS INOPL IDEAL  
     1      1      0      1  
 \ \$IF IVANFP = 1  
 \ \$      CES      IOD      XEN      KRY      TE      BA      SN      RU  
       0.000     0.0000     0.00     0.0     0.1e4     0.43e4     0.10e4     0.0  
 \ \$      MO      SR      RB      Y      TC      RH      PD      LA  
       0.83e4     0.43e4     0.00     0.0     0.0     0.0     0.0     0.41e4  
 \ \$      CE      PR      ND      SM      PU      AG      SB      NB  
       1.05e4     0.0      0.0     0.0     0.0     0.00     0.0     0.0  
 \ \$

# ACE L4 Input Deck

## L4 EXPERIMENT SERPENTINE-ORDINARY STRUCTURAL

\$ Phase 1 - concrete/metal insert interaction

\$ilyr icool igeom icon ichem ifp isur iabl isp ipin iflm first imov ipg  
0 0 2 0 01 2 1 0 0 40 10 0 0 1 0 0

\$ ITR IFVAN IVANFP

& 0 1 2 0

\$ deltim time0 timend dprin tprin  
5.0 -3000. 13000. 10000.

\$nray r0 z0  
40 0.0 0.

\$ zt rad hit radc rw hbb nbot ncorn  
1.0 28.0 1.0 0.1 28.8 0.5 10 6

\$concrete

\$ tic tdc ew rbr  
300.0 1780. .4 -0.74

\$ CONCRETE

\$ ninp

17

TIO2 0.000  
NA2O 0.0006  
K2O 0.001  
SiO2 0.343  
CaO 0.098  
FE2O3 0.064  
AL2O3 0.018  
MGO 0.307  
CO2 0.021  
MNO 0.0013  
BAO 0.0001  
SRO 0.00013  
CR2O3 0.0019  
H2OEVAP 0.021  
H2OCHEM 0.113  
ZRO2 0.0000  
NIO 0.002

\$ rho Tsol Tliq  
2700. 1500. 1900.

\$ for RBR

4

ZR 0.983  
FE 0.013  
CR 0.003  
NI 0.001

\$MELT

\$nosi	nmesi	Tox	Tml
5	4	2250.	2250.

UO2 192.0e4

ZRO2 43.2e4

SiO2 16.89e4

CAO 0.0

MGO 7.2e4

\$BAO 1.42e4

\$SRO 0.96e4

ZR 0.528e4

FE 0.0

NI 0.0

CR 0.0

\$POWER

\$COOLANT

\$ATMOSPHERE

\$

\$	VA	PA	TA	ngas
	5000.0	1.E5	1000.	1

N2 1.00

\$POWER FOR OXIDIC AND METALLIC PHASES (ONLY IF IFP=2)

12 0

-3000.	5.E8	600.	5.0E8	1200.	5.0E8	3600.	5.0E8
--------	------	------	-------	-------	-------	-------	-------

3650.	0.0E8	3670.	5.0E8	5700.	5.0E8	5710.	0.0
-------	-------	-------	-------	-------	-------	-------	-----

\$	6000.	0.0	6010.	5.0E8	9790.	5.0E8	9800.	0.0E48
----	-------	-----	-------	-------	-------	-------	-------	--------

\$ Special for Ozrin

6000.	0.0	6010.	5.0E8	19790.	5.0E8	19800.	0.0E48
-------	-----	-------	-------	--------	-------	--------	--------

\$SURROUNDING TEMPERATURE HISTORY

\$ NTP

3

-3000.	1300.	600.	1300.	17800.	1300.
--------	-------	------	-------	--------	-------

\$ABLATION

\$EMISSIONITIES

\$IREO IREM IRES

TIMETIMETIME

\$ NEO NEM NS

1	1	1
---	---	---

0.0	0.8
-----	-----

0.0	0.8
-----	-----

0.0	0.6
-----	-----

\$VANESA

\$IBUB KATIS INOPL IDEAL

1	1	0	1
---	---	---	---

\$IF IVANFP = 1

\$	CES	IOD	XEN	KRY	TE	BA	SN	RU
	0.000	0.0000	0.00	0.0	0.120e4	1.28e4	0.00	0.0



\$	MO	SR	RB	Y	TC	RH	PD	LA
	1.50e4	0.81e4	0.00	0.0	0.0	0.0	0.0	0.95e4
\$	CE	PR	ND	SM	PU	AG	SB	NB
	1.90e4	0.0	0.0	0.0	0.0	0.00	0.0	0.0

\$  
\$ Serpentine concrete

\$ Depth  
0.08

\$	tic	tdc	ew	rbr
	300.0	1550.	.6	0.0

\$ CONCRETE

\$ ninp  
17

TI02	0.000
NA20	0.0006
K20	0.001
SI02	0.343
CA0	0.098
FE203	0.064
AL203	0.018
MGO	0.307
CO2	0.021
MNO	0.0013
BA0	0.0001
SR0	0.00013
CR203	0.0019
H20EVAP	0.021
H20CHEM	0.113
ZR02	0.0000
NIO	0.002

\$	rho	Tsol	Tliq
	2340.	1500.	1900.

\$ Ordinary concrete

\$ Depth  
0.13

\$	tic	tdc	ew	rbr
	300.0	1550.	.6	0.0

\$ CONCRETE

\$ ninp  
17

TI02	0.0015
NA20	0.027
K20	0.016
SI02	0.691
CA0	0.108
FE203	0.017

AL2O3	0.088
MGO	0.007
CO2	0.042
MNO	0.0005
BAO	0.001
SRO	0.00036
CR2O3	0.00006
H2OEVAP	0.02
H2OCHEM	0.042
ZRO2	0.00009
NIO	0.00004

\$	rho	Tsol	Tliq
	2340.	1430.	1930.

# ACE L5 Input Deck

L5 EXPERIMENT. CONCRETE L/S

\$ilyr icool igeom icon ichem ifp isur iabl isp ipin iflm irst imov ipg  
 2 0 2 0 00 2 1 0 0 20 00 0 0 -2 0 0

\$ ITR IFVAN IVANFP

& 0 1 1 0

\$ deltim time0 timend dprin tprin  
 10.0 0. 7200. 10000.

\$nray r0 z0  
 40 0.0 0.

\$ zt rad hit radc rw hbb nbot ncorn  
 1.0 28.08 1.0 0.3 29.0 0.5 10 6

\$concrete

\$ tic tdc ew rbr  
 300.0 1600. .6 0.0

\$ CONCRETE

\$ ninp  
 17

TI02 0.0004

NA20 0.0005

K20 0.0009

SI02 0.383

CA0 0.240

FE203 0.008

AL203 0.017

MGO 0.086

CO2 0.2033

MNO 0.0005

BA0 0.0003

SRO 0.0003

CR203 0.00009

H2OEVAP 0.041

H2OCHEM 0.02

ZRO2 0.000

NIO 0.00000

\$ rho Tsol Tliq  
 2300. 1420. 1760.

\$ 2340. 1500. 1900.

\$MELT

\$nosi nmesi Tox Tml  
 7 0 2200. 2200.

UO2 184.2e4

ZRO2 34.0e4

FEO 49.1e4

NIO 5.2e4

CR203 13.4e4  
 BAO 0.00  
 SRO 0.00  
 \$MN 0.0056e4

\$POWER

\$COOLANT

\$ATMOSPHERE

\$

\$ VA PA TA ngas  
 5.0 1.E5 900. 1

N2 1.00

\$POWER FOR OXIDIC AND METALLIC PHASES (ONLY IF IFP=2)

3 0

0. 4.0e8 900. 6.0e8 9000. 6.0E8

\$SURROUNDING TEMPERATURE HISTORY

\$ NTP

3

0. 1850. 2400. 1650. 9000. 1650.

\$ ABLATION

\$ 6 0

\$FE

\$SI

\$MN

\$C

\$NI

\$CR

\$ time and flow rate

\$ 4 4 4 4 4 4

\$ 2690. 0. 2700. 138. 2800. 138. 2810. 0.0

\$ 2690. 0. 2700. 0.2 2800. 0.2 2810. 0.0

\$ 2690. 0. 2700. 0. 2800. 0.5 2810. 0.0

\$ 2690. 0. 2700. 0.6 2800. 0.6 2810. 0.0

\$ 2690. 0. 2700. 0.056 2800. 0.056 2810. 0.0

\$ 2690. 0. 2700. 0.056 2800. 0.05 2810. 0.0

\$ 0 2 0

\$ 0. 1600. 7200. 1600.

\$EMISSIONS

\$IREO IREM IRES

TIMETIMETIME

\$ NEO NEM NS

1 1 1

0.0 0.8

0.0 0.8

0.0 0.4

\$VANESA

\$IBUB KATIS INOPL IDEAL

	1	1	0	1					
\$	CES	IOD	XEN	KRY	TE	BA	SN	RU	
	0.000	0.0000	0.00	0.0	0.000	0.36e4	0.000	0.00	
\$	MO	SR	RB	Y	TC	RH	PD	LA	
	0.000	0.34e4	0.00	0.0	0.0	0.0	0.0	0.34e4	
\$	CE	PR	ND	SM	PU	AG	SB	NB	
	0.85e4	0.0	0.0	0.0	0.0	0.00	0.0	0.0	

# ACE L6 Input Deck

L6 EXPERIMENT S/C

\\$ Phase 1 - concrete/metal insert interaction

\\$ilyr icool igeom icon ichem ifp isur iabl isp ipin iflm irst imov ipg  
0 0 2 0 01 2 1 0 0 20 10 0 0 -2 0 0

\\$ ITR IFVAN IVANFP

& 0 1 2 0

\\$ deltim time0 timend dprin tprin  
10.0 800. 10000. 20000.

\\$nray r0 z0  
40 0.0 0.

\\$ zt rad hit radc rw hbb nbot ncorn  
1.0 28.0 1.0 0.01 28.8 0.5 10 6

\\$concrete

\\$ tic tdc ew rbr  
300.0 1745. .4 -0.6

\\$ CONCRETE

\\$ ninp

17

TIO2 0.008  
NA2O 0.007  
K2O 0.014  
SIO2 0.6962  
CAO 0.135  
FE2O3 0.01  
AL2O3 0.04  
MGO 0.007  
CO2 0.022  
MNO 0.0003  
BAO 0.0002  
SRO 0.0002  
CR2O3 0.0002  
H2OEVAP 0.017  
H2OCHEM 0.02  
ZRO2 0.0000  
NIO 0.0000

\\$ rho Tsol Tliq  
3100. 1500. 1900.

\\$ for rbr

4

ZR 0.687  
FE 0.19  
CR 0.059  
NI 0.028

\\$MELT



\\$nosi	nmesi	Tox	Tml
6	4	2525.	2525.

UO2	219.0e4
ZRO2	18.51e4
SIO2	16.89e4
CAO	7.20e4
\\$MGO	1.70e4
BAO	0.79e4
SRO	0.53e4
\\$LA2O3	0.63e4
\\$CEO2	1.28e4
ZR	1.50e4
FE	0.0
NI	0.0
CR	0.0

\\$POWER  
 \\$COOLANT  
 \\$ATMOSPHERE  
 \\$

\\$	VA	PA	TA	ngas
	5.0	1.E5	900.	1
N2		1.00		

\\$POWER FOR OXIDIC AND METALLIC PHASES (ONLY IF IFP=2)

20	0							
	0.	6.0e8	100.	5.0E8	300.	0.0E8	500.	6.5E8
	600.	4.2E8	700.	7.0E8	900.	0.0	1000.	6.0E8
	1500.	6.0E8	1800.	5.0E8	2200.	5.0E8	2400.	7.0E8
	3000.	7.0E8	3200.	0.0	3400.	0.0E8	3500.	7.0E8
	3600.	6.5E8	3700.	7.5E8	14800.	7.5E8	14900.	0.0E8

\\$SURROUNDING TEMPERATURE HISTORY

\\$ NTP

3						
	0.	1300.	900.	1300.	17500.	1300.

\\$EMISSIONITIES

\\$IREO IREM IRES

TIMETIMETIME

\\$ NEO NEM NS

1	1	1
	0.0	0.8
	0.0	0.8
	0.0	0.6

\\$VANESA

\\$IBUB KATIS INOPL IDEAL

1	1	0	1
---	---	---	---

\\$IF IVANFP = 1

\\$	CES	IOD	XEN	KRY	TE	BA	SN	RU
-----	-----	-----	-----	-----	----	----	----	----

	0.000	0.0000	0.00	0.0	0.14e4	0.e4	0.03e4	0.38e4
\\$	MO	SR	RB	Y	TC	RH	PD	LA
	0.94e4	0.53e4	0.00	0.0	0.0	0.0	0.0	0.63e4
\\$	CE	PR	ND	SM	PU	AG	SB	NB
	1.28e4	0.0	0.0	0.0	0.0	1.19e4	0.0	0.0
\\$ concrete								
\\$ Depth								
	0.07							
\\$	tic	tdc	ew	rbr				
	300.0	1653.	.6	0.0				
\\$ CONCRETE								
\\$ ninp								
	17							
TI02	0.008							
NA20	0.007							
K20	0.014							
SI02	0.6962							
CA0	0.135							
FE203	0.01							
AL203	0.04							
MGO	0.007							
CO2	0.022							
MNO	0.0003							
BA0	0.0002							
SRO	0.0002							
CR203	0.0002							
H2OEVAP	0.017							
H2OCHEM	0.02							
ZRO2	0.0000							
NIO	0.0000							
\\$	rho	Tsol	Tliq					
	2340.	1500.	1900.					

# ACE L7 Input Deck

## L7 EXPERIMENT

\\$ Phase 1 - concrete/metal insert interaction

\\$ilyr icool igeom icon ichem ifp isur iabl isp ipin iflm irst imov ipg  
0 0 2 0 01 2 1 0 0 10 10 0 0 -2 0 0

\\$ ITR IFVAN IVANFP

& 0 1 2 0

\\$ deltim time0 timend dprin tprin

\\$ 10.0 -1800. -1750. 10000.

10.0 -1800. 3200. 10000.

\\$nray r0 z0

40 0.0 0.

\\$ zt rad hit radc rw hbb nbot ncorn

0.0 28.2 1.0 0.10 29.02 0.5 10 6

\\$concrete

\\$ tic tdc ew rbr

300.0 1745. .4 -0.5

\\$ CONCRETE

\\$ ninp

17

TIO2 0.0014

NA2O 0.011

K2O 0.006

SIO2 0.283

CAO 0.2745

FE2O3 0.016

AL2O3 0.035

MGO 0.096

CO2 0.214

MNO 0.0005

BAO 0.0003

SRO 0.0003

CR2O3 0.00009

H2OEVAP 0.041

H2OCHEM 0.02

ZRO2 0.0002

NIO 0.0000

\\$ rho Tsol Tliq

2800. 1420. 1760.

\\$ for rbr

2

ZR 0.97

FE 0.03

\\$MELT

\\$nosi nmesi Tox Tml

```

5      4      2500.      2500.
UO2      188.5e4
ZRO2      59.4e4
SIO2      12.5e4
CAO      11.5e4
MGO      1.7e4
\BBAO      0.8e4
\BSRO      0.5e4
ZR      1.13e4
FE      0.07e4
NI      0.0
CR      0.1e4
\POWER
\COOLANT
\ATMOSPHERE
\$
\$      VA      PA      TA      ngas
      5.0      1.E5      900.      1
N2      1.00
\POWER FOR OXIDIC AND METALLIC PHASES (ONLY IF IFP=2)
4      0
-1800.      5.0E8      2350.      5.0E8      2400.      0.0      7500.      0.0
\SURROUNDING TEMPERATURE HISTORY
\$ NTP
3
-1800.      1600.      -200.      1600.      7500.      1600.
\$ABLATION
\$ 11
\$UO2
\$ZRO2
\$FEO
\$FPOX
\$FPALMET
\$FPHALOGN
\$FE
\$CR
\$NI
\$ZR
\$FPM
\$ 2      2      2      2      2      2      2      2      2      2
\$      7575.      4.920      29176.      0.
\$      7575.      1.018      29176.      0.
\$      7575.      .0926      29176.      0.
\$      7575.      .04568      29176.      0.
\$      7575.      .001184      29176.      0.
\$      7575.      .000048      29176.      0.

```

\\$	7575.	0.926	29176.	0.
\\$	7575.	.3426	29176.	0.
\\$	7575.	.1902	29176.	0.
\\$	7575.	1.267	29176.	0.
\\$	7575.	.01239	29176.	0.

\\$ 2 2

\\$	7575.	2000.	80000.	2000.
\\$	7575.	2000.	80000.	2000.

\\$SEMISSIVITIES

\\$IREO IREM IRES

TIMETIMETIME

\\$ NEO NEM NS IDEAL

1	1	1	1
	0.0		0.8
	0.0		0.8
	0.0		0.6

\\$VANESA

\\$IBUB KATIS INOPL IDEAL

1	1	0	1
---	---	---	---

\\$IF IVANFP = 1

\\$	CES	IOD	XEN	KRY	TE	BA	SN	RU
	0.000	0.0000	0.00	0.0	0.180e4	1.26e4	.016e4	0.0
\\$	MO	SR	RB	Y	TC	RH	PD	LA
	1.50e4	0.77e4	0.00	0.0	0.0	0.0	0.0	0.95e4
\\$	CE	PR	ND	SM	PU	AG	SB	NB
	1.86e4	0.0	0.0	0.0	0.0	0.00e4	0.0e4	0.0e4

\\$

\\$ Concrete

\\$ Depth

0.057

\\$	tic	tdc	ew	rbr
	300.0	1700.	.6	0.0

\\$ CONCRETE

\\$ ninp

17

TI02	0.0014
NA20	0.011
K20	0.006
SI02	0.283
CA0	0.2745
FE203	0.016
AL203	0.035
MGO	0.096
CO2	0.214
MNO	0.0005
BA0	0.0003

SR0	0.0003
CR203	0.00009
H20EVAP	0.041
H20CHEM	0.02
ZR02	0.0002
NIO	0.0000

\\$	rho	Tsol	Tliq
	2340.	1420.	1760.



# ACE L8 Input Deck

## L8 EXPERIMENT

\\$ Phase 1 - concrete/metal insert interaction

\\$ilyr icool igeom icon ichem ifp isur iabl isp ipin iflm first imov ipg  
0 0 2 0 01 2 1 0 0 50 10 0 0 0 0 0

\\$ITR IFVAN IVANFP IUSER

& 0 1 1 0

\\$ deltim time0 timend dprin tprin

\\$ 10.0 0. 620. 1000. 10000.

5.0 -600. 4200. 10000.

\\$nray r0 z0

60 0.0 0.

\\$ zt rad hit radc rw hbb nbot ncorn

0.0 28. 1.0 0.1 38.2 0.50 10 6

\\$concrete

\\$ tic tdc ew rbr

300.0 1745. .4 -0.44

\\$ CONCRETE

\\$ nimp

15

TIO2 0.001

NA2O 0.0003

K2O 0.004

SIO2 0.071

CAO 0.459

FE2O3 0.008

AL2O3 0.019

MGO 0.074

CO2 0.333

MNO 0.00017

BAO 0.00007

SRO 0.0003

CR2O3 0.00006

H2OEVAP 0.0374

H2OCHEM 0.0236

\\$ rho Tsol Tliq

2800. 1495. 2400.

\\$ for rb

1

ZR 1.0

\\$MELT

\\$nosi nmesi Tox Tml

6 1 2431. 1666.

UO2 211.5e4

ZRO2 41.6e4

```

SI02      3.4e4
CAO       20.6e4
FEO       1.74e3
AL2O3     1.73e3
ZR        1.1e4
\ZR       2.61e4
\FE       0.60e4
\BAO      0.8e4
\SSRO     0.5e4
\ZR       2.13e4
\FE       0.7e4
\NI       0.5e4
\SCR      0.1e4
\POWER
\COOLANT
\ATMOSPHERE
\$
\$      VA      PA      TA      ngas
      5.0      1.E5      900.      1
N2      1.00
\POWER FOR OXIDIC AND METALLIC PHASES (ONLY IF IFP=2)
      5      0
      -900.      7.5e8      300.      7.5E8      390.      3.5E8      6100.      3.5E8
      7500.      3.5E8
\SSURROUNDING TEMPERATURE HISTORY
\$ NTP
      3
      -900.      1650.      00.      1650.      7500.      1650.
\ABLATION
\$ 11
\UD2
\ZRO2
\FEO
\FPOX
\FPALKMET
\FPHALOGN
\FE
\SCR
\NI
\ZR
\FPM
\$ 2 2 2 2 2 2 2 2 2 2
\$ 7575. 4.920 29176. 0.
\$ 7575. 1.018 29176. 0.
\$ 7575. .0926 29176. 0.
\$ 7575. .04568 29176. 0.

```

\\$	7575.	.001184	29176.	0.
\\$	7575.	.000048	29176.	0.
\\$	7575.	0.926	29176.	0.
\\$	7575.	.3426	29176.	0.
\\$	7575.	.1902	29176.	0.
\\$	7575.	1.267	29176.	0.
\\$	7575.	.01239	29176.	0.

\\$ 2 2

\\$	7575.	2000.	80000.	2000.
\\$	7575.	2000.	80000.	2000.

\\$MISSIVITIES

\\$IREO IREM IRES

TIMETIMETIME

\\$ NEO NEM NS

1	1	1
0.0		0.8
0.0		0.8
0.0		0.6

\\$VANESA

\\$IBUB KATIS INOPL IDEAL

1	1	0	1
---	---	---	---

\\$IF IVANFP = 1

\\$	CES	IOD	XEN	KRY	TE	BA	SN	RU
	0.00000	0.0000	0.0	0.0	0.147e4	1.37e4	0.016e4	0.0
\\$	MO	SR	RB	Y	TC	RH	PD	LA
	1.84e4	0.87e4	0.0	0.0	0.0	0.0	0.0	1.1e4
\\$	CE	PR	ND	SM	PU	AG	SB	NB
	2.05e4	0.0	0.0	0.0	0.0	1.41e4	0.0	0.0

\\$

\\$ Depth

.043

\\$ Phase 2 - main concrete interaction

\\$	tic	tdc	ew	rbr
	300.0	1500.	.6	0.0

\\$ CONCRETE

\\$ ninp

15

TI02	0.001
NA20	0.0003
K20	0.004
SI02	0.071
CA0	0.459
FE203	0.008
AL203	0.019
MGO	0.074
CO2	0.333

MNO	0.00017		
BAO	0.00007		
SRO	0.0003		
CR203	0.00006		
H2OEVAP	0.0374		
H2OCHEM	0.0236		
\\$ rho	Tsol	Tliq	
2400.	1495.	2400.	
\\$ for rb			
\\$ 1			
\\$ZR	1.0		

# SURC-1 Input Deck

```

SURC1 met ZR 16.7 kg LIMESTONE concrete
\$ 55 kW of side loss power is assumed
\$ilyr icool igeom icon ichem ifp isur iabl isp ipin iflm irst imov ipg israb
    3    0    2    3    00    2    1    0    0    60    10    0    0    -2    0    0
\$ ITR IFVAN IVANFP IUSER
& 0 1 1 0
\$ deltim      time0      timend      dprin      tprin
\$    10.      9000.      17400.      20000.
    10.      8400.      16800.      19001.
\$
    17400.
\$nray      r0      z0
    47      0.0      0.
\$      zt      rad      hit      radc      rw      hbb nbot ncorn
    0.0      20.0      0.6      0.4      20.4      0.6 10 07
\$      tic      tdc      ew      rbr
    300.0      1600.      .6      0.0
\$ CONCRETE
\$MELT
\$nosi nmesi Tox Tml
    3    2    2600.    2600.
ZR02      45.98e4
UO2      138.32e4
SiO2      13.e4
FE      0.1e4
ZR      18.41e4
\$POWER
\$COOLANT
\$ATMOSPHERE
\$
\$      VA      PA      TA      ngas
    0.5      0.8E5      1100.      1
N2      1.00
\$POWER FOR OXIDIC AND METALLIC PHASES (ONLY IF IFP=2)
    6    0
    0.      0.5E8      13150.      0.5E8      13200.      3.5E8      17400.      3.5E8
    17405.      0.0      18000.      0.0
\$SURROUNDING TEMPERATURE HISTORY
\$ NTP
    3
    0.      2300.      600.      2300.      18000.      2300.
\$ABLATION
\$EMISSIONS
\$IREO IREM IRES
TIMETIMETIME

```

```

\$ NEO NEM NS
  1 1 3
    0.0 0.8
    0.0 0.8
    0.0 0.01 11000. 0.01 11200. 0.01 18000. 0.01
\$VANESA
\$IBUB KATIS INOPL IDEAL
  1 1 0 1
\$IF IVANFP = 1
\$ CES IOD XEN KRY TE BA SN RU
  0.000 0.0000 0.00 0.0 0.000 0.51e4 0.0 0.
\$ MO SR RB Y TC RH PD LA
  0.32e4 0.00 0.00 0.0 0.0 0.0 0.0 0.64e4
\$ CE PR ND SM PU AG SB NB
  0.61e4 0.0 0.0 0.0 0.0 0.00 0.0 0.74e4
\$
$POOL SCRUBBING PARAMETERS
  20 2.3 1 1 1.0 1.0

```



# SURC-2 Input Deck

```

SURC2 met ZR 18.7 kg BASALTIC concrete from programm standart
\$ilyr icool igeom icon ichem ifp isur iabl isp ipin iflm first imov ipg israb
  3 0 2 1 01 2 1 0 0 10 00 0 0 0 0 0
\$ ITR IFVAN IVANFP IUSER
& 0 1 1 0
\$ deltim time0 timend dprin tprin
  10. 7800. 16200. 19000.
\$ 16200.
\$nray r0 z0
  47 0.0 0.
\$ zt rad hit radc rw hbb nbot ncorn
  1.0 20. 1.0 0.4 0.4 4. 10 07
\$ tic tdc ew rbr
  300.0 1553. .6 0.0
\$ CONCRETE
\$ ninp
\$ 13
\$NA2O 0.015
\$SIO2 0.63
\$CAO 0.14
\$FE2O3 0.047
\$AL2O3 0.075
\$MGO 0.04
\$CO2 0.11
\$MNO 0.000
\$BAO 0.000
\$TIO2 0.011
\$CR2O3 0.0003
\$H2OEVAP 0.042
\$H2OCHEM 0.04
\$ rho Tsol Tliq
\$ 2340. 1353. 1650.
\$MELT
\$nosi nmesi Tox Tml
  4 3 2600. 2600.
ZRO2 45.25e4
UO2 138.58e4
SIO2 0.0e4
CAO 9.3e4
FE 0.1e4
NI 0.0
\$SCR 37.
\$FE 158.
\$ZR 18.7e4

```

```

ZR          15.7e4
\ $MN      0.025
\ $POWER
\ $COOLANT
\ $ATMOSPHERE
\ $
\ $      VA      PA      TA      ngas
        0.5      0.8E5    1100.    1
N2          1.00
\ $POWER FOR OXIDIC AND METALLIC PHASES (ONLY IF IFP=2)
  5      0
        0.      0.5E8    13200.    0.5E8    13250.    5.0E8    18000.    5.0E8
        18100.    0.0
\ $SURROUNDING TEMPERATURE HISTORY
\ $ NTP
  3
        0.      2300.    600.      2300.    18000.    2300.
\ $ABLATION
\ $EMISSIVITIES
\ $IREO IREM IRES
TIMETIMETIME
\ $ NEC  NEM  NS
    1    1    2
        0.0      0.8
        0.0      0.8
        0.0      0.01  18000.    0.01
\ $VANESA
\ $IBUB KATIS INOPL IDEAL
    1    1    0    1
\ $IF IVANFP = 1
\ $      CES      IOD      XEN      KRY      TE      BA      SN      KU
        0.000    0.0000    0.00      0.0      0.000    0.50e4    0.0      0.
\ $      MO      SR      RB      Y      TC      RH      PD      LA
        0.32e4    0.00      0.00      0.0      0.0      0.0      0.0      0.75e4
\ $      CE      PR      ND      SM      PU      AG      SB      NB
        0.75e4    0.0      0.0      0.0      0.0      0.00    0.0      0.86e4
\ $
\ $POOL SCRUBBING PARAMETERS
        20      2.3      1      1      1.0      1.0

```

# SURC-3 Input Deck

```

SURC3 met ZR 5.0 kg, standard LIMESTONE concrete
\$ 23 kW of sidewall power loss is assumed
\$ilyr icool igeom icon ichem ifp isur iabl isp ipin iflm irst imov ipg israb
  0 0 2 3 01 2 1 1 0 5 11 0 0 0 1 0
\$ ITR IFVAN IVANFP IUSER
& 0 1 1 0
\$ deltim time0 timend dprin tprin
  10. 5400. 14000. 100000.
\$nray r0 z0
  47 0.0 0.
\$ zt rad hit radc rw hbb nbot ncorn
  1.0 10.8 0.5 0.1 11.2 0.42 10 7
\$ tic tdc ew rbr
  300.0 1700. .6 0.0
\$ CONCRETE
\$MELT
\$nosi nmesi Tox Tml
  1 3 2100. 2100.
ZR02 0.5e4
FE 31.5e4
NI 4.5e4
CR 9.0e4
\$ATMOSPHERE
\$
\$ VA PA TA ngas
  0.5 0.8E5 1100. 1
N2 1.00
\$POWER FOR OXIDIC AND METALLIC PHASES (ONLY IF IFP=2)
  0 4
  5400. 0.0E3 5700. 0.0E8 5750. 1.2e8 14400. 1.2e8
\$SURROUNDING TEMPERATURE HISTORY
\$ NTP
  3
  0. 1400. 600. 1400. 15000. 1400.
\$ABLATION
  1 0
ZR
  10
  0.0 0.0 7979.0 0.00 7980.0 0.083e4 8030.0 0.083e4
  8031.0 0.0 10619.0 0.00 10620.0 0.083e4 10670.0 0.083e4
  10671.0 0.0 15000.0 0.0
  0 2 0
  0.0 1700. 15000. 1700.
\$EMISSIONS

```

\\$IREO IREM IRES

TIMETIMETIME

\\$ NEO NEM NS

\\$ 1 1 5

1 1 1

0.0 0.8

0.0 0.8

0.0 0.6

\\$ 0.0 0.6 6900. 0.6 6902. 0.01 8000. 0.01

\\$ 8025. 0.6

\\$VANESA

\\$IBUB KATIS INOPL IDEAL

1 1 0 1

\\$IF IVANFP = 1

\\$ CES IOD XEN KRY TE BA SN RU

0.000 0.0000 0.00 0.0 0.5e4 0.45e4 0.0 0.

\\$ MO SR RB Y TC RH PD LA

0.5e4 0.00 0.00 0.0 0.0 0.0 0.0 0.43e4

\\$ CE PR ND SM PU AG SB NB

0.41e4 0.0 0.0 0.0 0.0 0.00 0.04 0.35e4

\\$

\\$POOL SCRUBBING PARAMETERS

20 2.3 1 1 1.0 1.0

# SURC-3A Input Deck

SURC3A met ZR 5.0 kg LIMESTONE concrete from programm standart 2-D

\\$ilyr icool igeom icon ichem ifp isur iabl isp ipin iflm irst imov ipg israb  
 0 0 2 3 01 2 1 1 0 00 01 0 0 0 1 0

\\$ ITR IFVAN IVANFP IUSER

& 0 0 1 0

\\$ deltim time0 timend dprin tprin  
 \\$ 05. 1800.0 6100. 10000.

-5. 1800. 6100. 10000.

1. 30. 1900.

10. 30. 2800.

1. 30. 3100.

20. 30. 6100.

-4.

100. 1900.

100. 2800.

100. 3100.

100. 6100.

-4.

\\$nray r0 z0  
 47 0.0 0.

\\$ zt rad hit radc rw hbb nbot ncorn  
 1.0 0.1 2.5 0.04 0.4 4. 7 05

\\$ tic tdc ew rbr  
 300.0 1650. .6 0.0

\\$ CONCRETE

\\$ ninp

\\$ 13

\\$NA20 0.015

\\$SIO2 0.63

\\$CAO 0.14

\\$FE203 0.047

\\$AL203 0.075

\\$MGO 0.04

\\$CO2 0.11

\\$MNO 0.000

\\$BAO 0.000

\\$TIO2 0.011

\\$CR203 0.0003

\\$H2OEVAP 0.042

\\$H2OCHEM 0.04

\\$ rho Tsol Tliq  
 \\$ 2340. 1635. 1873.

\\$MELT

\\$nosi nmesi Tox Tml

```

1      3      2150.  2150.
\ $ZRO2      45.98
\ $UO2      138.32
SI02      .100
FE      28.0
NI      4.0
CR      08.0
\ $FE      158.
\ $ZR      16.41
\ $MN      0.025
\ $POWER
\ $COOLANT
\ $ATMOSPHERE
\ $
\ $      VA      PA      TA      ngas
      0.5      0.8E5      1100.      1
N2      1.00
\ $POWER FOR OXIDIC AND METALLIC PHASES (ONLY IF IFP=2)
0      6
      0.      1.1E5      4500.      1.1E5      4600.      7.7E4      9300.      7.7E4
      9400.      0.0      15000.      0.0
\ $SURROUNDING TEMPERATURE HISTORY
\ $ NTP
3
      0.      1600.      600.      1600.      15000.      1600.
\ $ABLATION
1      0
ZR
6
0.0      0.0      2810.      0.00      2820.      0.095      2840.      0.095
2841.      0.0      15000.      0.0
0      2      0
0.0      1600.      15000.      1600.
\ $EMISSIVITIES
\ $IREO IREM IRES
TIMETIMETIME
\ $ NEO NEM NS
\ $ 1 1 5
1 1 1
0.0 0.8
0.0 0.8
0.0 0.6
\ $ 0.0 0.6 6900. 0.6 6902. 0.01 8000. 0.01
\ $ 8025. 0.6
\ $VANESA
\ $IBUB KATIS INOPL

```



```

      1   1   0
\ $IF IVANFP = 1
\ $      CES      IOD      XEN      KRY      TE      BA      SN      RU
      0.000  0.0000  0.00  0.0  0.000  0.50  0.0  0.
\ $      MO      SR      RB      Y      TC      RH      PD      LA
      0.50  0.00  0.00  0.0  0.0  0.0  0.0  0.50
\ $      CE      PR      ND      SM      PU      AG      SB      NB
      0.50  0.0  0.0  0.0  0.0  0.00  0.0  0.50
\ $
\ $POOL SCRUBBING PARAMETERS
      20      2.3      1      1      1.0      1.0

```

# SURC-4 Input Deck

```

SURC4 met ZR 20 kg ss-304 BASALTIC EXPERIMENT beta
\$ilyr icool igeom icon ichem ifp isur iabl isp ipin iflm irst imov ipg israb iaopac
  1 0 2 1 01 2 1 1 0 10 00 0 0 0 1 0
\$ ITR IFVAN IVANFP IUSER
& 0 1 1 0
\$ deltim time0 timend dprin tprin
  5. 6300. 9600. 10000.
\$nray r0 z0
  47 0.0 0.
\$ zt rad hit radc rw hbb nbot ncorn
  1.0 20.0 0.6 0.3 40. 4. 17 03
\$ tic tdc ew rbr
  300.0 1650. .6 0.0
\$ CONCRETE
\$ ninp
\$ 13
\$NA2O 0.0185
\$SiO2 0.552
\$CAO 0.088
\$FE2O3 0.063
\$AL2O3 0.083
\$MGO 0.062
\$CO2 0.025
\$MNO 0.000
\$BAO 0.000
\$TiO2 0.011
\$CR2O3 0.000
\$H2OEVAP 0.022
\$H2OCHEM 0.02
\$ rho Tsol Tliq
\$ 2340. 1353. 1650.
\$MELT
\$nosi nmesi Tox Tml
  0 3 1780. 1780.
\$ZRO2 0.00
\$SiO2 0.05
FE 142.4e4
NI 16.5e4
\$CR 37.
\$FE 158.
CR 37.0e4
\$MN 0.025
\$POWER
\$COOLANT

```

```

\ $ATMOSPHERE
\ $
\ $      VA      PA      TA      ngas
      0.5      0.8E5      1100.      1
N2      1.00
\ $POWER FOR OXIDIC AND METALLIC PHASES (ONLY IF IFP=2)
      00      13
      6000.      4.2E8      7449.      4.2E8      7450.      0.      7902.      0.
      7908.      4.2E8      8660.      4.2E8      8650.      4.2E8      8756.      4.2E8
      8762.      4.2E8      9750.      4.2E8      9755.      0.      9800.      0.e4
      15000.      0.E4
\ $SURROUNDING TEMPERATURE HISTORY
\ $ NTP
      3
      0.      1700.      600.      1700.      15000.      1700.
\ $ABLATION
      1      0
ZR
      8
      6300.      0.0      6900.      0.0      6901.      .000      7140.      0.0
      7141.      0.2e4      7240.      0.2e4      7241.      .0      15000.      0.0
      0      2      0
      0.0      1900.      15000.      1900.
\ $EMISSIONS
\ $IREO IREM IRES
TIMETIMETIME
\ $ NEO NEM NS
      1      1      5
\ $      1      1      1
      0.0      0.8
      0.0      0.3
\ $      0.0      0.6
      0.0      0.01      7100.      0.01      7101.      0.01      7500.      0.01
      9999.      0.01
\ $VANESA
\ $IBUB KATIS INOPL IDEAL
      1      1      0      1
\ $IF IVANFP = 1
\ $      CES      IOD      XEN      KRY      TE      BA      SN      RU
      1.000      1.0000      0.00      0.0      0.5e4      1.1e4      0.0      0.
\ $      MO      SR      RB      Y      TC      RH      PD      LA
      2.00e4      0.00      0.00      0.0      0.0      0.0      0.0      1.17e4
\ $      CE      PR      ND      SM      PU      AG      SB      NB
      1.23e4      0.0      0.0      0.0      0.0      0.00      0.0      0.0
\ $
\ $POOL SCRUBBING PARAMETERS

```

20

2.3

1

1

1.0

1.0

# SWISS-1 Input Deck

```

swiss 1 met coolant 46kg ss-304 l/c sand EXPERIMENT
\ $ilyr icool igeom icon ichem ifp isur iabl isp ipin iflm irst imov ipg
    0    0    2    0    01    2    1    1    0    15    1    0    1    1    1    0
\ $ ITR IFVAN IVANFP IUSER
& 0 0 1 0
\ $ deltim      time0      timend      dprin      tprin
    8.          0.        3000.          10000.
\ $ nray        r0        z0
    40         0.0       0.
\ $          zt      rad      hit      radc      rw      hbb nbot ncorn
    1.0      0.108    2.9854    0.05     0.406     0.5  10   6
\ $          tic      tdc      ew      rbr
    300.0    1550.     .6      0.0
\ $ CONCRETE
\ $ ninp
    13
NA2O      0.0015
SiO2      0.1298
CAO       0.4556
FE2O3     0.0033
AL2O3     0.0125
MGO       0.008
CO2       0.400
MNO       0.0003
BAO       0.0002
SRO       0.0002
CR2O3     0.0001
H2OEVAP   0.011
H2OCHEM   0.0017
\ $      rho      Tsol      Tliq
    2400.    1423.    1673.
\ $MELT
\ $nosi nmesi Tox Tml
    1    4    1980.  1980.
ZRO2      0.25
FE         32.2
NI         4.6
CR         9.2
MN         0.25
\ $POWER
\ $COOLANT
\ $ATMOSPHERE
\ $
\ $      VA      PA      TA      ngas

```

```

      0.5      1.E5      900.      1
N2          1.00
\ $POWER FOR OXIDIC AND METALLIC PHASES (ONLY IF IFP=2)
      0      13
      0.      0.0E4      180.      0.      185.      48000.      480.      47000.
      600.      3.0E4      840.      4.0E4      1294.      5.0E4      1300.      0.0E4
      1500.      0.E4      1505.      40000.      2400.      47000.      2405.      0.e4
      8000.      0.E4
\ $SURROUNDING TEMPERATURE HISTORY
\ $ NTP
      3
      0.      1650.      600.      1750.      7500.      1750.
\ $ABLATION
      1      0
H2OCLN
      8
      0.0      0.0      2084.      0.0      2085.      0.92      2164.      0.92
      2169.      0.02      2370.      0.01      2375.      0.00      8000.      0.01
      0      0      2
      0.0      350.      8000.      350.
\ $EMISSIONS
\ $IREO IREM IRES
TIMETIMETIME
\ $ NEO NEM NS
      1      1      1
      0.0      0.8
      0.0      0.8
      0.0      0.6
\ $VANESA
\ $IBUB KATIS INOPL
      1      1      0
\ $IF IVANFP = 1
\ $      CES      IOD      XEN      KRY      TE      BA      SN      RU
      0.002      0.0001      0.00      0.0      0.000      0.24      0.0      0.
\ $      MO      SR      RB      Y      TC      RH      PD      LA
      0.24      0.00      0.00      0.0      0.0      0.0      0.0      0.2
\ $      CE      PR      ND      SM      PU      AG      SB      NB
      0.25      0.0      0.0      0.0      0.0      0.00      0.0      0.0
\ $
\ $POOL SCRUBBING PARAMETERS
      20      2.3      1      1      1.0      1.0

```



# SWISS-2 Input Deck

```

swiss 2 met coolant 46kg ss-304 l/c sand
\$ Sidewall loss was assumed to be 30 kW
\$ Water addition was justified to provide 1.4 m of water thickness
\$ilyr icool igeom iccn ichem ifp isur iabl isp ipin iflm first imov ipg isr
    0    0    2    2    01    2    1    0    0    10    1    0    0    -2    1    0
\$ ITR  IFVAN  IVANFP  IUSER
&  0    1    1    0
\$ deltim      time0      timend      dprin      tprin
    5.        0.        2460.        10000.
\$nray      r0      z0
    57      0.0      0.
\$      zt      rad      hit      radc      rw      hbb nbot ncorn
    0.0      10.8    10.0000    0.10      11.0      0.30  10    7
\$      tic      tdc      ew      rbr
    300.0     1600.      .6      0.0
\$MELT
\$nosi nmesi  Tox      Tml
    1    4     1980.    1980.
ZRO2      0.25e4
FE         32.2e4
NI         4.6e4
CR         9.2e4
MN         0.25e4
\$ATMOSPHERE
\$
\$      VA      PA      TA      ngas
    0.5      1.E5    900.    1
N2         1.00
\$POWER FOR OXIDIC AND METALLIC PHASES (ONLY IF IFP=2)
    0    13
        0.      0.0E4      25.      0.      30.      4.5e8      480.      4.5e8
    1456.      4.5E8      1460.      0.0E8      1610.      0.0E8      1615.      4.5E8
    2125.      4.5E8      2130.      0.0e8      2225.      0.0e8      2230.      4.5e8
    2460.      4.5E8
\$SURROUNDING TEMPERATURE HISTORY
\$ NTP
    4
        0.      340.      2080.      340.      2085.      340.      2500.      340.
\$ABLATION
    1    0
\$COOLANT
H2OCLN
    8
    0.0      0.0      90.      0.0      95.      1.00e4      115.      1.00e4

```

```

120.      0.15e4      400.      0.15e4      405.      0.10e4      2600.  0.10e4
\$ temperature of water addition
\$ ncts nmts ncts
    0    0    2
0.0      300.      8000.      300.
\$EMISSIVITIES
\$IREO IREM IRES
TIMETIMETIME
\$ NEO  NEM  NS
    1    1    1
      0.0      0.8
      0.0      0.8
      0.0      0.6
\$VANESA
\$IBUB KATIS INOPL IDEAL
    1    1    1    1
\$IF IVANFP = 1
\$      CES      IOD      XEN      KRY      TE      BA      SN      RU
    0.0000    0.0000    0.00    0.0    0.000    0.24e4    0.0    0.
\$      MO      SR      RB      Y      TC      RH      PD      LA
    0.25e4    0.00    0.00    0.0    0.0    0.0    0.0    0.2e4
\$      CE      PR      ND      SM      PU      AG      SB      NB
    0.25e4    0.0    0.0    0.0    0.0    0.00    0.0    0.0
\$
\$POOL SCRUBBING PARAMETERS
    20      2.3      1      1      1.0      1.0

```

# BETA 7.1 Input Deck

BETA V7.1 MCCI. DATA OF IAE

\\$ilyr icool igeom icon ichem ifp isur iabl isp ipin iflm irst imov ipg  
 0 0 4 0 01 2 1 0 0 60 00 0 0 1 0 0

\\$ ITR IFVAN IVANFP

& 0 0 2 0

\\$ deltim time0 timend dprin tprin  
 2.0 0. 3600. 10000.

\\$nray r0 z0  
 63 0.0 0.3

\\$ zt rad hit radc rw hbb nbot ncorn  
 3 0.14 0.72 4.

.0 3.0  
 .159 2.996  
 .176 2.984  
 .186 2.968  
 .190 2.948  
 .190 2.900  
 .190 2.850  
 .190 2.800  
 .190 2.750  
 .190 2.700  
 .190 2.650  
 .190 2.600  
 .190 2.550  
 .190 2.500  
 .190 2.49  
 .190 2.48  
 .190 2.47  
 .190 2.46  
 .190 2.450  
 .190 2.445  
 .190 2.444  
 .190 2.442  
 .190 2.440  
 .190 2.438  
 .190 2.436  
 .190 2.435  
 .190 2.43  
 .19C 2.425  
 .190 2.42  
 .190 2.415  
 .190 2.41  
 .190 2.400  
 .190 2.368

.190	2.362
.191	2.358
.193	2.355
.194	2.352
.195	2.349
.198	2.329
.1985	2.321
.199	2.319
.1991	2.317
.1993	2.315
.200	2.312
.203	2.310
.216	2.261
.225	2.212
.238	2.053
.255	1.975
.281	1.858
.299	1.780
.333	1.624
.377	1.529
.402	1.411
.437	1.255
.480	1.060
.498	.982
.519	.884
.714	.003

\ \$concrete				
\ \$	tic	tdc	ew	rbr
	300.0	1653.	.6	0.0

\ \$ CONCRETE

\ \$ nimp  
17

TIO2	0.000
NA2O	0.0127
K2O	0.00
SIO2	0.335
CAO	0.0703
FE2O3	0.0493
AL2O3	0.0195
MGO	0.293
CO2	0.0106
MNO	0.00
FEO	0.0215
SRO	0.000
CR2O3	0.00

H2OEVAP 0.0376  
H2OCHEM 0.1105  
ZRO2 0.0000  
NIO 0.00

\\$ rho Tsol Tliq  
2400. 1493. 1653.

\\$MELT

\\$nosi nmesi Tox Tml  
7 4 1650. 2190.

UO2 0.0  
ZRO2 0.  
SiO2 10.0  
CAO 7.5  
MGO 0.0  
BAO 0.0  
SRO 0.0  
ZR 80.0  
FE 270.0  
NI 15.0  
CR 15.0

\\$POWER

\\$COOLANT

\\$ATMOSPHERE

\\$

\\$ VA PA TA ngas  
5000.0 1.E5 900. 1

N2 1.00

\\$POWER FOR OXIDIC AND METALLIC PHASES (ONLY IF IFP=2)

0 28

0.	5.74E5	61.	5.74E5	62.	7.72E5	200.	6.37E5
295.	4.25E5	310.	6.76E5	350.	6.18E5	400.	5.6E5
425.	5.79E5	600.	4.01E5	800.	3.09E5	1000.	2.41E5
1160.	1.8E5	1165.	2.22E5	1300.	1.93E5	1400.	2.22E5
1600.	2.41E5	1800.	2.48E5	2000.	2.27E5	2200.	2.12E5
2400.	1.93E5	2600.	1.83E5	2800.	1.64E5	3000.	1.64E5
3200.	1.5E5	3400.	1.5E5	3599.	1.45E5	3600.	0.0

\\$SURROUNDING TEMPERATURE HISTORY

\\$ NTP

\\$ 7

\\$0. 293. 100. 850. 160. 850. 300. 585.

\\$ 400. 460. 1200. 413. 3660. 413.

2

0. 1300. 4000. 1300.

\\$ABLATION

\\$EMISSIONS

\\$IREO IREM IRES

TIMETIMETIME

\\$ NEO NEM NS  
1 1 1

0.0 0.8

0.0 0.8

0.0 0.8

\\$VANESA

\\$IBUB KATIS INOPL

1 1 0

\\$IF IVANFP = 1

\\$	CES	IOD	XEN	KRY	TE	BA	SN	RU
	0.000	0.0000	0.00	0.0	0.147	1.42	0.20	0.0
\\$	MO	SR	RB	Y	TC	RH	PD	LA
	1.70	0.96	0.00	0.0	0.0	0.0	0.0	1.14
\\$	CE	PR	ND	SM	PU	AG	SB	NB
	2.32	0.0	0.0	0.0	0.0	1.40	0.3	0.3
\\$								

## DISTRIBUTION LIST

U.S. Nuclear Regulatory Commission  
Office of Nuclear Regulatory Research  
Washington, D.C. 20555

Attn: C.E. Ader, T-10K8  
S. Basu, T-10K8  
A. Behbahani, T-10K8  
Y. S. Chen, T-10K8  
J. M. Cortez, T-10F12  
F. Eltawila, T-10E47  
R. B. Foulds, T-10K8  
C. Gingrich, T-10K8  
M.W. Hodges, T-10E37  
T.L. King, T-10E37  
R. Lee, T-10K8  
D.L. Morrison, T-10F12  
J. A. Murphy, T-10F12  
A. Notafrancesco, T-10K8  
J. N. Ridgely, T-10K8  
A.M. Rubin, T-10K8  
T.P. Speis, T-10F12  
A. Szukiewicz, T-10E19  
C.G. Tinkler, T-10K8

U.S. Nuclear Regulatory Commission  
Office of International Programs  
Washington, D.C. 20555  
Attn: J. R. Shea, O-3B21

U.S. Nuclear Regulatory Commission  
Office of the EDO  
Washington, D.C. 20555  
Attn: L. Soffer, O-17G21

U.S. Nuclear Regulatory Commission  
Public Documents Room  
L Street, N.W.  
Washington, D.C.

AECL Technologies  
Whiteshell Laboratories  
Pinawa, Manitoba  
CANADA R0E 1L0  
Attn: L.A. Simpson

Agenzia Nazionale per la Protezione dell'  
Ambiente (ANPA/DISP)  
Via Vitaliano Brancati, 48  
I-00144 Rome, ITALY  
Attn: G. Petrangelli

Argonne National Laboratory  
9700 South Cass Avenue  
Argonne, IL 60439  
Attn: B. Spencer

Battelle Columbus Laboratories  
505 King Avenue  
Columbus, OH 43201  
Attn: J. Gieseke

Battelle Pacific Northwest Lab  
P.O. Box 999  
Richland, WA 99352  
Attn: Librarian

Belgonucleaire  
Rue de Champs de Mars, 25  
B-1050 Bruxelles  
BELGIUM  
Attn: E. Stubbe

Brookhaven National Laboratory  
Dept. of Nuclear Energy  
Upton, NY 11973  
Attn: I. Madni

B&W Nuclear Services Company  
Technical Library  
P.O. Box 10935  
Lynchburg, VA 24506  
Attn: Librarian

CNSNS  
Dr. Barragan 779  
Col Narvarte  
03020 MEXICO, D.F.  
Attn: R. A. Cano



Centre d'Etudes Nucleaires de Grenoble  
CEA-C.E.N.G  
Dept. Thermohydraulique de Physique  
B P 85X, F-38041 Grenoble Cedex  
FRANCE  
Attn: M. Georges Berthoud

Commission of The European Communities  
Directorate-General for Science, Research  
and Development (DG XII/F)  
Rue de la Loi, 200 (TE61-09)  
B-1049 Bruxelles  
BELGIUM  
Attn: E. Della Loggia

Commission of the European Communities  
Joint Research center, Ispra  
I-201020 Ispra (Varese)  
ITALY  
Attn: A.V. Jones

Committee on the Use of Atomic Energy for  
Peaceful Purposes  
69 Shipchenski Prokhorod Blvd.  
1574, Sofia BULGARIA  
Attn: Y. Yanev

Consejo de Seguridad Nuclear  
Justo Dorado 11  
28040 Madrid  
SPAIN  
Attn: A. Alonso

Cornell University  
Nuclear Science and Engineering  
Ithaca, NY 14853-7701  
Attn: K. B. Cady

Electric Power Research Institute  
3412 Hillview Avenue  
Palo Alto, CA 94303  
Attn: M. Merilo

Energy Research Inc.  
P.O. Box 2034  
Rockville, MD 20852  
Attn: M. Khatib-Rahbar

Fauske and Associates  
16W070 West 83rd Street  
Burr Ridge, IL 60521  
Attn: R. Henry

Federal Nuclear Radiation Authority of  
Russia  
Taganskaya, 34  
Moscow 109147  
RUSSIA  
Attn: A. Gutsalov

Finnish Center for Radiation and Nuclear  
Safety  
P.O. Box 268  
SF-00101 Helsinki  
FINLAND  
Attn: J.V. Sandberg

Forschungszentrum Karlsruhe (FZK)  
Postfach 3640  
D-76021 Karlsruhe  
GERMANY  
Attn: H. Alsmeyer

GRS Forschungsgelände  
W-8046, Garching  
GERMANY  
Attn: M. Firnhaber

Health and Safety Executive  
Nuclear Installations Inspectorate  
St. Peters House  
Balliol Road, Bootle  
Merseyside, ENGLAND  
Attn: J.P. Rothwell

Hungarian Atomic Energy Commission  
P.O. Box 565  
H-1374 Budapest  
HUNGARY  
Attn: L. Voross

Idaho National Engineering Laboratory  
P.O. Box 1625  
Idaho Falls, ID 83415  
Attn: Librarian

Institut de Protection et de Surete Nucleaire  
CEA-IPSN  
F-92265 Fontenay-aux-Roses, Cedex  
FRANCE  
Attn: M. Gomolinski

Institute for Atomic Energy Research  
H-1525 Budapest  
P.O. Box 49  
HUNGARY  
Attn: G. Gyenes

Institute of Nuclear Energy Research  
P.O. Box 3  
Lung-tan, TAIWAN 325, ROC  
Attn: S.I. Chang

International Atomic Energy Agency  
Div. Nuclear Reactor Safety  
Wagranestrasse 5  
A/1400 Vienna, AUSTRIA  
Attn: M. Janowski

Japan Atomic Energy Research Institute  
Severe Accident Research Laboratory  
Tokai-Mura, Ibaraki-Ken 319-11  
JAPAN  
Attn: J. Sugimoto

Jozef Stefan Institute  
Jamova 39  
61111 Ljubljana  
SLOVENIA  
Attn: B. Mavko

KEMA Netherland B.V.  
Utrechtseweg 310  
NL-6800 ET Arnhem  
NETHERLANDS  
Attn: P.J.T. Bakker

Knolls Atomic Power Laboratory  
P.O. Box 1072  
Schenectady, NY 12501  
Attn: J. Conine

Korea Atomic Energy Research Institute  
150 Dukjin-dong, Yoosung-gu  
Taejeon 305-353  
KOREA  
Attn: H.D. Kim

Korea Institute of Nuclear Safety  
P.O. Box 16, Daeduk-Danji  
Taejeon 305-353  
KOREA  
Attn: J.J. Lee

Los Alamos National Laboratory  
P.O. Box 1663  
Los Alamos, NM 87545  
Attn: Librarian

Massachusetts Institute of Technology  
Nuclear Engineering Department  
77 Massachusetts Avenue  
Cambridge, MA 02139  
Attn: M. Kazimi

Netherlands Energy Research Foundation  
P.O. Box 1, 1755 ZG Petten  
NETHERLANDS  
Attn: P. Stoop

Nuclear Power Engineering Corporation  
17-1 3-Chome, Toranoman, Minato-Ku  
Tokyo, 105  
JAPAN  
Attn: K. Takumi

Nuclear Regulatory Authority  
Bajkalska 27  
827 21 Bratislava  
SLOVAK REPUBLIC  
Attn: M. Stubna

Oak Ridge National Laboratory  
P.O. Box Y  
Oak Ridge, TN 37830  
Attn: Librarian

OECD Nuclear Energy Agency  
Le Seine-Saint Germain  
F-92130 Issy-les Moulineaux  
FRANCE  
Attn: J. Royen

Paul Scherer Institute  
Programm LWR-Sicherheit  
CH-5232 Villigen - PSI  
SWITZERLAND  
Attn: P. Hosemann

Pennsylvania State University  
Nuclear Engineering Department  
231 Sackett Building  
University Park, PA 16802  
Attn: A.J. Baratta

Purdue University  
Engineering Library  
West Lafayette, IN 47907  
Attn: Librarian

Rensselaer Polytechnic Institute  
Dept. of Nucl. Engr. & Engr. Physics  
Troy, NY 12180  
Attn: M.Z. Podowski

Royal Institute of Technology  
Division of Nuclear Power Safety  
100 44 Stockholm  
SWEDEN  
Attn: B.R. Sehgal

Russian Academy of Sciences  
Nuclear Safety Institute  
52 B. Tulsкая  
Moscow 113191  
RUSSIA  
Attn: L. Bolshov  
V. Strizhov (25)

Russian Research Center  
Nuclear Safety Department  
Moscow 123182  
RUSSIA  
Attn: V. Asmalov (5)  
V. Nikulshin

Sandia National Laboratories  
P.O. Box 5800  
Organization 6400  
Albuquerque, NM 87185  
Attn: J. Kelly  
D. Powers

State Office of Nuclear Safety  
Slezská 9  
120 00 Prague 2  
CZECH REPUBLIC  
Attn: M. Hrehor

Statens Kärnkraft Inspektion  
P.O. Box 27106  
S-10252 Stockholm  
SWEDEN  
Attn: W. Frid

Swiss Federal Nuclear Safety Inspectorate  
CH-5232 Villigen - HSK  
SWITZERLAND  
Attn: S. Chakraborty

Technical Research Center of Finland  
Vuorimiehentie 5  
SF-02150 Espoo  
FINLAND  
Attn: L. Mattila

Tractabel Energy Engineering  
Nuclear Department  
Avenue Ariane, 7/5D  
B-1200 Bruxelles  
BELGIUM  
Attn: J. Snoeck

UKAEA Winfrith Technology Center  
Winfrith  
Dorchester, Dorset DT2 8DH  
UNITED KINGDOM  
Attn: S. Kinnersly  
B.D. Turland

Ukrainian State Committee on Nuclear  
Radiation and Safety  
11-1 Observatorna Street  
24502, Kiev  
UKRAINE  
Attn: N. Steinberg

Universidad Politecnica de Madrid  
E.T.S. Ingenieros Industriales  
Jose Guterrez Abascal, 2  
28006 Madrid  
SPAIN  
Attn: F. Martin-Fuertes

U.S. Department of Energy  
Energy Library, Room G 034/GTN  
Washington, DC 20585  
Attn: Librarian

University of Maryland  
Engineering & Physical Science Library  
College Park, MD 20742  
Attn: Librarian

VATESI  
Gediminis Prospect 36  
Vilnius  
LITHUANIA  
Attn: A. Kaliatka

Vattenfall Energisystem AB  
Nuclear Safety/Avd GES  
Jamtlandsgatan 99  
S-162 15 Vallingby  
SWEDEN  
Attn: V. Gustavsson

NRC FORM 335 (2-89) NRCM 1102, 3201, 3202	U.S. NUCLEAR REGULATORY COMMISSION  <b>BIBLIOGRAPHIC DATA SHEET</b> <i>(See instructions on the reverse)</i>	1. REPORT NUMBER (Assigned by NRC, Add Vol., Supp., Rev., and Addendum Numbers, if any.)  <div style="text-align: center;">NUREG/IA-0129 Part I</div>				
2. TITLE AND SUBTITLE  An Assessment of the CORCON-Mod3 Code Part I: Thermal-Hydraulic Calculations		3. DATE REPORT PUBLISHED <table border="1" style="width: 100%; border-collapse: collapse;"> <tr> <td style="width: 50%; text-align: center;">MONTH</td> <td style="width: 50%; text-align: center;">YEAR</td> </tr> <tr> <td style="text-align: center;">September</td> <td style="text-align: center;">1996</td> </tr> </table>	MONTH	YEAR	September	1996
MONTH	YEAR					
September	1996					
5. AUTHOR(S)  V. Strizhov, V. Kanukova, T. Vinogradova, E. Aksenov/Russian Academy of Sciences V. Nikulshin/Russian Research Center		4. FIN OR GRANT NUMBER  6. TYPE OF REPORT  7. PERIOD COVERED (Inclusive Dates)				
8. PERFORMING ORGANIZATION - NAME AND ADDRESS (If NRC, provide Division, Office or Region, U.S. Nuclear Regulatory Commission, and mailing address, if contractor, provide name and mailing address.)  <table style="width: 100%;"> <tr> <td style="width: 50%;">           Institute of Nuclear Safety (IBRAE)            Russian Academy of Sciences            Moscow, Russia 113191         </td> <td style="width: 50%;">           Nuclear Safety Institute            Russian Research Center Kurchatov Institute            Moscow, Russia 123182         </td> </tr> </table>			Institute of Nuclear Safety (IBRAE) Russian Academy of Sciences Moscow, Russia 113191	Nuclear Safety Institute Russian Research Center Kurchatov Institute Moscow, Russia 123182		
Institute of Nuclear Safety (IBRAE) Russian Academy of Sciences Moscow, Russia 113191	Nuclear Safety Institute Russian Research Center Kurchatov Institute Moscow, Russia 123182					
9. SPONSORING ORGANIZATION - NAME AND ADDRESS (If NRC, type "Same as above"; if contractor, provide NRC Division, Office or Region, U.S. Nuclear Regulatory Commission, and mailing address.)  Division of Systems Technology Office of Nuclear Regulatory Research U.S. Nuclear Regulatory Commission Washington, DC 20555-0001						
10. SUPPLEMENTARY NOTES  Report published under an international agreement with the Russian Research Center and the Russian Academy of Sciences						
11. ABSTRACT (200 words or less)  <p>This report deals with the subject of CORCON-Mod3 code validation (thermal-hydraulics modeling capability only) based on MCC1 experiments conducted under different programs in the past decade. Thermal-hydraulic calculations (i.e., concrete ablation, melt temperature, melt energy, concrete temperature, and condensable and non-condensable gas generation) were performed with the code, and compared with the data from 15 experiments, conducted at different scales using both simulant (metallic and oxidic) and prototypic melt materials, using different concrete types, and with and without an overlying water pool. Sensitivity studies were performed in a few cases involving, for example, heat transfer from melt to concrete, condensed phase chemistry, etc. Further, special analysis was performed using the ACE L8 experimental data to illustrate the differences between the experimental and the reactor conditions, and to demonstrate that with proper corrections made to the code, the calculated results were in better agreement with the experimental data.</p> <p>Generally, in the case of dry cavity and metallic melts, CORCON-Mod3 thermal-hydraulic calculations were in good agreement with the test data. For oxidic melts in a dry cavity, uncertainties in heat transfer models played an important role for two melt configurations -- a stratified geometry with segregated metal and oxide layers, and a heterogeneous mixture. Some discrepancies in the gas release data were noted in a few cases. These discrepancies were attributed, in part, to condensed phase chemical reactions modeling and, in part, to experimental uncertainties. In the case of wet cavity, good agreement was found between the experimental data and code calculations except, again, for the gas release data. With proper corrections made to the code to account for correct condensed phase chemistry and with corrections made to the input data to account for experimental uncertainties, better agreement between code calculations and experimental data was noted.</p>						
12. KEY WORDS/DESCRIPTORS (List words or phrases that will assist researchers in locating the report.)  MOLTEN CORE-CONCRETE INTERACTIONS (MCCI), MCCI CODE, MCCI EXPERIMENTS, ACE, SURC, BETA, SWISS, MACE, CODE VALIDATION, MELT POOL THERMAL-HYDRAULICS, CONCRETE ABLATION, GAS GENERATION, CONDENSED PHASE CHEMISTRY, AEROSOLS, FISSION PRODUCTS RELEASE, HEAT TRANSFER MODELS, SLAG FILM MODEL, GAS FILM MODEL, INTERLAYER MIXING, EQUILIBRIUM CHEMISTRY, NON-EQUILIBRIUM CHEMISTRY, CORCON-MOD3, VANESA		13. AVAILABILITY STATEMENT <div style="text-align: center;">unlimited</div> 14. SECURITY CLASSIFICATION <div style="text-align: center;">(This Page) unclassified (This Report) unclassified</div> 15. NUMBER OF PAGES  16. PRICE				

UNITED STATES  
NUCLEAR REGULATORY COMMISSION  
WASHINGTON, DC 20555-0001

OFFICIAL BUSINESS  
PENALTY FOR PRIVATE USE, \$300

SPECIAL STANDARD MAIL  
POSTAGE AND FEES PAID  
USNRC  
PERMIT NO. G-67

120555139531 1 1AN1CI1R4  
US NRC-OADM  
DIV FOIA & PUBLICATIONS SVCS  
TPS-PDR-NUREG  
2WFN-6E7  
WASHINGTON DC 20555